

SELECTIVE TRANSFORMATION THROUGH TUNING CATALYTIC
MICROENVIRONMENTS FOR SUSTAINABILITY

A Dissertation

Presented to the Faculty of the Graduate School
of Cornell University

In Partial Fulfillment of the Requirements for the Degree of
Doctor of Philosophy

by

MICHELLE LEE

AUGUST 2020

© 2020 MICHELLE LEE

SELECTIVE TRANSFORMATION THROUGH TUNING CATALYTIC MICROENVIRONMENTS FOR SUSTAINABILITY

Michelle Lee, Ph. D.

Cornell University 2020

Selective transformations in chemical processes play an essential role in achieving sustainability, especially in developing energy-, cost-, and atom-efficient processes and obtaining clean energy. A highly selective catalyst is needed to achieve a selective chemical transformation. In this thesis, in an effort to achieve highly selective catalysts, we tune the catalytic microenvironment in two important chemical reactions; i.e. the nucleophilic ring-opening of trans-2,3-disubstituted epoxides, and the electroreduction of carbon dioxide to hydrocarbons. The understanding enabled by these studies reveals design principles for the development of selective catalysts and provides further insights into the reaction mechanism of existing catalysts.

To demonstrate how tuning catalytic microenvironment can increase the selectivity of chemical transformation, in the first study, we present a mechanism-inspired catalyst design for epoxide transformation to β -amino alcohol, an important building block in natural product synthesis and pharmaceuticals. We demonstrate that we can achieve a selective transformation by tuning the catalyst's first and second coordination sphere, ultimately, allowing for the development of a highly regioselective general methodology for nucleophilic ring-opening of trans-2,3-disubstituted epoxides.

In an effort to accurately evaluate how tuning catalytic microenvironment control the selectivity of electrochemical CO₂ reduction, in the second study, we identify factors that affect the measured performance of electrocatalysts that involve organic materials in CO₂ reduction reaction and propose standard protocols to improve the accuracy and precision of the reported data. We present several experiments necessary to ensure that the observed CO₂ reduction performance is from the electrocatalyst catalyzes the reduction of CO₂ molecules instead of potential side reactions. We show that standardizing the measurement and reporting protocols will facilitate the development of highly selective and active electrocatalysts.

To understand the effect of confined reaction space in controlling the selectivity in electrochemical CO₂ reduction, in the third study, we report design strategies for the synthesis of novel electrocatalysts for carbon dioxide reduction, where we demonstrate that the confined reaction space enables changes in reaction selectivity and can impart atypical catalytic capabilities to metals that are not otherwise active for CO₂R. We utilize metal-organic frameworks (MOFs) to provide the tailored confined reaction space for CO₂ reduction. These design strategies have the potential to provide a framework for catalyst design with improved catalytic activity.

To further gain mechanistic understanding in improving electrocatalysts' selectivity toward CO₂ reduction, in the fourth study, we utilize *in situ* and *ex situ* X-ray absorption spectroscopy (XAS) to investigate the electrocatalyst transformation in MOFs. We also develop a novel *in situ* XAS methodology to determine the active form of the electrocatalyst under operating conditions and to investigate the chemical state and the surrounding environment of the catalytic site during the electrochemical

CO₂ reduction. The combination of XAS measurements and product detection provides the mechanistic understanding that can stimulate the rational design for new classes of materials as CO₂ reduction electrocatalysts.

After gaining selectivity control for important C₁ products, such as CO and formic acid, we would like to understand how to obtain more energy-dense hydrocarbon, like ethylene. In the fifth study, we investigate the role of surface and subsurface oxygen on the production of organic products from CO₂ reduction over copper electrocatalysts through experiments and theoretical DFT calculation. Experimentally, we performed electrochemical CO₂ reduction on copper with various concentrations of buried oxygen as a function of time, showing that the ethylene production is time-dependent and prolonged-time leads only to H₂ evolution with negligible ethylene production. We utilize grand canonical potential-kinetics (GCP-K) DFT calculations to understand the experimental results. The combination of experimental results and theoretical calculation confirms the significance of surface and subsurface oxygen for the ethylene production in electrochemical CO₂ reduction on the copper surface.

Overall, these studies demonstrate that the activity and selectivity of the catalysts in chemical processes are not only dependent on the metal centers, but they are also heavily influenced by the local environment surrounding the metal centers. Therefore, to further improve the catalytic performance, it is crucial to also tune the catalytic microenvironments.

BIOGRAPHICAL SKETCH

Michelle Lee was born in Jember, Indonesia. Upon graduating high school in 2010, she attended Foothill College, a two-year community college in Los Altos Hills, CA. Then, she transferred to UC Berkeley as a chemistry major. She started her research experience as a chemist in a mechanical engineering laboratory at Stanford University. During her undergraduate years at UC Berkeley, she expands her research experience by working on the synthesis of molecular precursors to facilitate the bottom-up production of organic semiconductors. She was granted several fellowships and scholarships for her academic excellence and research contribution at Foothill College and UC Berkeley.

After graduating with a High Honor Bachelor in Science in Chemistry, she started her doctoral study in Chemistry at Cornell University in 2014. Following her passion to work on projects that contribute to sustainability, she joined Professor Geoffrey Coates' group to develop highly selective and active molecular catalysts for epoxides transformations to important pharmaceuticals building blocks and sustainable polymers. After gaining expertise in controlling molecular catalysts' selectivity, in 2018, she moved to Berkeley, CA to start collaboration projects with Dr. Francesca M. Toma's group at Lawrence Berkeley National Laboratory to design novel electrocatalysts for electrochemical carbon dioxide reduction. Under Professor Christopher Ober's and Dr. Toma's guidance, she developed novel electrocatalysts to selectively reduce carbon dioxide, a greenhouse gas, to chemical feedstock and fuels. Outside lab, she engaged in science outreach, developed STEM programs for K-12 students, and mentored Indonesian students who are applying to universities in the US.

She believes that education provides the tools to solve the most pressing problems the world facing today.

To my parents, brother, and friends who have believed in me and supported me
through this journey.

ACKNOWLEDGMENTS

This work was performed at Cornell University and Lawrence Berkeley National Laboratory and supported by a special committee consisting of Professor Christopher K. Ober (graduate advisor, Chemistry and Materials Science and Engineering), Dr. Francesca M. Toma (Lawrence Berkeley National Laboratory), Professor Paulette Clancy (Chemical and Biomolecular Engineering), and Professor Lara Estroff (Chemistry and Chemical Biology).

“Sometimes, it only takes one person to change your life. One to be there for you, to push you, and to believe in you.” I feel very fortunate and forever grateful to have not just one but also a group of people who help transform my Ph.D. journey.

I am would like to acknowledge the special committee members who have been generous with their time to guide and support my Ph.D. journey. Thank you for making the completion of my Ph.D. possible. I also would like to thank them for always encouraging me to be a productive and yet creative researcher.

I would like to especially thank Dr. Francesca M. Toma who has been a dear mentor since I started my undergraduate research at UC Berkeley. She has given me the freedom to explore my scientific curiosities and to expand my research projects and turn them into high interdisciplinary projects through collaborations. I am also grateful for the ability to have as many discussions as needed and developed new projects together. With your guidance and advice, I was able to grow to be the researcher that I am today.

I would like to acknowledge all of my colleagues and collaborators that I have had

the pleasure of working with since starting my Ph.D. journey. Our discussions have significantly influenced the progress of my research and my professional development. Specifically, I would like to acknowledge Professor Geoff Coates, Dr. Ivan Keresztes, Dr. Anne LaPointe, Dr. Maria Sanford, and Dr. Jessica Lamb at Cornell. I would like to acknowledge my colleagues at the Toma's lab: Dr. Aya Buckley, Dr. Alberto De Riccardis, Dr. Roman Kazantsev, Dr. Guiji Liu, Dr. Guosong Zeng, and David Larson. I would like to acknowledge my collaborators at Joint Center for Artificial Photosynthesis (JCAP): Dr. Walter Drisdell, Dr. Junko Yano, Dr. Jason K. Cooper, Dr. Wenhui Li, and Dr. Hui Li. I would like to acknowledge my collaborators at UC Berkeley: Professor Martin Head-Gordon, Professor F. Dean Toste, and Dr. Zhou Lin. Finally, I also would like to acknowledge my collaborators at Caltech: Professor William A. Goddard, Dr. Tao Cheng, and Dr. Soonho Kwon.

I would like to acknowledge my undergraduate mentees, Patrick Yorgkitis and Jennifer Garrison, whom I have the pleasure to work with. Thank you for allowing me to learn how to be an effective mentor.

Finally, I would like to thank my family and friends for their constant love and support. I am especially grateful to my parents, Koesworo Adisaputro and Lidya Falentina, for always believing in me and being my #1 supporters.

TABLE OF CONTENTS

BIOGRAPHICAL SKETCH.....	v
TABLE OF CONTENTS	x
LIST OF FIGURES	xv
LIST OF TABLES	xxii
LIST OF SCHEMES	xxv
LIST OF CHARTS	xxvi
CHAPTER 1	27
1.1. Abstract.....	28
1.2. Motivation	28
1.3. General challenges and approaches.....	30
1.4. Selective catalyst for epoxide transformations.....	34
1.4.1. The importance of epoxide transformations.....	34
1.4.2. Overview of nucleophilic ring opening (NRO) of epoxides	35
1.5. Selective catalyst for electrochemical carbon dioxide reduction	37
1.5.1. Introduction to electrochemical CO ₂ reduction.....	37
1.5.2. Challenges: reaction selectivity	38
REFERENCES	42
CHAPTER 2	49
2.1. Abstract	50

2.2. Introduction	50
2.3. Reaction Optimizations	52
2.4. Substrate Scope	56
2.5. Conclusion	60
2.6. Experimental Procedures	61
2.6.1. General Considerations	61
2.6.2. Synthetic Procedures	65
2.6.4. Characterization of complex 1i	67
CHAPTER 3	113
3.1. Abstract.....	114
3.2. Introduction	114
3.3. Factor to consider when measuring electrocatalytic activity	115
3.3.1. The effect of impurities on electrocatalytic activity	115
3.3.2. Reporting electrocatalytic activity.....	116
3.3.3. The importance of control experiments in electrocatalytic activity	123
3.4. Experimental procedure.....	133
3.4.1. Materials	133
3.4.2. Instrumentation	134
3.4.3. Electrochemical methods and product detection	134
3.4.4. Electrochemical experiments.....	136
3.5. Acknowledgements	138
REFERENCES	140
CHAPTER 4	143

4.1. Abstract.....	144
4.2. Introduction	144
4.3. Synthesis, Fabrication, and Characterization of MIL-53(Al)	147
4.4. Electrocatalytic Performance of MIL-53(Al).....	150
4.5. Conclusion.....	155
4.6. Experimental Procedures.....	156
4.6.1. Materials and Methods	156
4.6.2. Synthetic and Electrode Fabrication Procedures and Characterizations ..	158
4.6.3. Electrochemical Testing and Characterizations	162
4.7. Acknowledgements	175
REFERENCES	176
CHAPTER 5	182
5.1. Abstract.....	183
5.2. Introduction	184
5.3. Catalytic activity of MIL-53(Ga) for electrocatalytic CO ₂ R	187
5.4. XANES of MIL-53(Ga) under Electrochemical CO ₂ R conditions	192
5.5. Ex Situ XAS MIL-53(Al).....	196
5.6. In Situ EXAFS.....	198
5.7. Possible In Situ Formation of Single Atom Catalyst.....	200
5.8. Conclusion.....	202
5.9. Experimental Procedures.....	203
5.9.1. Materials.....	203
5.9.2. MIL-53(Ga) Synthesis.....	203

5.9.3. Preparation of Carbon Paper	204
5.9.4. Preparation of MIL-53(Ga) Suspension	205
5.9.6. Electrolyte preparation	205
5.9.7. Product detection	206
5.9.8. Materials characterization techniques.	207
5.10. Supplementary Figures	209
5.11. Supplementary Tables	219
5.12. Acknowledgements	224
REFERENCES	226
CHAPTER 6	232
6.1. Abstract.....	233
6.2. Introduction	233
6.3. Theoretical Prediction on Rates of HER and C ₂ Production	235
6.4. Experimental CO ₂ RR Activities of Cu and Cu ₂ O Catalysts	239
6.5. Long-term CO ₂ RR Activities of Cu and Cu ₂ O Catalysts.....	245
6.6. Conclusion.....	249
6.8. Experimental Procedures.....	251
6.9. Supplementary Figures	256
6.9.1. H ₂ and C ₂ production on Cu metal embedded in oxidized matrix (MEOM) model	256
6.10. Supplementary Tables	271
6.11. Acknowledgements	275
REFERENCES	276

CHAPTER 7	283
7.1. Abstract.....	284
7.2. Conclusions	284
7.3. Future direction	287
REFERENCES	290

LIST OF FIGURES

Figure 1-1. United Nations Sustainable Development Goals (SDGs).	29
Figure 1-2. Selective transformation, a chemical process that requires catalyst to selectively produce the desired products.	30
Figure 1-3. Homogeneous and heterogeneous catalysis.....	32
Figure 1-4. Selected epoxides transformations.	35
Figure 1-5. The importance of nucleophilic ring opening (NRO) of epoxides.	36
Figure 1-6. The synthesis of (S)-(-)-Metoprolol and (-)-Bulgecinine require a highly regioselective NRO.	36
Figure 1-7. Limitation of the existing methodologies for NRO of internal epoxides. .	37
Figure 1-8. The aqueous heterogeneous electrochemical CO ₂ reduction is performed using two-compartment electrochemical cell. The process can produce up to 16 different carbon-based products and the competing reaction of hydrogen evolution reaction (HER).	38
Figure 1-9. Observed reaction selectivity of metal foils as electrocatalyst for CO ₂ R.	39
Figure 2-1. Stejskal-Tanner plot of a 500 MHz ¹ H diffusion NMR experiment of 1i in CDCl ₃ at -55°C. The slope of each line corresponds to the negative of the diffusion coefficient. With the exception of CH ₂ Cl ₂ , each data point represents the average of two or three well-resolved resonances.	71
Figure 3-1. Modifiers to promote H ₂ , CO or formic acid formation.	117
Figure 3-2. Partial current densities for H ₂ , CO and formic acid as determined by GC and HPLC (left) and normalized by double layer capacitance (right).	119

Figure 3-3. Partial current densities for H ₂ , CO and formic acid as determined by GC and HPLC (left) and normalized by double layer capacitance (right).....	120
Figure 3-4. Plot of partial current of formic acid vs. partial current of H ₂ from Ox Cu and modified surfaces.....	121
Figure 3-5. Plot of partial current of CO vs. partial current of formic acid from Ox Cu and modified surfaces.....	122
Figure 3-6. Plot of partial current of CO vs. partial current of H ₂ from Ox Cu and modified surfaces.....	123
Figure 3-7. Chronoamperometry of Cu modified with 9, both with and without Nafion binder.....	125
Figure 3-8. Chronoamperometry traces for Ox Cu and experiments with 1 and 2.	127
Figure 3-9. Chronoamperometry traces of neutral polymers as modifiers on Cu.	128
Figure 3-10. Chronoamperometry traces of cationic molecules as modifiers on Cu.	129
Figure 3-11. Cyclic voltammetry of CoPc-Pyr (A) and CoPc (B) deposited on carbon paper under CO ₂ (red) and N ₂ (blue) atmospheres in 0.05 M K ₂ CO ₃ at 100 mV/s with 5 sccm for the flow rate of CO ₂ (pH = 6.8). CV of carbon paper (CP) in CO ₂ atmosphere (black) is reported for comparison.	131
Figure 3-12. (A) Schematic of a two-chamber electrochemical cell used for CO ₂ R experiments (left). Carbon paper cathode with physisorbed CoPc-Pyr used as working electrode (right). Chronoamperometry measurements for (B) CoPc-Pyr and (C) CoPc at various potentials under CO ₂ R conditions.....	132
Figure 4-1. Synthesis and characterization of Al-confined metal organic framework, MIL-53(Al).....	147

Figure 4-2. Fabrication and characterization of working electrodes	149
Figure 4-3. Characterization of MIL-53(Al) electrocatalysts for CO ₂ R	150
Figure 4-4. Faradaic efficiency of different CO ₂ R products	152
Figure S4-1. White powder of synthesized MIL-53(Al) was placed on top of carbon tape that was attached to a disposable SEM stage. Several SEM images of the synthesized MIL-53(Al) were taken at different magnifications.	160
Figure S4-2. Two-compartment flow cell used for electroreduction of carbon dioxide.	164
Figure S4-3. Using two-compartment flow cell electrochemical setup, the electrolyte solution in the working compartment was sparged for 10 minutes with N ₂ or CO ₂ . .	165
Figure S4-4. Scanning electron microscopes-energy-dispersive X-Ray (SEM-EDX) of Al of the surface of the working electrodes before and after 4 hours 30 minutes electrochemical testing at five different potentials (-1.1 V, -1.0 V, -0.9 V, -0.8 V, and -0.7 V vs RHE) to ensure the presence of the elemental components of MIL-53(Al) on the surface of working electrodes.....	167
Figure S4-5. Mechanism of CO ₂ reduction through two different pathways: carbon-bound pathway leads to CO formation and oxygen-bound pathway or direct addition of CO ₂ to a surface metal-hydride lead to formic acid formation. ^{35,39}	170
Figure S4-6. Scanning electron microscopes-energy-dispersive X-Ray (SEM-EDX) of Al of the surface of the working electrodes before and after 3 hours and 15 minutes electrochemical testing at three different potentials (-1.1 V, -1.0 V, and -0.9 V vs. RHE) to ensure the presence of the elemental components of Al(OH) ₃ on the surface of working electrodes.	172

Figure S4-7. Exponential relationship between applied potential (V vs RHE) and turnover frequency (TOF) for carbon-based products.....	174
Figure 5-1. Electrocatalytic performance evaluation of MIL-53(Al) and MIL-53(Ga) as electrocatalyst for carbon dioxide reduction.	189
Figure 5-2. In situ XAS and electrochemical testing for MIL-53(Ga).	192
Figure 5-3. Ex situ XANES for MIL-53(Al).	198
Figure 5-4. R-space of EXAFS measurement and fitting of Ga foil, MIL-53(Ga) working electrode before and after	200
Figure S5-1. Powder x-ray diffraction (XRD) of the synthesized MIL-53(Ga) showing experimental (red pattern) and simulated (black pattern). ³⁶	209
Figure S5-2. Similarities in powder x-ray diffraction (XRD) of synthesized MIL-53(Ga) (experimental (red pattern) and simulated (black pattern)) with powder XRD of simulated MIL-53(Al). ^{35,36}	210
Figure S5-3. Scanning electron microscope (SEM) imaging of: a.) MIL-53(Ga) b.) MIL-53(Al).....	211
Figure S5-4. Scheme to fabricate working electrodes. ¹²	211
Figure S5-5. Two-compartment flow cell used for electroreduction of carbon dioxide.	212
Figure S5-6. In situ XAS setup in beamline 9-3 at Stanford Synchrotron Radiation Lightsource.	213
Figure S5-7. Modified working electrode for in situ XAS to allow x-rays to be reflected back to the detector.	214
Figure S5-8. The second cycle of 3 hours cycle of in situ XANES measurement of the	

same MIL-53(Ga) working electrode after being used in 3 hours electrochemical testing in CO ₂ -saturated 0.05 M of potassium carbonates at three different applied potentials for 1 hour each.	214
Figure S5-9. NH ₂ -MIL-53(Ga) electrode in CO ₂ -saturated 0.05 M potassium carbonates are exposed to the beam for 8 scans with 8 minutes exposure per scan...	215
Figure S5-10. EXAFS measurement and fitting of MIL-53(Ga) working electrode after three different applied potentials starting from -0.9 V vs. RHE to -1.1 V vs. RHE for 65 minutes each. a.) in R-space b.) in K-space. The fitted R range is 0 - 6 Å and k range is 2.5 – 9.1 Å ⁻¹	217
Figure S5-11. Scanning electron microscopes-energy-dispersive X-Ray (SEM-EDX) of Ga of the surface of the working electrodes before and after 6 hours 30 minutes electrochemical testing at three different potentials (-1.1 V, -1.0 V, and -0.9 V vs. RHE) to ensure the presence of the elemental components of MIL-53(Ga) on the surface of working electrodes.	218
Figure 6-1. GPC-K DFT calculations for different Cu phases and their relation to C ₂ production.	237
Figure 6-2. Stable phases and catalytic activities of polycrystalline Cu and Cu ₂ O under CO ₂ RR.	241
Figure 6-3. Monitoring surface topography or roughness over Cu and Cu ₂ O under CO ₂ RR <i>Quasi in-situ</i> EC-AFM images of polycrystalline Cu.	244
Figure 6-4. Long-term CO ₂ RR measurements over Cu, Cu ₂ O (thin) and Cu ₂ O (thick)	247
Figure 6-5. Chemical composition analysis of polycrystalline Cu through long-term	

CO ₂ RR.....	249
Figure S6-1. Top and side views of various surface phases considered in surface free energy diagrams.....	257
Figure S6-2. Full relaxation after removing all oxygen from Cu ₂ O(111).....	258
Figure S6-3. The atomic configurations of CO dimerization reaction.....	259
Figure S6-4. The atomic configurations of Volmer reactions.....	260
Figure S6-5. The atomic configurations of Heyrovsky reactions.....	261
Figure S6-6. SEM images of (A) as-prepared Cu; (B) as-prepared Cu ₂ O; (C) Cross-section of as-prepared Cu ₂ O.....	262
Figure S6-7. <i>ex-situ</i> GIXRD analysis of Cu ₂ O over 1h electrolysis (A) at -1.0 V _{RHE} in N ₂ -saturated 0.1 M KHCO ₃ electrolyte (pH 8); (B) at -0.3 V _{RHE} and -0.6 V _{RHE} in CO ₂ -saturated 0.1 M K ₂ CO ₃ electrolyte (pH 7).....	262
Figure S6-8. Two-compartment flow cell used for bulk electrolysis of carbon dioxide.	263
Figure S6-9. XPS analysis on as-prepared Cu: (A) Cu _{2p} spectra of Cu; (B) O _{1s} spectra of Cu.	264
Figure S6-10. SEM images of (A) thin-Cu ₂ O; (B) Cross-section of thin-Cu ₂ O.	264
Figure S6-11. Pt _{4d} spectra of Cu through long-term CO ₂ RR at -1 V _{RHE} in 0.1 M K ₂ CO ₃ electrolyte (pH 7), a Pt foil was used as comparison	265
Figure S6-12. <i>ex-situ</i> GIXRD analysis of thick-Cu ₂ O over 16 h CO ₂ RR at -1.0 V _{RHE} in CO ₂ -saturated 0.1 M K ₂ CO ₃ electrolyte (pH 7).	266
Figure S6-13. AR-XPS analysis of Cu _{2p} spectra on Cu through long-term CO ₂ RR..	267
Figure S6-14. AR-XPS analysis of Cu LMM spectra on Cu through long-term CO ₂ RR	

.....	268
Figure S6-15. AR-XPS analysis of Cu _{2p} spectra on thin-Cu ₂ O through long-term CO ₂ RR.....	269
Figure S6-16. AR-XPS analysis of O _{1s} spectra on Cu through long-term CO ₂ RR.....	270
Figure 7-1. The developed selective transformations in this thesis can offer solutions for the highlighted UN SDGs. ¹	286
Figure 7-2. The combination of homogeneous and heterogeneous catalysis allows for more stable catalysts particle with molecularly defined active sites.	287
Figure 7-3. Maps of product distribution of various metal-organic frameworks (MOFs) as electrocatalysts for CO ₂ R. ^{4, 9-12}	289

LIST OF TABLES

Table 2-1. Catalyst optimization ^a	54
Table 2-2. Reaction optimization for 1i using epoxide 2a and aniline (3a) ^a	56
Table 2-3. Epoxide substrate scope using aniline (3a) as the nucleophile	58
Table 2-4. Nucleophile scope using 2a as the substrate ^a	59
Table S2-1. Chemical shifts for 1i and Al-Cl determined at -55 °C in CDCl ₃	71
Table 3-1. Faradaic efficiencies and total current of Ox Cu and Cu functionalized solely with Nafion at varying loadings.....	124
Table 3-2 . Faradaic efficiency data with and without Nafion with 8	126
Table 3-3. Faradaic efficiency data with and without Nafion with 9	126
Table 3-4. Functionalized Cu under N ₂	130
Table S4-1. Fabricated working electrode containing MIL-53(Al) under N ₂ atmosphere.....	166
Table S4-2. Background: plain carbon paper under CO ₂ atmosphere.....	166
Table S4-3. Background: plain carbon paper and Nafion (0.17 μL) under CO ₂ atmosphere.....	166
Table S4-4. Initial screening of CO ₂ R at applied potentials of -0.7 V vs RHE and -0.8 V vs RHE.....	167
Table S4-5. Faradaic efficiency of MIL-53(Al) catalyzed CO ₂ reduction at different applied potentials.....	168
Table S4-6. Average and error analysis of faradaic efficiency of MIL-53(Al) catalyzed CO ₂ reduction at different applied potentials.	168

Table S4-7. Activity and selectivity of Molecular Organic Frameworks as CO ₂ R electrocatalysts.	169
Table S4-8. Activity and selectivity of MIL-53(Al) compared to Al foil as CO ₂ R electrocatalysts.	170
Table S4-9. Faradaic efficiency of Al(OH) ₃ catalyzed CO ₂ reduction at different applied potentials.	171
Table S4-10. Average and error analysis of faradaic efficiency of Al(OH) ₃ catalyzed CO ₂ reduction at different applied potentials.	171
Table S4-11. Turnover frequency (TOF) calculation based on faradaic efficiency and current using:	173
Table S5-1. Fabricated working electrode containing MIL-53(Ga) under Ar atmosphere.	219
Table S5-2. Background: plain carbon paper under CO ₂ atmosphere.	219
Table S5-3. Background: plain carbon paper and Nafion (0.17 μL) under CO ₂ atmosphere.	220
Table S5-4. Faradaic efficiency of MIL-53(Ga) catalyzed CO ₂ reduction at different applied potentials.	220
Table S5-5. Average and error analysis of faradaic efficiency of MIL-53(Ga) catalyzed CO ₂ reduction at different applied potentials.	221
Table S5-6. Turnover frequency (TOF) calculation based on faradaic efficiency and current using	221
Table S5-7. Faradaic efficiency of MIL-53(Ga) catalyzed CO ₂ reduction in modified cell designed for in situ XAS at different applied potentials.	223

Table S5-8. Average and error analysis of faradaic efficiency of MIL-53(Ga) catalyzed CO ₂ reduction in modified cell designed for in situ XAS at different applied potentials.....	223
Table S5-9. EXAFS fitting results for MIL-53(Ga) working electrode after three different applied potentials (-0.9 V, -1.0 V and -1.1 V)	224
Table S6-1. Total energy (F), number of electrons (n), electrochemical potential (mu) for all eight states considered in surface Pourbaix diagram.	271
Table S6-2. Total energy (F), number of electrons (n), electrochemical potential (mu) for all elementary reactions considered in this study.	273
Table S6-3. Faradaic efficiencies of CO ₂ RR and total current for (A) Cu and (B) Cu ₂ O, reported in Fig. 2E.	274

LIST OF SCHEMES

Scheme 2-1. Regioselective ring opening of different classes of epoxides.	50
--	----

LIST OF CHARTS

Chart 2-1. Catalysts screened for the regioselective ring opening of epoxides.....	53
--	----

CHAPTER 1

INTRODUCTION

1.1. Abstract

Selective transformations in chemical processes play an essential role in achieving sustainability, especially in developing energy-, cost-, and atom-efficient processes and obtaining clean energy. A highly selective catalyst is required to achieve selective transformation. However, most highly selective catalysts are made unsustainably out of transition metals. Therefore, it is necessary to establish novel design strategies to develop highly selective catalysts from earth-abundant metals. This chapter will provide motivation and general challenges for selective transformation for sustainability. This thesis will focus on developing selective catalysts for two important chemical reactions, epoxide transformations and electrochemical CO₂ reduction.

1.2. Motivation

Earth's resources are abundant yet finite. We as humans are increasingly aware that we need to secure the needs of the present without compromising the ability of future generations to meet their own needs.¹ Therefore, there is a need for a strategy to obtain sustainability through the design of chemical processes that have reduced impacts on humans and the environment.² Realizing that to achieve sustainability will require the development of both scientific innovations and social policies, the United Nations (UN) adopted 17 sustainable development goals (SDGs) in Fall 2015 where all of the countries of the world agreed to work on achieving these goals by 2030 (Figure 1-1).³



Figure 1-1. United Nations Sustainable Development Goals (SDGs).

Chemistry is instrumental in achieving these sustainable goals because of its ability to offer a solution, specifically in increasing energy efficiencies, reducing greenhouse gas (GHG) emission, developing sustainable materials, and promoting new uses for current waste.^{4, 5} Specifically, chemical catalytic processes play an important role in achieving sustainability through chemistry (Figure 1-2). The catalyst in chemical processes helps reduce waste products as a result of side reactions by increasing the selectivity of chemical reactions and increases productivity by accelerating the rates of reactions, ultimately resulting in a selective transformation.¹ As a result of added benefits, such as lower energy consumption, reduced GHG emissions, and overall financial benefit, chemical processes with catalysts have become ubiquitous in our daily lives with more than 90% of current chemical processes involving catalysts.⁶ Therefore, a selective transformation has the potential to improve the energy-, cost-, and atom-efficiency of chemical processes allowing us to achieve significant steps toward sustainability.



Figure 1-2. Selective transformation, a chemical process that requires catalyst to selectively produce the desired products.

1.3. General challenges and approaches

The key challenge to achieving selective transformations for sustainability is developing highly selective and active catalysts for that specific chemical processes. For example, the discovery of TS-1, titanium-doped zeolite with the MFI (Mordenite Framework Inverted) type framework,⁷ has enabled the development of large-scale processes for the synthesis of important chemical building blocks, such as propylene oxides that are important for the production of polyether polyols and polyurethane, and caprolactam that is widely used for nylon 6 filament, fibers and plastic production, by using hydrogen peroxide as oxidant.⁸ Prior to using TS-1 catalyst, to produce propylene oxides, the hydroperoxide processes also produce 3 times more of the side products than propylene oxides. This old process is unselective and uneconomical.⁹ These new processes with the TS-1 catalyst, which shows exceptional catalytic activity in hydroxylation and oxidation reactions,¹⁰⁻¹² have reduced process complexity and risks compared to the previous processes, lower energy consumption, and reduced waste. By using a transition metal catalyst in a zeolite type framework in chemical processes to produce propylene oxides, caprolactam, and phenols, it allows more sustainable chemical processes. Therefore, it is important to have a capability to develop a

highly selective catalyst to achieve a more sustainable chemical process.

To develop a high performing catalyst, we need to understand different types of catalysts. In general, there are two types of catalysts, a homogeneous and a heterogeneous catalyst (Figure 1-3). A homogeneous catalyst is a catalyst that is in the same phase as the reactants, while a heterogeneous catalyst is in a different phase than the reactants. Both catalysts have their advantages; a homogeneous catalyst has the predictable control of both activity and selectivity upon ligand modifications, while a heterogeneous catalyst is often more stable compared to a homogeneous catalyst. To improve the catalyst's performance, it is common to tune several components surrounding the catalytic active sites. In most cases, the catalytic active site is the metal center.

In homogeneous catalysis, the catalyst is usually a molecularly defined compound consisting of a metal center surrounded by ligands.¹³ In a catalyst, ligands are defined as the array of molecules and ions that are directly attached to the metal center. Tuning the ligand can also be referred to as tuning the first coordination sphere. Additionally, there are solvents and counteranions/cations that can be tuned to improve catalytic performance. The interaction between catalyst and solvent and counteranion/cation is also called the second coordination sphere interaction. The second coordination sphere interaction in homogeneous catalysis can be categorized as the catalytic microenvironment.

In heterogeneous catalysis, it is common to improve catalytic performance by changing the active sites that are usually metal centers. We can also tune the catalytic microenvironment that consists of the solvent and environment surrounding the active sites within the catalyst particles to achieve selective transformations. In both homogeneous and heterogeneous catalytic systems,

catalytic performance with specific metal centers can be further improved by tuning the catalytic microenvironments.

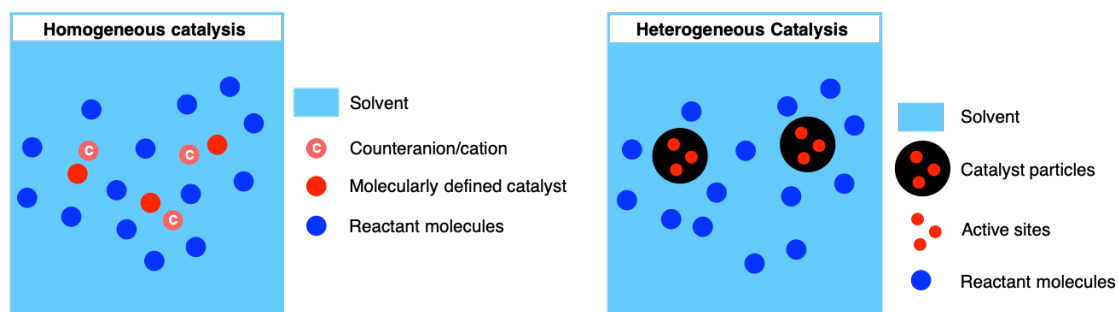


Figure 1-3. Homogeneous and heterogeneous catalysis.

Currently, for the vast majority of chemical transformations, extensive efforts have been devoted to studying catalysts that are derived from transition metals, especially from precious metals. Precious metals are the transition metal elements that can be found in the second and third rows of the periodic table and have high economic value because of their limited availability in the earth's crust.¹⁴ The commonly used precious metals are rhodium, palladium, platinum, ruthenium, iridium, gold, silver, and osmium.¹⁵ The catalysts with these precious metals are preferred because of their stability,¹⁶ enhanced activity, and unique selectivity.¹⁷ These catalysts' stability toward corrosion and oxidation allows for the transformations to be performed under ambient conditions without the need for a rigorously air-free environment that is a more expensive process. These precious metal catalysts demonstrate enhanced catalytic activity because they can readily undergo two-electron oxidation-state changes to facilitate many important metal catalyst mediated transformations via oxidative addition or reductive elimination. Finally, they show unique selectivity for a specific type of transformation depending on metal center.¹⁷

However, these precious metal catalysts have some challenges associated with

their continued use in chemical processes. These precious metals are scarce and expensive.¹⁸ The mining and refining to obtain these metals are often energy-intensive and result in increased GHG emissions. These precious metals are often toxic and require special treatments for the waste produced by the chemical processes.¹⁹ Overall, most of the existing catalysts are not energy- and cost-effective and still produce harmful waste, thus, not the sustainable approaches.

Using the low cost, high natural abundance, and low toxicity metals is the more sustainable approach. These metals include first-row transition metals, such as titanium, vanadium, chromium, manganese, iron, cobalt, nickel and copper, and main group metals, such as aluminum. However, less effort is invested in this more sustainable approach due to some significant challenges that come with these more sustainable metals. These metals are often easily oxidized and require an inert atmosphere. They also prefer to undergo a single-electron transfer process instead of a two-electron redox process that is commonly required in the metal catalysts mediated processes. Therefore, the single-electron transfer ability limits the applicability of catalysts with these more sustainable metals. Additionally, the single-electron transfer process usually results in the generation of free radicals that can lead to unselective chemical processes.

Even though there are many challenges with the use of first-row transition metals and main group metals as catalysts, the potential benefits for more sustainable chemical processes are significant. In recent years, many successful approaches to improving their catalytic performance have been reported.²⁰⁻²⁵ The most notable approach is by drawing inspiration from highly efficient enzymatic systems in which earth-abundant elements catalyze chemical transformations with high selectivities, such as the *Mycobacterium tuberculosis* CYP121 that contains a

heme-iron center.²⁰ Challenging catalytic transformations would benefit from similar design principles, in which catalytic metal centers are placed in uniquely tailored, confined reaction spaces that promote specific reaction pathways to enhance selectivity.^{26, 27} In this thesis, we focus our efforts on achieving highly selective catalysts by tuning the catalytic microenvironment of the chemical processes. We provide different examples of catalytic systems that can reveal design principles that enable the development of selective catalysts and provide further insights into the reaction mechanism on existing catalysts. To demonstrate how tuning catalytic microenvironment can increase the selectivity of chemical transformation, we present a mechanism-inspired catalyst design for epoxide transformation to β -amino alcohol, an important building block in natural product synthesis and pharmaceuticals. We also provide design strategies for the synthesis of novel electrocatalysts for carbon dioxide reduction with controlled and improved selectivity and activity.

1.4. Selective catalyst for epoxide transformations

1.4.1. The importance of epoxide transformations

Epoxides transformations are important because they can be transformed into a broad variety of useful products and intermediates (Figure 1-4). They can be transformed into a variety of useful polymers, such as polyethers through homopolymerization, polycarbonates through copolymerization with carbon dioxide, and polyesters through copolymerization with cyclic anhydrides (Figure 1-4.A-C).²⁸⁻³⁰ Epoxides can also undergo carbonylation reactions to produce β -lactones,^{34, 35} isomerization to produce aldehydes or ketones,^{32, 36} and deoxygenation to produce alkenes³⁷⁻³⁹ (Figure 1-4.D-F). Nucleophiles can attack the electrophilic carbons resulting in the most commonly studied class of reactions,

nucleophilic ring-opening of epoxides (NRO) (Figure 1-4.G).³¹⁻³³ NRO is an important class of reactions because it has a broad substrate scope for the epoxides and nucleophiles. This class of reaction will be further discussed in the next section. Overall, epoxides are highly important and versatile building blocks in organic synthesis accompanied by two possible stereogenic centers upon ring-opening of the epoxides.

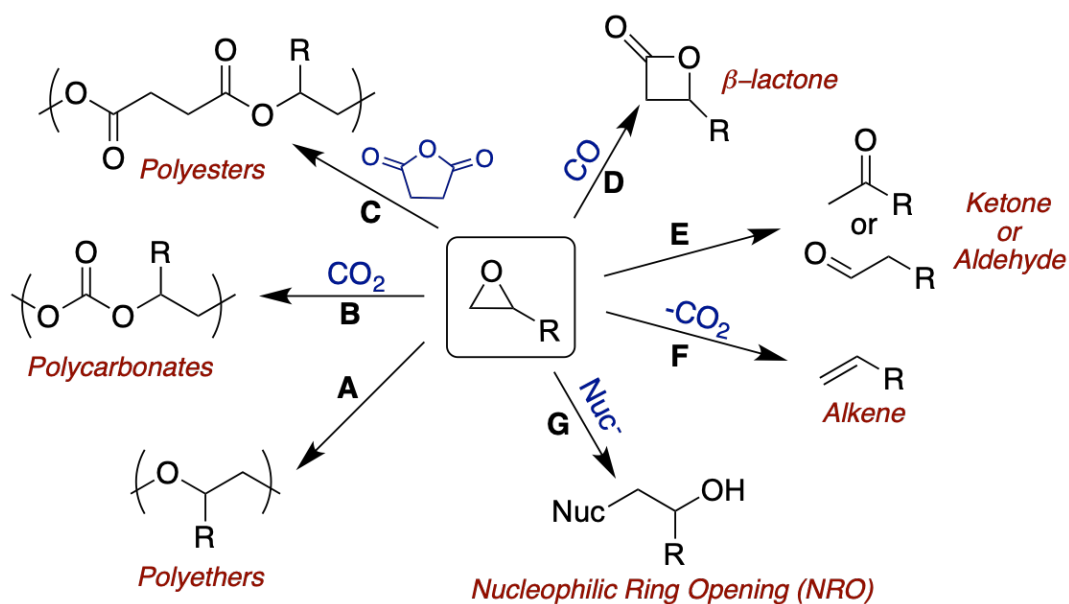


Figure 1-4. Selected epoxides transformations.

1.4.2. Overview of nucleophilic ring opening (NRO) of epoxides

Nucleophilic ring opening (NRO) of epoxides is the most commonly studied epoxide transformation because it has a broad substrate scope of epoxides and nucleophiles making these transformations highly versatile. Additionally, upon ring-opening of the epoxides, they provide two possible stereogenic centers making NRO an important reaction to synthesize intermediates in asymmetric synthesis. Furthermore, this transformation is important in forming building blocks or intermediates for natural product synthesis and pharmaceuticals, including (S)-(-) metoprolol,⁴⁰ a potential cardiovascular drug; (-)-bulgecinine,⁴¹ an antibacterial

and antifungal agent, BMS-200475,⁴² an anti-HBV agent; and Liposidomycins B,⁴³ a class of antibiotics (Figure 1-5).

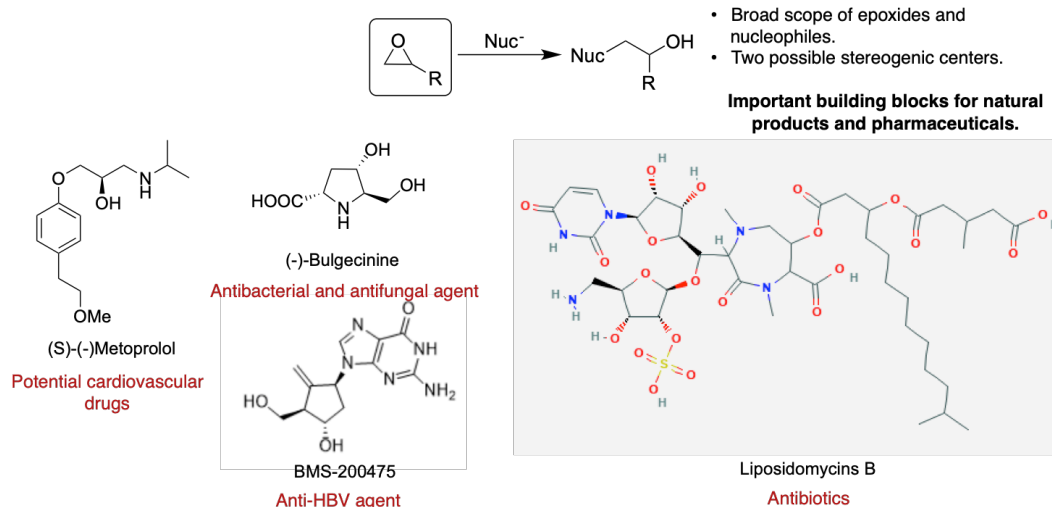


Figure 1-5. The importance of nucleophilic ring opening (NRO) of epoxides.

The synthesis of (S)-(-)-Metoprolol requires a highly regioselective NRO of a terminal epoxide while (-)-Bulgecinine requires a highly regioselective NRO of an internal epoxide (Figure 1-6).

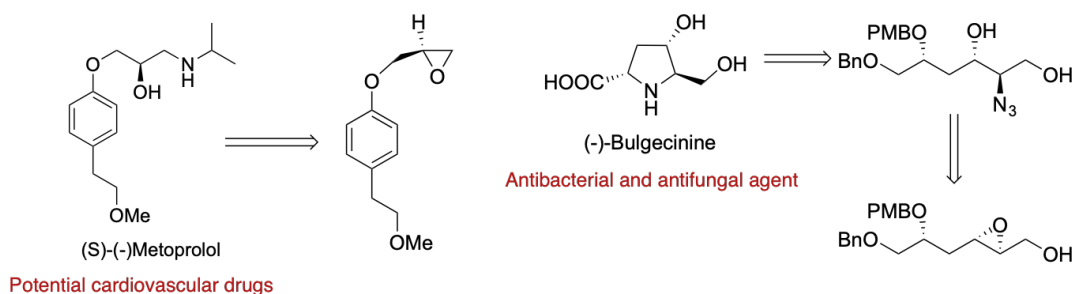


Figure 1-6. The synthesis of (S)-(-)-Metoprolol and (-)-Bulgecinine require a highly regioselective NRO.

Many reported general methodologies can selectively open terminal epoxides. However, these methodologies are often not selective for internal epoxides (Figure 1-7) because the regioselectivity is not catalyst-controlled, but substrate-controlled.

Previous work: **substrate-controlled** regioselective NRO

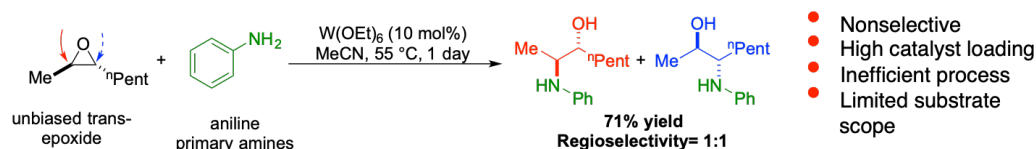


Figure 1-7. Limitation of the existing methodologies for NRO of internal epoxides.

In chapter 2, we will discuss in detail our design strategy for a highly regioselective NRO methodology for unbiased epoxides to achieve β -amino alcohol, an important building block in natural product synthesis and pharmaceuticals, and how this methodology addresses the limitation of existing methodologies.

1.5. Selective catalyst for electrochemical carbon dioxide reduction

1.5.1. Introduction to electrochemical CO₂ reduction

The extensive use of fossil fuels has led to the progressive accumulation of carbon dioxide (CO₂), a greenhouse gas (GHG), in the atmosphere.^{44, 45} The increase of GHG in the atmosphere has contributed to global warming. Electrochemical reduction of carbon dioxide (CO₂R) offers an efficient strategy to tackle global warming by reducing the presence of GHG in the atmosphere while concurrently producing numerous valuable carbon-based products.^{46, 47} In this thesis, we will discuss aqueous heterogeneous electrochemical CO₂R, a process where CO₂ is electrochemically reduced in an ambient environment with the help of water, electricity that can be made renewable through solar or wind energy, and electrocatalyst.⁴⁸ The process happens in a two-compartment electrochemical cell (Figure 1-8). In the cathode side, electrical energy drives electrons from the cathode in an electrochemical cell to reduce CO₂ molecules dissolved in a water-based, ionically conducting electrolytes. In the anode side, electrical energy drives

The diagram illustrates the electrochemical reduction of CO₂ in a reactor. On the left, the overall reaction is shown: $\text{CO}_2 + n(\text{H}^+ + \text{e}^-) \xrightarrow{\text{Cu}} \text{P} + m(\text{H}_2\text{O})$. Below this, a list of 16 chemical products is displayed, including alkenes, alcohols, aldehydes, ketones, and carboxylic acids. A green label states "Up to 16 products".

On the right, a schematic of the reactor is shown. It consists of a Cathode, a Membrane, and an Anode. The Cathode is connected to a power source (A) and a voltmeter (V). The Membrane separates the Cathode and Anode compartments. The Anode is connected to a power source (A) and a voltmeter (V). The Cathode compartment contains a solution of CO₂ and H₂O. The Anode compartment contains a solution of H₂O. The overall reaction at the anode is shown as $2(\text{H}^+ + \text{e}^-) \longrightarrow \text{H}_2$.

1.5.2. Challenges: reaction selectivity

38

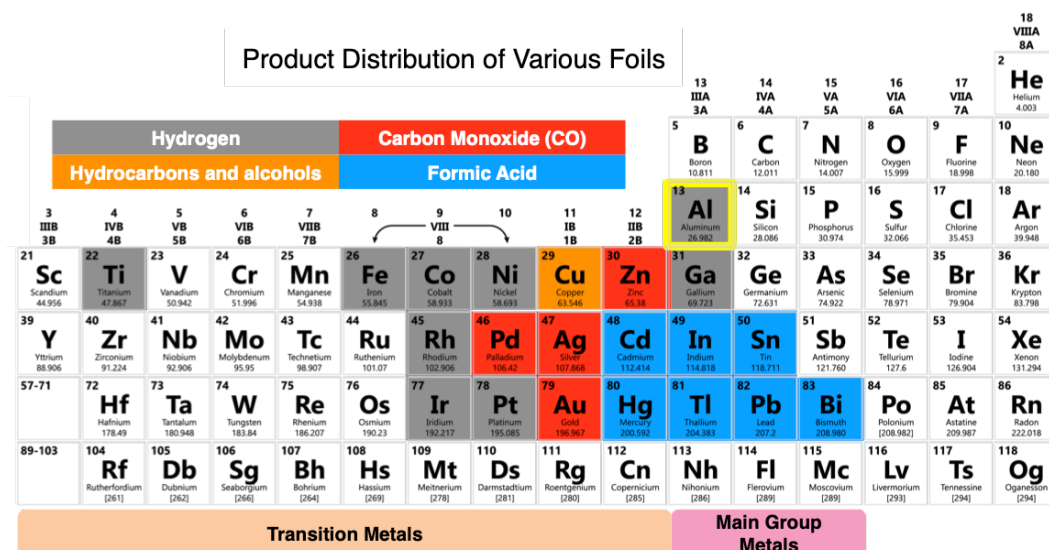


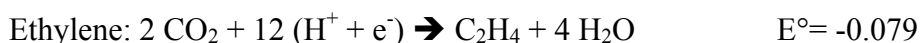
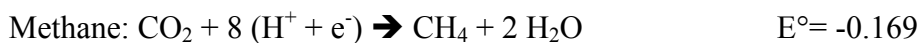
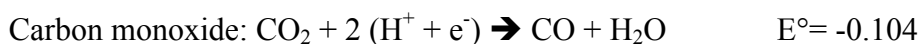
Figure 1-9. Observed reaction selectivity of metal foils as electrocatalyst for CO₂R.

Copper surfaces have drawn interest because they are the only single-metal electrodes that produce significant amounts of carbon-based products. Cu metal foil as electrocatalyst is capable to produce up to 16 different carbon-based products including gaseous products, such as carbon monoxide (CO), methane (CH₄), and ethylene (C₂H₄), and liquid products such as formic acid (HCOOH), methanol (CH₃OH), and ethanol (C₂H₅OH) (Figure 1-8).^{48, 50} However, its inability to tune the selectivity among the 16 observed products, particularly under mild, aqueous conditions, poses a challenge.⁴⁸⁻⁵⁰

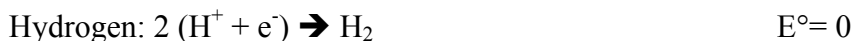
Observing the electrochemical half reaction for the common carbon-based products and HER further confirms the challenges in achieving selectivities among these carbon-based products.

The electrochemical half reactions listed below with their standard reduction potentials (E°) relative to the standard hydrogen electrode (SHE) in water at pH=0 at 25 °C.⁵²

CO₂ reduction:



Competing reaction:



All of the CO₂R reactions have standard thermodynamic potentials ranging from -0.2 V and 0.2 V resulting in difficulties to achieve selectivities among these carbon-based products. Additionally, many of the CO₂R reactions not only share similar thermodynamics but also share kinetic similarities with a common rate-determining step (RDS) in the reaction mechanism.

To address the selectivity challenges, we provide design strategies for the synthesis of novel electrocatalysts for carbon dioxide reduction through tuning the catalytic microenvironments. In chapter 3, we present a series of suggestions for the standard protocols for measuring and reporting electrocatalytic performance in electrochemical CO₂R that involve organic materials to ensure the validity and reproducibility of the reported results. Then, in chapters 4 and 5, we demonstrate that the confined reaction space enables changes in reaction selectivity and can

impart atypical catalytic capabilities to metals that are not otherwise active for CO₂R. These design strategies have the potential to provide a framework for catalyst design with improved catalytic activity. Finally, in chapters 6, we report important factors that will enhance copper selectivity toward the more energy-dense product, ethylene.

REFERENCES

1. Christensen, C. H., Catalysis for Sustainability. *Topics in Catalysis* **2009**, 52 (3), 205-205.
2. Anastas, P. T.; Warner, J. C. Green Chemistry: Theory and Practice, Oxford University Press, New York, 1998.
3. Ritchie, Roser, Mispy, Ortiz-Ospina. "Measuring progress towards the Sustainable Development Goals." SDG Tracker.org, website (2018)
4. Centi, G.; Perathoner, S., Catalysis, a driver for sustainability and societal challenges. *Catalysis Today* **2008**, 138 (1), 69-76.
5. Descorme, C.; Gallezot, P.; Geantet, C.; George, C., Heterogeneous Catalysis: A Key Tool toward Sustainability. *ChemCatChem* **2012**, 4 (12), 1897-1906.
6. Zhou, Q.-L., Transition-Metal Catalysis and Organocatalysis: Where Can Progress Be Expected? *Angewandte Chemie International Edition* **2016**, 55 (18), 5352-5353.
7. Taramasso, M.; Perego, G.; B. Notari, B. U.S. Patent 4410501,1983.
8. Centi G, Cavani F, Trifiro` F (2001) In: Twigg MV, Spencer MS (eds) Selective oxidation by heterogeneous catalysis. Recent developments. Fundamental and applied catalysis (series). Kluwer/ Plenum Publishing Corporation, New York, London
9. Nijhuis, T. A.; Makkee, M.; Moulijn, J. A.; Weckhuysen, B. M., The Production of Propene Oxide: Catalytic Processes and Recent Developments. *Industrial & Engineering Chemistry Research* **2006**, 45 (10), 3447-3459.

10. Wu, P.; Komatsu, T.; Yashima, T., Hydroxylation of Aromatics with Hydrogen Peroxide over Titanosilicates with MOR and MFI Structures: Effect of Ti Peroxo Species on the Diffusion and Hydroxylation Activity. *The Journal of Physical Chemistry B* **1998**, 102 (46), 9297-9303.
11. Notari, B., Microporous Crystalline Titanium Silicates. In *Advances in Catalysis*, Eley, D. D.; Haag, W. O.; Gates, B., Eds. Academic Press: 1996; Vol. 41, pp 253-334.
12. Vayssilov, G. N., Structural and Physicochemical Features of Titanium Silicalites. *Catalysis Reviews* **1997**, 39 (3), 209-251.
13. Hartwig, J. F., *Organotransition metal chemistry : from bonding to catalysis*. University Science Books: Sausalito, Calif., 2010; p 1 online resource.
14. Ludwig, J. R.; Schindler, C. S., Catalyst: Sustainable Catalysis. *Chem* **2017**, 2 (3), 313-316.
15. Fürstner, A., Iron Catalysis in Organic Synthesis: A Critical Assessment of What It Takes To Make This Base Metal a Multitasking Champion. *ACS Central Science* **2016**, 2 (11), 778-789.
16. Holland, P. L., Distinctive Reaction Pathways at Base Metals in High-Spin Organometallic Catalysts. *Accounts of Chemical Research* **2015**, 48 (6), 1696-1702.
17. Freyschlag, C. G.; Madix, R. J., Precious metal magic: catalytic wizardry. *Materials Today* **2011**, 14 (4), 134-142.
18. Umile, T.P., ed. (2015). *Catalysis for Sustainability: Goals, Challenges, and Impacts* (CRC Press).

19. Bauer, E.B. (2015). Iron Catalysis: Historic Overview and Current Trends. In *Topics in Organometallic Chemistry*, Volume 50, E.B. Bauer, ed. (Springer International Publishing), pp. 1–18.
20. Belin, P.; Le Du, M. H.; Fielding, A.; Lequin, O.; Jacquet, M.; Charbonnier, J.-B.; Lecoq, A.; Thai, R.; Courçon, M.; Masson, C.; Dugave, C.; Genet, R.; Pernodet, J.-L.; Gondry, M., Identification and structural basis of the reaction catalyzed by CYP121, an essential cytochrome P450 in *Mycobacterium tuberculosis*. *Proceedings of the National Academy of Sciences* 2009, **106** (18), 7426.
21. Hoyt, J. M.; Schmidt, V. A.; Tondreau, A. M.; Chirik, P. J., Iron-catalyzed intermolecular [2+2] cycloadditions of unactivated alkenes. *Science* 2015, **349** (6251), 960.
22. Casey, C. P.; Guan, H., An Efficient and Chemoselective Iron Catalyst for the Hydrogenation of Ketones. *Journal of the American Chemical Society* 2007, **129** (18), 5816-5817.
23. Pal, S.; Uyeda, C., Evaluating the Effect of Catalyst Nuclearity in Ni-Catalyzed Alkyne Cyclotrimerizations. *Journal of the American Chemical Society* 2015, **137** (25), 8042-8045.
24. Hennessy, E. T.; Betley, T. A., Complex N-Heterocycle Synthesis via Iron-Catalyzed, Direct C–H Bond Amination. *Science* 2013, **340** (6132), 591.
25. Ludwig, J. R.; Zimmerman, P. M.; Gianino, J. B.; Schindler, C. S., Iron(III)-catalysed carbonyl–olefin metathesis. *Nature* 2016, **533** (7603), 374-379.
26. Kaphan, D. M.; Levin, M. D.; Bergman, R. G.; Raymond, K. N.; Toste, F. D., A supramolecular microenvironment strategy for transition metal catalysis. *Science* 2015, **350** (6265), 1235.

27. Gross, E.; Dean Toste, F.; Somorjai, G. A., Polymer-Encapsulated Metallic Nanoparticles as a Bridge Between Homogeneous and Heterogeneous Catalysis. *Catalysis Letters* **2015**, **145** (1), 126-138.
28. Hirahata, W.; Thomas, R. M.; Lobkovsky, E. B.; Coates, G. W., Enantioselective Polymerization of Epoxides: A Highly Active and Selective Catalyst for the Preparation of Stereoregular Polyethers and Enantiopure Epoxides. *Journal of the American Chemical Society* **2008**, **130** (52), 17658-17659.
29. Cheng, M.; Lobkovsky, E. B.; Coates, G. W., Catalytic Reactions Involving C1 Feedstocks: New High-Activity Zn(II)-Based Catalysts for the Alternating Copolymerization of Carbon Dioxide and Epoxides. *Journal of the American Chemical Society* **1998**, **120** (42), 11018-11019.
30. Longo, J. M.; Sanford, M. J.; Coates, G. W., Ring-Opening Copolymerization of Epoxides and Cyclic Anhydrides with Discrete Metal Complexes: Structure–Property Relationships. *Chemical Reviews* **2016**, **116** (24), 15167-15197.
31. Wang, C.; Luo, L.; Yamamoto, H., Metal-Catalyzed Directed Regio- and Enantioselective Ring-Opening of Epoxides. *Accounts of Chemical Research* **2016**, **49** (2), 193-204.
32. Huang, C.-Y.; Doyle, A. G., The Chemistry of Transition Metals with Three-Membered Ring Heterocycles. *Chemical Reviews* **2014**, **114** (16), 8153-8198.
33. Jacobsen, E. N., Asymmetric Catalysis of Epoxide Ring-Opening Reactions. *Accounts of Chemical Research* **2000**, **33** (6), 421-431.
34. Getzler, Y. D. Y. L.; Mahadevan, V.; Lobkovsky, E. B.; Coates, G. W., Synthesis of β -Lactones: A Highly Active and Selective Catalyst for Epoxide

- Carbonylation. *Journal of the American Chemical Society* 2002, **124** (7), 1174-1175.
35. Mahadevan, V.; Getzler, Y. D. Y. L.; Coates, G. W., [Lewis Acid]⁺[Co(CO)₄]⁻ Complexes: A Versatile Class of Catalysts for Carbonylative Ring Expansion of Epoxides and Aziridines. *Angewandte Chemie International Edition* 2002, **41** (15), 2781-2784.
36. Gorzynski Smith, J., Synthetically Useful Reactions of Epoxides. *Synthesis* 1984, **1984** (08), 629-656.
37. Corey, E. J.; Su, W. G., Total synthesis of a C₁₅ ginkgolide, (+-)-bilobalide. *Journal of the American Chemical Society* 1987, **109** (24), 7534-7536.
38. Song, L.; Liu, Y.; Tong, R., Cephalosporolide B Serving as a Versatile Synthetic Precursor: Asymmetric Biomimetic Total Syntheses of Cephalosporolides C, E, F, G, and (4-OMe-)G. *Organic Letters* 2013, **15** (22), 5850-5853.
39. Johnson, W. S.; Plummer, M. S.; Reddy, S. P.; Bartlett, W. R., Cation-stabilizing auxiliaries in polyene cyclizations. 7. The fluorine atom as a cation-stabilizing auxiliary in biomimetic polyene cyclizations. 4. Total synthesis of dl-.beta.-amyrin. *Journal of the American Chemical Society* 1993, **115** (2), 515-521.
40. Pujala, B.; Rana, S.; Chakraborti, A. K., Zinc Tetrafluoroborate Hydrate as a Mild Catalyst for Epoxide Ring Opening with Amines: Scope and Limitations of Metal Tetrafluoroborates and Applications in the Synthesis of Antihypertensive Drugs (R)_S/(R)/(S)-Metoprolols. *The Journal of Organic Chemistry* 2011, **76** (21), 8768-8780.

41. Das, B.; Kumar, D. N., Highly Diastereoselective Construction of Substituted Pyrrolidines: Formal Synthesis of (-)-Bulgecinine. *Synlett* **2011**, **2011** (09), 1285-1287.
42. Boa, A. N.; Clark, S.; Hirst, P. R.; Westwood, R., Ring opening reactions of quinoline substituted epoxides. *Tetrahedron Letters* **2003**, **44** (52), 9299-9302.
43. Moore, W. J.; Luzzio, F. A., Synthetic studies directed toward the liposidomycins: Preparation and reactions of serine-derived epoxides. *Tetrahedron Letters* **1995**, **36** (37), 6599-6602.
44. Falkowski, P.; Scholes, R. J.; Boyle, E.; Canadell, J.; Canfield, D.; Elser, J.; Gruber, N.; Hibbard, K.; Högberg, P.; Linder, S.; Mackenzie, F. T.; Moore III, B.; Pedersen, T.; Rosenthal, Y.; Seitzinger, S.; Smetacek, V.; Steffen, W., The Global Carbon Cycle: A Test of Our Knowledge of Earth as a System. *Science* **2000**, **290** (5490), 291.
45. Davis, S. J.; Caldeira, K.; Matthews, H. D., Future CO₂ Emissions and Climate Change from Existing Energy Infrastructure. *Science* **2010**, **329** (5997), 1330.
46. Artz, J.; Müller, T. E.; Thenert, K.; Kleinekorte, J.; Meys, R.; Sternberg, A.; Bardow, A.; Leitner, W., Sustainable Conversion of Carbon Dioxide: An Integrated Review of Catalysis and Life Cycle Assessment. *Chemical Reviews* **2018**, **118** (2), 434-504.
47. Seh, Z. W.; Kibsgaard, J.; Dickens, C. F.; Chorkendorff, I.; Norskov, J. K.; Jaramillo, T. F., Combining theory and experiment in electrocatalysis: Insights into materials design. *Science* **2017**, **355** (6321).

48. Kuhl, K. P.; Cave, E. R.; Abram, D. N.; Jaramillo, T. F., New insights into the electrochemical reduction of carbon dioxide on metallic copper surfaces. *Energy & Environmental Science* 2012, **5** (5).
49. Qiao, J.; Liu, Y.; Hong, F.; Zhang, J., A review of catalysts for the electroreduction of carbon dioxide to produce low-carbon fuels. *Chemical Society Reviews* 2014, **43** (2), 631-675.
50. Hori, Y., Electrochemical CO₂ Reduction on Metal Electrodes. In *Modern Aspects of Electrochemistry*, Vayenas, C. G.; White, R. E.; Gamboa-Aldeco, M. E., Eds. Springer New York: New York, NY, 2008; pp 89-189.
51. Hidetomo, N.; Shoichiro, I.; Yoshiyuki, O.; Kazumoto, I.; Masunobu, M.; Kaname, I., Electrochemical Reduction of Carbon Dioxide at Various Metal Electrodes in Aqueous Potassium Hydrogen Carbonate Solution. *Bulletin of the Chemical Society of Japan* 1990, **63** (9), 2459-2462.
52. Wagman, D. D.; Evans, W. H.; Parker, V. B.; Schumm, R. H.; Halow, I.; Bailey, S. M.; Churney, K. L.; Nuttall, R. L. The NBS tables of chemical thermodynamic properties - selected values for inorganic and C1 and C2 organic substances in si units. *J. Phys. Chem. Ref. Data* 1982, 11 .

CHAPTER 2

SELECTIVE TRANSFORMATION FOR SMALL MOLECULE SYNTHESIS: NUCLEOPHILIC RING OPENING OF TRANS-2,3- DISUBSTITUTED EPOXIDES TO β -AMINO ALCOHOLS WITH CATALYST-CONTROLLED REGIOSELECTIVITY

Reproduced adapted from Lee, M.;⁺ Lamb, J. R.;⁺ Sanford, M. J.; LaPointe, A. M.;

Coates, G. W. *Chem. Commun.*, 2018, 54, 12998-13001. DOI:

10.1039/C8CC07200K with permission from The Royal Society of Chemistry.

2.1. Abstract

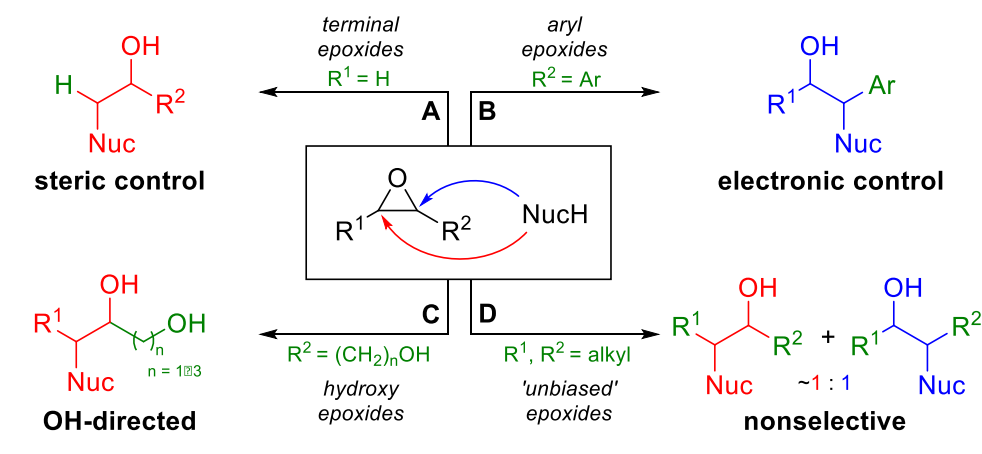
We report the nucleophilic ring opening of unsymmetrical *trans*-epoxides to β -amino alcohols with *catalyst-controlled regioselectivity*. This cationic aluminum salen catalyst, which contains bulky mesityl groups in the *ortho*-position of the phenoxide and a 2,2'-diamino-1,1'-binaphthalene backbone, transforms a variety of epoxides with high regioselectivity using nitrogen-containing nucleophiles. Unlike most reports, in which regioselectivity is substrate controlled, the regioselectivity in this system is catalyst controlled and allows selective nucleophilic ring opening of unbiased *trans*-epoxides.

2.2. Introduction

Nucleophilic ring opening (NRO) of epoxides is a well-established method to access diverse, highly-functionalized molecules, such as β -amino

Scheme 2-1. Regioselective ring opening of different classes of epoxides^{1,3c,e,f}

Previous work: regioselective ring opening of epoxides



alcohols.¹ These products are an important class of compounds used as catalysts, chiral auxiliaries, and intermediates for the synthesis of natural products and pharmaceuticals.² Classically, highly regioselective, catalytic systems for epoxide ring opening rely on strong substrate bias to control the regioselectivity.¹ For example, terminal epoxides are often used to sterically bias the nucleophilic attack to the less-hindered methylene carbon (Scheme 1A). Aromatic epoxides are also commonly employed to electronically bias the nucleophilic attack to the benzylic position. (Scheme 1B). Additionally, alcohol-, ether-, and sulfonamide-directed variants have been developed to achieve high regioselectivity through a chelating effect (Scheme 1C),³ but the requirement for a nearby directing group limits the scope of the reaction. Most existing methods, however, cannot achieve good regioselectivity for 2,3-disubstituted epoxides with different alkyl substituents that are both sterically and electronically similar (referred to as ‘unbiased’ substrates). When non-aromatic 2,3-disubstituted epoxides are used in these reactions, symmetrical substrates are generally used to show activity, or enantioselectivity through *meso*-desymmetrization, while avoiding the issue of regioselectivity.⁴ Examples using unsymmetrical, unbiased substrates lead to a mixture of products (Scheme 1D).^{3c,5,6} One report from Kobayashi and coworkers demonstrated good regio- and enantioselectivity for unsymmetrical, unbiased *cis*-epoxides using a *meso*-desymmetrization catalyst, but no *trans*-epoxides were reported.⁷ A general, catalyst-controlled regioselective NRO of unbiased *trans*-epoxides has not been reported and would be a useful addition to current methodology.

Our group has reported the regioselective carbonylation⁸ and isomerization⁹ of unbiased internal epoxides using bimetallic Al–salen cobaltate complexes. Additionally, one of the catalyst precursors could be used to promote the nucleophilic ring opening of *cis*-epoxides with similarly high selectivities using a latent HCl source.^{8b} Herein, we expand upon this work by optimizing a cationic Al–salen Lewis acid paired with a non-nucleophilic anion for the regioselective ring opening of various unbiased *trans*-epoxides using nitrogen-containing nucleophiles (Scheme 1E).

2.3. Reaction Optimizations

We first optimized the salen ligand by varying the diamine linker as well as the *ortho*- and *para*-positions of the phenoxide (R¹ and R², respectively) (Chart 2-1). The catalyst variations (**1a–h**) were screened in THF for the ring opening of *trans*-2-octene oxide (**2a**) with aniline (**3a**) (Table 2-1). Initially, we tested the first-generation catalysts [salphAl(THF)₂]⁺[SbF₆][−] (**1a**)¹⁰ and [*rac*-salcyAl(THF)₂]⁺[SbF₆][−] (**1b**),¹¹ resulting in minimal regioselectivity (Table 2-1, entries 1 and 2), which was expected for unbiased internal epoxides.^{5a} In our previous work, we observed that bulky aryl-substituents, particularly in the *ortho*-position, greatly improved regioselectivity for 2,3-disubstituted epoxides,^{8,9} but only marginal improvement in regioselectivity was observed when *ortho*-aryl groups were paired with the 1,2-cyclohexyldiamine backbone (**1c** and **1d**, Table 2-1, entries 3 and 4).

We then tested the 2,2'-diamino-1,1'-binaphthalene (BINAM)¹³ backbone because these ligands have previously been used to improve both regio- and enantioselectivity in NRO reactions of epoxides.^{3c} Additionally, our group has used BINAM-based salen catalysts to achieve high selectivity for internal epoxide carbonylations.^{8b,14} Similar to the salph and salcy catalysts, the di-*tert*-butyl variant (**1e**) resulted in unselective ring opening (entry 5), but further optimization led to 10 : 1 regioselectivity with catalyst **1h**, which features a bulky mesityl substituent in the *ortho*-position and a methyl group in the *para*-position (Table 2-1, entry 8). Changing the counter-anion from SbF₆⁻ to BPh₄⁻ (**1i**) improved the regioselectivity even further to 12 : 1 (Table 2-1, entry 9).¹⁵ While the exact mechanism through which regioselectivity is conferred is unknown, we hypothesize that a favorable epoxide binding geometry is dictated by the salen ligand and that a combination of the bulky mesityl substituents and the tight ion pair¹⁶ between the cationic aluminum metal center and tetraphenylborate anion

Chart 2-1. Catalysts screened for the regioselective ring opening of epoxides¹²

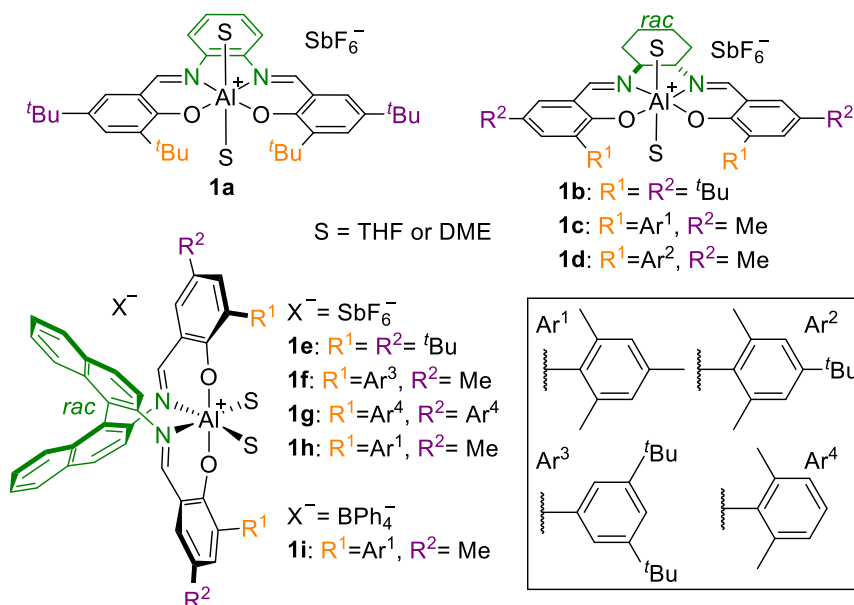
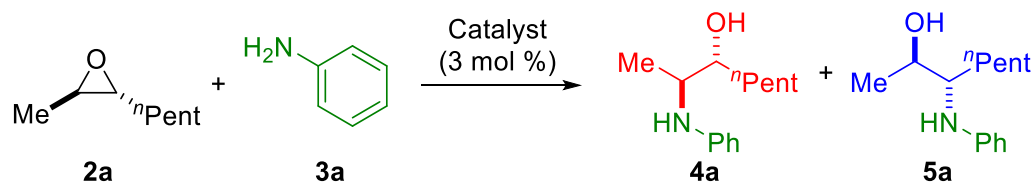


Table 2-1. Catalyst optimization^a

Entry	Catalyst	Conv. (%) ^b	4a : 5a ^b
1	1a	17	1 : 1.4
2	1b	22	1.2 : 1
3	1c	50	3.6 : 1
4	1d	85	2.5 : 1
5	1e	67	1.5 : 1
6	1f	13	1.2 : 1
7	1g	7	1.6 : 1
8	1h	90	10 : 1
9 ^c	1i	77	12 : 1

^a Conditions: 3 mol % catalyst (formed *in situ* from L_nAl–Cl + NaSbF₆),¹⁶ THF (0.3 M), 22 °C, 18 h. ^b Determined by ¹H NMR spectroscopy of the crude reaction mixture. ^c NaBPh₄ used instead of NaSbF₆.

blocks nucleophilic attack to one epoxy carbon.

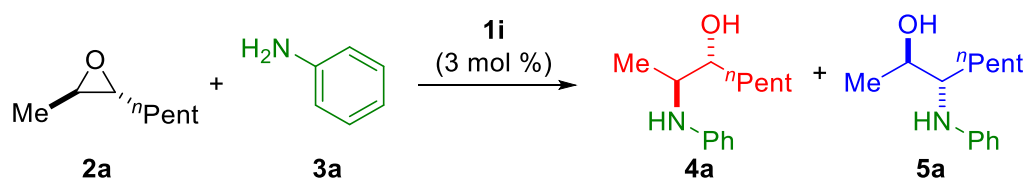
The reaction conditions for **1i** were then further optimized for regioselectivity, conversion, and reaction time (Table 2-2). A solvent screen revealed no activity in non-donating toluene and high selectivity in 1,4-dioxane, diethyl ether, and DME (Table 2, entries 1–5). 1,4-Dioxane significantly slowed the reaction and the volatility of ether resulted in lower reproducibility, so DME was chosen as the optimal solvent. Increasing the

substrate concentration from 0.3 to 2.0 M led to both an increase in conversion and selectivity (Table 2, entries 5–8). Further increasing the concentration to 3.6 M and heating the reaction to 40 °C allowed the reaction to proceed to full conversion in 4 h while maintaining 19 : 1 regioselectivity (entry 9). This result can be directly compared to recent reports which yield a 1 : 1 mixture of **4a** and **5a** when ring-opening *trans*-2-octene oxide with aniline.^{3c}

2.4. Substrate Scope

Once the optimized reaction conditions were determined, we explored the scope of the reaction using aniline as the nucleophile (Table 2-3). To ensure full conversion of all epoxides, the reaction was run for 6 hours instead of 4 hours. A series of unbiased *trans*-epoxides with one methyl and one alkyl substituent were ring-opened with excellent regioselectivity for attack at the

Table 2-2. Reaction optimization for 1i using epoxide 2a and aniline (3a)^a



Entry	Solvent	Conc. (M)	Conv. (%) ^b	4a : 5a ^b
1	THF	0.3	77	12 : 1
2	Toluene	0.3	<5	n.d.
3	1,4-Dioxane	0.3	30	15 : 1
4	Et ₂ O	0.3	92	14 : 1
5	DME	0.3	69	15 : 1
6	DME	0.6	95	16 : 1
7	DME	1.2	>99	16 : 1
8	DME	2.0	>99	19 : 1
9 ^c	DME	3.6	>99	19 : 1

^a Conditions: 3 mol % 1i (formed *in situ* from L_nAl-Cl and NaBPh₄),¹⁶ 22 °C, 18

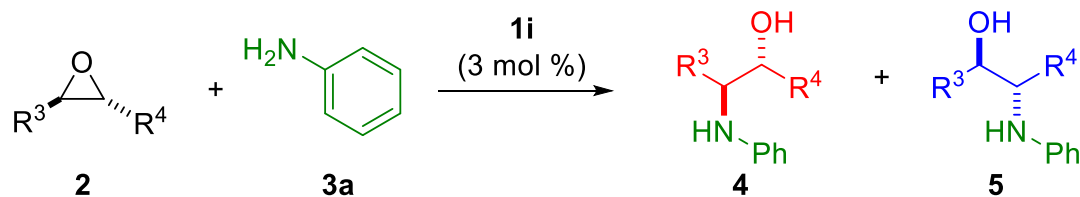
h. ^b Determined by ¹H NMR spectroscopy of the crude reaction mixture. ^c 40 °C,

4 h. n.d. = not determined.

2-position (yielding **4**) instead of the 3-position (yielding **5**) (Table 3, entries 1–4). Longer alkyl substituents generally led to higher regioselectivity, demonstrating additional substrate-control, but all of the β -amino alcohols were isolated in high yields. For epoxide **2e**, in which neither substituent is a methyl group, the selectivity dropped substantially to 2.4 : 1 (Table 3, entry 5), but this still represents a significant improvement on existing methods that yield $\sim 1 : 1$ selectivity for dialkyl substrates using *racemic* catalysts.^{3c,5a,c,e,f} This is in agreement with our previous results with these types of catalysts⁹ and can be explained by the exceedingly similar sterics and electronics of the ethyl and *n*-butyl substituents.

Additional substrates with larger substituent differences, such as benzyl-substituted epoxides (**2f–2h**), resulted in excellent regioselectivities and good yields (Table 3, entry 6–8). The TBS-protected epoxy alcohol **2i** showed high regioselectivity and a single regioisomer was isolated in 84% yield (Table 3, entry 9). As previously seen,⁹ the relative stereochemistry of the epoxide (i.e. *cis* versus *trans*) strongly influences the efficacy of the catalyst. When *cis*-2-octene oxide (**2j**) was subjected to the standard reaction conditions, no regioselectivity was observed, but the product mixture was still isolated in high yield (Table 3, entry 10).

Table 2-3. Epoxide substrate scope using aniline (**3a**) as the nucleophile



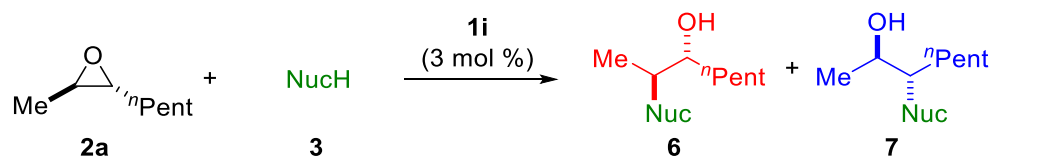
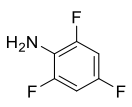
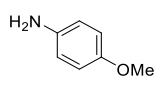
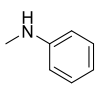
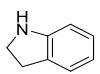
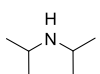
Entry	Epoxide	R ³	R ⁴	Yield (%) ^b	4 : 5 ^c
1	2b	Me	Et	63	6 : 1
2	2c	Me	ⁿ Pr	88	8 : 1
3	2a	Me	ⁿ Pent	98	17 : 1
4	2d	Me	ⁿ Hex	97	15 : 1
5	2e	Et	ⁿ Bu	82	2.4 : 1
6	2f	Me	<i>p</i> -MeBn	91	>50 : 1
7	2g	Me	<i>m</i> -MeBn	78	>20 : 1
8	2h	Me	<i>o</i> -MeBn	86	14 : 1
9	2i	Me	CH ₂ OTBS	84	>50 : 1
10	<i>cis</i> - 2j	Me	ⁿ Pent	95	1 : 1

^a Conditions: 3 mol % **1i**, 0.46 mmol of epoxide, **3a** (1.1 eq, 8 M stock solution in DME), 40 °C, 6 h. ^b Isolated yield. ^c Determined by ¹H NMR spectroscopy of the crude reaction mixture.

We also explored the nucleophile scope of the reaction using *trans*-2-octene oxide (**2a**) as the substrate (Table 4). Aromatic amines were our focus due to their attenuated nucleophilicity, which avoids the unselective background ring-opening reaction not mediated by the Lewis acid catalyst. Less nucleophilic secondary and electron-poor nucleophiles required longer reaction times compared to aniline, so all reactions – except the electron-rich

p-anisidine – were run for 20 hours. The electron-withdrawing 2,4,6-trifluoroaniline (**3b**) resulted in higher regioselectivity (>20 : 1) but lower isolated yield (Table 4, entry 1).¹⁷ Using *p*-anisidine (**3c**), 88% conversion was reached in only 6h, but the products were formed with slightly lower selectivity (12 : 1) and modest isolated yield (55%, Table 4, entry 2) compared to the unsubstituted aniline (98%, Table 3, entry 3). This electron-rich nucleophile is of particular interest because of the potential to reveal the free amine through deprotection.¹⁸

Table 2-4. Nucleophile scope using **2a** as the substrate^a

					
Entry	NucH	3	Conv. (%) ^b	Yield (%) ^c	6 : 7 ^d
1		3b	97	51	>20 : 1
2 ^e		3c	88	55	12 : 1
3		3d	78	32	>50 : 1
4		3e	86	60	>20 : 1
5		3f	<5	<1	n.d.

^a Conditions: 3 mol % **1i**, [epoxide] = 3.6 M in DME, 40 °C, 20 h. ^b Determined by ¹H NMR spectroscopy of the crude reaction mixture. ^c Isolated yield. ^d Determined by ¹H NMR spectroscopy of the isolated yield. ^e *t*_{rxn} = 6h. n.d. = not determined.

The secondary nucleophiles were also explored to expand the scope of the reaction. *N*-Methyl aniline (**3d**) yielded clean **6d** in 32% isolated yield (Table 4, entry 3). Indoline (**3e**) resulted in high regioselectivity for attack at the 2-position (**6e**) over the 3-position (**7e**) (Table 4, entry 4), but product instability and free indoline co-elution made purification difficult.¹⁹ Bulkier diisopropylamine (**3f**) did not show appreciable product formation by ¹H NMR spectroscopy after 20 h, though the exact mass of the product was observed in high-resolution mass spectrometry DART analysis suggesting trace amounts of product was present (Table 4, entry 5). This result is presumably due to diisopropylamine's significantly reduced nucleophilicity as well as catalyst decomposition, indicated by ligand crashing out of the reaction solution.

2.5. Conclusion

In conclusion, we report a general system to achieve catalyst-controlled regioselective NRO of unbiased *trans*-2,3-disubstituted epoxides. The catalyst consists of a cationic Al–salen Lewis acid and the non-coordinating anion such as BPh₄[−]. The backbone and substituents on the salen ligand framework as well as the counter-anion were found to have dramatic effects on the regioselectivity of the reaction. A variety of epoxides were successfully ring opened by aniline with very high regioselectivity and in high yields, and both primary and secondary amines were employed to access internal β-amino alcohols that could not be selectively synthesized using existing methods. Future directions include the development of enantioselective variants using the enantiopure BINAM backbone to expand

asymmetric NRO methodology beyond terminal and *meso*-epoxides. With this more general method for NRO in hand, complex β -amino alcohols will be more easily accessible, facilitating future synthesis of natural products and pharmaceuticals.

2.6. Experimental Procedures

2.6.1. General Considerations

2.6.1.1. Methods and Instruments

Unless stated otherwise, all synthetic manipulations were carried out using standard Schlenk techniques under a nitrogen atmosphere or in an MBraun Unilab glovebox under an atmosphere of purified nitrogen. Reactions were carried out in oven-dried glassware cooled under vacuum. ^1H and $^{13}\text{C}\{^1\text{H}\}$ NMR Spectra were recorded on Bruker AV III HD spectrometer with a broad band Prodigy cryoprobe (^1H , 500 MHz), (^{13}C , 126 MHz)), Varian INOVA 400 MHz (^1H , 400 MHz), or Varian INOVA 600 MHz (^1H , 600 MHz), spectrometer at 22 °C, unless otherwise noted, and were referenced to the residual chloroform (7.26 ppm for ^1H , 77.16 ppm for ^{13}C). All *J* values are given in Hertz. Deuterated chloroform was purchased from Cambridge Isotope Laboratories and stored over K_2CO_3 . DART-HRMS analyses were performed on a Thermo Scientific Exactive Orbitrap MS system with an Ion Sense DART ion source.

Pre-made catalyst vials were made by dispensing stock solutions using a Freeslate Core Module 3 (CM3) robotic platform located inside an MBraun drybox. All solutions were dispensed robotically using a syringe dispense, which was designed and executed using Library Studio™ and Automation Studio™

software. The solvent was then removed *in vacuo* in a vacuum centrifuge.

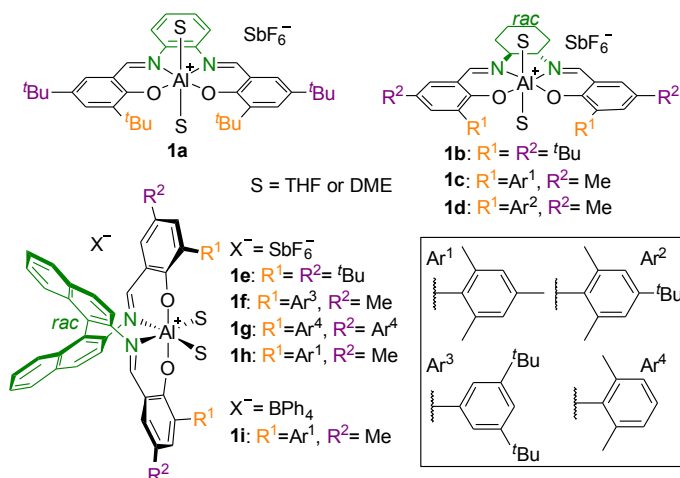
2.6.1.2. Chemicals

Anhydrous 1,4-dioxane was purchased from Sigma-Aldrich. It was dried over 3Å molecular sieves, filtered using a syringe filter the next day, and sparged under nitrogen for 30 minutes prior to use. Anhydrous toluene, dichloromethane (DCM), hexanes, diethyl ether, and tetrahydrofuran (THF) were purchased from Fischer Scientific and sparged vigorously with nitrogen for 40 minutes prior to first use. The solvents were further purified by passing them under nitrogen pressure through two packed columns of neutral alumina (THF was also passed through a third column packed with activated 4Å molecular sieves) or through neutral alumina and copper(II) oxide (for toluene and hexanes). THF, diethyl ether, and dichloromethane were degassed via three freeze-pump-thaw cycles prior to use. All epoxides used in this study were dried over calcium hydride and degassed via three freeze-pump-thaw cycles prior to use. All non-dried solvents used were reagent grade or better and used as received.

All other chemicals were purchased from Aldrich, Alfa-Aesar, TCI America, Strem, or Macron and used as received. Flash column chromatography was performed with silica gel (particle size 40–64 µm, 230–400 mesh) using mixtures of ethyl acetate and hexanes as eluent.

The following compounds were prepared according to literature procedures:

a) catalysts and catalyst precursors



salphAl-Cl (precursor to **1a**, salph = 6,6'-((1*E*,1'*E*)-(1,2-phenylenebis(azanylylidene))bis(methanylylidene))bis(2,4-di-*tert*-butylphenolate))²⁰

rac-salcyAl-Cl (precursor to **1b**, salcy = *N,N'*-bis(3,5-di-*tert*-butyl-salicylidene)-1,2-cyclohexanediamine)²¹

rac-3,3''-((1*E*,1'*E*)-((1*S*,2*S*)-Cyclohexane-1,2-diylbis(azanylylidene))bis(methanylylidene))bis(2',4',5,6'-tetramethyl-[1,1'-biphenyl]-2-olate)aluminum chloride (precursor to **1c**)²²

rac-3,3''-((1*E*,1'*E*)-((1*S*,2*S*)-Cyclohexane-1,2-diylbis(azanylylidene))bis(methanylylidene))bis(4'-(*tert*-butyl)-2',5,6'-trimethyl-[1,1'-biphenyl]-2-olate)aluminum chloride (precursor to **1d**)²³

rac-*t*BuBinamAl-Cl (precursor to **1e**, *rac*-*t*BuBinam = *rac*-*N,N'*-bis(2-hydroxy-3,5-di-*tert*-butylbenzylidene)-1,1'-binaphthyl-2,2'-diamine, *rac* complex made analogously to the *R* complex shown)²⁴

3,3''-((1*E*,1'*E*)-([1,1'-Binaphthalene]-2,2'-diylbis(azanylylidene))-bis(methanylylidene))bis(3',5'-di-tert-butyl-5-methyl-[1,1'-biphenyl]-2-olate)aluminum chloride (precursor to **1f**)²⁵

Rac-Xyl₂BinamAl-Cl (precursor to **1g**, *rac*-Xyl₂Binam = *rac*-5',5''''-((1*E*,1'*E*)-([1,1'-binaphthalene]2,2'-diylbis(azanylylidene))bis(methanylylidene))-bis(2,2'',6,6''-tetramethyl-[1,1',3',1''-perphenyl]-4'-olate, *rac* complex made analogously to the *R* complex shown)²⁶

3,3''-((1*E*,1'*E*)-([1,1'-Binaphthalene]-2,2'-diylbis(azanylylidene))-bis(methanylylidene))bis(2',4',5,6'-tetramethyl-[1,1'-biphenyl]-2-olate)aluminum chloride (precursor to **1h** and **1i**)²⁶

b) epoxides

rac-trans-2-methyl-3-pentyloxirane (**2a**)²⁷

rac-trans-2-ethyl-3-methyloxirane (**2b**)²⁸

rac-trans-2-methyl-3-propyloxirane (**2c**)²²

rac-trans-2-hexyl-3-methyloxirane (**2d**)²⁷

rac-trans-2-butyl-3-ethyloxirane (**2e**)²⁹

rac-trans-2-methyl-3-[(4-methylphenyl)methyl]-oxirane (**2f**)²³

rac-trans-2-methyl-3-[(3-methylphenyl)methyl]-oxirane (**2g**)²³

rac-trans-2-methyl-3-[(2-methylphenyl)methyl]-oxirane (**2h**)²³

rac-tert-butyldimethyl((*trans*-3-methyloxiran-2-yl)methoxy)-silane (**2i**)³⁰

rac-cis-2-methyl-3-pentyloxirane (**2j**)²⁶

2.6.2. Synthetic Procedures

2.6.2.1. General procedure A: Preparation of catalyst and dispensing of stock solution

In a glove box, a 20 ml scintillation vial was charged with (*rac*)-3,3'-((([1,1'-binaphthalene]-2,2'-diylbis(azanylylidene))bis(methanylylidene))bis(2',4',5,6'-tetramethyl-[1,1'-biphenyl]-2-olate))AlCl₃ (precursor to **1i**, 0.202 g, 0.250 mmol), NaBPh₄ (0.102 g, 0.297 mmol), and a magnetic stir bar. DME (2.4 ml, 0.1 M DME) was added using an automatic pipettor. The vial was sealed, taken out of the glovebox, and put in a preheated heating block (60 °C) for 18 hours. The vial was then cooled to room temperature before filtering the solution via syringe filter in the glovebox. Pentane (~2.5 ml) was layered on top of the filtered reaction solution, which was then sealed and placed in the freezer to crystallize for 24 hours. The solid was collected via filtration and dried under vacuum for 20 hours to give catalyst **1i** (0.254 g, 0.210 mmol, 86% yield). A stock solution of **1i** (16.51 mg) in DCM (4.27 ml, 0.05 M) was made. A robotic syringe dispense was used to transfer 278 µl of the stock solution (0.0165 g, 0.0139 mmol of **1i**) to several 4 ml scintillation vials equipped with magnetic stir bars. Vials were placed in a vacuum centrifuge at 40 °C for one hour to remove DCM.

2.6.2.2. General procedure B: Nucleophilic ring opening with aniline

In a glove box, an aniline stock solution (64 µl, 0.51 mmol, 8.0 M DME, 1.1 equiv) was added to a pre-made catalyst vial (see General Procedure A) using an automatic pipettor. Neat epoxide (0.46 mmol, 1.0 equiv) was added by weight using a syringe, resulting in [epoxide] = 3.6 M. The vial was sealed, taken out of

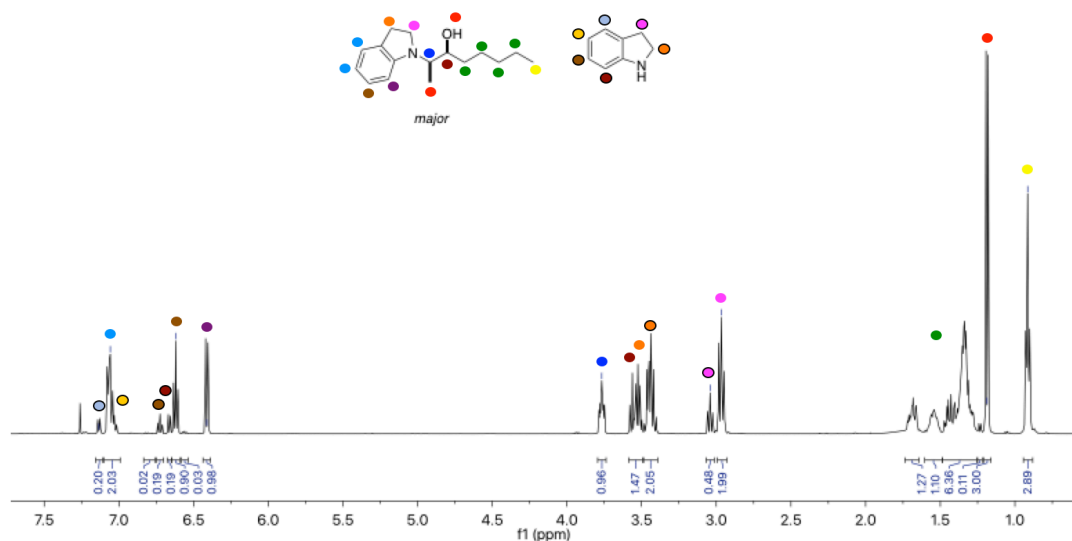
the glovebox, and put in a preheated heating block (40 °C) for 6 hours. The vial was then cooled to room temperature before loading directly onto a column for purification (silica gel, hexanes/ethyl acetate).

2.6.2.3. General procedure C: Nucleophilic ring opening of 2a using different nucleophiles and pre-made catalyst vials

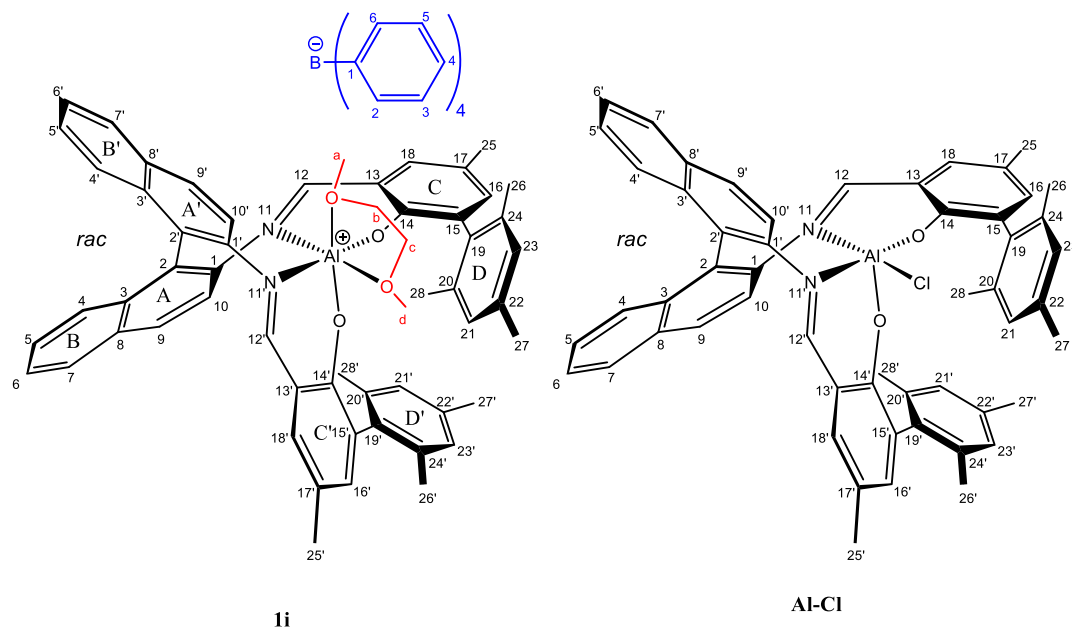
In a glove box, the nucleophile (0.51 mmol, 1.1 equiv) was added by weight to a pre-made catalyst vial (see General Procedure A). Neat *rac-trans*-2-methyl-3-pentyloxirane (0.07 ml, 0.059 g, 0.46 mmol, 1.0 equiv) was added by weight using an automatic pipettor. Solution was diluted to [epoxide] = 3.6 M using DME. The vial was sealed, taken out of the glovebox, and put in a preheated heating block (40 °C) for 20 hours. The vial was then cooled to room temperature before loading directly onto a column for purification (silica gel, hexanes/ethyl acetate).

2.6.2.4. General procedure D: Nucleophilic ring opening of 2a using different nucleophiles without pre-made catalyst vials

In a glove box, a 4 ml scintillation vial was charged with catalyst **1i** (0.0139 mmol, 3 mol%), the nucleophile (0.51 mmol, 1.1 equiv), and a magnetic stir bar. Neat *rac-trans*-2-methyl-3-pentyloxirane (0.07 ml, 0.059 g, 0.46 mmol, 1.0 equiv) was added by weight using an automatic pipettor. Solution was diluted to [epoxide] = 3.6 M using DME. The vial was sealed, taken out of the glovebox, and put in a preheated heating block (40 °C) for 20 hours. The vial was then cooled to room temperature before loading directly onto a column for purification (silica gel, hexanes/ethyl acetate).



2.6.4. Characterization of complex **1i**



Complex **1i** was characterized by 1- and 2-dimensional NMR spectroscopy in CDCl_3 at $-55\text{ }^\circ\text{C}$ to freeze out intramolecular dynamics which resulted in significant line broadening at ambient temperature. During characterization, $\sim 30\%$ of the sample underwent ligand substitution with chloride from solvent to generate the neutral complex **Al-Cl**. The sample also contained minor unidentified aromatic

components, dichloromethane, and excess DME. This made characterization more challenging, but we were able to unambiguously assign most ^1H and ^{13}C chemical shifts in both complexes based on high-resolution HSQC, HMBC and ROESY spectra (Table S2-5). 2D spectra were acquired on a 500 MHz Varian INOVA spectrometer, running VnmrJ 3.2A/Chempack 6.1 and using a Varian 5 mm z-PFG inverse-detection, broadband probehead. The spectra were processed and analyzed with MestReNova 12.0.2-20910 (2018, Mestrelab Research S.L.). The multiplicity-edited $^1\text{H}/^{13}\text{C}$ HSQC was acquired using the HSQCAD sequence optimized for 145 Hz couplings with spectral widths of 4200 and 25141 Hz in F2 and F1, respectively. 800 complex points were collected in F1 with two scans per increment and acquisition time of 0.15s. Broadband ^{13}C decoupling was applied during acquisition. Data were zero filled to 4k (F1) x 2k (F2) complex points and no window functions were applied prior to Fourier transform. The 2D-HMBC spectrum was acquired using the gHMBCAD sequence optimized for 8 Hz couplings with spectral widths of 4200 and 30167 Hz in F2 and F1, respectively. 1600 complex points were collected in F1 with two scans per increment and acquisition time of 0.3s. Data were zero filled to 8k (F1) x 2k (F2) complex points and unshifted sine bell as well as 5 Hz Gaussian window functions were applied in F2 prior to Fourier transform. The spectrum was analyzed in phase sensitive mode. A 2D ROESY was acquired using the ROESYAD sequence with a mixing time of 0.2s and spectral width of 4200 Hz. 512 complex points were collected in F1 with four scans per increment and an acquisition time of 0.4 s. Data were zero filled to 2k x 2k complex points, and Gaussian window functions were applied in both dimensions prior to Fourier transform. A diffusion-ordered NMR experiment was acquired using the convection-compensated, bipolar pulsed field-gradient double

stimulated experiment (Dbppste_cc sequence modified to include a longitudinal eddy current delay) (Insert reference to <https://doi.org/10.1006/jmre.1997.1123>). Diffusion delay (150 ms) and bipolar gradient pulse duration (3 ms) were optimized to achieve at least 95% attenuation of all signals corresponding to four half-lives of decay. Gradient strength was varied from 2 to 55.6 G/cm in 32 increments. Each increment was acquired with 2 steady-state scans and eight scans, acquisition time and relaxation delay were 1.2 and 2.5 s, respectively.

Chemical shift assignments were accomplished starting with C-12s and C-12', which were identified by their downfield ^{13}C chemical shifts (168–175 ppm) in the HSQC spectrum. The biphenyl portion of the ligand (C-13 to C-28) was easily assigned based on the HMBC, with aromatic hydrogens giving almost exclusively $^3J_{\text{C,H}}$ correlations and methyl substituents showing both $^2J_{\text{C,H}}$ and $^3J_{\text{C,H}}$ correlations. The BINAM portion of the ligand (C-1 to C-10) was more challenging due to overlap between H-9s and H-7s, but complete assignment was possible even without uniquely identifying all HMBC correlations. Assignment of the tetraphenyl borate anion was accomplished starting with the *ipso* carbon at 163.62 ppm, which appeared as a 1:1:1:1 quartet in F1 of the HMBC due to $^1J_{\text{B,C}}$ of 48 Hz. In addition to free dimethoxyethane (DME, CH_3 : 3.44/59.46 ppm; CH_2 : 3.59/71.65 ppm), we identified a complete set of resonances for a dimethoxyethane (DME) molecule—with two unique methyl resonances and two pairs of diastereotopic methylene hydrogens—that ROESY crosspeaks to the ligand of **1i** confirmed to be bound to the complex as a bidentate ligand.

The configuration of **1i** was derived from the ROESY spectrum in conjunction with molecular mechanics calculations (MM2, Chem3D Pro, 16.0.1.4, Perkin Elmer Informatics. Inc.) to visualize the complex. The stereochemistry of the Al

center was constrained by the presence of inter-ring ROESY correlations H-10/H-28' and H-28/H27'. The presence of *both* of these correlations indicate that the oxygen atoms attached to C-14 and C-14' are *cis* relative to each other. This conformation creates a “cleft” surrounded by rings C, D, A' and C'. The bound DME is situated in this cleft as indicated by ROESY correlations between H-a and H-12, 18, 9', 10'; H-c' and H-10'; as well as H-d and H-23 and 28. We also observed strong ROESY correlations to the *ortho*-hydrogen of BPh₄⁻ from H-b', H-c'' as well as H-10' indicating that **1i** exists as a tight ion-pair in solution, with the anion located on top of the bound DME ligand. Tight ion-pairing was further confirmed by diffusion-ordered NMR that showed experimentally indistinguishable diffusion coefficients for **1i** ligand, bound DME, and PPh₄⁻ resonances. (**Error! Reference source not found.**) This diffusion coefficient was also found to be significantly slower than that of the **Al-Cl** complex. Tight ion-pairing in a specific orientation likely explains the low rate of DME exchange. We also believe this tight ion pairing assists with the observed high regioselectivity and may explain why other bulky anions result in lower selectivity (ie. if other anions do not have a tight ion pair the selectivity may be lower).

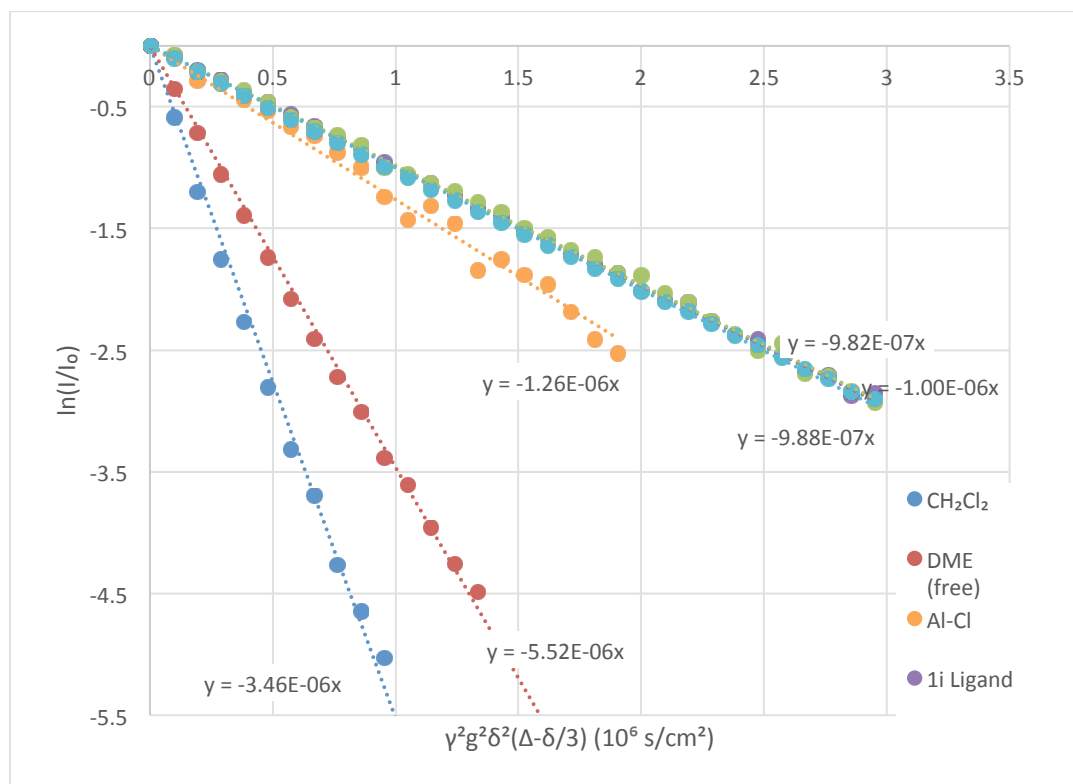


Figure 2-1. Stejskal-Tanner plot of a 500 MHz ^1H diffusion NMR experiment of **1i** in CDCl_3 at -55°C . The slope of each line corresponds to the negative of the diffusion coefficient. With the exception of CH_2Cl_2 , each data point represents the average of two or three well-resolved resonances.

Table S2-5. Chemical shifts for **1i** and **Al-Cl** determined at -55°C in CDCl_3

Atom #	1i		Al-Cl	
	^{13}C (ppm)	^1H (ppm)	^{13}C (ppm)	^1H (ppm)
1	144.62	—	143.8	—
2	124.9	—	126.1	—
3	131.57	—	131.81	—
4	126.67	6.83	126.93	7.04
5	127.49	7.27	126.98	7.27
6	126.56	7.5	126.18	7.5

Atom #	1i		Al-Cl	
	¹³ C (ppm)	¹ H (ppm)	¹³ C (ppm)	¹ H (ppm)
7	128.33	7.89	128.13	7.93
8	132.25	—	132.35	—
9	130.73	7.95	129.96	7.92
10	125.2	7.21	125.51	7.42
12	173.44	8.48	174.09	8.4
13	118.2	—	118.92	—
14	160.26	—	163.15	—
15	n/d	—	n/d	—
16	140.6	7.12	140.99	7.03
17	126.37	—	125.8	—
18	133.07	7	132.56	6.92
19	133.71	—	135.06	—
20	134.5	—	137.62	—
21	128.1	7.09	127.74	6.98
22	136.94	—	135.88	—
23	127.33	6.67	127.54	7.11
24	138.64	—	136.85	—
25	20.42	2.22	20.41	2.15
26	21.61	2.00	21.26	2.05
27	21.33	2.38	21.43	2.46
28	18.45	1.22	20.47	1.89
1'	143.76	—	144.02	—

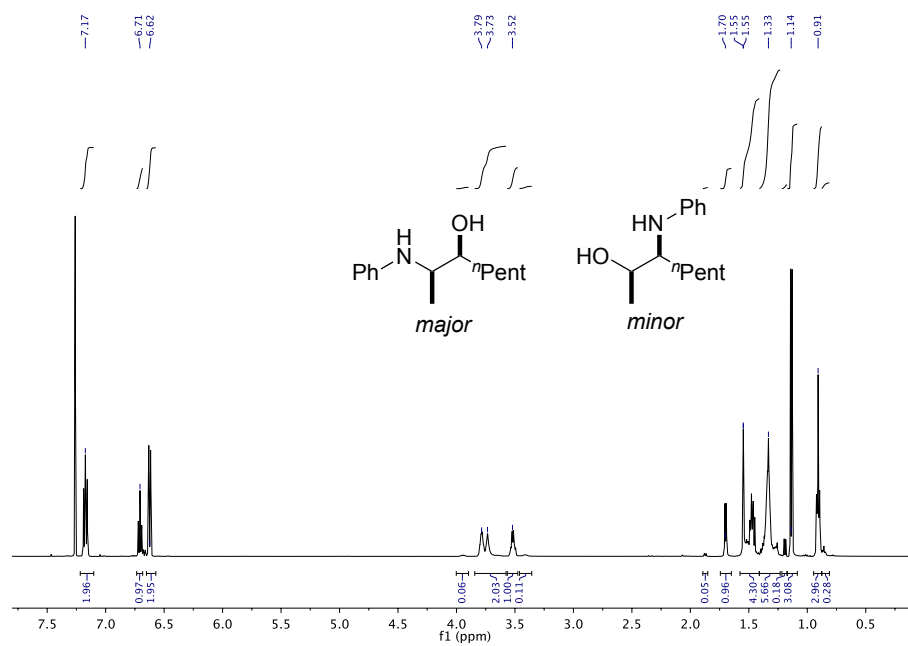
Atom #	1i		Al-Cl	
	¹³ C (ppm)	¹ H (ppm)	¹³ C (ppm)	¹ H (ppm)
2'	125.59	—	125.16	—
3'	131.92	—	131.82	—
4'	126.49	7.10	126.5	7.13
5'	127.68	7.34	126.82	7.31
6'	126.65	7.55	125.96	7.53
7'	128.52	8.00	128.46	7.98
8'	131.51	—	132.11	—
9'	131.3	8.00	129.42	8.04
10'	121.94	6.27	126.21	7.61
12'	171.22	8.01	169.12	8.26
13'	118.23	—	118.48	—
14'	159.85	—	159.13	—
15'	n/d	—	n/d	—
16'	140.87	7.04	139.91	7.07
17'	126.63	—	126.29	—
18'	133.51	6.95	132.68	6.96
19'	133.82	—	133.76	—
20'	134.89	—	135.22	—
21'	128.2	7.05	127.79	6.86
22'	136.51	—	135.69	—
23'	127.66	6.82	127.78	6.79
24'	137.44	—	138.9	—

Atom #	1i		Al-Cl	
	¹³ C (ppm)	¹ H (ppm)	¹³ C (ppm)	¹ H (ppm)
25'	20.34	2.20	20.31	2.19
26'	20.9	2.01	21.73	1.93
27'	21.15	2.31	21.32	2.38
28'	20.69	1.80	19.06	1.63
a	59.5	1.99	—	—
b	68.27	2.56, 2.73	—	—
c	68.01	0.90, 2.97	—	—
d	61.1	2.11	—	—
BPh ₄ -1	163.62	—	—	—
BPh ₄ -2	136.01	7.40	—	—
BPh ₄ -3	125.75	7.05	—	—
BPh ₄ -4	122.09	6.95	—	—

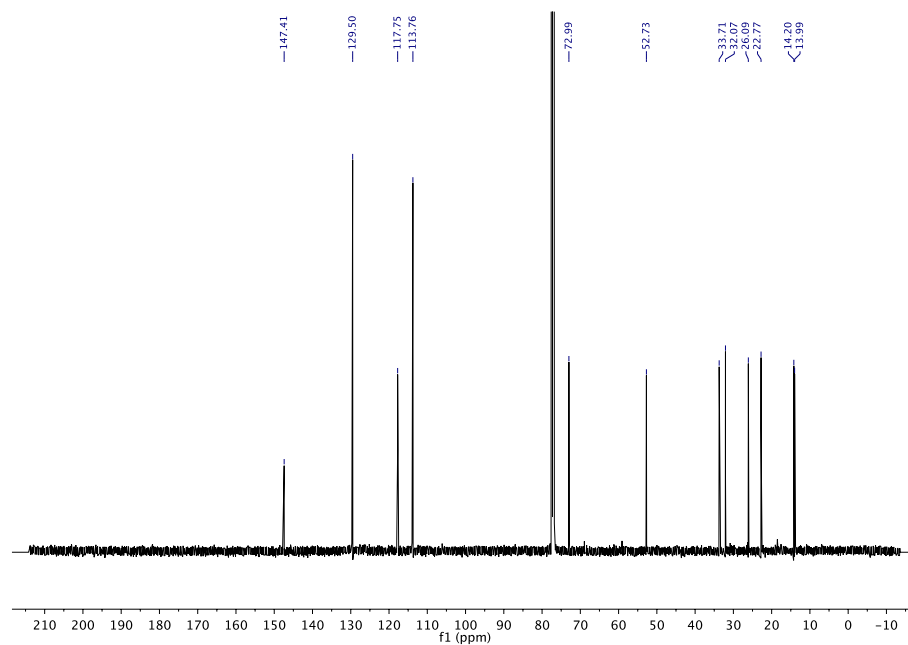
Copies of ^1H and $^{13}\text{C}\{^1\text{H}\}$ NMR spectra

(2*R*,3*S*)-*rel*-2-(Phenylamino)-3-octanol (4a) + (2*R*,3*S*)-*rel*-3-(phenylamino)-2-octanol (5a)

^1H NMR (500 MHz, CDCl_3)

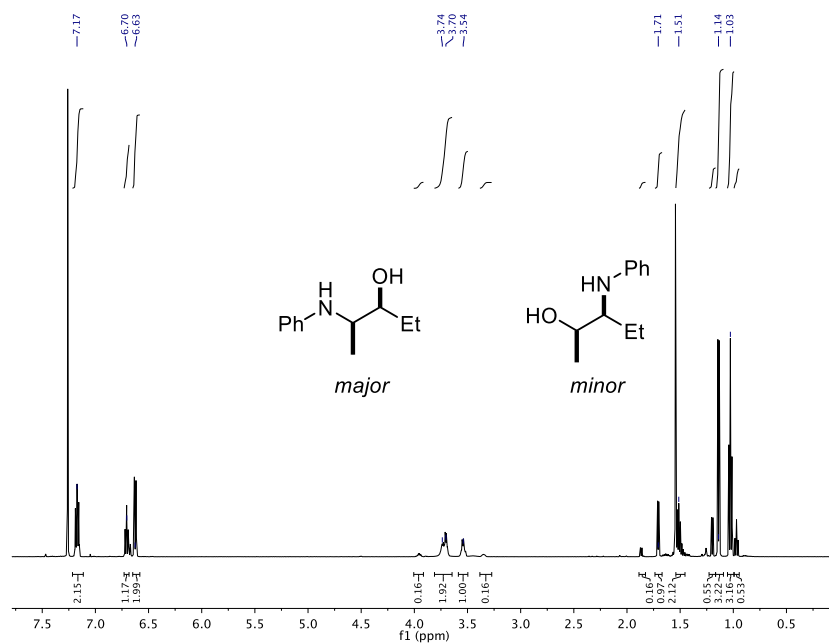


$^{13}\text{C}\{^1\text{H}\}$ NMR (126 MHz, CDCl_3)

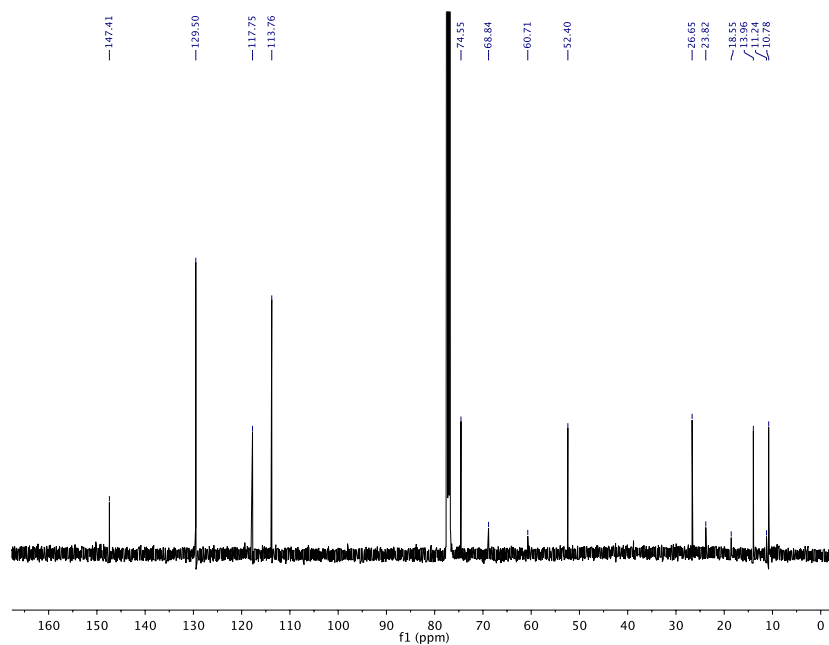


(2*R*,3*S*)-rel-2-(Phenylamino)-3-pentanol (4b) + (2*R*,3*S*)-rel-3-(phenylamino)-2-pentanol (5b)

¹H NMR (500 MHz, CDCl₃)

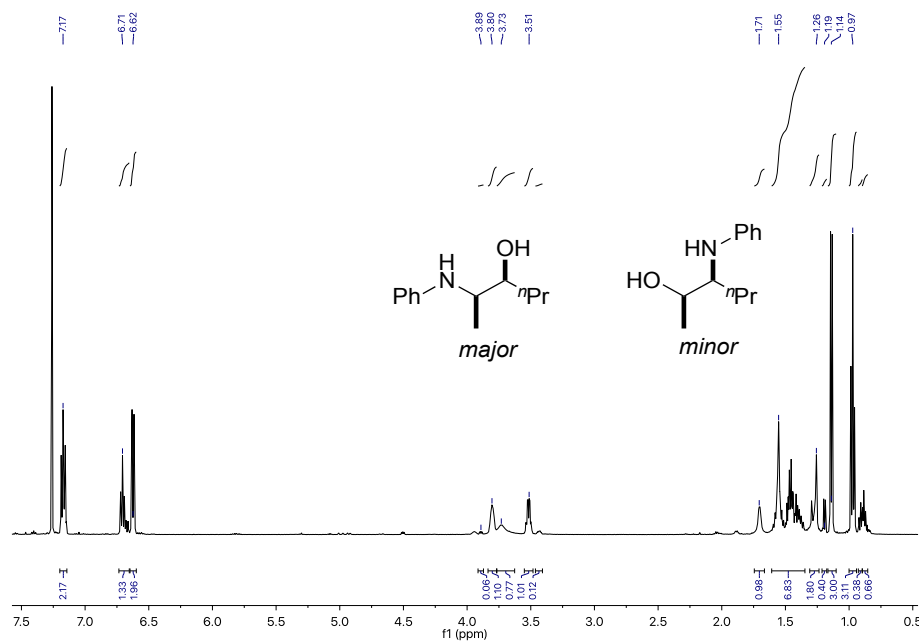


¹³C{¹H} NMR (126 MHz, CDCl₃)

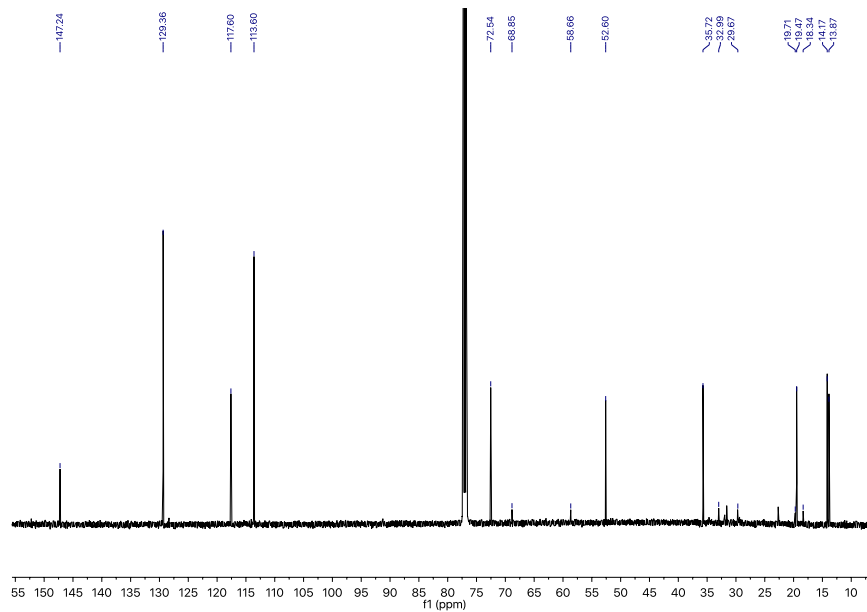


(2*R*,3*S*)-rel-2-(Phenylamino)-3-hexanol (4c) + (2*R*,3*S*)-rel-3-(phenylamino)-2-hexanol (5c)

¹H NMR (500 MHz, CDCl₃)

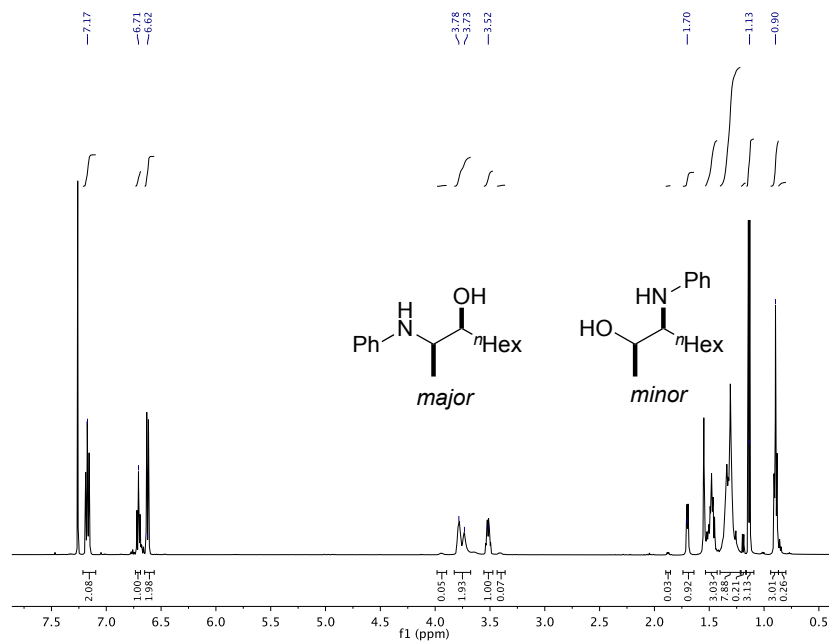


¹³C{¹H} NMR (126 MHz, CDCl₃)

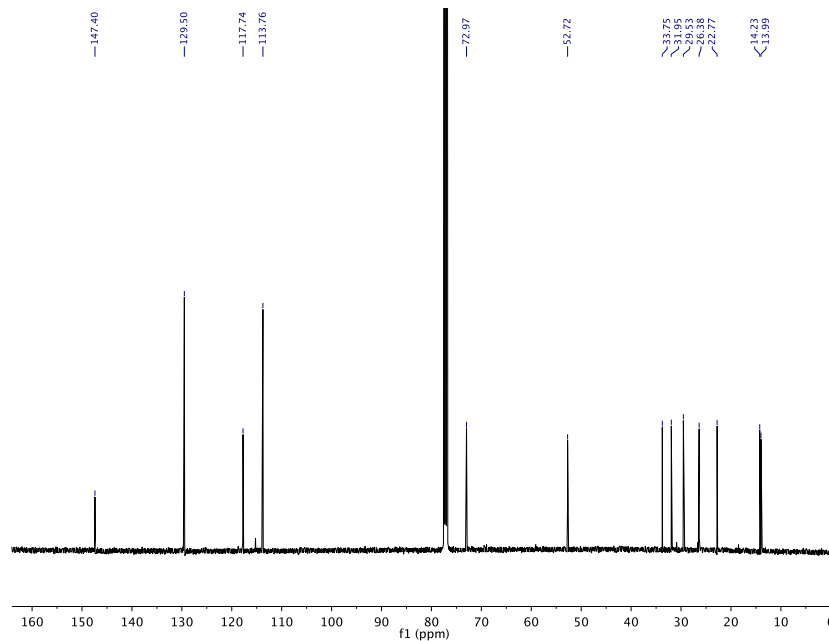


(2*R*,3*S*)-rel-2-(Phenylamino)-3-nonanol (4d) + (2*R*,3*S*)-rel-3-(phenylamino)-2-nonanol (5d)

¹H NMR (500 MHz, CDCl₃)

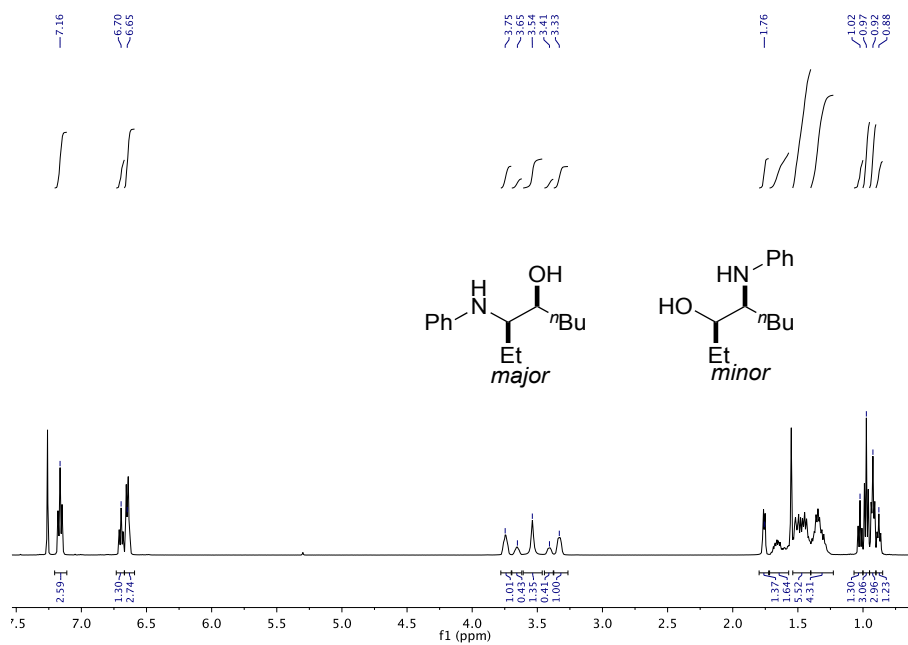


¹³C{¹H} NMR (126 MHz, CDCl₃)

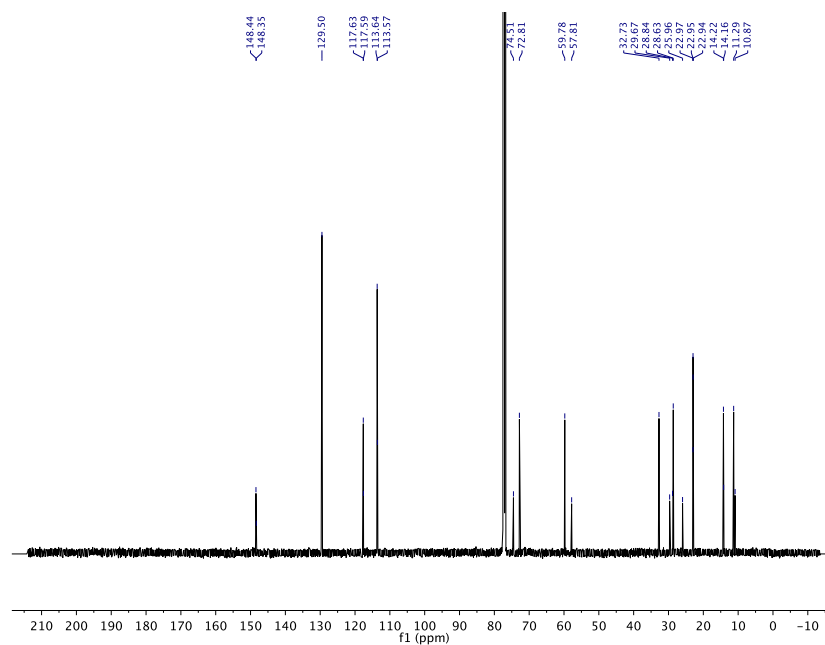


(3*R*,4*S*)-rel-3-(Phenylamino)-4-octanol (4e) + (3*R*,4*S*)-rel-4-(phenylamino)-3-octanol (5e)

¹H NMR (500 MHz, CDCl₃)

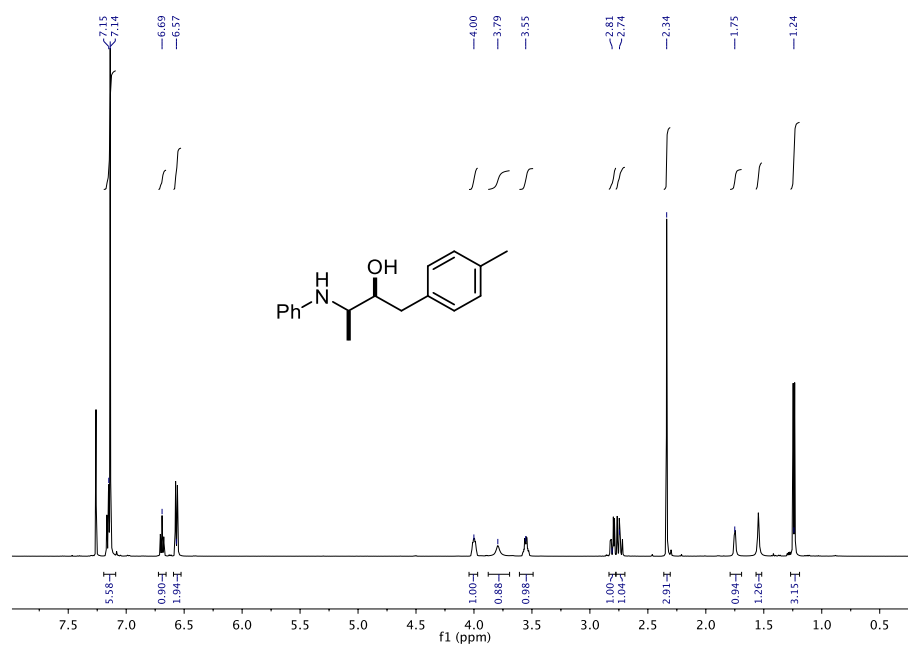


¹³C{¹H} NMR (126 MHz, CDCl₃)

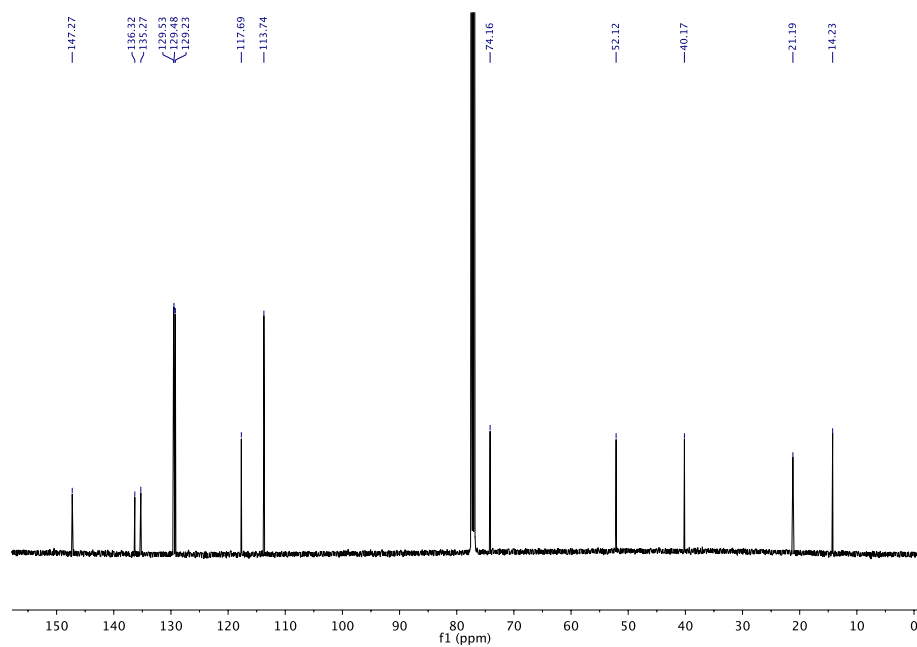


(2*R*,3*S*)-*rel*-3-(Phenylamino)-1-(*p*-tolyl)butan-2-ol (4f)

^1H NMR (500 MHz, CDCl_3)

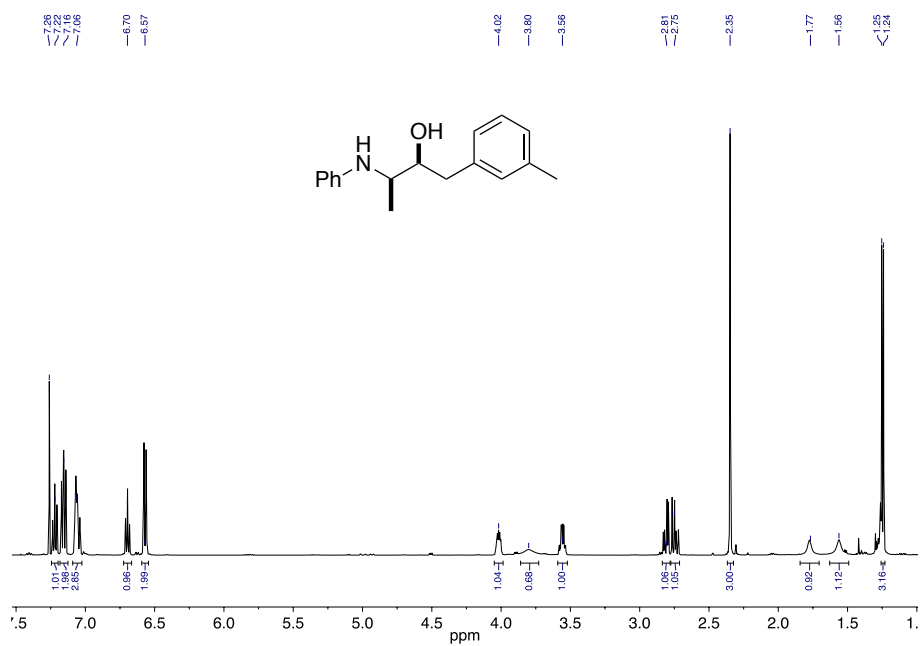


$^{13}\text{C}\{^1\text{H}\}$ NMR (126 MHz, CDCl_3)

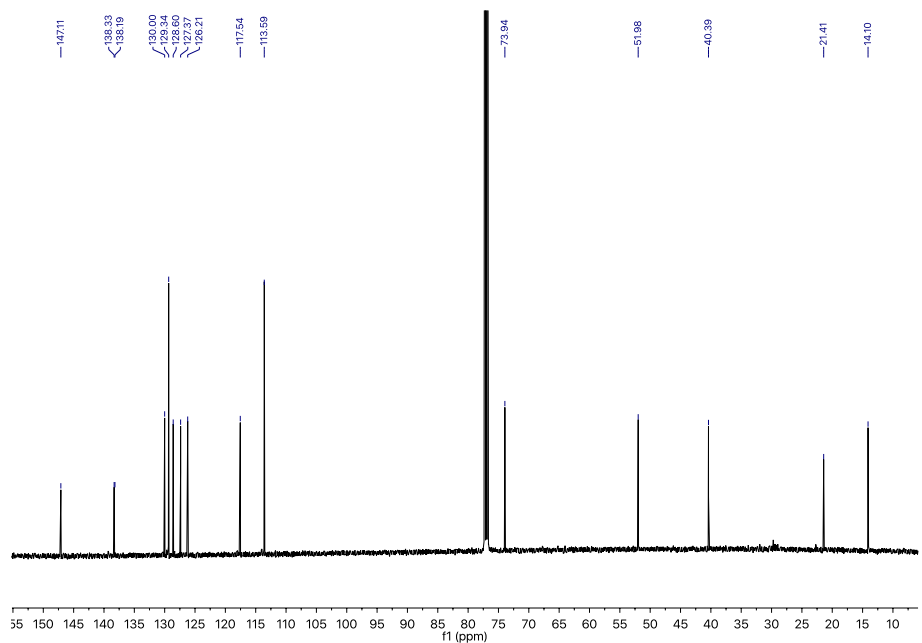


(2*S*,3*R*)-rel-3-(Phenylamino)-1-(*m*-tolyl)butan-2-ol (4g)

^1H NMR (500 MHz, CDCl_3)

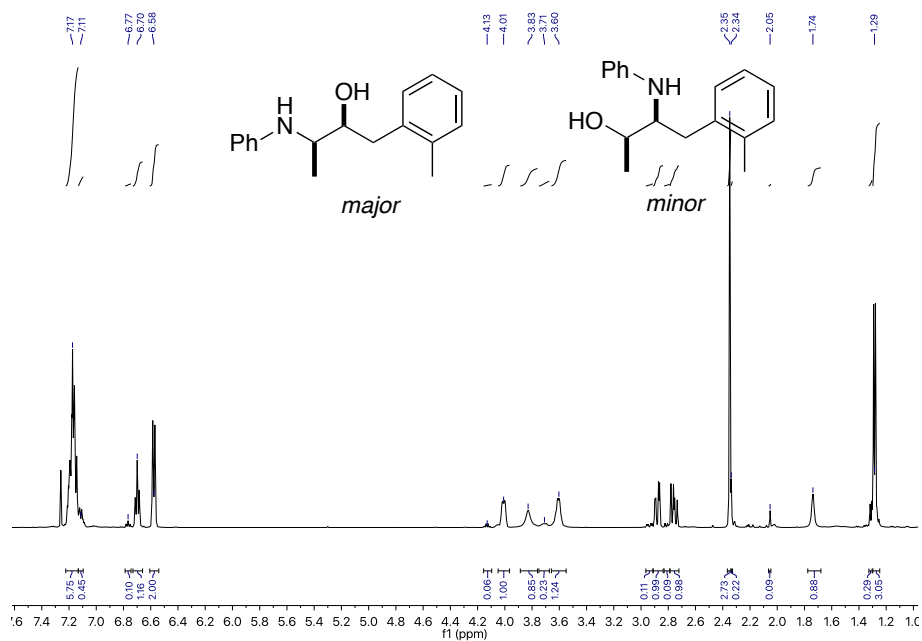


$^{13}\text{C}\{^1\text{H}\}$ NMR (126 MHz, CDCl_3)

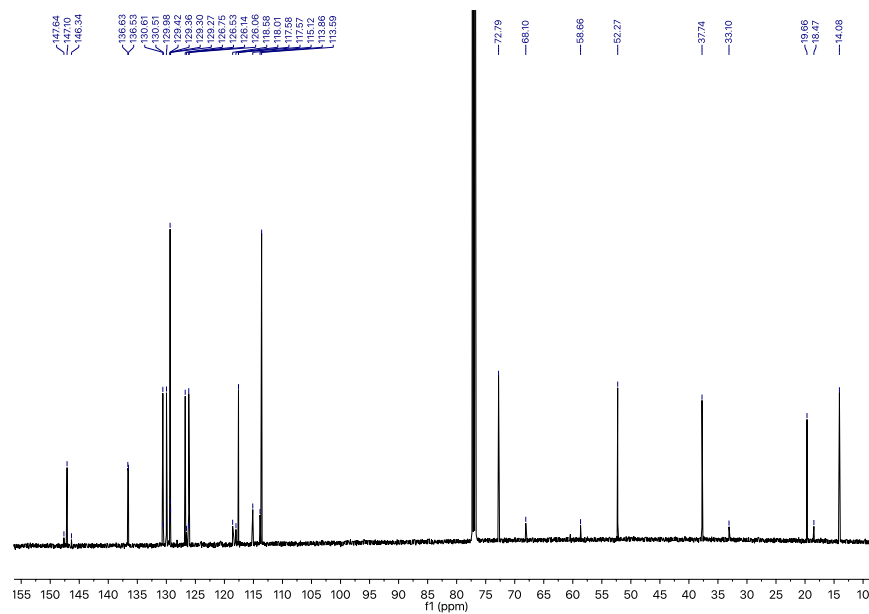


((2S,3R)-rel-3-(Phenylamino)-1-(o-tolyl)butan-2-ol (4h) + (2S,3R)-rel-2-(phenylamino)-1-(o-tolyl)butan-3-ol (5h)

^1H NMR (500 MHz, CDCl_3)

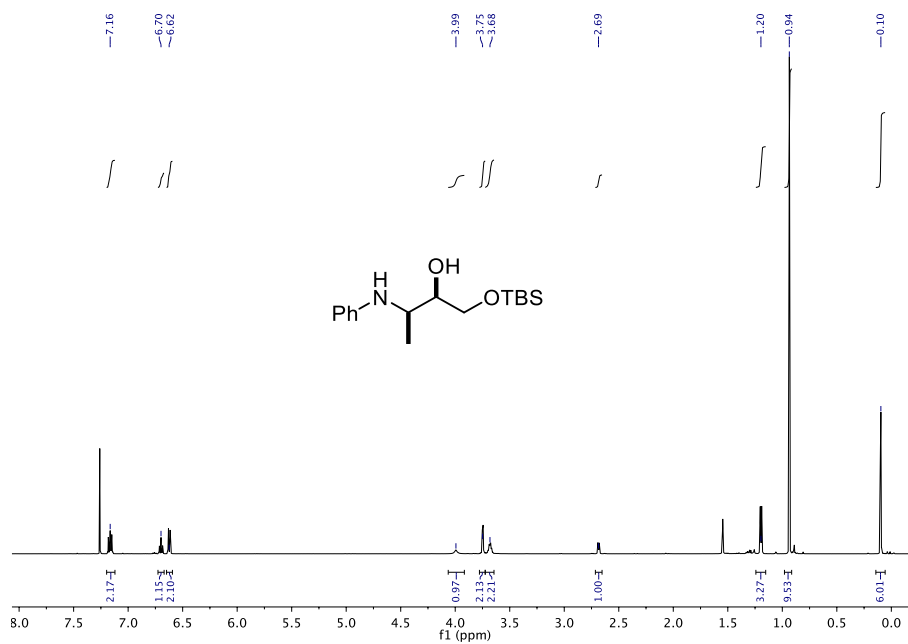


$^{13}\text{C}\{^1\text{H}\}$ NMR (126 MHz, CDCl_3)

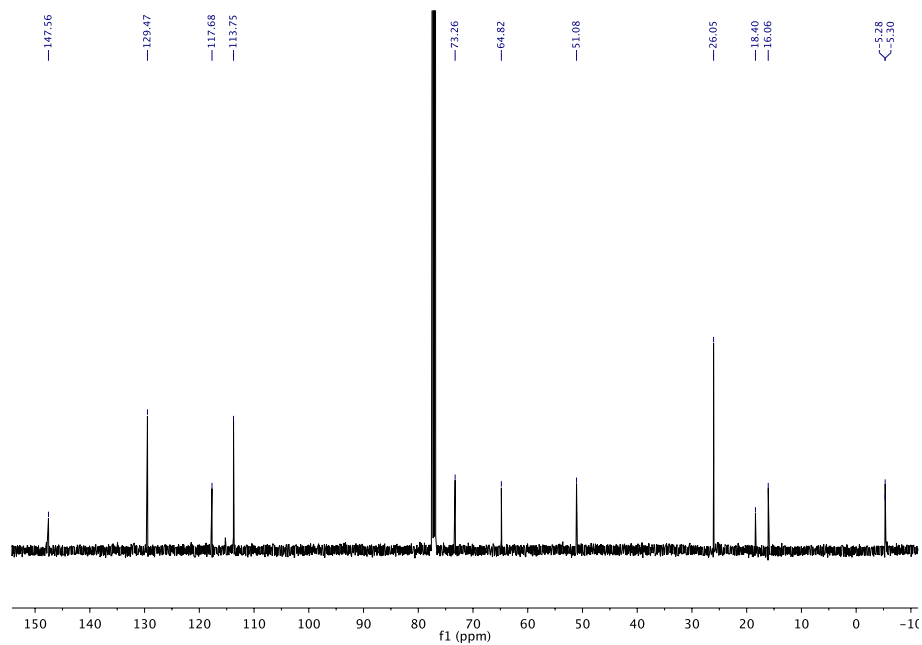


(2*R*,3*R*)-rel-1-((*tert*-Butyldimethylsilyl)oxy)-3-(phenylamino)butan-2-ol (4i)

^1H NMR (500 MHz, CDCl_3)

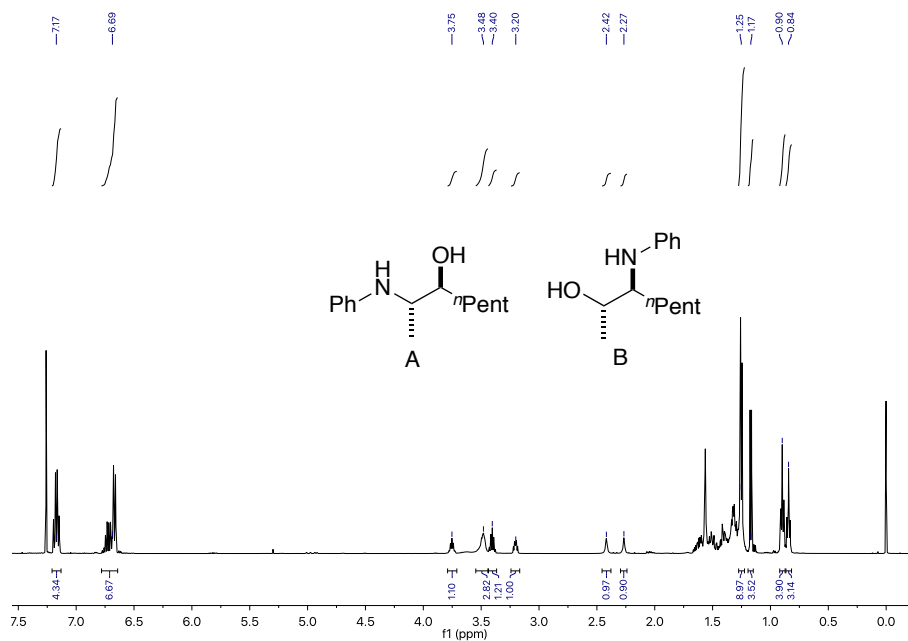


$^{13}\text{C}\{^1\text{H}\}$ NMR (126 MHz, CDCl_3)

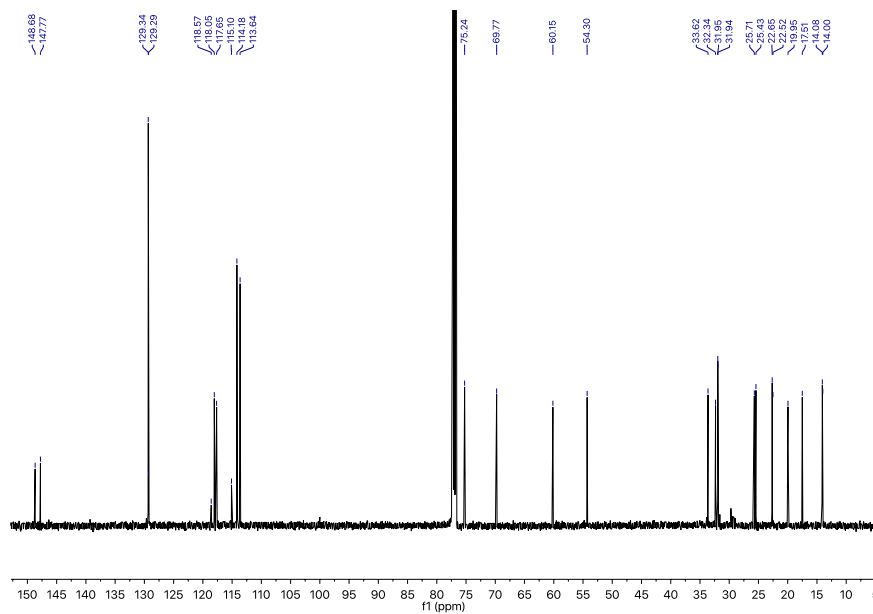


(2*S*,3*S*)-*rel*-2-(Phenylamino)-3-octanol (4j) + (2*S*,3*S*)-*rel*-3-(phenylamino)-2-octanol (5j)

¹H NMR (500 MHz, CDCl₃)

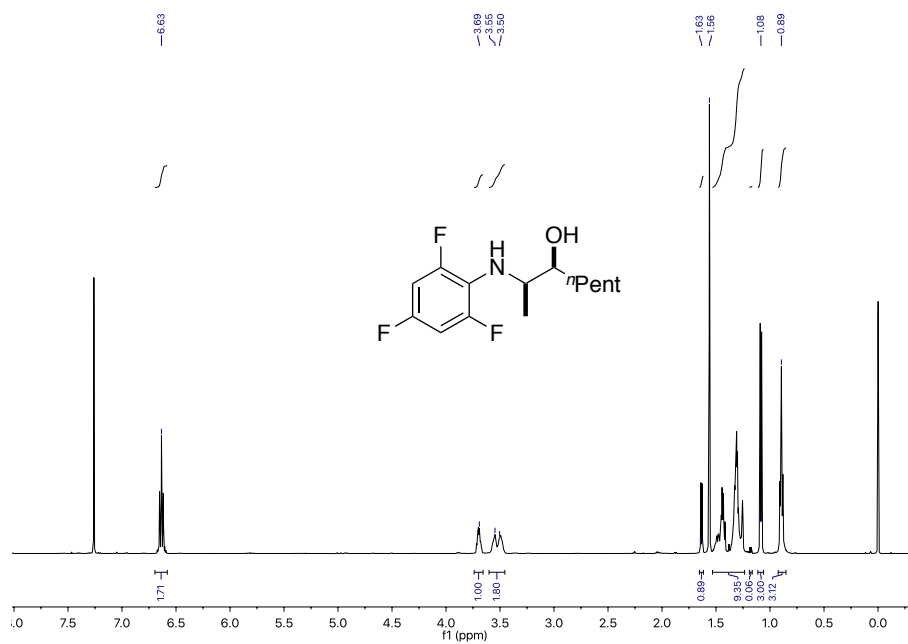


¹³C{¹H} NMR (126 MHz, CDCl₃)

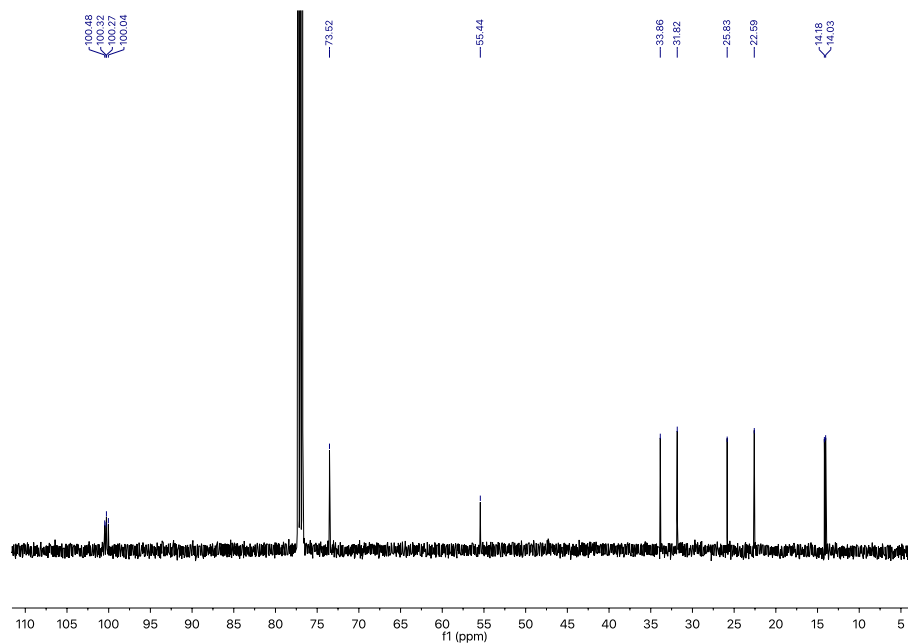


(2*R*,3*S*)-rel-2-(2,4,6-Trifluorophenyl)amino)octan-3-ol (6b)

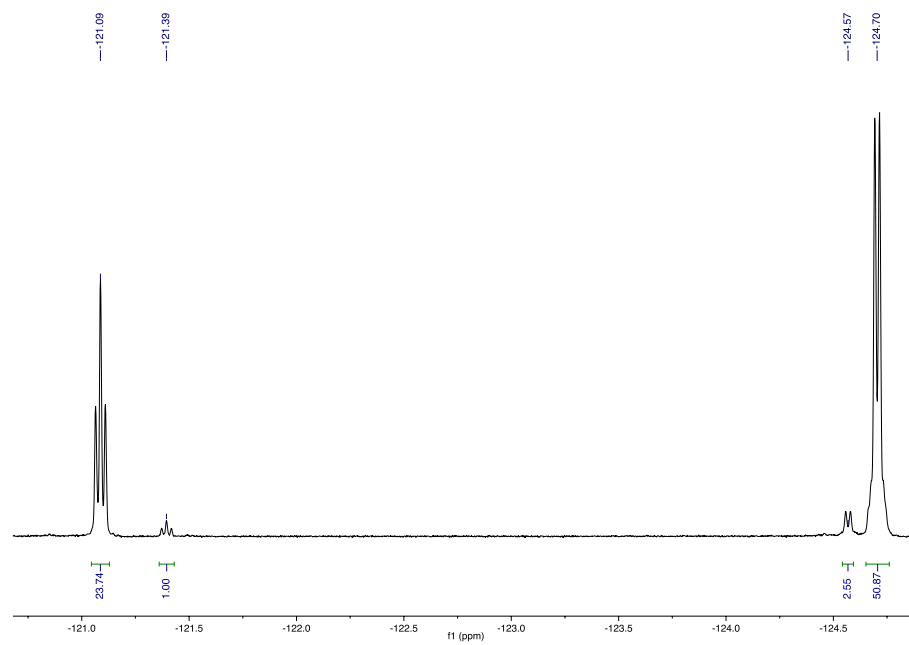
^1H NMR (500 MHz, CDCl_3)



$^{13}\text{C}\{^1\text{H}\}$ NMR (126 MHz, CDCl_3)

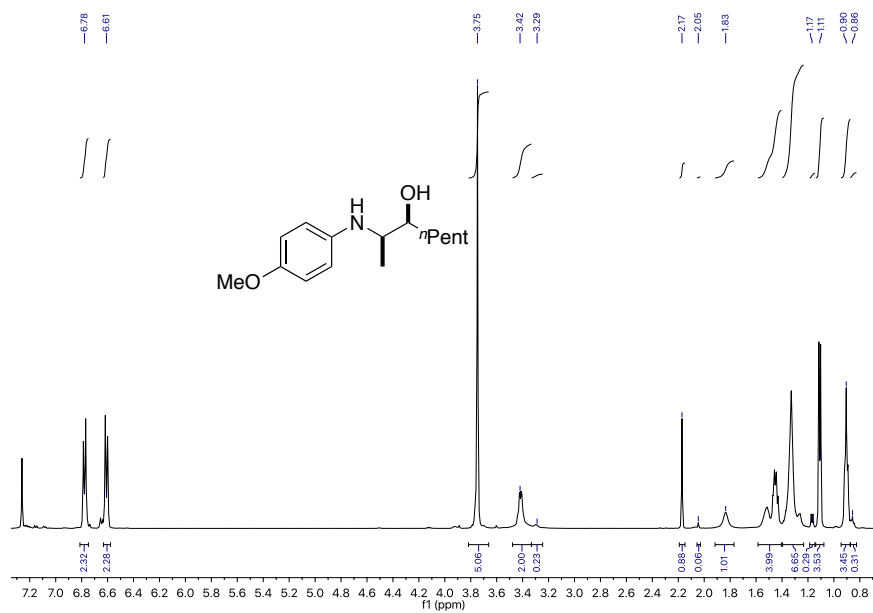


^{19}F { ^1H } NMR (400 MHz, CDCl_3)

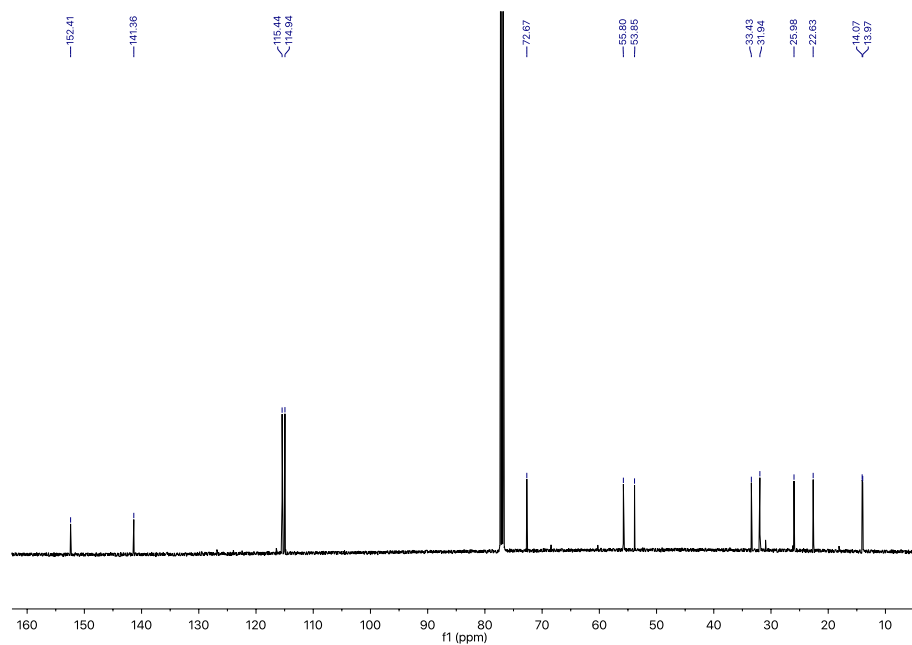


(2*R*,3*S*)-rel-2-((4-Methoxyphenyl)amino)octan-3-ol (6c)

¹H NMR (500 MHz, CDCl₃)

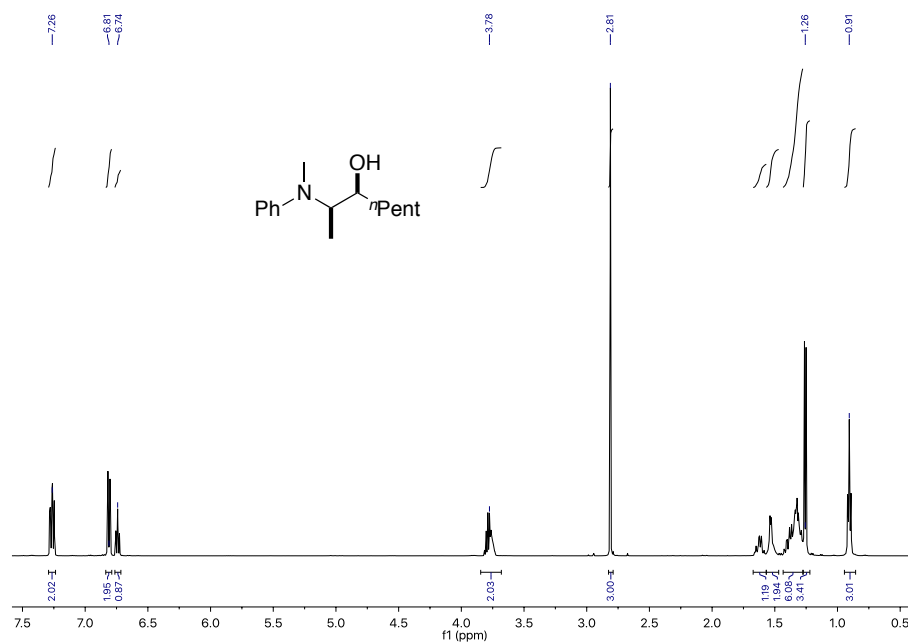


¹³C{¹H} NMR (126 MHz, CDCl₃)

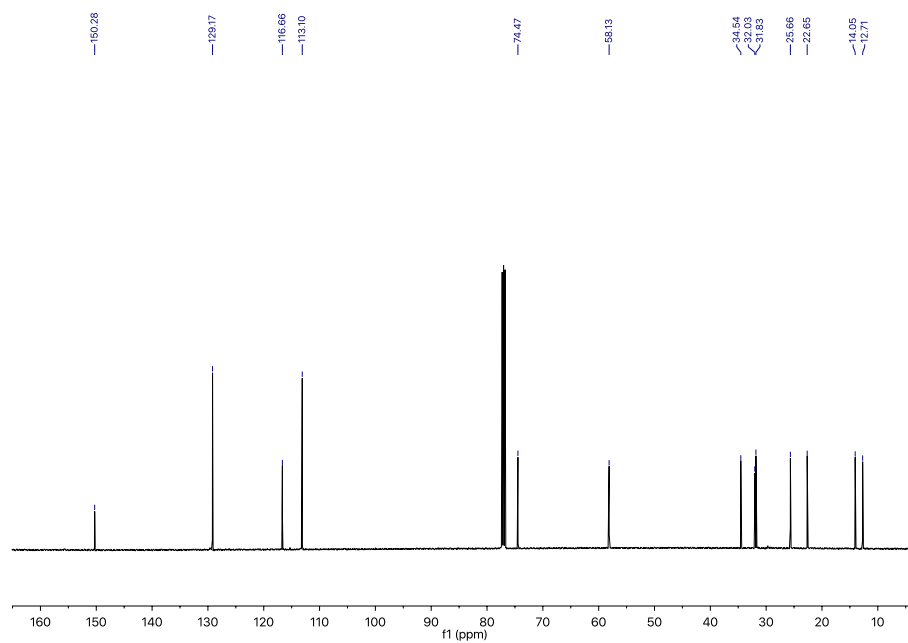


(2*R*,3*S*)-rel-2-(Methyl(phenyl)amino)octan-3-ol (6d)

^1H NMR (500 MHz, CDCl_3)

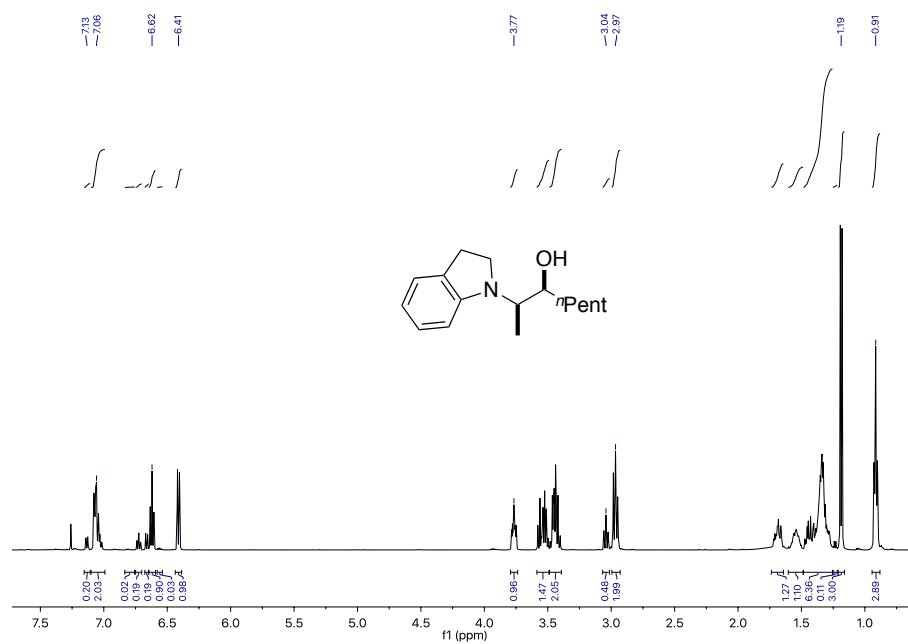


$^{13}\text{C}\{^1\text{H}\}$ NMR (126 MHz, CDCl_3)

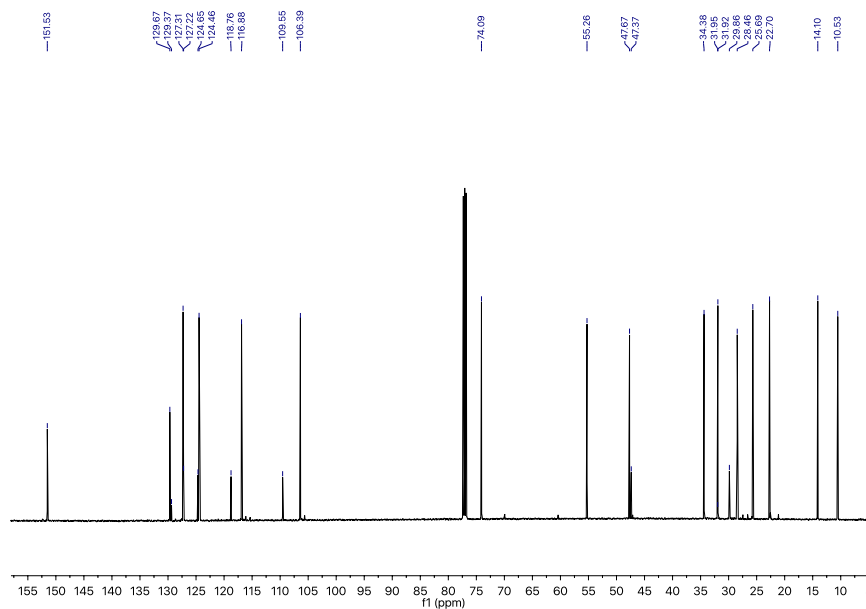


(2*R*,3*S*)-*rel*-2-(Indolin-1-yl)octan-3-ol (6e)

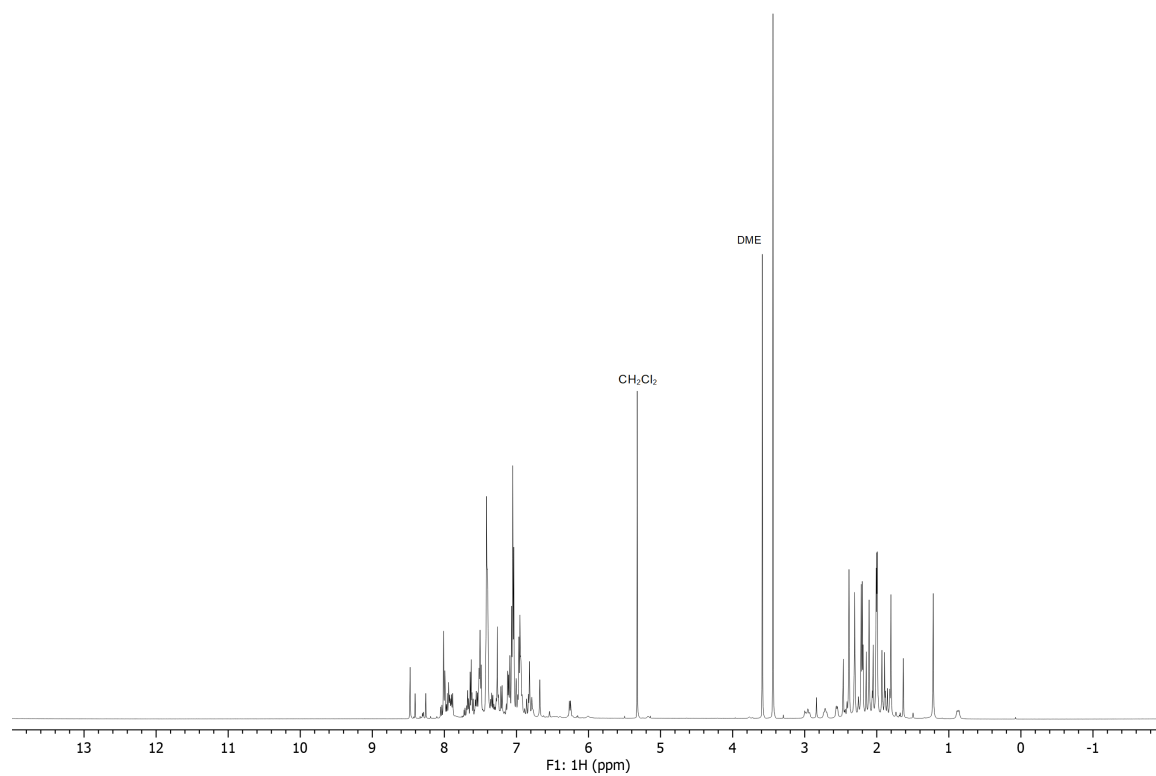
^1H NMR (500 MHz, CDCl_3)



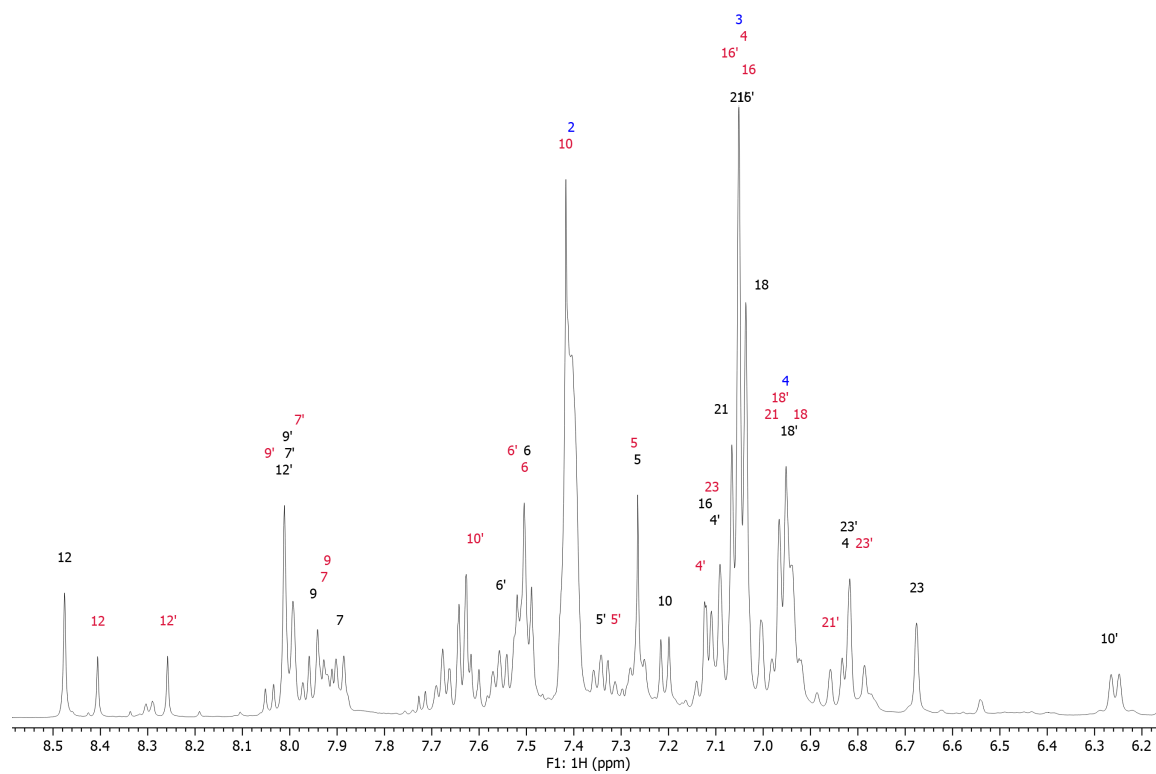
$^{13}\text{C}\{^1\text{H}\}$ NMR (126 MHz, CDCl_3)



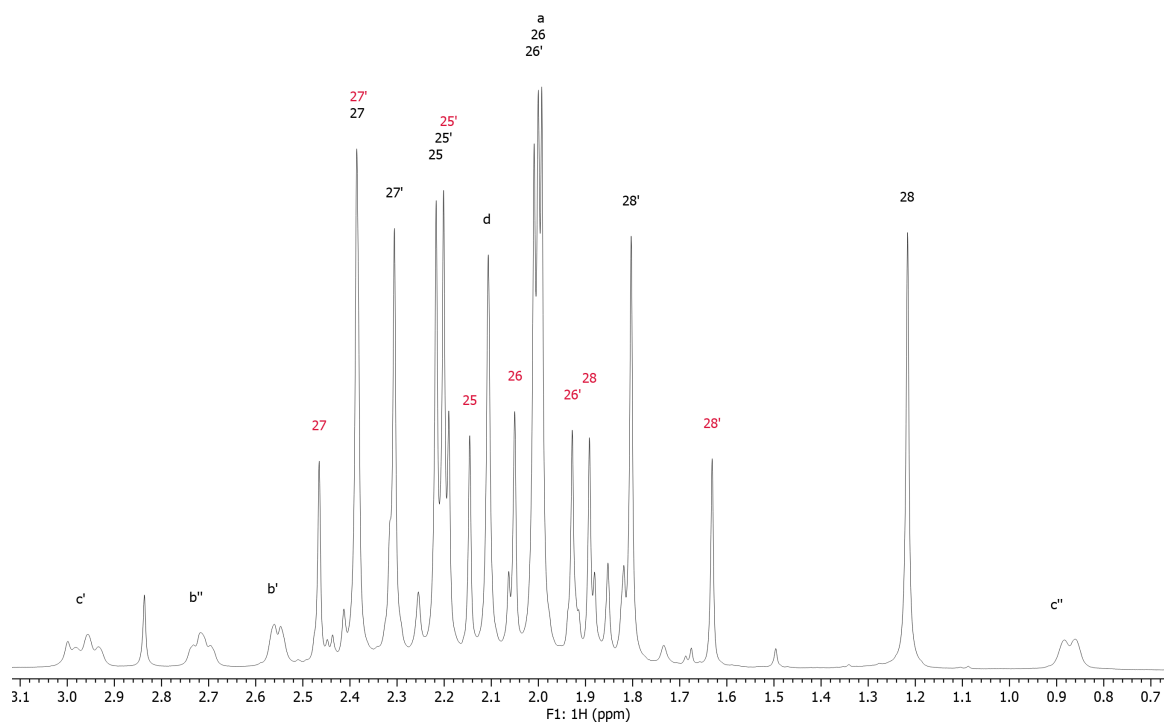
NMR spectra for **1i** in CDCl_3 at -55°C on a 500 MHz spectrometer



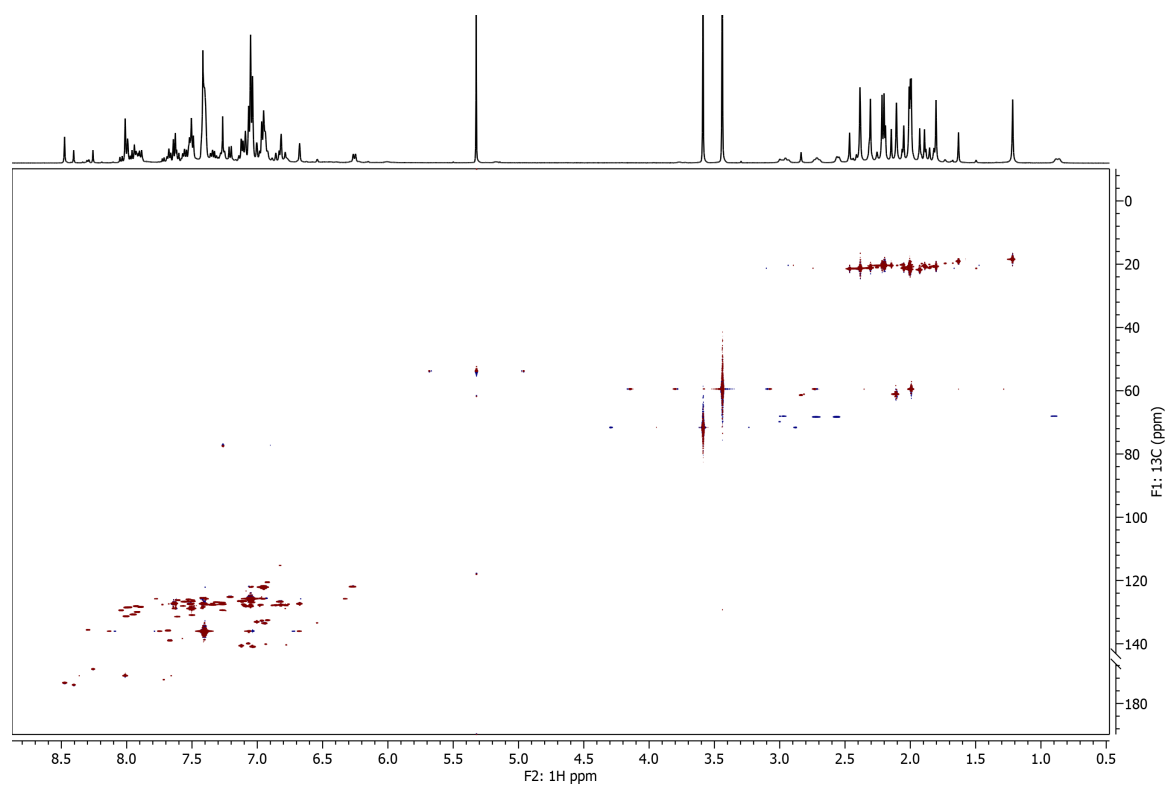
^1H NMR: Expansion of aromatic region. Numbers in black, blue and red indicate assignments for **1j**, BPh_4^- and **Al-Cl**, respectively.



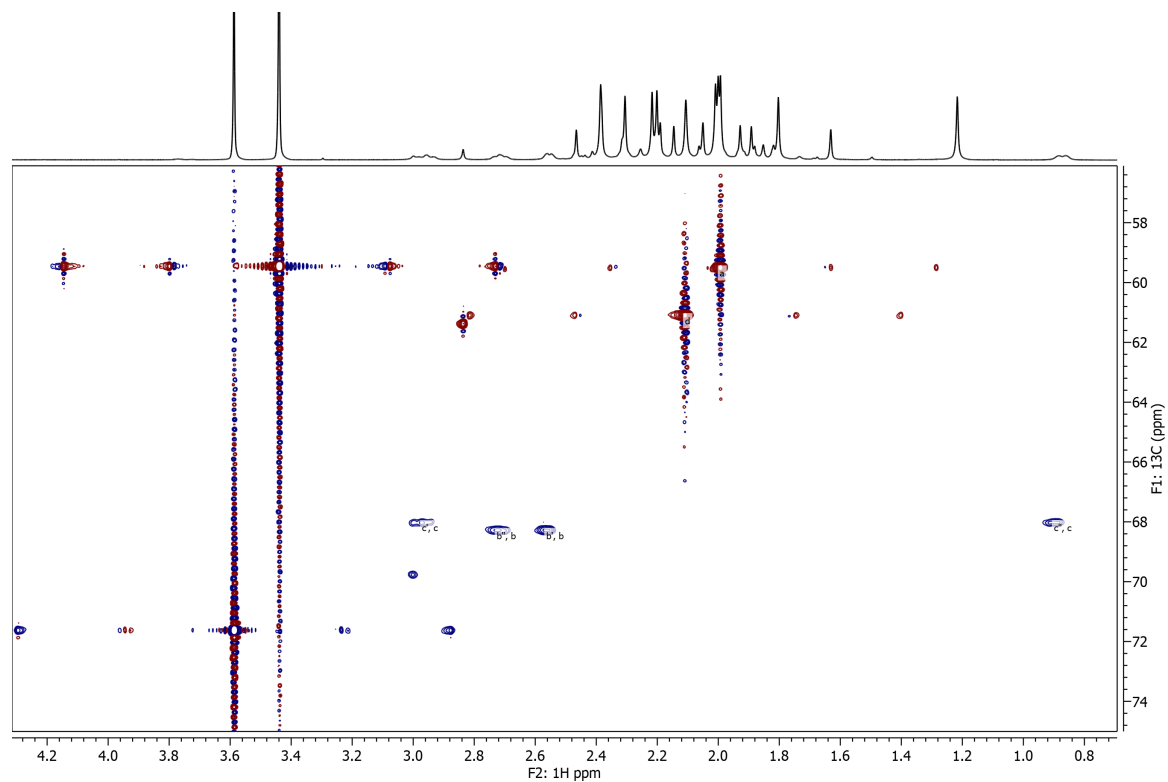
^1H NMR: Expansion of aliphatic region. Numbers in black and red indicate assignments for **1j** and **Al-Cl**, respectively.



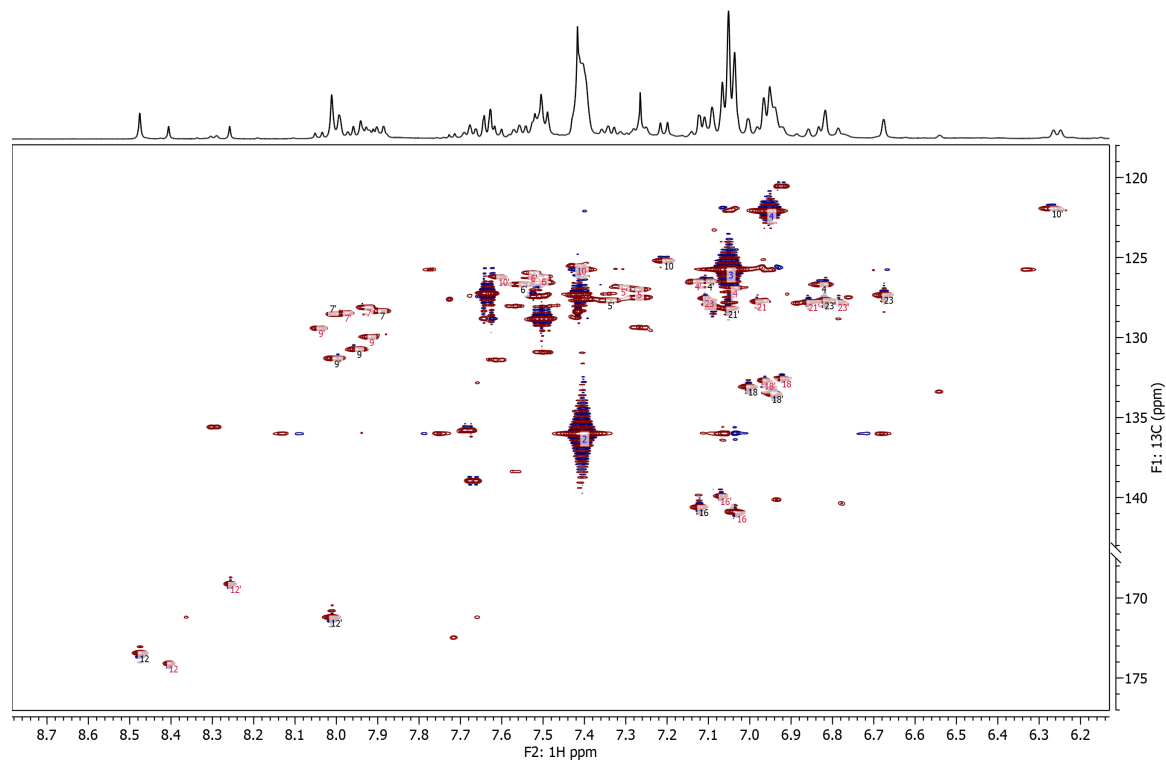
HSQC: Full Spectrum



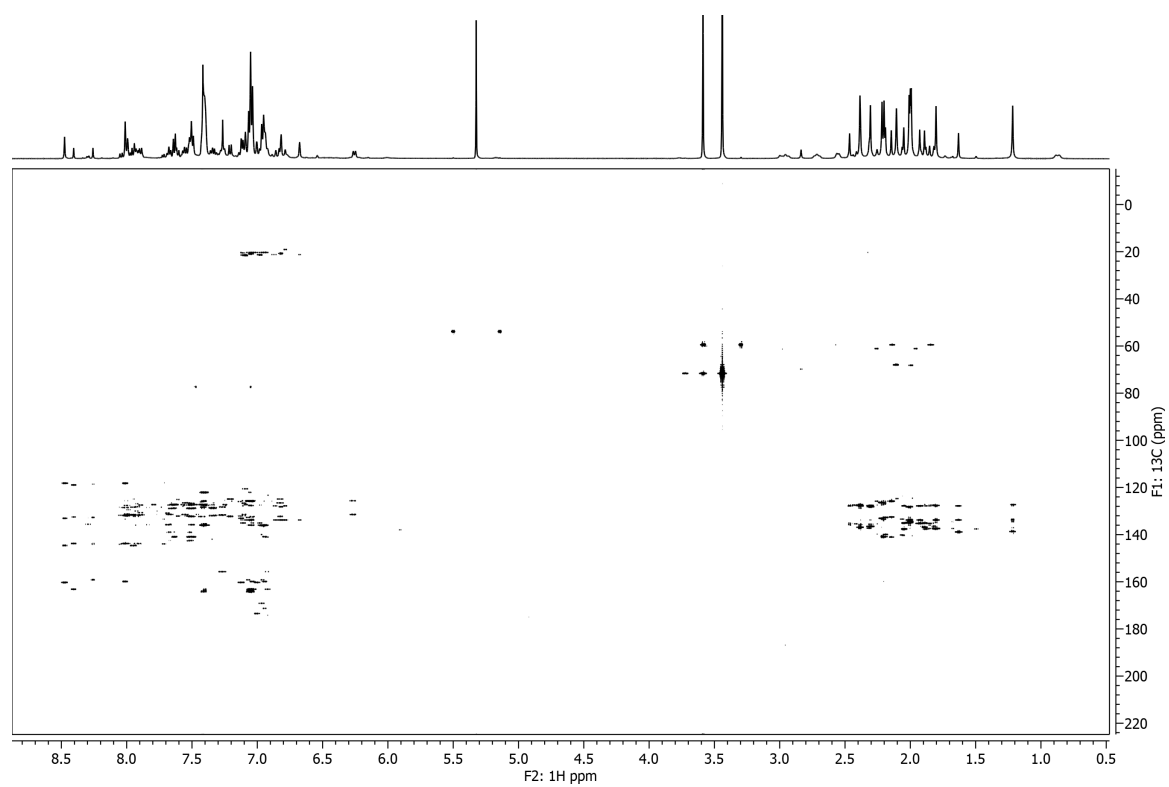
HSQC: Expansion of dimethoxyethane region. Numbers in black and red indicate assignments for **1j** and **Al-Cl**, respectively.



HSQC: Expansion of aromatic region. Numbers in black and red indicate assignments for **1j** and **Al-Cl**, respectively.

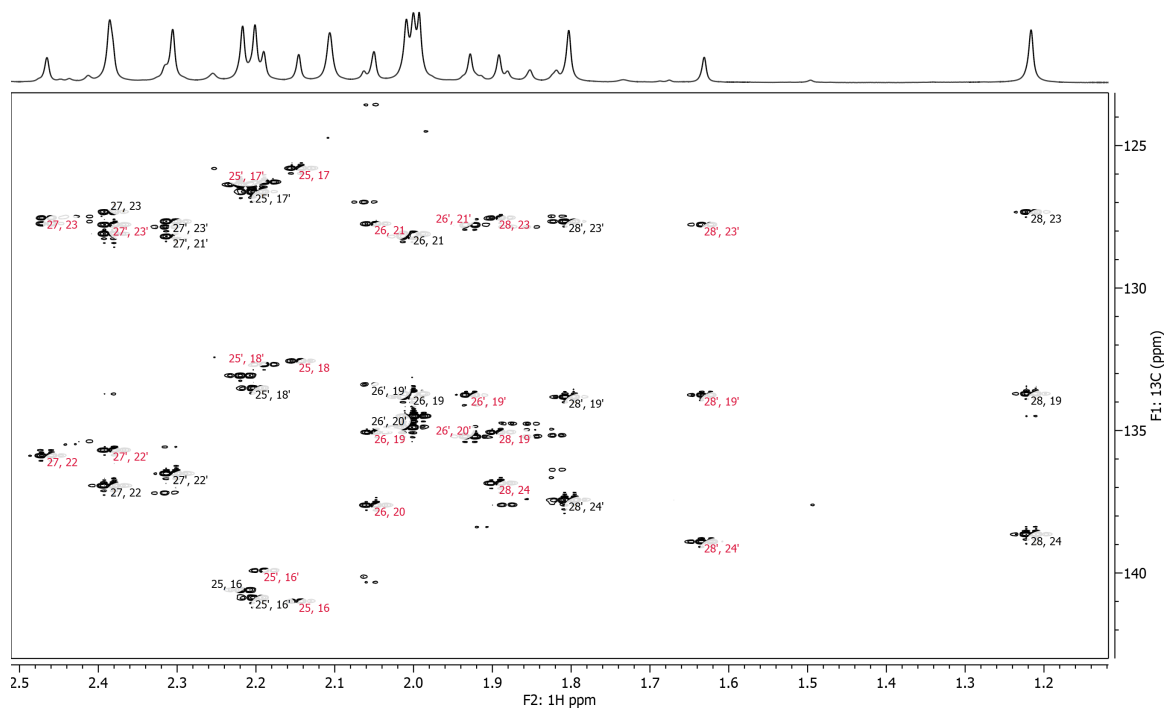


HMBC: Full spectrum

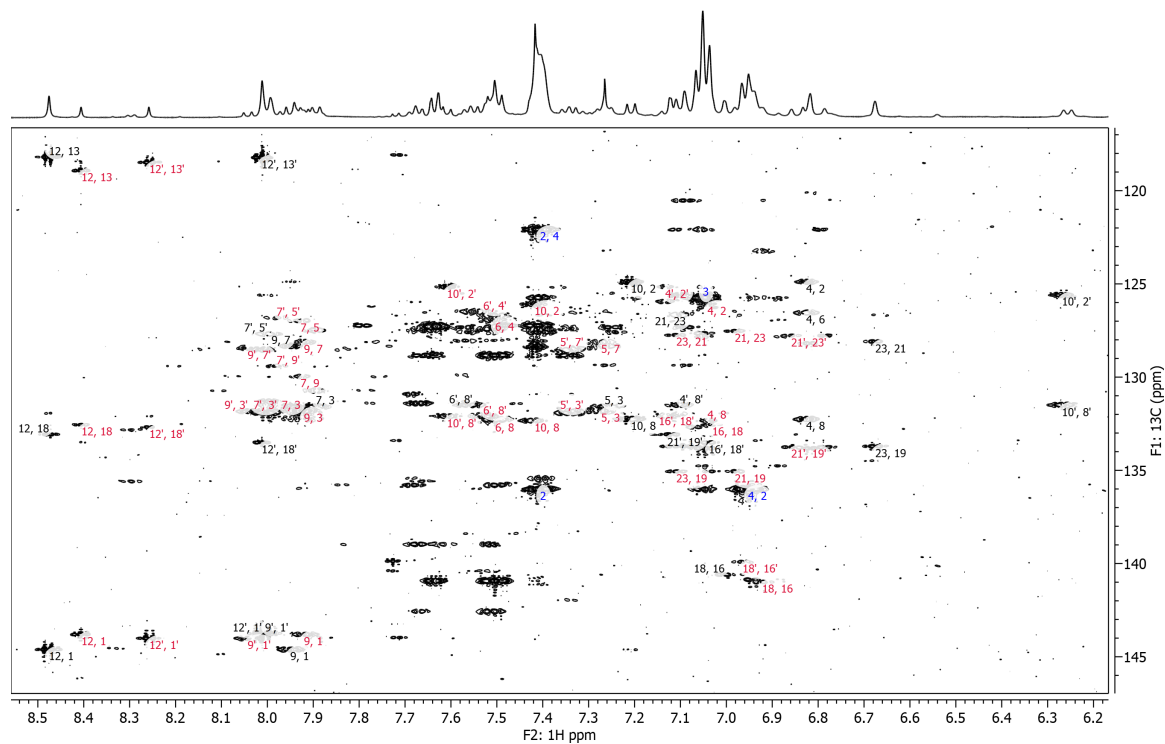


[illegible]

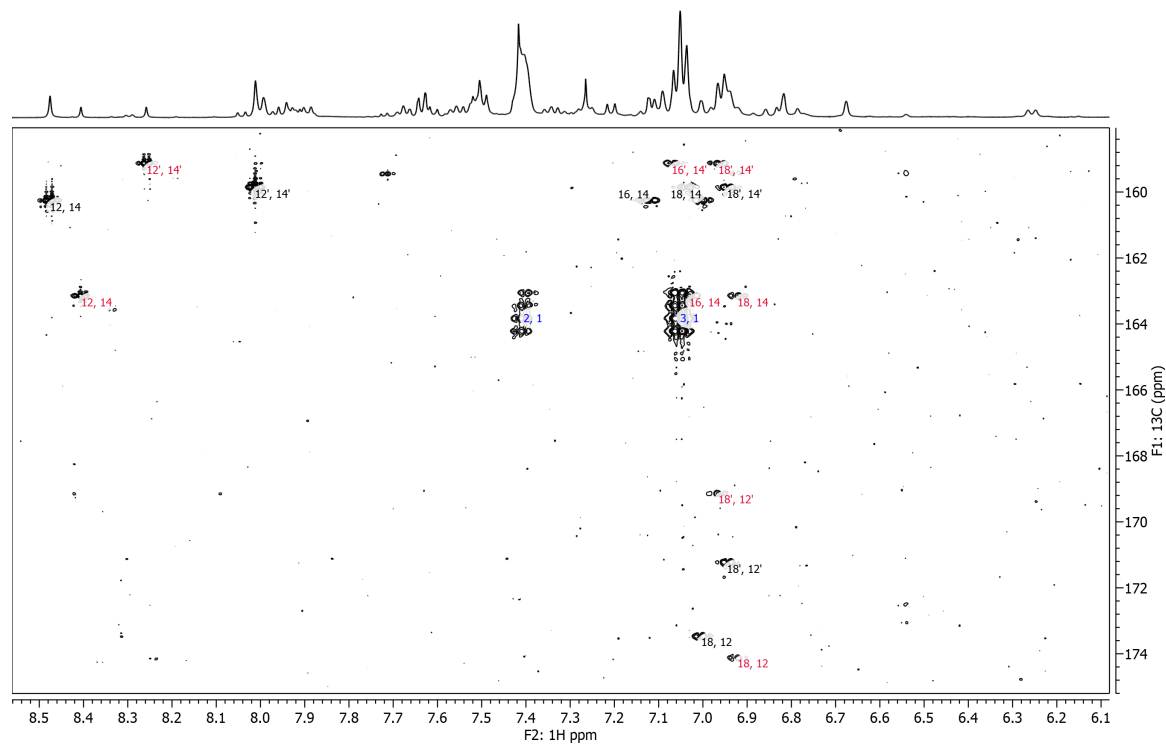
HMBC: Expansion of aliphatic to aromatic region. Numbers in black and red indicate assignments for **1j** and **Al-Cl**, respectively.



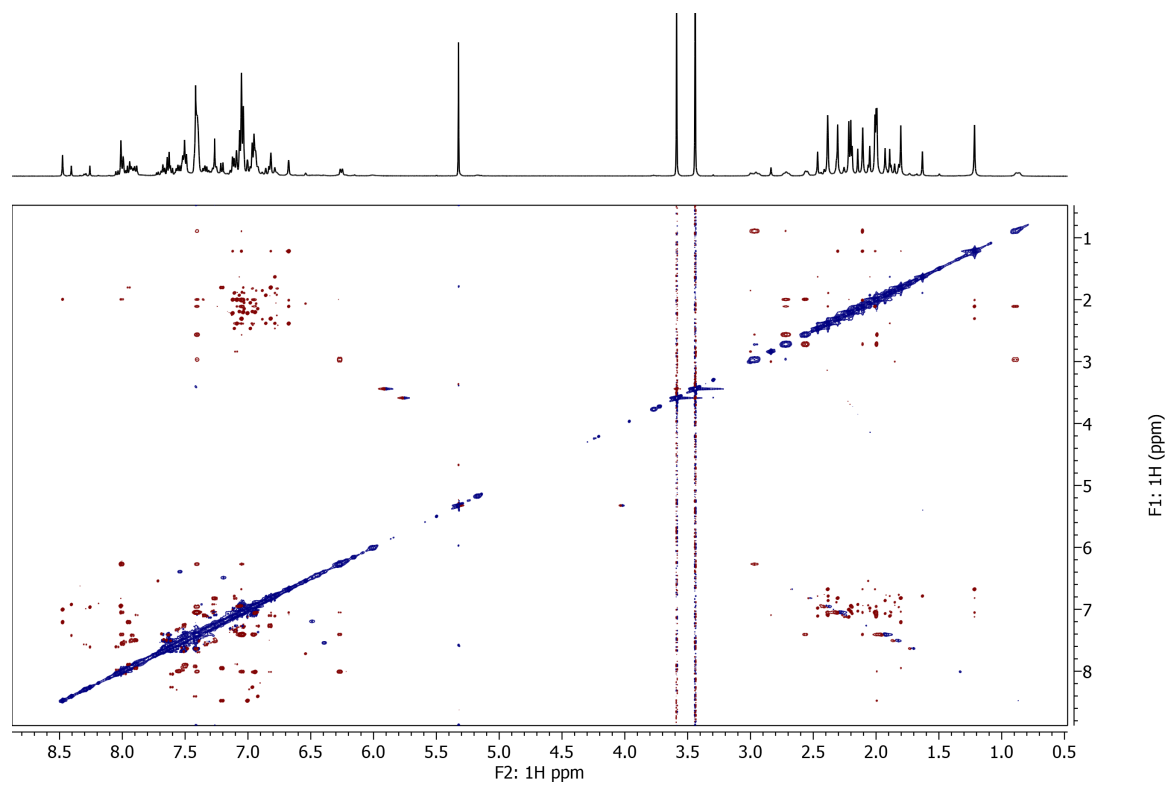
HMBC: Expansion of aromatic to low aromatic region. Numbers in black and red indicate assignments for **1j** and **Al-Cl**, respectively.



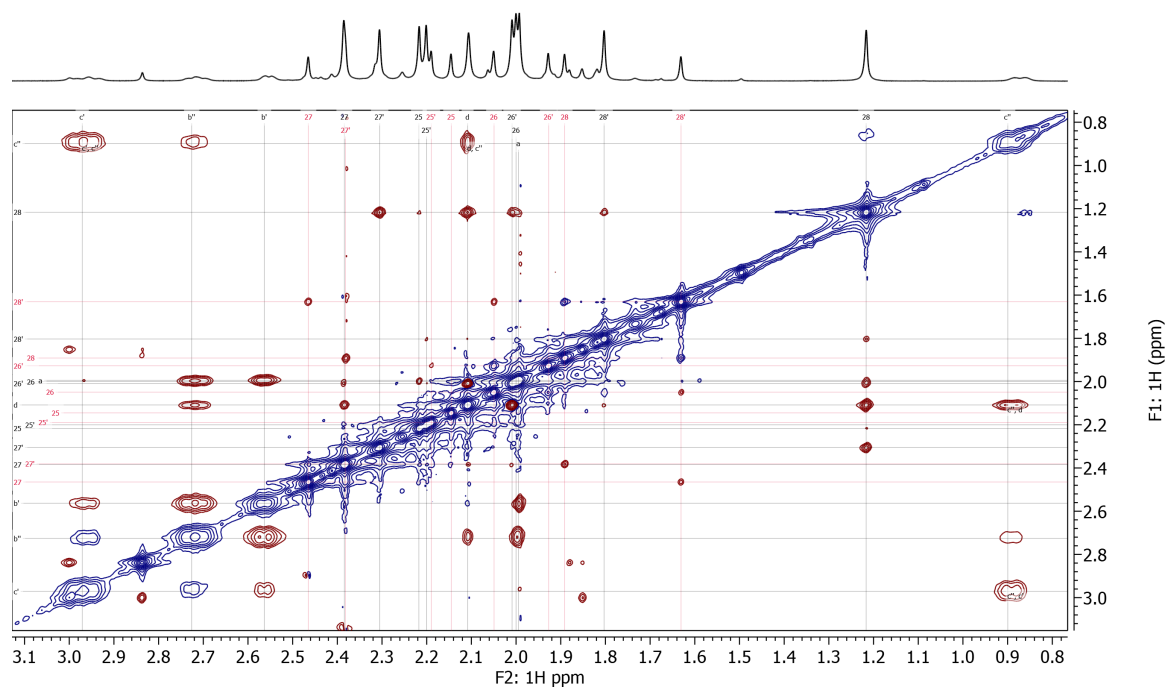
HMBC: Expansion of aromatic to high aromatic region. Numbers in black and red indicate assignments for **1j** and **Al-Cl**, respectively.



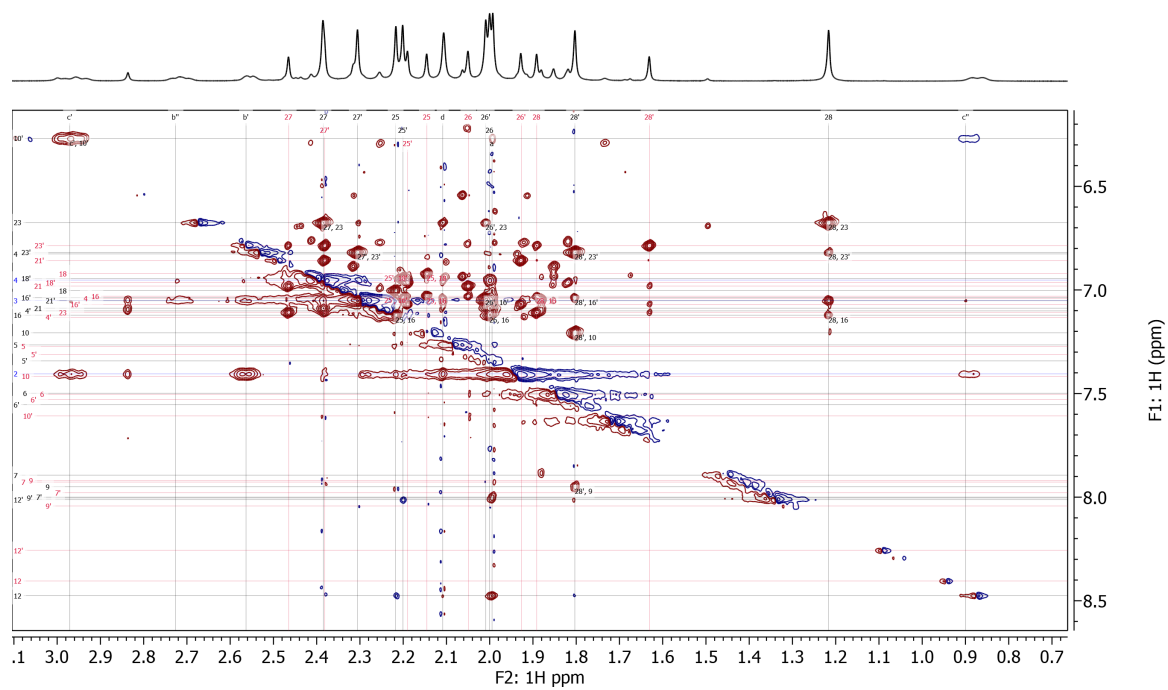
ROESY: Full Spectrum



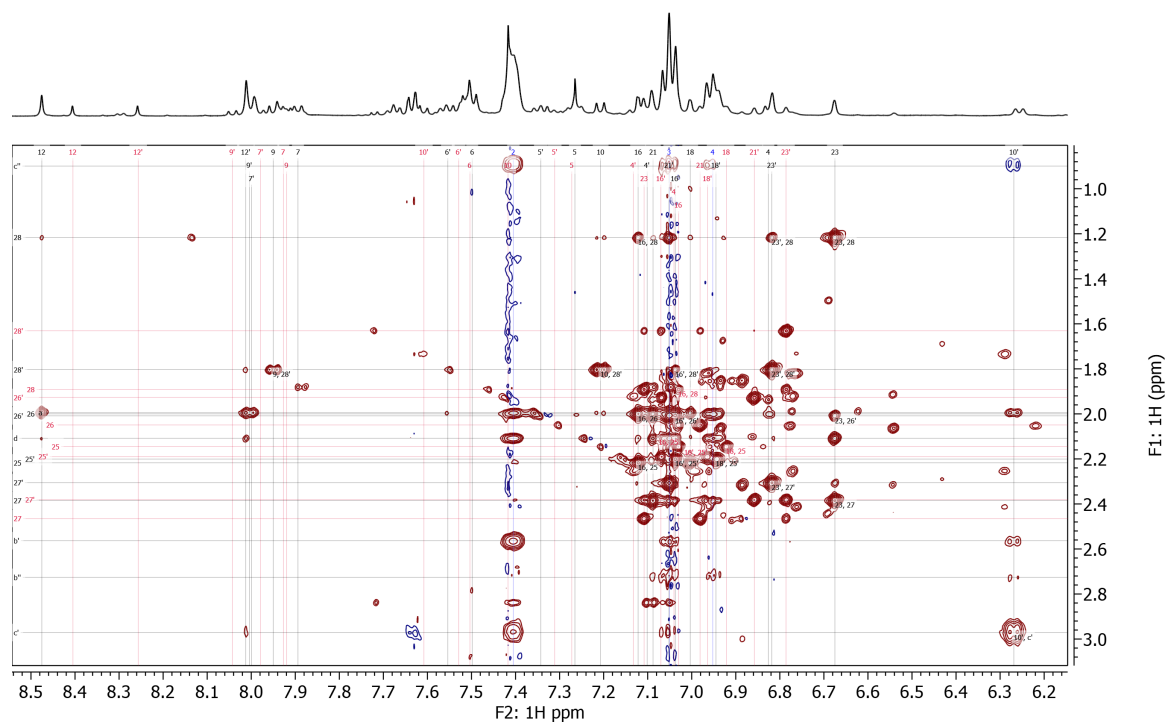
ROESY: Expansion of aliphatic region. Numbers in black and red indicate assignments for **1j** and **Al-Cl**, respectively.



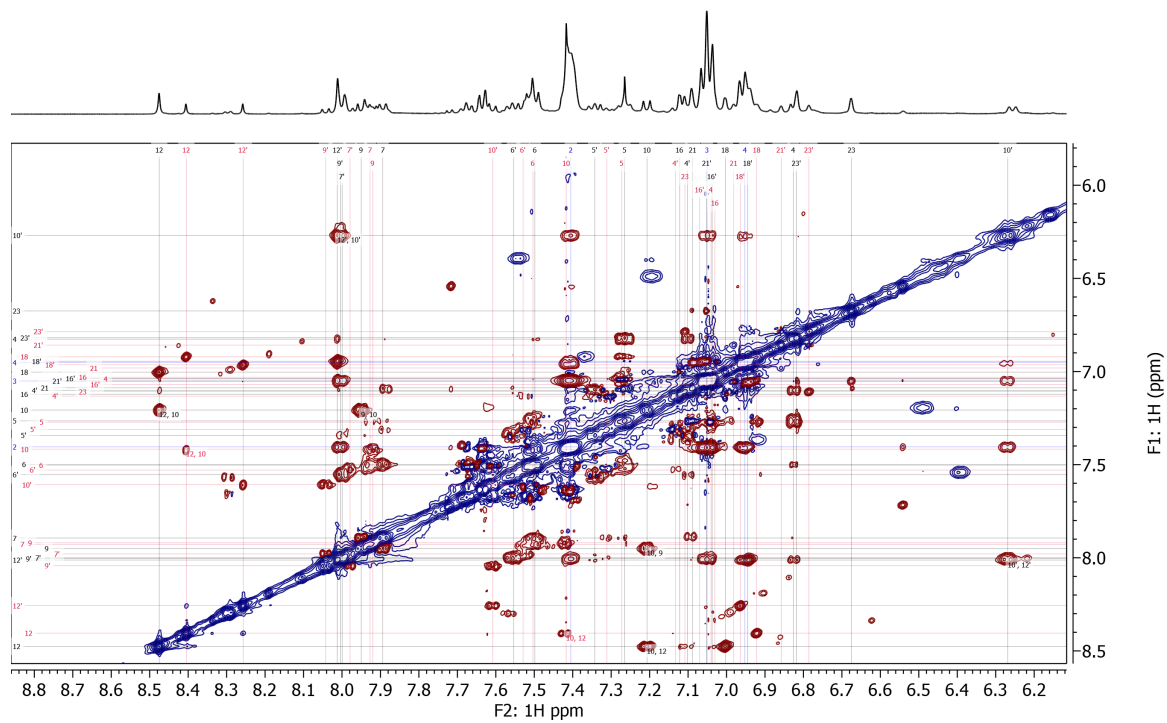
ROESY: Expansion of aliphatic to aromatic region. Numbers in black, blue and red indicate assignments for **1j**, BPh₄[−] and Al–Cl, respectively.



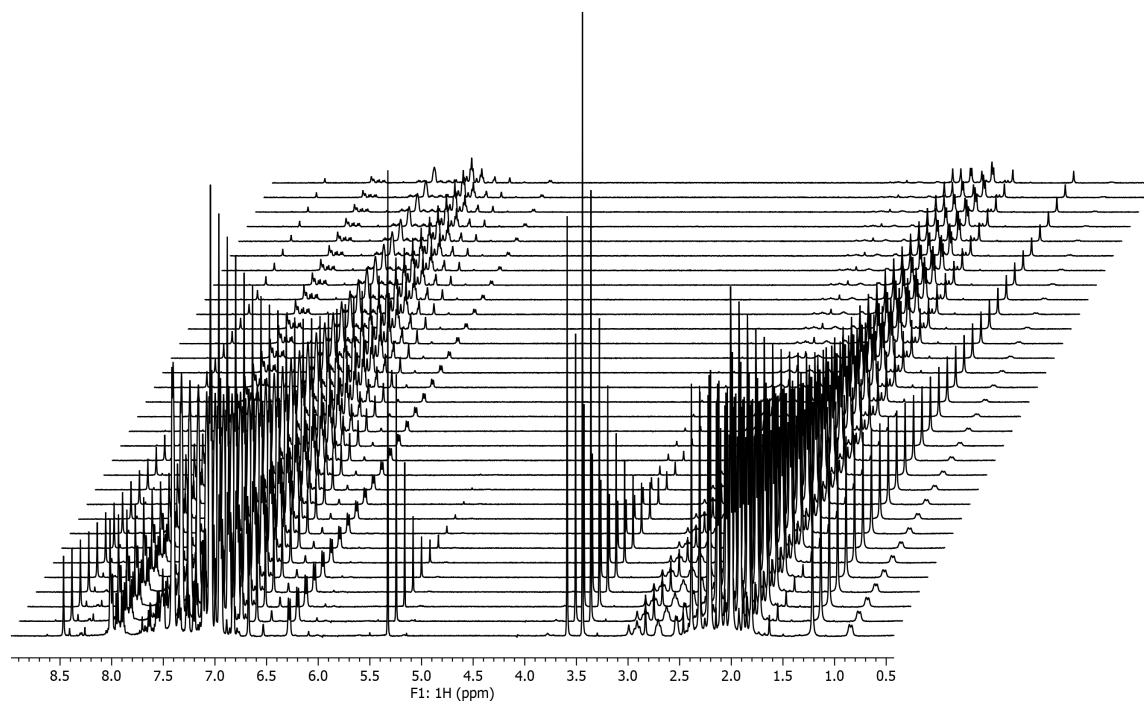
ROESY: Expansion of aromatic to aliphatic region. Numbers in black, blue and red indicate assignments for **1j**, BPh₄[−] and Al-Cl, respectively.



ROESY: Expansion of aromatic region. Numbers in black, blue and red indicate assignments for **1j**, BPh₄⁻ and Al-Cl, respectively.



Diffusion NMR: Stack plot of full spectrum



2.7. Acknowledgements

We are grateful to the Department of Energy (DE-FG02-05ER15687) and the National Science Foundation (DGE-1144153, fellowship to JRL) for funding. We also thank Dr. Ivan Keresztes for help with the characterization of the catalyst. This work made use of the NMR facility at Cornell University which is supported, in part, by the National Science Foundation (CHE-1531632).

REFERENCES

1. For reviews, see: (a) Jacobsen, E. N., *Acc. Chem. Res.* 2000, **33**, 421–431; (b) Saddique, F. A.; Zahoor, A. F.; Faiz, S.; Naqvi, S. A. R.; Usman, M.; Ahmad, M. *Synth. Commun.* 2016, **46**, 831–868; (c) Bonollo, S.; Lanari, D.; Vaccaro, L. *Eur. J. Org. Chem.* 2011, 2587–2598; (d) Shivani, Pujala, B.; Chakraborti, A. K. *J. Org. Chem.* 2007, **72**, 3713–3722.
2. (a) Ager, D. J.; Prakash, I.; Schaad, D. R. *Chem. Rev.* 1996, **96**, 835–875; (b) Chng, B. L.; Ganesan, A. *Bioorg. Med. Chem. Lett.* 1997, **7**, 1511–1514; (c) Williams, P. G.; Yoshida, W. Y.; Moore, R. E.; Paul, V. J. *J. Nat. Prod.* 2002, **65**, 29–31; (d) Goosen, L. J.; Liu, H.; Dress, K. R.; Sharpless, K. B. *Angew. Chem., Int. Ed.* 1999, **38**, 1080–1083; (e) Muzart, J. *Tetrahedron: Asymmetry* 2014, **25**, 697–704; (f) Wayman, K. A.; Sammakia, T. *Org. Lett.* 2003, **5**, 4105–4108; (g) Burguette, M. I.; Garcia-Verdugo, E.; Vicent, M. J.; Luis, S. V.; Pennemann, H.; Graf von Keyserling, N.; Martens, J. *Org. Lett.* 2002, **4**, 3947–3950.
3. (a) Sasaki, M.; Tanino, K.; Hirai, A.; Miyashita, M. *Org. Lett.* 2003, **5**, 1789–1891; (b) Wang, C.; Yamamoto, H. *J. Am. Chem. Soc.* 2015, **137**, 4308–4311; (c) Wang, C.; Luo, L.; Yamamoto, H. *Acc. Chem. Res.*, 2016, **49**, 193–204; (d) Azzena, F.; Calvani, F.; Crotti, P.; Gardelli, C.; Macchia, F.; Pineschi, M. *Tetrahedron* 1995, **51**, 10601–10626; (e) Wang, C.; Yamamoto, H. *J. Am. Chem. Soc.* 2014, **136**, 6888–6891 (f) Wang, C.; Yamamoto, H.; *Org. Lett.* 2014, **16**, 5937–5939.

4. (a) Martinez, L. E.; Leighton, J. L.; Carsten, D. H.; Jacobsen, E. N. *J. Am. Chem. Soc.* 1995, **117**, 5897–5898; (b) Kumar, M.; Kureshy, R. I.; Saravanan, S.; Verma, S.; Jakhar, A.; Khan, N. H.; Abdi, S. H. R.; Bajaj, H. C. *Org. Lett.* 2014, **16**, 2798–2801.
5. (a) Brandes, B. D.; Jacobsen, E. N. *Synlett* 2001, 1013–1015; (b) Gansäuer, A.; Fan, C.-A.; Keller, F.; Karbaum, P. *Chem. Eur. J.* 2007, **13**, 8084–8090; (c) Yu, M.; Snider, B. B. *Org. Lett.* 2009, **11**, 1031–1032; (d) Cravador, A.; Krief, A. *Tetrahedron Lett.* 1981, **22**, 2491–2494; (e) Righi, G.; Pietrantonio, S.; Bonini, C. *Tetrahedron* 2001, **57**, 10039–10046; (f) Otera, J.; Niibo, Y.; Tatsumi, N.; Nozaki, H. *J. Org. Chem.* 1988, **53**, 275–278.
6. Gupta and coworkers reported that lanthanide-based coordination polymers can act as heterogeneous catalysts for the ring opening of 2,3-pentene oxide, resulting in a single peak in the gas chromatogram, but the NMR data, GC conditions, and stereochemical configurations of the epoxide and product were not reported. See: (a) Kumar, G.; Gupta, R. *Inorg. Chem.* 2013, **52**, 10773–10787; (b) Kumar, G.; Kumar, G.; Gupta, R. *RSC Adv.* 2016, **6**, 21352–21361.
7. Arai, K.; Lucarini, S.; Salter, M. M.; Ohta, K.; Yamashita, Y.; Kobayashi, S. *J. Am. Chem. Soc.* 2007, **129**, 8103–8111.
8. (a) Mulzer, M.; Whiting, B. T.; Coates, G. W. *J. Am. Chem. Soc.* 2013, **135**, 10930–10933; (b) Mulzer, M.; Coates, G. W. *J. Org. Chem.* 2014, **79**, 11851–11862; (c) Mulzer, M.; Ellis, W. C.; Lobkovsky, E. B.; Coates, G. W. *Chem. Sci.* 2014, **5**, 1928–1933.

9. Lamb, J. R.; Mulzer, M.; LaPointe, A. M.; Coates, G. W. *J. Am. Chem. Soc.* 2015, **137**, 15049–15054.
10. Salph = 6,6'-((1*E*,1'*E*)-(1,2-phenylenebis(azanylylidene))-bis(methanylylidene))bis(2,4-di-*tert*-butylphenolate)
11. Salcy = *N,N'*-bis(3,5-di-*tert*-butyl-salicyl-idene)-1,2-cyclohexanediamine)
12. The generic structure for catalysts **1e–1i** is shown as C2 symmetric on the basis of a crystal structure containing the ligand for **1i**.^{14a} However, NMR data of **1i** in solution supports a C1 symmetric structure.¹⁶
13. For a review on salen-based catalysts bearing the BINAM backbone, see: Che, C.-H.; Huang, J.-S. *Coord. Chem. Rev.*, 2003, **242**, 97–113.
14. (a) Mulzer, M.; Ellis, W. C.; Lobkovsky, E. B.; Coates, G. W. *Chem. Sci.* 2014, **5**, 1928–1933; (b) Mulzer, M.; Lamb, J. R.; Nelson, Z.; Coates, G. W. *Chem. Commun.* 2014, **50**, 9842–9845.
15. Other counter-anions – such as PF₆[−], BAr^F₄[−] (Ar^F = 3,5-bis(trifluoromethyl)phenyl), and BF₄[−] – were tested, but resulted in lower conversion and selectivity compared to SbF₆[−] and BPh₄[−]. Ion pairing may play a role in the observed selectivity differences.¹⁶
16. See ESI for more details.
17. In a preliminary trial, 4-chloroaniline resulted in no conversion after 20 h. At this time, we do not have an explanation for the difference between 4-chloroaniline and 2,4,6-trifluoroaniline.
18. (a) Verkade, J. M. M.; van Hemert, L. J. C.; Zuaedflieg, P. J. L. M.; Schoemaker, H. E.; Schürmann, M.; van Delft, F. L.; Rutjes, F. P. J. T. *Adv.*

- Synth. Catal.* 2007, **349**, 1332–1336; (b) Verkade, J. M. M.; van Hemert, L. J. C.; Quaedflieg, P. J. L. M.; Alsters, P. L.; van Delft, F. L.; Rutjes, F. P. J. T. *Tetrahedron Lett.* 2006, **47**, 8109–8113; (c) Marin, S. D. L.; Martens, T.; Mioskowski, C.; Royer, J. *J. Org. Chem.* 2005, **70**, 10592–10595; (d) Hata, S.; Iguchi, M.; Iwasawa, T.; Yamada, K.; Tomioka, K. *Org. Lett.* 2004, **6**, 1721–1723.
19. Some free indoline can be seen in the ^1H and ^{13}C NMR spectra of the purified product, but the reported yield corrects for the mass of indoline based on the integrations of the ^1H NMR spectrum.¹⁶
 20. Getzler, Y. D. Y. L.; Mahadevan, V.; Lobkovsky, E. B.; Coates, G. W. *J. Am. Chem. Soc.* **2002**, *124*, 1174–1175.
 21. Getzler, Y. D. Y. L.; Mahadevan, V.; Lobkovsky, E. B.; Coates, G. W. *Pure Appl. Chem.* **2004**, *76*, 557–564.
 22. Mulzer, M.; Whiting, B. T.; Coates, G. W. *J. Am. Chem. Soc.* **2013**, *135*, 10930–10933.
 23. Lamb, J. R.; Mulzer, M.; LaPointe, A. M.; Coates, G. W. *J. Am. Chem. Soc.* **2015**, *137*, 15049–15054.
 24. Evans, D. A.; Janey, J. M.; Magomedov, N.; Tedrow, J. S. *Angew. Chem., Int. Ed.* **2001**, *113*, 1936–1940.
 25. Mulzer, M.; Coates, G. W. *J. Org. Chem.* **2014**, *79*, 11851–11862.
 26. Mulzer, M.; Ellis, W. C.; Lobkovsky, E. B.; Coates, G. W. *Chem. Sci.* **2014**, *5*, 1928–1933.

27. Kroutil, W.; Mischitz, M.; Faber, K. *J. Chem. Soc., Perkin Trans. I* **1997**, 3629–3636.
28. Hobson, L. A.; Thomas, E. J. *Org. Biomol. Chem.* **2012**, *10*, 7510–7526.
29. Cornforth, J. W.; Cornforth, R. H.; Mathew, K. K. *J. Chem. Soc.* **1959**, 112–127.
30. Gao, Y.; Hanson, R. M.; Klunder, J. M.; Ko, S. Y.; Masamune, H.; Sharpless, K. B. *J. Am. Chem. Soc.* **1987**, *109*, 5765–5780.

CHAPTER 3

STANDARD PROTOCOLS FOR MEASURING AND REPORTING CATALYTIC DATA FOR ELECTROCHEMICAL CO₂ REDUCTION

Portions are excerpted from

Buckley, A. K.; Lee, M.; Cheng, T.; Kazantsev, R. V.; Larson, D. M.; Goddard, W.

A.; Toste, F. D.; Toma, F. M. *J. Am. Chem. Soc.* 2019, 141, 18, 7355-7364.

Riccardis, A. D.; Lee, M.; Kazantsev, R. V.; Garza, A. J.; Zeng, G.; Larson, D. M.;

Clark, E. L.; Lobaccaro, P.; Burroughs, P. W. W.; Bloise, E.; Ager, J. W.; Bell, A. T.;

Head-Gordon, M.; Mele, G.; Toma, F. M. *ACS Appl. Mater. Interfaces* 2020, 12, 5,

5251-5258.

Copyright © 2020 American Chemical Society

3.1. Abstract

Objective evaluation of electrocatalytic's performance for carbon dioxide reduction has been complicated due to the lack of standardized measuring and reporting protocols, especially for electrocatalysts that involve organic materials. In this chapter, we report several factors that we identified important in developing a standard protocol for measuring and reporting the selectivity and activity of electrocatalysts that involve organic materials for this process that is reproducible and can facilitate a meaningful comparison of activity data between various research groups.

3.2. Introduction

Electrocatalytic reduction of carbon dioxide (CO₂R) offers an efficient strategy to reduce the presence of greenhouse gases in the atmosphere while concurrently producing valuable carbon-based products.^{1, 2} Extensive efforts have been devoted to developing a highly active and selective electrocatalyst for this process.³⁻⁶ However, objective evaluation of the performance of electrocatalysts for CO₂R has been complicated due to the lack of standardized protocols for measuring and reporting the selectivity and activity of the electrocatalysts;⁷ especially for electrocatalysts that involve organic materials, such as metal organic frameworks (MOFs), molecular catalysts, and metal foil catalysts with organic modifiers. Having a standard measuring protocol is critical because the observed performance of the electrocatalysts is significantly influenced not only by the composition and morphology of the electrocatalysts but also by the purity of the electrocatalysts and electrolytes.

Additionally, electrocatalysts that involve organic materials require more control experiments to ensure that the carbon-based products result from the electrochemical CO₂R, rather than from side reactions.

In this chapter, we briefly summarize several factors to consider in measuring the selectivity and activity of electrocatalysts to develop a standard protocol to obtain reproducible data that show the electrocatalytic performance that can be attributed to the properties of the catalyst itself. We also explain several ways to report electrocatalytic activity and selectivity of catalysts so that the data would facilitate a meaningful comparison of activity data between various research groups.

3.3. Factor to consider when measuring electrocatalytic activity

3.3.1. The effect of impurities on electrocatalytic activity

To measure the electrocatalysts' intrinsic properties, its activity and selectivity must be determined in the absence of significant surface contamination from the presence of impurities. It is critical to distinguish whether the observed catalytic performance results of the performance of the catalyst itself or the results of impurities introduced to the surface of the catalyst. In general, transition metal impurities on the electrocatalyst surface will increase its activity toward hydrogen evolution reaction (HER).^{8, 9} Even trace quantities (<10 μ M) of transition metal impurities can significantly affect the electrocatalyst to lose its CO₂R activity.¹⁰ Therefore, it is crucial to avoid contaminating the surface of the electrocatalyst.

In the electrochemical CO₂R process used in the remainder of this thesis, we have identified several sources of the contamination. The contamination can come from the

improperly cleaned electrochemical cell, improper electrode preparations, and electrolytes. Therefore, all the experiments used the purest water available (Millipore water), electrolyte salts, and electrode materials. Additionally, all of the cell and electrode components were cleaned with nitric acid before use to remove trace metallic impurities.^{10, 11}

3.3.2. Reporting electrocatalytic activity

There are several ways to report electrocatalytic activity and selectivity of catalysts. Faradaic efficiency (FE) is a commonly used metric for selectivity, which is defined as the fraction of Faradaic charge utilized to produce given product.⁷ FE is a useful tool to describe the selectivity of the electrocatalysts. For example, in figure 3-7, the FE plot can illustrate the change in selectivity with each added modifier by comparing to the unfunctionalized Cu electrode (Ox Cu). Compared to the unfunctionalized Cu electrode (Ox Cu), selectivity for formic acid (blue), CO (red), or H₂ (gray) improved in the presence of 1, 2, or 3, respectively (Figure 3-1). The other observed products (yellow) were present in traces at this potential and largely consisted of ethylene and ethane. In the presence of 1, the Faradaic efficiency (i.e. the percentage of electrons that were transferred to a given product) for formic acid increased to $45\% \pm 2\%$ from $34\% \pm 3\%$ in the Ox Cu case, accompanied by an increase in H₂ selectivity to $43\% \pm 1\%$ from $28\% \pm 2\%$. In the presence of 2, CO selectivity increased slightly from $28\% \pm 2\%$ in the Ox Cu case to $33.8\% \pm 0.9\%$. H₂ selectivity drastically increased to $97\% \pm 2\%$ with the addition of 3, as compared to $28\% \pm 2\%$ with Ox Cu.

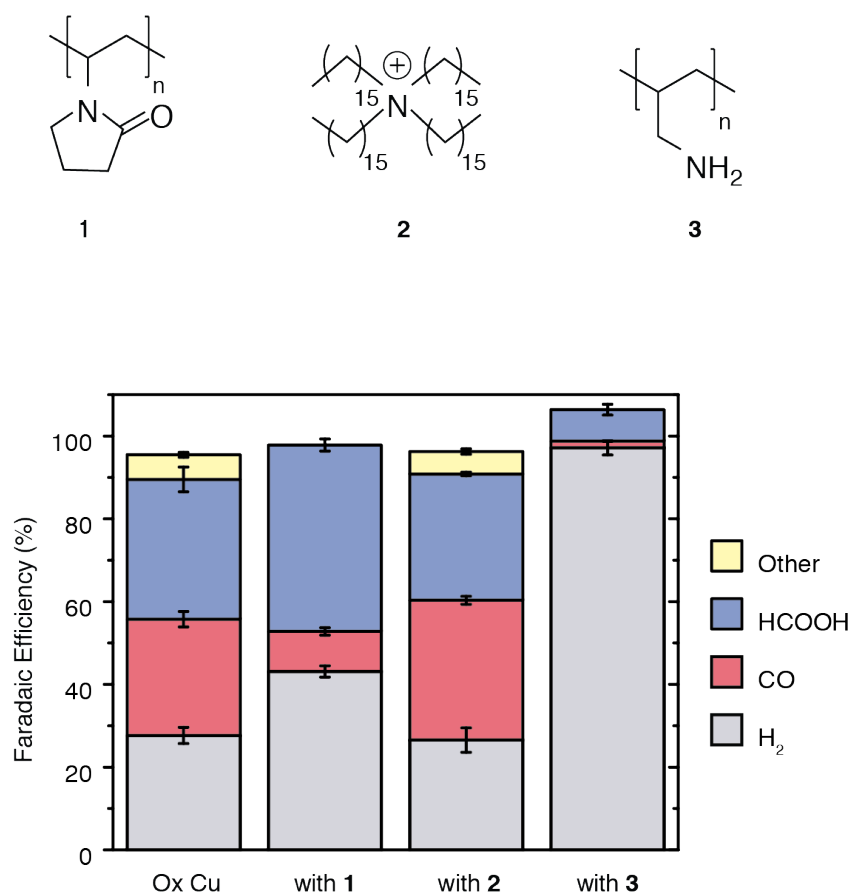


Figure 3-1. Modifiers to promote H₂, CO or formic acid formation.

Unfunctionalized Cu or Oxide-derived Cu (Ox Cu) and functionalized Cu (Ox Cu with organic modifier) with three modifiers, namely polyvinylpyrrolidone (1), tetrahexadecylammonium (2) with bromide anion not shown, and polyallylamine (3), tested to promote H₂ (gray), CO (red), or formic acid (blue) formation on Cu at -0.7 V vs. RHE. Traces of other products (yellow) indicate the presence of ethylene and ethane. Plots of product selectivity in terms of the Faradaic efficiencies of unfunctionalized Cu (Ox Cu) and of Ox Cu with 1, 2, and 3 illustrate the change in selectivity with each added modifier. Values and error bars are calculated from at least three trials. Error bars are reported as standard error of the mean.

In addition to the Faradaic efficiencies, we need to consider the partial current densities towards each product, which depict the amount of current transferred to generate a given product (Figure 3-2). These data provide more information regarding whether an increase in selectivity is due to a higher amount of product formed, or whether it is due to the selective suppression of other products caused by a decrease of the total current. Figure 3-2 illustrates that the increase in Faradaic efficiency for H₂, CO and formic acid is accompanied by an increase in the partial current density as well. The partial current for formic acid, for example, increased from $0.25 \text{ mA/cm}^2 \pm 0.03 \text{ mA/cm}^2$ in the unfunctionalized case to $0.36 \text{ mA/cm}^2 \pm 0.02 \text{ mA/cm}^2$ with the addition of 1, an increase of 44%. The partial current for CO increased from $0.20 \text{ mA/cm}^2 \pm 0.02 \text{ mA/cm}^2$ to $0.31 \text{ mA/cm}^2 \pm 0.01 \text{ mA/cm}^2$ with the addition of 2, an increase of 55%. The partial current for H₂ increased 27 times from Ox Cu to the sample modified with 3. These reported values are based upon geometric current densities; current densities normalized by electrochemically active surface area demonstrate similar trends (Figure 3-2). For many of the modifiers discussed in this text, increases in selectivity are accompanied by increases in partial current densities, thus demonstrating that these organic modifiers may be used to enhance the amount of product formed.

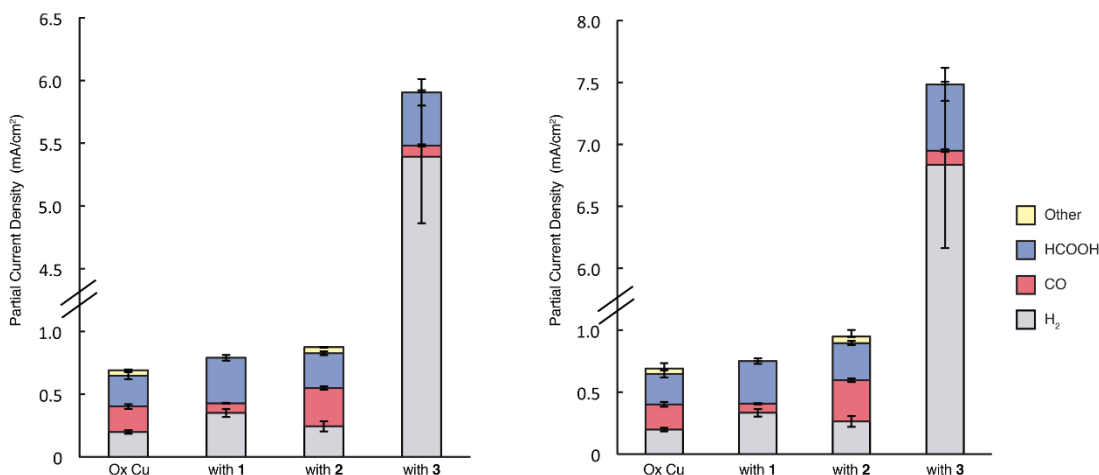


Figure 3-2. Partial current densities for H₂, CO and formic acid as determined by GC and HPLC (left) and normalized by double layer capacitance (right).

The double layer capacitance of the modified surface after chronoamperometry was compared to that of unmodified oxide-derived copper, and the ratio of these values was used to normalize the partial current densities. Error bars illustrate the standard error of the mean.

In some cases, an increase in selectivity may not be accompanied by an increase in the rate at which a certain product is produced. Therefore, FE as the only descriptor should not be used to describe electrocatalysts' activity, especially when comparing various electrocatalysts with drastically different activities. It is tempting to conclude that the electrocatalyst with high FE toward a certain product is active for producing that certain product. However, FE should be accompanied by the rate of product generation that is proportional to its partial current density, a much less ambiguous descriptor, to determine catalytic activity.

Measured partial current density must be normalized by the number of available catalytic sites to make a fair comparison between various catalysts.¹⁴ However, normalization to the number of active sites can be difficult to identify. To address this

problem while obtaining meaningful data, we can normalize the measured activity by measuring the electrochemically active surface area (ECSA).¹⁵ The ECSA can be estimated by measuring the double-layer capacitance of the electrode-electrolyte interface.¹⁶ Figure 3-3 illustrates the difference between the partial current density and the normalized partial current density, especially with modifier 8 where the total current density is increased by 6 times.

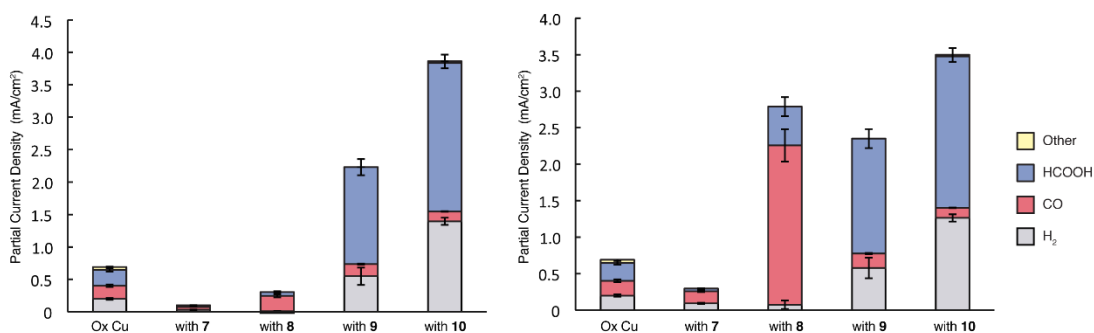


Figure 3-3. Partial current densities for H₂, CO and formic acid as determined by GC and HPLC (left) and normalized by double layer capacitance (right).

The double layer capacitance of the modified surface after chronoamperometry was compared to that of unmodified oxide-derived copper, and the ratio of these values was used to normalize the partial current densities. Error bars illustrate the standard error of the mean.

Additionally, the normalized partial current density can provide better understanding about the relationship between the formations of hydrogen, CO, and formic acid by plotting the partial current densities towards these products generated with Ox Cu and modified surfaces (excluding protic modifiers **3** and **5**) against each other. Figure 3-4 suggests that the formation of formic acid and H₂ may be related, while no such relationship emerges from Figure 3-5 and Figure 3-6.

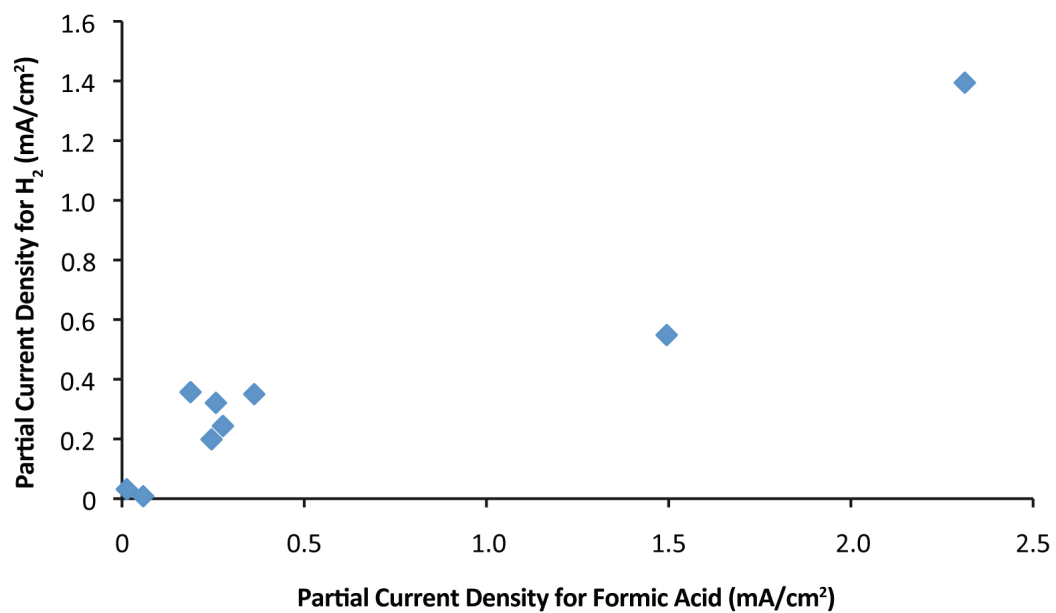


Figure 3-4. Plot of partial current of formic acid vs. partial current of H₂ from Ox Cu and modified surfaces.

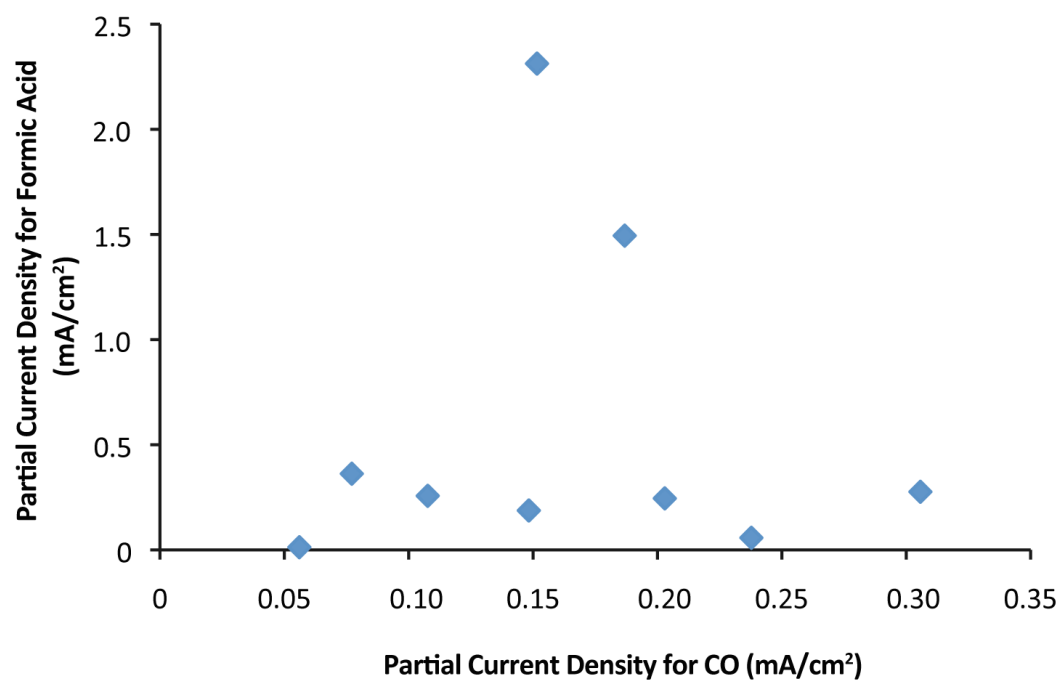


Figure 3-5. Plot of partial current of CO vs. partial current of formic acid from Ox Cu and modified surfaces.

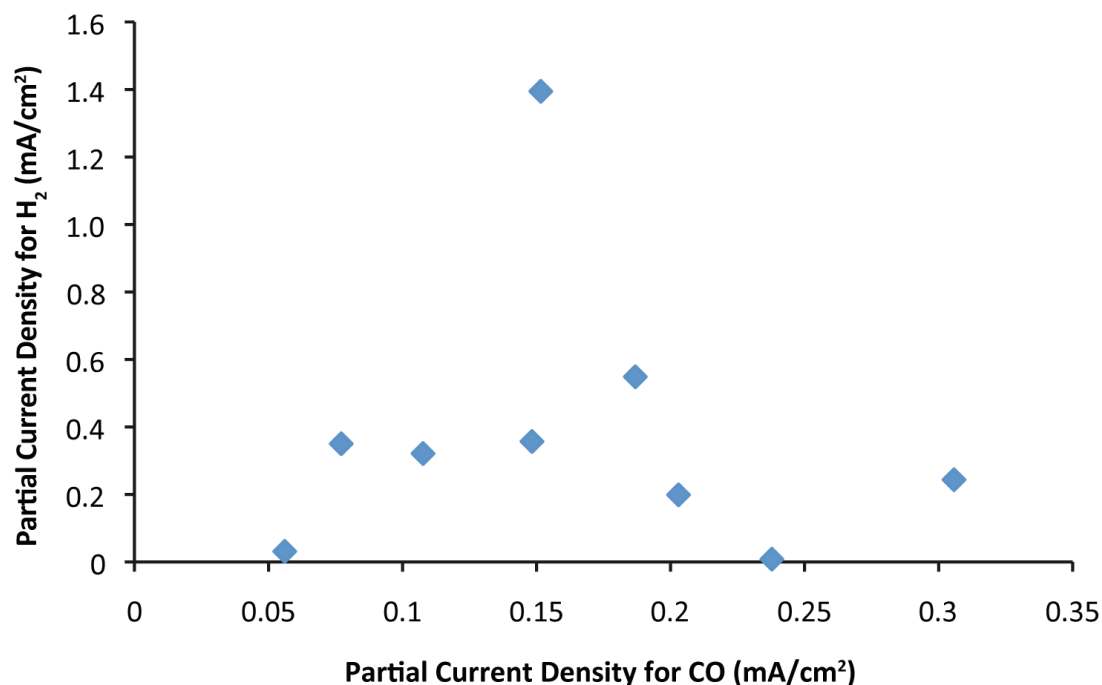


Figure 3-6. Plot of partial current of CO vs. partial current of H₂ from Ox Cu and modified surfaces.

3.3.3. The importance of control experiments in electrocatalytic activity

Specifically, in testing electrocatalysts that involves organic materials, it is crucial to distinguish if the carbon-based products come from the electrocatalyst reducing CO₂ or the decomposition of the organic material. Control experiments are needed to further assess the catalytic activity of the electrocatalysts and the stability of the organic materials. In this section, we will discuss the control experiments needed for metal foil catalyst with organic modifiers and molecular catalyst on a carbon substrate.

CO₂R experiments with copper (Cu) foils with organic modifiers as electrocatalysts are used as an example for electrochemical CO₂R with metal foil catalysts with organic modifiers as an electrocatalyst. To properly attach the organic modifiers onto the Cu surfaces, Nafion is needed as a binder. Cu surfaces were tested

with Nafion in the absence of other modifiers to evaluate whether Nafion on its own influenced the product selectivity. The data below, collected at the lowest and highest loadings of Nafion, suggest that Nafion does not affect the CO₂R selectivity of Cu.

Table 3-1. Faradaic efficiencies and total current of Ox Cu and Cu functionalized solely with Nafion at varying loadings.

Reported values are averages from at least three trials.

	H ₂	CO	Formic Acid	Other	Total FE	Total Current (mA/cm ²)
Ox Cu	28%	28%	34%	6%	96%	0.73
1 μ L Nafion per mL iPrOH ^a	27%	30%	31%	5%	93%	0.75
10 μ L Nafion per mL iPrOH ^b	29%	31%	30%	4%	95%	0.80
15.8 μ L Nafion per mL iPrOH ^c	27%	29%	30%	4%	90%	0.82

^a5 μ L Nafion was dissolved in 5 mL iPrOH. 100 μ L of this solution was dropcast onto oxide-derived Cu. ^b10 μ L Nafion was dissolved in 1 mL iPrOH. 100 μ L of this solution was dropcast onto oxide-derived Cu. ^c15.8 μ L Nafion was dissolved in 1 mL iPrOH. 100 μ L of this solution was dropcast onto oxide-derived Cu.

In addition, experiments with modifiers *dihexadecyldimethylammonium bromide* (**8**) and *didecyldimethylammonium bromide* (**9**) were conducted with and without Nafion to evaluate the role of the binder. Chronoamperometry traces collected with Nafion were less noisy than traces without Nafion (**Figure 3-7**). Furthermore, in the absence of Nafion, the electrolyte was observed to bubble more vigorously out of the cell, particularly in studies with more hydrophilic species. This observation suggests

that in the absence of Nafion, the modifiers dissolve more readily in the electrolyte and yield a soapy solution. Therefore, Nafion was applied in all of the studies in the remainder of the thesis.

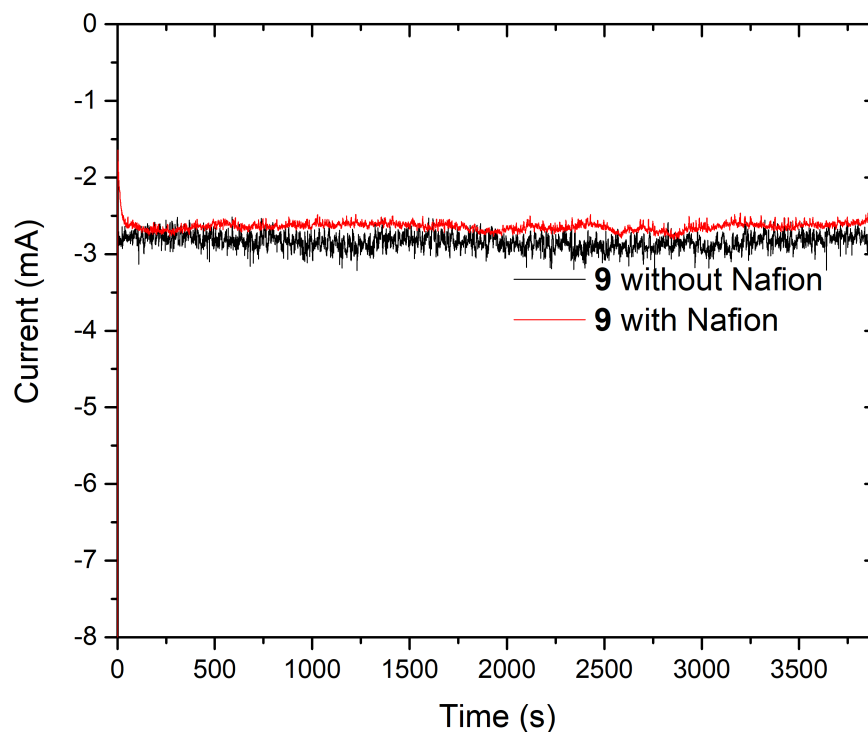


Figure 3-7. Chronoamperometry of Cu modified with **9**, both with and without Nafion binder. In the presence of Nafion, the CA trace appears less noisy than in the absence of Nafion. Therefore, Nafion binder was employed as a binder for the experiments in the remainder of the thesis. CA in the above figure was conducted at -0.7 V vs. RHE.

The product distribution for these experiments without Nafion demonstrated the same trend as experiments with Nafion: **8** yielded more CO than the unfunctionalized surface, while **9** yielded more formic acid.

Table 3-2. Faradaic efficiency data with and without Nafion with 8

	H₂	CO	Formic Acid	Other	Total FE	Total Current (mA/cm²)
with Nafion	3%	76%	18%	0	97%	0.31
no Nafion	7%	63%	31%	0	101%	0.34

Table 3-3. Faradaic efficiency data with and without Nafion with 9

	H₂	CO	Formic Acid	other	Total FE	Total Current (mA/cm²)
with Nafion	21%	8%	62%	0	91%	2.45
no Nafion	21%	6%	73%	0	100%	2.84

Chronoamperometry (CA) is used as electrocatalysts' stability test and to determine whether the organic modifiers cause mass transport limitation. Chronoamperometry traces indicate that for experiments with **Ox Cu**, **Ox Cu** with *Polyvinylpyrrolidone* (**1**) and *Tetrahexadecylammonium bromide* (**2**), the currents remain stable over the course of the 65-minute experiment (**Figure 3-8**). The total current is also similar for the three traces, suggesting that mass transfer of CO₂ and protons is not substantially inhibited by the presence of the modifiers.

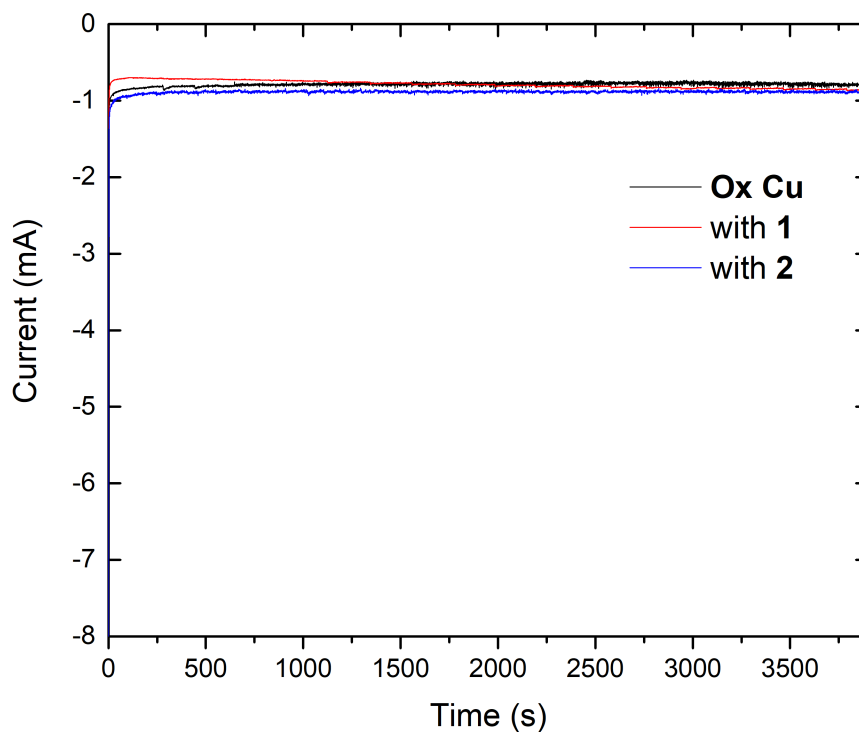


Figure 3-8. Chronoamperometry traces for Ox Cu and experiments with 1 and 2.

Further stability tests using CA were done to various organic modifiers, such as: (a) neutral polymers (**Figure 3-9**): *polyallylamine* (**3**), *Polystyrene* (**4**), *Polyvinyl alcohol* (**5**), and *Polyethylene glycol* (**6**); and cationic molecules (**Figure 3-10**): *Tetrahexadecylammonium bromide* (**2**), *Trihexyltetradecylphosphonium bromide* (**7**), *dihexadecyldimethylammonium bromide* (**8**), *didecyldimethylammonium bromide* (**9**) and *cetyltrimethylammonium bromide* (**10**). CA traces indicate that the currents remain stable over the course of the 65-minute experiment.

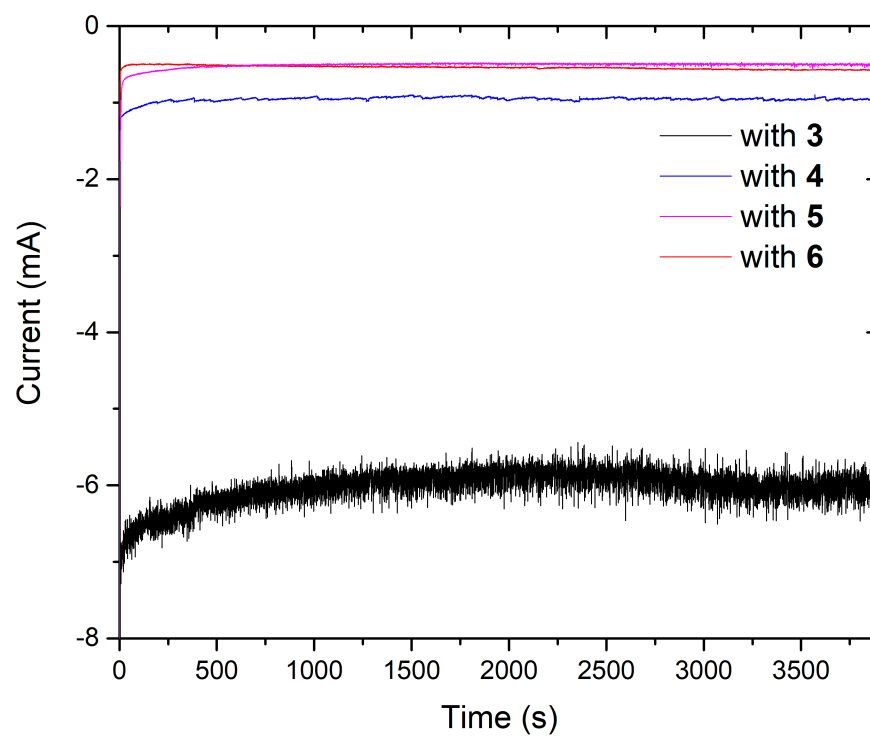


Figure 3-9. Chronoamperometry traces of neutral polymers as modifiers on Cu.

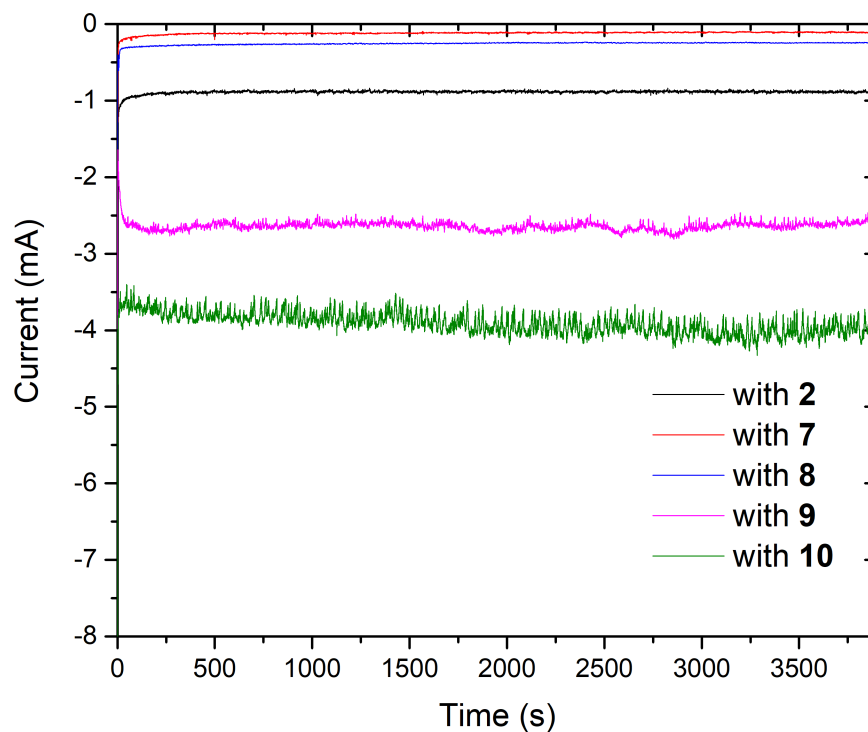


Figure 3-10. Chronoamperometry traces of cationic molecules as modifiers on Cu

The substrates that demonstrated enhanced selectivity for CO₂R products were also examined under N₂. Experiments under N₂ were conducted with the same process as electrochemical CO₂R testing, except with N₂ flow instead of CO₂. Faradaic efficiencies and total current for these trials are reported below. CO₂R activity disappears, indicating that the carbon-based products observed originate from CO₂R, and not from decomposition of the modifier. The low FE for H₂ and low total FE observed with **8** are due to the low total current, which would yield an amount of H₂ that is close to the detection limit of our instrument.

Table 3-4. Functionalized Cu under N₂.

	H₂	CO	Formic Acid	other	Total FE	Total Current (mA/cm²)
Ox Cu-under N ₂	108.2%	0.2%	0%	0%	108.4%	0.41
With 1 under N ₂	115.0%	0.1%	0%	0%	115.0%	0.57
With 2 under N ₂	113.4%	0%	0%	0%	113.4%	0.31
With 6 under N ₂	113.9%	0.2%	0%	0%	114.1%	0.20
With 7 under N ₂	108.5%	0.1%	0%	0%	108.6%	0.12
With 8 under N ₂	31.6%	0.7%	0%	0%	32.3%	0.03
With 9 under N ₂	117.5%	0.2%	1.6%	0%	119.3%	0.35
With 10 under N ₂	109.6%	0%	0%	0%	109.6%	0.47

CO₂R experiments with cobalt phthalocyanine (CoPc) and a pyridine substituted cobalt phthalocyanine (CoPc-Pyr) on carbon paper as electrocatalysts are used as an example for electrochemical CO₂R with molecular catalyst on carbon substrate. To assess the catalytic performance of CoPc-Pyr, cyclic voltammetry (CV) of both CoPc and CoPc-Pyr was performed under CO₂ and N₂ atmosphere to determine the catalytic activity (Figure 3-11). The electrochemical reduction of CoPc in absence of CO₂ shows a reversible peak around 0.15 V vs RHE and a quasi-reversible one at -0.4 V vs Ag/AgCl. The first redox couple arises from the reduction of Co(II) to Co(I) (generating [Co(I)Pc-Pyr]¹⁻), while the second reduction produces [Co(I)Pc-Pyr]²⁻ where the charge can be delocalized onto the macrocycle. These peaks are still

present, even if slightly shifted, when the solution is saturated with CO₂. Moreover, the second peak is closely associated with the onset potential for CO₂ reduction (-0.4 V vs RHE), suggesting that [Co(I)Pc-Pyr^{•-}]²⁻ is the catalytically active species. In the absence of molecular catalysts, CoPc and CoPc-Pyr, carbon paper (CP) shows no electrocatalytic currents under the operating condition. This results further confirm that the molecular catalysts is necessary to observe catalytic activity under CO₂ atmosphere.

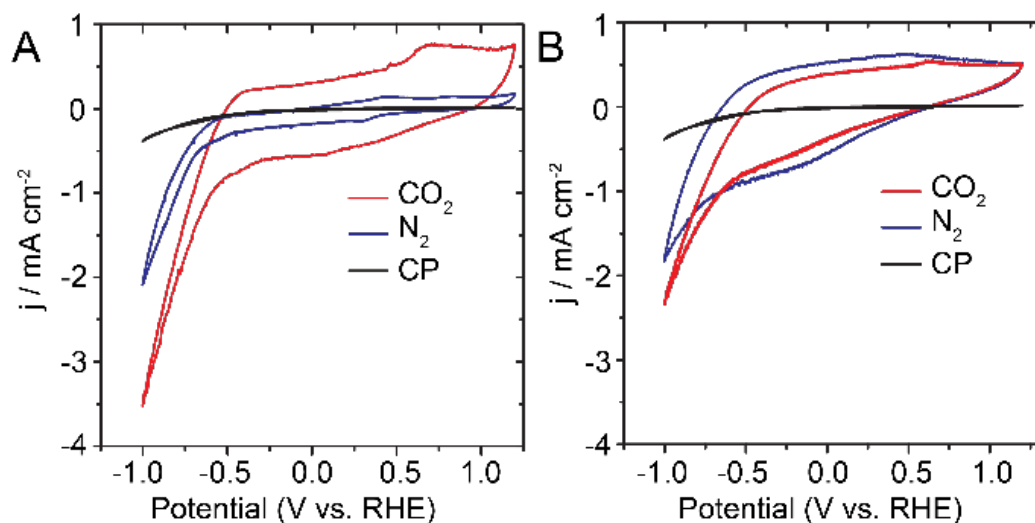


Figure 3-11. Cyclic voltammetry of CoPc-Pyr (A) and CoPc (B) deposited on carbon paper under CO₂ (red) and N₂ (blue) atmospheres in 0.05 M K₂CO₃ at 100 mV/s with 5 sccm for the flow rate of CO₂ (pH = 6.8). CV of carbon paper (CP) in CO₂ atmosphere (black) is reported for comparison.

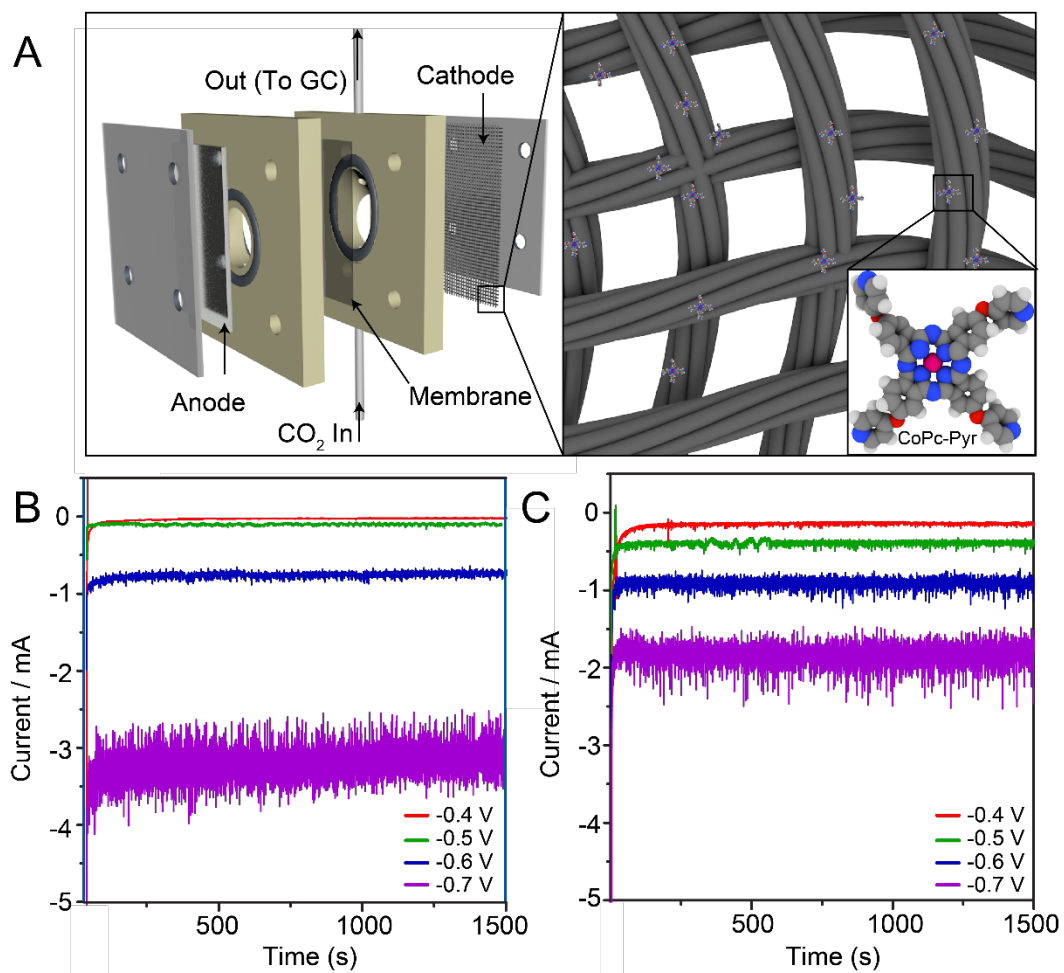


Figure 3-12. (A) Schematic of a two-chamber electrochemical cell used for CO₂R experiments (left). Carbon paper cathode with physisorbed CoPc-Pyr used as working electrode (right). Chronoamperometry measurements for (B) CoPc-Pyr and (C) CoPc at various potentials under CO₂R conditions.

Chronoamperometric measurements are used as a stability test. The measurements show a stable current during operation for both catalysts, thus supporting no degradation of the molecules or decrease in activity (Figure 3-12. B-C). A few studies have further shown the stability of similar complexes, and have concluded that the carbon-based product, CO, does not originate from catalyst degradation.^{12, 13} At -0.7 V vs RHE, CoPc-Pyr has higher current than CoPc, while maintaining higher selectivity as already mentioned. Additionally, both of the molecules are not soluble in water at pH 6.8 confirming that it is a heterogenized catalytic system with molecular catalysts, instead of a homogeneous catalytic system.

3.4. Experimental procedure

3.4.1. Materials

All chemicals were obtained from commercial suppliers and used without further purification, unless otherwise noted. Copper foil (0.254 mm thick, 99.9%) was purchased from Alfa Aesar and cut with a bench shear into 2 cm x 3 cm electrodes before use. Carbon dioxide (99.995%) and nitrogen (99.999%) were obtained from Praxair. Polyvinylpyrrolidone (average MW 40,000), polyallylamine (average MW 17,000, 20 wt% in water), polyvinyl alcohol (MW 89,000-98,000, 99+% hydrolyzed), polyethylene glycol (average MW 20,000), polystyrene (average MW 192,000), didecyldimethylammonium bromide (98%), dihexadecyldimethylammonium bromide (97%), tetrahexadecylammonium bromide (98%), and trihexyltetradecylphosphonium bromide (95%) were purchased from Sigma-Aldrich. Cetyltrimethylammonium

bromide (98%) was obtained from Spectrum Chemical. Dimethylformamide (DMF), potassium carbonates, dichloromethane, methanol, hydrochloric acid, 1,8-Diazabicyclo[5.4.0]undec-7-ene (DBU), 1-hexanol, dimethyl sulfoxide (DMSO), 4-nitrophthalonitrile, and 4-hydroxy-Pyridine were purchased from Sigma-Aldrich. And, they were used as received. Selemion AMV anion-exchange membrane was purchased from AGC Engineering Co., LTD.

3.4.2. Instrumentation

Gas chromatography (GC) data was collected on a multiple gas analyzer #5 from SRI Instruments. High performance liquid chromatography (HPLC) was performed with an UltiMate 3000 HPLC from Thermo Fisher Scientific. ^1H NMR data was collected on an Ascend 500 MHz NMR from Bruker. Contact angle measurements were performed with a VCA Optima instrument from AST Products.

3.4.3. Electrochemical methods and product detection

Electrochemical experiments were conducted in a two-compartment flow cell fabricated from PEEK following a reported design.¹⁷ A Selemion AMV anion-exchange membrane separated the two chambers. A Pt foil was used as the counter electrode.

A Leak-Free Ag/AgCl electrode (LF-1, 1.0 mm outer diameter, Innovative Instruments, Inc.) was used as the reference electrode. The reference electrode was calibrated against a second reference electrode, which in turn was calibrated in a two-electrode system with H_2 bubbled over a Pt wire as the counter electrode and a 1M

H₂SO₄ solution as the electrolyte.

The applied potentials were converted from Ag/AgCl scale to the RHE scale via the equation: $E_{\text{RHE}} = E_{\text{Ag/AgCl}} + 0.197 + 0.059 \cdot \text{pH}$, where the pH used is the bulk pH for the CO₂-saturated electrolyte (6.8).

CA experiments were conducted in the cell with a CO₂ flow rate of 5 sccm using a Biologic potentiostat (SP-300). Prior to CA experiments, linear scan voltammetry was conducted from the open circuit potential to -1.05V vs. RHE at a scan rate of 20 mV/s in order to reduce any oxidized Cu. The impedance was then measured and correction for the ohmic resistance was applied to the CA experiment as described in a reported procedure.¹⁸ Each trial was run at -0.7 V vs. RHE for 65 minutes. The outlet of the electrochemical cell was connected to an in-line gas chromatograph (GC), and the gaseous products were injected into the chromatograph at 15, 30, 45 and 60 minutes after the beginning of the experiment. The average values from the four injections are reported. At the end of the experiment, the liquid from both the cathode and anode were analyzed via high performance liquid chromatography (HPLC) to quantify the amount of formic acid produced, including formate that had diffused through the membrane during the experiment. Product selectivities and activities in terms of Faradaic efficiencies (%) and partial current densities (mA/cm²) are reported with error calculated via standard error of the mean and standard deviations.

3.4.4. Electrochemical experiments

3.4.4.1. Electrolyte preparation

Potassium carbonate solution (0.05M) was prepared from high purity potassium carbonate (99.995%, Sigma Aldrich) and water from a Milli-Q Water Purification System (resistivity of 18.2 M Ω -cm, Millipore). The solution was saturated with CO₂ for a minimum of 10 minutes within the experimental cell setup immediately prior to all electrochemical experiments.

3.4.4.2. Preparation of functionalized samples

The Cu foils were prepared as described in the Methods section of the main text, and the functionalized samples were prepared as described below:

Polyvinylpyrrolidone (1) and polyallylamine (3): 10 mg of polymer was dissolved in iPrOH (1 mL), and 100 μ L of this solution was dropcast onto the Cu foil. Once dry, 100 μ L of Nafion solution (10 μ L of commercial Nafion solution in 1 mL iPrOH) was dropcast onto the Cu surface.

Tetrahexadecylammonium bromide (2): 5 mg of ammonium salt was suspended in iPrOH (5 mL) and heated briefly at 60°C to dissolve. 100 μ L of this solution was dropcast onto the Cu foil. Once dry, 100 μ L of Nafion solution (5 μ L of commercial Nafion solution in 5 mL iPrOH) was dropcast onto the Cu surface.

Polystyrene (4): 10 mg of polymer was dissolved in toluene (1 mL), and 100 μ L of this solution was dropcast onto the Cu foil. Once dry, 100 μ L of Nafion solution (10 μ L of commercial Nafion solution in 1 mL iPrOH) was dropcast onto the Cu surface.

Polyvinyl alcohol (5): 10 mg of polymer was suspended in water (400 μ L) and heated to 70°C to dissolve. An additional 600 μ L of MeOH was added to the solution. 100

μL of this solution was dropcast onto the Cu foil. Once dry, 100 μL of Nafion solution (10 μL of commercial Nafion solution in 1 mL iPrOH) was dropcast onto the Cu surface.

Polyethylene glycol (6): 10 mg of polymer was suspended in MeOH (1 mL) and heated briefly at 60°C to dissolve. 100 μL of this solution was dropcast onto the Cu foil. Once dry, 100 μL of Nafion solution (10 μL of commercial Nafion solution in 1 mL iPrOH) was dropcast onto the Cu surface.

Trihexyltetradecylphosphonium bromide (7), *dihexadecyldimethylammonium bromide (8)*, *didecyldimethylammonium bromide (9)* and *cetyltrimethylammonium bromide (10)*: 0.0274 mmol of the organic species was dissolved in iPrOH (1 mL), and 100 μL of this solution was dropcast onto the Cu foil. Once dry, 100 μL of Nafion solution (1 μL of commercial Nafion solution per mg of organic species added to 1 mL iPrOH) was dropcast onto the Cu surface.

3.4.4.3. Electrode preparation

3.4.4.3.1. Copper foils with organic modifiers as electrocatalysts

Cu foil was mechanically polished (1200G Wetordry sandpaper, 3M) and then electropolished as described in a reported procedure.¹⁹ The two-compartment flow cell was assembled with the Cu foil, and cyclic voltammetry was run as described in previous reports in order to generate an oxide-derived Cu surface.^{17, 20} Specifically, an electrolyte solution of 0.05 M K_2CO_3 and 4 mM KCl was prepared. After addition of this electrolyte, three cycles of cyclic voltammetry were performed from 0.9 to -1.05V

vs. RHE at a rate of 5 mV/s. This high surface area structure was chosen in order to generate greater amounts of product and facilitate product detection.

The cell was disassembled, the electrode was dried under N₂ flow and solutions of the organic modifier were dropcast onto the Cu surface. Once dry, a solution of Nafion binder was dropcast onto the Cu surface. The electrode, once dry, was reassembled in the flow cell for electrochemical analyses.

3.4.4.3.2. Cobalt Phthalocyanine on carbon paper as electrocatalysts

The carbon paper electrode (Sigracet 29BC) was cut in a circle with a diameter of 1.26 cm and immersed for 15 min in 65% HNO₃ to remove iron impurities possibly present in the fibers.¹⁰ Application of the catalyst to the electrode was achieved by dip coating. The carbon paper was dip coated for 1 min in a solution of 10⁻⁴ M CoPc-Pyr in trifluoroethanol and 10⁻⁴ M CoPc-Pyr in DMF solution and allowed to dry overnight under vacuum at 80 °C to remove the possible trace of solvent. The same procedure was followed also for the CoPc catalyst. In particular 23.2mg of CoPc were dissolved in 4 mL of DMF resulting in a 0.6*10⁻³ M solution of phthalocyanine in DMF. This solution was further diluted in order to obtain the dip coating solution. The final loading of catalyst on the carbon electrode was estimated to be about 2.3*10⁻⁹ mmol by integration of the cyclic voltammetry peak at around 0.14 V vs RHE.

3.5. Acknowledgements

This material is based on work performed at the Joint Center for Artificial Photosynthesis, a DOE Energy Innovation Hub, supported through the Office of Science of the U.S. Department of Energy under Award DE-SC00004993. We

acknowledge Dr. Jason K. Cooper, Dr. Adam Z. Weber, Ms. Philomena Weng, Dr. Anna Wuttig, Dr. Drew Higgins and Prof. Miquel Salmeron for fruitful discussions.

REFERENCES

1. Artz, J.; Müller, T. E.; Thenert, K.; Kleinekorte, J.; Meys, R.; Sternberg, A.; Bardow, A.; Leitner, W., Sustainable Conversion of Carbon Dioxide: An Integrated Review of Catalysis and Life Cycle Assessment. *Chemical Reviews* **2018**, *118* (2), 434-504.
2. Seh, Z. W.; Kibsgaard, J.; Dickens, C. F.; Chorkendorff, I.; Norskov, J. K.; Jaramillo, T. F., Combining theory and experiment in electrocatalysis: Insights into materials design. *Science* **2017**, *355* (6321).
3. Kim, D.; Resasco, J.; Yu, Y.; Asiri, A. M.; Yang, P., Synergistic geometric and electronic effects for electrochemical reduction of carbon dioxide using gold–copper bimetallic nanoparticles. *Nature Communications* **2014**, *5* (1), 4948.
4. Li, C. W.; Kanan, M. W., CO₂ Reduction at Low Overpotential on Cu Electrodes Resulting from the Reduction of Thick Cu₂O Films. *Journal of the American Chemical Society* **2012**, *134* (17), 7231-7234.
5. Lu, Q.; Rosen, J.; Zhou, Y.; Hutchings, G. S.; Kimmel, Y. C.; Chen, J. G.; Jiao, F., A selective and efficient electrocatalyst for carbon dioxide reduction. *Nature Communications* **2014**, *5* (1), 3242.
6. Mistry, H.; Varela, A. S.; Bonifacio, C. S.; Zegkinoglou, I.; Sinev, I.; Choi, Y.-W.; Kisslinger, K.; Stach, E. A.; Yang, J. C.; Strasser, P.; Cuenya, B. R., Highly selective plasma-activated copper catalysts for carbon dioxide reduction to ethylene. *Nature Communications* **2016**, *7* (1), 12123.
7. Clark, E. L.; Resasco, J.; Landers, A.; Lin, J.; Chung, L.-T.; Walton, A.; Hahn, C.; Jaramillo, T. F.; Bell, A. T., Standards and Protocols for Data Acquisition

and Reporting for Studies of the Electrochemical Reduction of Carbon Dioxide. *ACS Catalysis* **2018**, 8 (7), 6560-6570.

8. Hori, Y.; Konishi, H.; Futamura, T.; Murata, A.; Koga, O.; Sakurai, H.; Oguma, K., "Deactivation of copper electrode" in electrochemical reduction of CO₂. *Electrochimica Acta - ELECTROCHIM ACTA* **2005**, 50, 5354-5369.

9. Wuttig, A.; Surendranath, Y., Impurity Ion Complexation Enhances Carbon Dioxide Reduction Catalysis. *ACS Catalysis* **2015**, 5 (7), 4479-4484.

10. Lum, Y.; Kwon, Y.; Lobaccaro, P.; Chen, L.; Clark, E. L.; Bell, A. T.; Ager, J. W., Trace Levels of Copper in Carbon Materials Show Significant Electrochemical CO₂ Reduction Activity. *ACS Catalysis* **2016**, 6 (1), 202-209.

11. Wang, L.; Ambrosi, A.; Pumera, M., "Metal-Free" Catalytic Oxygen Reduction Reaction on Heteroatom-Doped Graphene is Caused by Trace Metal Impurities. *Angewandte Chemie International Edition* **2013**, 52 (51), 13818-13821.

12. Zhu, M.; Ye, R.; Jin, K.; Lazouski, N.; Manthiram, K., Elucidating the Reactivity and Mechanism of CO₂ Electroreduction at Highly Dispersed Cobalt Phthalocyanine. *ACS Energy Letters* **2018**, 3 (6), 1381-1386.

13. Zhu, M.; Yang, D.-T.; Ye, R.; Zeng, J.; Corbin, N.; Manthiram, K., Inductive and electrostatic effects on cobalt porphyrins for heterogeneous electrocatalytic carbon dioxide reduction. *Catalysis Science & Technology* **2019**, 9 (4), 974-980.

14. Boudart, M., Turnover Rates in Heterogeneous Catalysis. *Chemical Reviews* **1995**, 95 (3), 661-666.

15. Benck, J. D.; Hellstern, T. R.; Kibsgaard, J.; Chakthranont, P.; Jaramillo, T. F., Catalyzing the Hydrogen Evolution Reaction (HER) with Molybdenum Sulfide Nanomaterials. *ACS Catalysis* **2014**, *4* (11), 3957-3971.
16. Trasatti, S.; Petrii, O. A. Real surface area measurements in electrochemistry. *Pure Appl. Chem.* 1991, *63*, 711–734.
17. Lobaccaro, P.; Singh, M. R.; Clark, E. L.; Kwon, Y.; Bell, A. T.; Ager, J. W., Effects of temperature and gas–liquid mass transfer on the operation of small electrochemical cells for the quantitative evaluation of CO₂ reduction electrocatalysts. *Physical Chemistry Chemical Physics* **2016**, *18* (38), 26777-26785.
18. Han, Z.; Kortlever, R.; Chen, H.-Y.; Peters, J. C.; Agapie, T., CO₂ Reduction Selective for C_{≥2} Products on Polycrystalline Copper with N-Substituted Pyridinium Additives. *ACS Central Science* **2017**, *3* (8), 853-859.
19. Kuhl, K. P.; Cave, E. R.; Abram, D. N.; Jaramillo, T. F., New insights into the electrochemical reduction of carbon dioxide on metallic copper surfaces. *Energy & Environmental Science* **2012**, *5* (5).
20. Roberts, F. S.; Kuhl, K. P.; Nilsson, A., High Selectivity for Ethylene from Carbon Dioxide Reduction over Copper Nanocube Electrocatalysts. *Angewandte Chemie International Edition* **2015**, *54* (17), 5179-5182.

CHAPTER 4

ALUMINUM METAL-ORGANIC FRAMEWORK TRIGGERS CARBON DIOXIDE REDUCTION ACTIVITY

Reprinted adapted with permission from Lee, M.; Riccardis, A. D.; Kazantsev, R. V.;
Copper, J. K.; Buckley, A. K.; Burroughs, P. W. W.; Larson, D. M.; Mele, G.; Toma,
F. M. *ACS Appl. Energy Mater.* 2020, 3, 2, 1286-1291.

Copyright © 2020 American Chemical Society

4.1. Abstract

Confinement of metal centers is a powerful tool to manipulate reactivity and tune selectivity in chemical transformations. While aluminum as a foil is inactive for carbon dioxide reduction and shows high selectivity for the hydrogen evolution reaction, here we show that aluminum confined in a metal organic framework, MIL-53(Al), suppresses hydrogen evolution reaction activity and unexpectedly enhances carbon dioxide reduction. Aluminum confined in MIL-53 can electrochemically reduce CO₂ to both carbon monoxide and formic acid, as valuable carbon-based products. Control experiments support that the catalytic activity is related to the presence of aluminum and that the confined reaction environment promoted by the organic ligands is key to obtaining carbon dioxide reduction behavior. The observation of Al⁰ after electrochemical CO₂ reduction indicates that the active form of the catalyst may involve the presence of aluminum in this oxidation state. This aluminum MOF can produce up to 40% Faradaic efficiency for carbon monoxide and formic acid, with a turnover frequency of 93 h⁻¹ for carbon monoxide and 89 h⁻¹ for formic acid. This study demonstrates that the confined reaction space enables changes in reaction selectivity and can impart atypical catalytic capabilities to metals.

4.2. Introduction

Nature has been successful in providing highly efficient enzymatic systems in which earth abundant elements catalyze chemical transformations with high selectivity. This selectivity is achieved within a confined reaction space called an enzymatic pocket. Drawing inspiration from biological systems, challenging catalytic

transformations would benefit from similar design principles, in which catalytic metal centers are placed in confined cavities that promote specific reaction pathways to enhance selectivity.¹⁻²

The electrochemical reduction of CO₂ (CO₂R) is a process in which multiple proton-electron transfers are necessary to yield valuable carbon-based products. CO₂R is one example of a process in which a confined reaction environment may be necessary to improve product selectivity. Considerable effort has been devoted to developing both heterogeneous and homogeneous catalysts for selective and efficient electrochemical CO₂ reduction.³⁻⁵ However, an examination of single-metal foils, for example, demonstrates that the majority of these elements show high activity for the competing hydrogen evolution reaction (HER), in addition to low selectivities between numerous CO₂R products.⁶ Thus, a confined reaction environment offers the opportunity to target the suppression of HER as well as the promotion of selectivity within CO₂R products.

In this context, metal organic frameworks (MOFs) have been reported to provide interesting confinement effects.⁷⁻⁸ They allow for efficient heterogeneous catalysis while providing the structural modularity typical of homogeneous catalysts.⁹⁻¹¹ MOFs as catalysts have demonstrated superior catalytic selectivity, lifetime, and turnover numbers by offering a confined reaction environment and stabilization of the active catalyst.⁷⁻⁸ For example, in Friedel-Crafts alkylations and hydrogenation reactions, MOFs have shown to provide a confined reaction environment that increases the lifetime of the active catalysts.¹²⁻¹⁴ In addition, in amination of C(sp₃)-H bond reactions, MOFs have proven to stabilize the active form of the catalyst, thus enabling

a unique catalytic performance.¹⁵

Herein, we report the facile synthesis and characterization of an aluminum MOF derivative that is active under electrochemical CO₂R conditions and able to produce important carbon-based products, carbon monoxide (CO), and formic acid. CO is a valuable intermediate in chemical synthesis and towards all other observed products in electrochemical CO₂R. Formic acid is also an attractive product because it can be used as a fuel with practical applications in hydrogen storage and direct formic acid fuel cells.¹⁶ By changing the environment around the Al centers, this metal, which is otherwise only active for HER, is now active in the electrochemical reduction of CO₂ to carbon-based products. To the best of our knowledge, MIL-53(Al) is the first reported MOF that electrocatalytically reduces CO₂ to both CO and formic acid. Most reported MOFs and covalent organic frameworks (COFs) used as CO₂R electrocatalysts in aqueous conditions make use of different metals and can only reduce CO₂ to either CO or formic acid.^{9,10} At the potential of -1.1 V vs. RHE, the turnover frequency (TOF) for carbon-based products reaches 182 h⁻¹ per unit cell, with 93 h⁻¹ toward CO and 89 h⁻¹ toward formic acid, comparable to the TOF for the best performing COFs.¹⁷ Notably, we also generate Al⁰ in addition to Al³⁺ while exposing MIL-53(Al) to electrochemical CO₂R. The presence of Al⁰ supports the transformation of Al metal centers in MIL-53 under the catalytic conditions, and we hypothesize that this species is responsible for the observed catalytic activity towards CO₂R. In addition, the presence of Al⁰, which usually readily oxidizes to Al³⁺ in air, indicates that the organic framework can stabilize the metal center in the confined environment. Thus, MIL-53(Al) demonstrates that the search for improved CO₂R

catalysts should not be limited to metals that are traditionally used in this process, but rather, that the confined environment can be used to drastically tune the catalytic behavior.

4.3. Synthesis, Fabrication, and Characterization of MIL-53(Al) Electrode

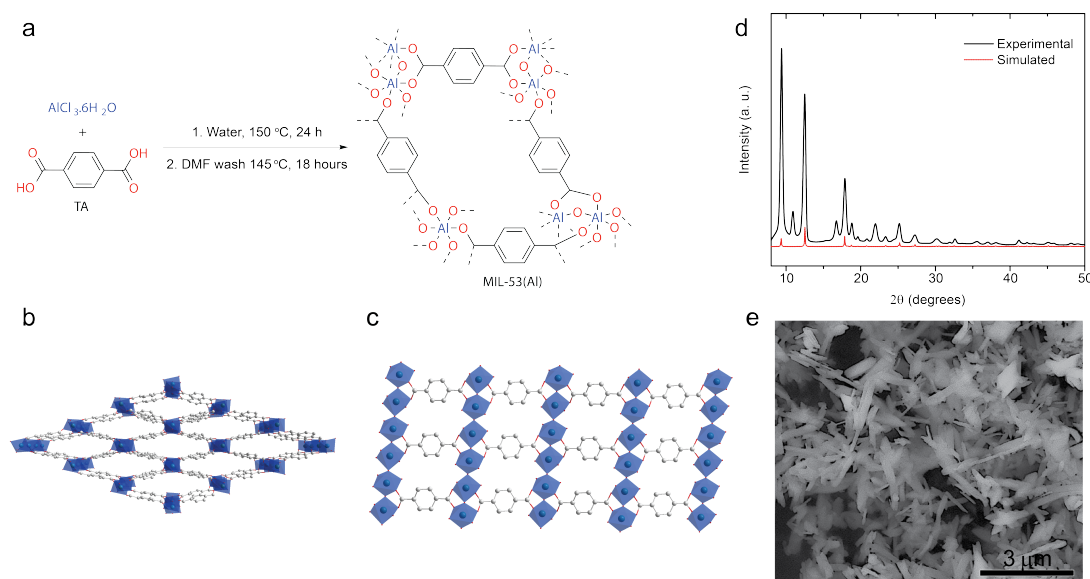


Figure 4-1. Synthesis and characterization of Al-confined metal organic framework, MIL-53(Al). (a) Synthesis of MIL-53(Al) from 1:1 $\text{AlCl}_3 \cdot 6\text{H}_2\text{O}$ and terephthalic acid (TA). (b) View of 3D structure of MIL-53(Al) *lt* (monohydrate form) (c) View of MIL-53(Al) *lt* from the side showing Al metal centers are connected through the organic linker, terephthalates. (d) Powder XRD of synthesized MIL-53(Al) showing experimental (solid black) and simulated (dash red) patterns. (e) SEM image of the needle-like crystal structured synthesized MIL-53(Al). Brightness and contrast were adjusted in Figure 1e to improve image quality, and the originally acquired image is shown in Figure S1c.

Briefly, MIL-53(Al) was synthesized in a hydrothermal reactor from $\text{AlCl}_3 \cdot 6\text{H}_2\text{O}$ and terephthalic acid (TA) with a slightly modified procedure from the literature (Figure 1a).¹⁸⁻¹⁹ A 1:1 ratio of $\text{AlCl}_3 \cdot 6\text{H}_2\text{O}$ and TA was dissolved in ultrapure water in a Teflon-lined steel autoclave, and it was heated at 150 °C for 24 hours (see

supporting information for full details). The resulting white powder was washed with ultrapure water and dimethylformamide (DMF) to remove the unreacted starting materials. The final product was dried under vacuum. MIL-53(Al) forms one dimensional pores made of TA linkers, which coordinate AlO_6 octahedra (Figure 1b,c).

X-ray diffraction (XRD) illustrates the high crystallinity of the final synthesized material, with peaks at 9.4° , 12.5° , and 17.9° , which are in agreement with simulated powder XRD of monohydrate MIL-53(Al) or MIL-53(Al) *lt*, where the channel contracts due to hydrogen bonding between the oxygen atoms of the MOF and exogenous water molecules¹⁸ (Figure 1d). Scanning electron microscopy (SEM) images further support the high crystallinity of MIL-53(Al) (Figure 1e, Figure S1). The synthesized MIL-53(Al) has a needle-like morphology of approximately 1 μm in length.

Working electrodes were prepared by drop casting a MIL-53 suspension onto acid-treated carbon paper (Figure 2a, see supporting information for full details). First, the carbon paper was treated with 70% nitric acid for 15 min to remove metallic impurities that may affect CO₂R catalysis.²⁰ Depositing MOFs onto carbon paper, a highly conductive, porous material, provides highly conductive pathways and improved mass transport, for an increased number of active sites for catalysis.¹⁰ The resulting electrode has an exposed active area of $\sim 1.25 \text{ cm}^2$.

SEM-Energy Dispersive X-ray (EDX) maps and X-ray photoelectron spectroscopy (XPS) measurements were taken to ensure the presence of MIL-53(Al) on the surface of the carbon paper electrodes. SEM-EDX maps showed that aluminum

(Al, blue) was present and evenly distributed on the surface of the working electrode (Figure 2b). The presence of oxygen and carbon was also detected (not shown) due to the support, carbon paper, in addition to the MOFs' organic linker. XPS analysis of MIL-53(Al) powder shows that the Al 2p peak has binding energy of 74.69 eV, that is supportive of the presence of Al^{3+} (Figure 2c).²¹ XPS also confirms the presence of Al^{3+} on the surface of the fabricated working electrode, with an Al 2p peak at a binding energy of 74.69 eV, in agreement with the binding energy of the Al 2p peak for the synthesized MIL-53(Al) powder. These data confirm that MIL-53(Al) was successfully deposited on the surface of the working electrode.

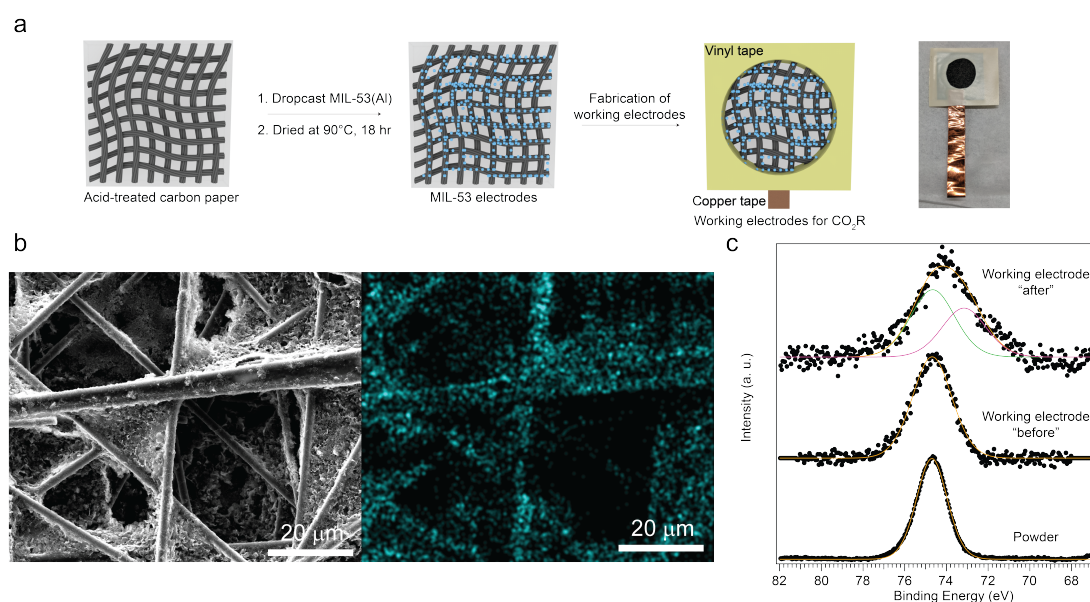


Figure 4-2. Fabrication and characterization of working electrodes. (a) Scheme to fabricate working electrodes. (b) SEM image (left) showing the topography and corresponding EDX map (right) showing the Al (light blue) distribution (Al $K\alpha$) on the fabricated working electrode. Al is evenly distributed on the electrode. (c) XPS of Al 2p comparing the powder (bottom) of MIL-53 with the working electrode before (middle) and after (top) electrochemical testing with spectral fitting analysis.

4.4. Electrocatalytic Performance of MIL-53(Al)

To assess the catalytic performance of MIL-53(Al), cyclic voltammetry (CV) of the working electrode was performed under CO₂ atmosphere (Figure 3a and Figure S3) in a two-compartment flow cell (Figure S2). While the carbon paper has no catalytic current in the potential window under study, the MIL-53(Al) working electrode shows an electrocatalytic current with an onset at about -0.4 V vs. RHE. To

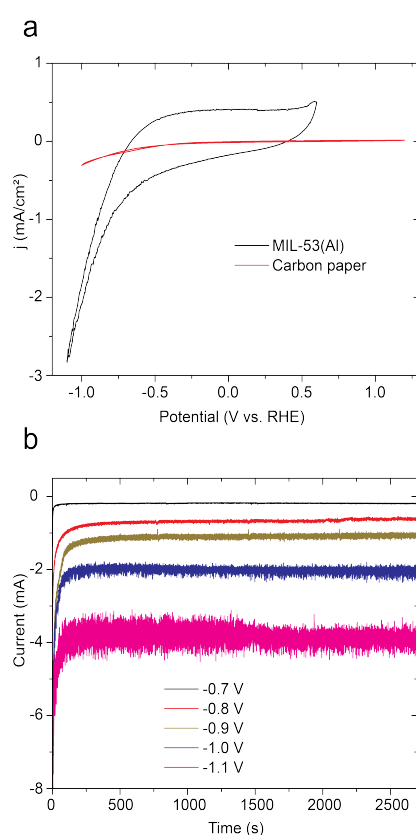


Figure 4-26. Characterization of MIL-53(Al) electrocatalysts for CO₂R. (a) Cyclic voltammograms of MIL-53(Al) working electrode (blue) and bare carbon paper electrode (red) in CO₂ atmosphere. (b) Chronoamperometry was conducted at five different potentials (-0.7 V, -0.8 V, -0.9 V, -1.0 V, and -1.1 V vs RHE, black, red, ochre, blue, and magenta, respectively) in CO₂-saturated 0.05 M potassium carbonate electrolyte (pH=6.8) to investigate the electrocatalyst stability under the reaction conditions.

ensure that the production of CO and formic acid are derived from reduction of CO₂ molecules rather than from catalyst decomposition, experiments under nitrogen atmosphere confirmed the absence of carbon products (Table S1). In addition, blank experiments in CO₂ atmosphere using a working electrode of acid treated carbon paper or carbon paper coated with Nafion, which is used here as the MIL-53(Al) binder, also resulted in no detection of

CO₂R products (Table S2 and Table S3). Thus, we can conclude that MIL-53(Al) is the active electrode component in CO₂R to CO and formic acid in MIL-53(Al).

To further test this hypothesis and in order to provide insights into the catalytically active form of the catalyst under operating conditions, we performed XPS analysis after electrochemical testing. Notably, in addition to the Al³⁺ present in the starting material, XPS analysis shows the rise of a second Al 2p component at 73.38 eV, compatible with the presence of Al⁰ present in the material after electrochemical testing (Figure 2c).²¹ Further spectral fitting analysis showed that the ratio of Al⁰ and Al³⁺ is approximately 1:1. This result indicates that Al³⁺ in MIL-53(Al) may undergo transformation during the electrochemical reaction to form an active catalyst that could involve Al⁰. According to the Pourbaix diagram,²²⁻²³ Al⁰ is reported to be unstable at the potentials and at the pH under study. Therefore, the presence of Al⁰, which usually rapidly oxidizes to the more stable Al³⁺ species in air,²³ indicates that the confined reaction environment provided by MIL-53 organic framework can stabilize this active form of the catalyst. Chronoamperometry (CA) tests show that the current is stable over time, and SEM-EDX performed after electrochemical testing confirms that Al is still evenly distributed on the surface after electrochemical testing (Figure S4), which further supports stability of MIL-53(Al) electrodes under operating conditions.

The working electrode was tested at five different potentials from -1.1 V vs. RHE to -0.7 V vs. RHE with 0.1 V increments by conducting CA for approximately 45 minutes at each potential (Figure 3b) to further assess the activity of MIL-53(Al) under CO₂R conditions. MIL-53(Al) shows an onset potential for CO and formic acid

production as low as -0.7 V vs. RHE, with about 10% Faradaic efficiency (FE) towards these products (Figure 4, Table S4). At more negative potentials ranging from -0.9 V vs. RHE to -1.1 V vs. RHE, substantial CO and formic acid production was detected with 40% FE (Figure 4, Table S5, and Table S6). The formation of CO increased at more negative potentials starting from 8% FE and reaching up to 21% FE, at -0.9 V and -1.1 V vs. RHE respectively. Similarly, the FE of formic acid increased from 14% to 19%, at -0.9 V and at -1.1 V vs. RHE. The increased CO₂R activity at more negative potential is in agreement with previous reports.^{17, 24} Notably, while Al metal foil is known to only be active for HER,^{6, 25} we find that confining Al in MOFs, such as MIL-53(Al), provides an active construct for CO₂R at potentials ranging from -1.1 V to -0.9 V vs. RHE with faradaic efficiencies reaching up to 21% for CO production and 19% for formic acid production. In comparison to the best existing MOFs for CO₂R, which exclusively produce CO (Table S7),^{17, 24} MIL-53(Al) can produce both CO and formic acid. These two products are easy to separate since CO is gaseous and formic acid is present in the liquid phase.

We also characterized the catalytic performance by evaluating the partial current density as a measure of the activity of the electrocatalyst. Comparing MIL-53(Al) to Al foil at -1.0 V vs. RHE, MIL-53(Al) has more than 60 times partial current density toward CO₂R and HER products (Table S8).⁶ This observation further supports that the confined reaction environment on Al provided by MIL-53 improves Al's electrocatalytic activity.

Production of CO involves a carbon-bound mechanism, which leads to a *COOH intermediate that results in CO formation. On the other hand, production of formic

acid can occur *via* two different mechanisms,²⁶ which involve either an oxygen-bound intermediate or the direct addition of CO₂ to a surface of metal-hydride (Figure S5). In the latter metal-hydride mechanism, the interaction between the confined Al centers and CO₂ molecules weakens the metal-hydride bonds, thus favoring formic acid formation. However, as stated, formic acid formation may also occur *via* an oxygen-bound mechanism, which leads to a *OCHO intermediate ²⁷ (Figure S5). The oxophilic character of Al may corroborate this latter hypothesis. In this scenario, the confinement of Al centers in the environment provided by MIL-53 may enhance the interaction between the confined Al centers with CO₂ molecules through metal-oxygen binding, thus enabling the reaction pathway via an oxygen-bound intermediate. While diverse, the two reaction mechanisms are both supportive of an enhanced interaction between Al metal centers and CO₂ molecules that is aided by the confined environment provided by the metal organic framework.

To provide further insights on the mechanism and on the active site of MIL-53(Al) electrocatalyst, we performed experiments on Al(OH)₃ drop-casted onto acid-treated carbon paper (see supporting information for full details) as a working electrode to electrochemically reduce CO₂. Al(OH)₃ may resemble the active site of the catalyst in the absence of the confined reaction environment provided by the metal organic framework. Using the fabricated working electrode with Al(OH)₃, we conducted electrochemical testing at three different potentials ranging from -1.1 V to -0.9 V vs. RHE at which MIL-53(Al) is active for CO₂R. Interestingly, at these potentials, we found that the Al(OH)₃ basic sites yield the production of hydrogen and formic acid (Table S9, Table S10, Figure S6). Additionally, without the confined

environment provided by MIL-53, the Al^{3+} metal center is not capable to reduce CO_2 to CO, which, together with formic acid, is one of the main carbon-based products from electroreduction of CO_2 catalyzed by MIL-53(Al). Therefore, we can conclude that a confined reaction environment is needed to enhance CO_2 reduction capabilities to yield both CO and formic acid formation at higher total faradaic efficiency. This observation also points out to the possibility to further tune the local environment around the catalytic center to impart unique catalytic activity.

Finally, to provide further insights into the catalytic performance, we evaluated the activity of the electrocatalysts by calculating the turnover frequency (TOF) for carbon-based products, CO and formic acid (Table S11). At -0.9 V vs. RHE, we observed a combined TOF of 34 h^{-1} . At a potential of -1.0 V vs. RHE, the combined TOF showed a 2.5-fold increase to 84 h^{-1} . Additionally, at -1.1 V, the combined TOF

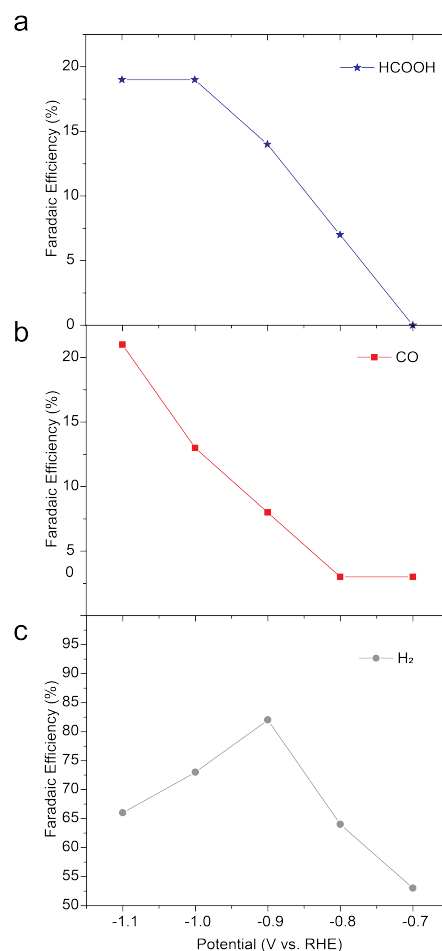


Figure 4-28. Faradaic efficiency for different CO_2R products. Product detection of CO_2R using MIL-53(Al) as electrocatalyst at various potentials resulted in formic acid (a), CO (b), and H_2 (c) formation.

increased to 182 h^{-1} , which is supportive of the expected exponential correlation between applied potential and TOF (Figure S7).²⁸ The TOF for CO ranges from 12 h^{-1} at -0.9 V vs. RHE to 93 h^{-1} at -1.1 V vs. RHE . The TOF for formic acid ranges from 22 h^{-1} at -0.9 V vs. RHE to 89 h^{-1} at -1.1 V vs. RHE . Interestingly, at -1.1 V vs. RHE , MIL-53(Al) shows higher CO₂R activity compared to that of COF-367-Co (165 h^{-1}), one of the best performing molecular organic frameworks for electrochemical CO₂R, at an applied potential of -0.67 V vs. RHE (Table S7).¹⁷ A comparison at the same overpotential cannot be conducted because COF-367-Co started to degrade after an hour of CA at an applied potential more negative than -0.7 V vs. RHE .¹³ On the other hand, MIL-53(Al) requires an activation potential more negative than -0.7 V vs. RHE (Table S4). At an applied potential of -1.1 V vs. RHE , MIL-53(Al) also has comparable activity to that of [Al₂(OH)₂TCPP-Co] MOF, which is one of the best performing MOFs used for aqueous CO₂R and has a maximum TOF of $\sim 200\text{ h}^{-1}$ at -0.67 V vs. RHE , where it is most stable.²⁴ In addition to the reported MOFs' stability at low overpotentials, these electrocatalysts exclusively produced CO while, as mentioned above, MIL-53(Al) produces both CO and formic acid.

4.5. Conclusion

In conclusion, we demonstrate that MIL-53(Al) can electrochemically reduce CO₂ and produce carbon-based products, reaching up to a total 40% FE of CO and formic acid at an applied potential of -1.1 V vs. RHE . This study demonstrates that confining Al centers in MIL-53 frameworks can suppress HER activity and significantly enhance Al centers' ability to electrochemically reduce aqueous CO₂. By modifying

the environment surrounding the metal center and providing a restricted reaction space that mimics an enzymatic cavity, this heterogeneous electrocatalyst allows MIL-53 to impart atypical capability to Al centers to reduce CO₂ to valuable carbon-based products. This electrocatalyst is active for CO₂R in aqueous solution and can be systematically tuned like homogeneous electrocatalysts, thus providing a novel route to the design of low-cost, active, and selective CO₂R electrocatalysts with enhanced CO₂ capture capability. Future directions will include studying the effect of substituents in organic linkers to develop more efficient MOFs for CO₂ capture and electroreduction, as well as *in situ* studies to further understand the mechanism by which the metal center in MOFs catalyzes the electrochemical reduction of CO₂ molecules to valuable carbon-based products. Future studies will be also directed to the use of MIL-53(Al) membranes as gas diffusion electrodes for efficient electrochemical CO₂R systems to convert atmospheric CO₂ to valuable carbon-based products in gas phase, thus overcoming possible CO₂ solubility limitations in aqueous environment. Our findings open new opportunities to further explore confinement effects of metal centers for metals that traditionally favor the reduction of protons.

4.6. Experimental Procedures

4.6.1. Materials and Methods

4.6.1.1. Chemicals

Anhydrous N,N-Dimethylformamide (DMF) (99.8%), nitric acid (70%), aluminum chloride hexahydrates (AlCl₃·6H₂O) (99%), terephthalic acid (98%), Nafion 117 solution, 2,2,2-trifluoroethanol, and high purity potassium carbonate (99.995%) were

purchased from Sigma Aldrich. Hydrochloric acid (36.5 – 38%) was purchased from VWR. Isopropyl alcohol (100%) was purchased from KMG electronic chemicals. Water used for all of the synthesis and electrochemical experiments (MilliQ water) was from a Milli-Q Water Purification System (resistivity of 18.2 M Ω -cm, Millipore). Selemion AMV anion-exchange membrane was purchased from AGC Engineering Co., LTD. Carbon paper (Sigracet 29BC) was purchased from Fuel Cell Store. Carbon dioxide (99.995%) and nitrogen (99.999%) were obtained from Praxair.

4.6.1.2. Characterizations Techniques

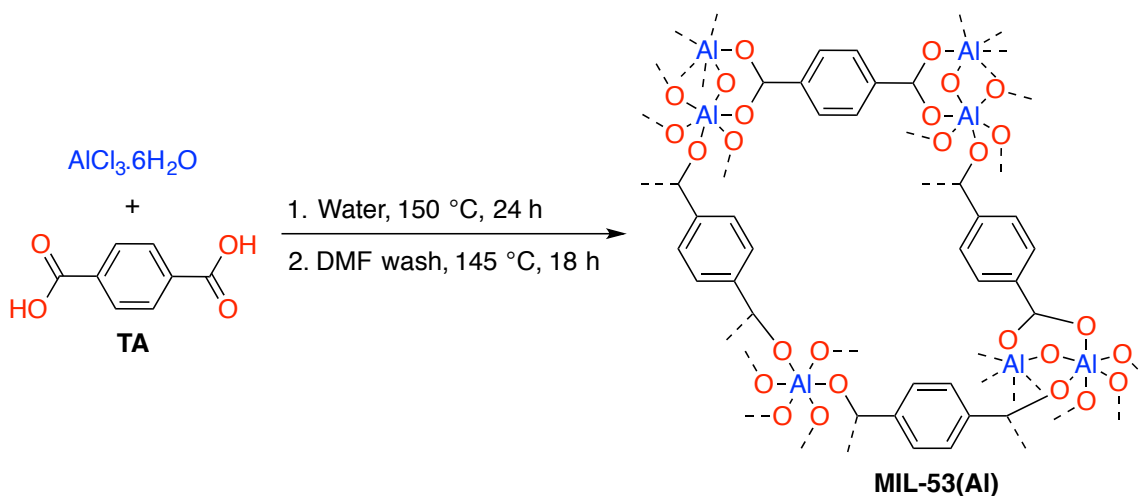
Powder X-ray diffraction (PXRD) patterns were acquired with a Rigaku-SmartLab diffractometer using Cu K α ($\lambda=0.15406$ nm).

Scanning electron microscopy images of synthesized MIL-53(Al) were acquired with a FEI Quanta FEG250. In addition, scanning electron microscopy images of Al(OH)₃ electrodes before and after electrochemical testing were acquired with a Zeiss Gemini Supra 55 VP-SEM.

X-ray Photoelectron Spectroscopy (XPS) was performed using a monochromatized Al K α source ($h\nu=1486.6$ eV), operated at 225 W, on a Kratos Axis Ultra DLD system at a takeoff angle of 0° relative to the surface normal and a pass energy for the narrow scan core level and valence band spectra of 20 eV to observe the electronic state of the elements within the material. Spectral fitting was conducted using Casa XPS analysis software. Spectral positions were corrected using adventitious carbon by shifting the C 1s core level position to 284.8 eV and curves were fit with quasi-Voigt lines following Shirley background subtraction.

4.6.2. Synthetic and Electrode Fabrication Procedures and Characterizations

4.6.2.1. MIL-53(Al) Synthesis



MIL-53(Al) was synthesized with a slightly modified procedure already present in the literature²⁹. In a fume hood, a 22 mL Teflon reactor was charged with $\text{AlCl}_3 \cdot 6\text{H}_2\text{O}$ (1.97 g, 8 mmol). 20 mL of MilliQ water were carefully added. After all the HCl evolved from the hydrolysis was removed, terephthalic acid (TA, 1.38 g, 8 mmol) was added. The Teflon reactor was sealed and placed in a stainless steel autoclave reactor. The reactor was heated in a preheated oven (150 °C) for 24 hours. The reactor was then allowed to cool down to room temperature before filtering the reaction mixture to obtain a white gel via Buchner filtration. The white gel was added into a 50 mL centrifuge tube. MilliQ water (~30 mL) was added into the centrifuge tube. It was centrifuged for 20 minutes (Eppendorf centrifuge 5804). The supernatant was disposed to remove the unreacted AlCl_3 . The white gel was washed again several times using this centrifuge method. The washed white gel was briefly dried in a preheated

BINDER oven (90 °C) for 1 hour before it was suspended in DMF (~15 mL) in a 22 mL Teflon reactor. The Teflon reactor was sealed and placed in a stainless steel autoclave reactor. The reactor was put in preheated sand bath (145 °C) for 18 hours to remove any unreacted TA that may be trapped in the porous cavity of the MOF.³⁰ The reactor was then allowed to cool down to room temperature before filtering the reaction mixture to obtain a white solid via Buchner filtration. The white solid was washed several times with isopropyl alcohol (IPA) by centrifugation to replace DMF that may be coordinated to the MOF. The supernatant was removed, leaving a white solid. The white solid was dried in a Lindberg Blue M vacuum oven from Thermo Fisher Scientific at 140 °C and 10 mmHg for 18 hours to remove the remaining DMF and IPA.

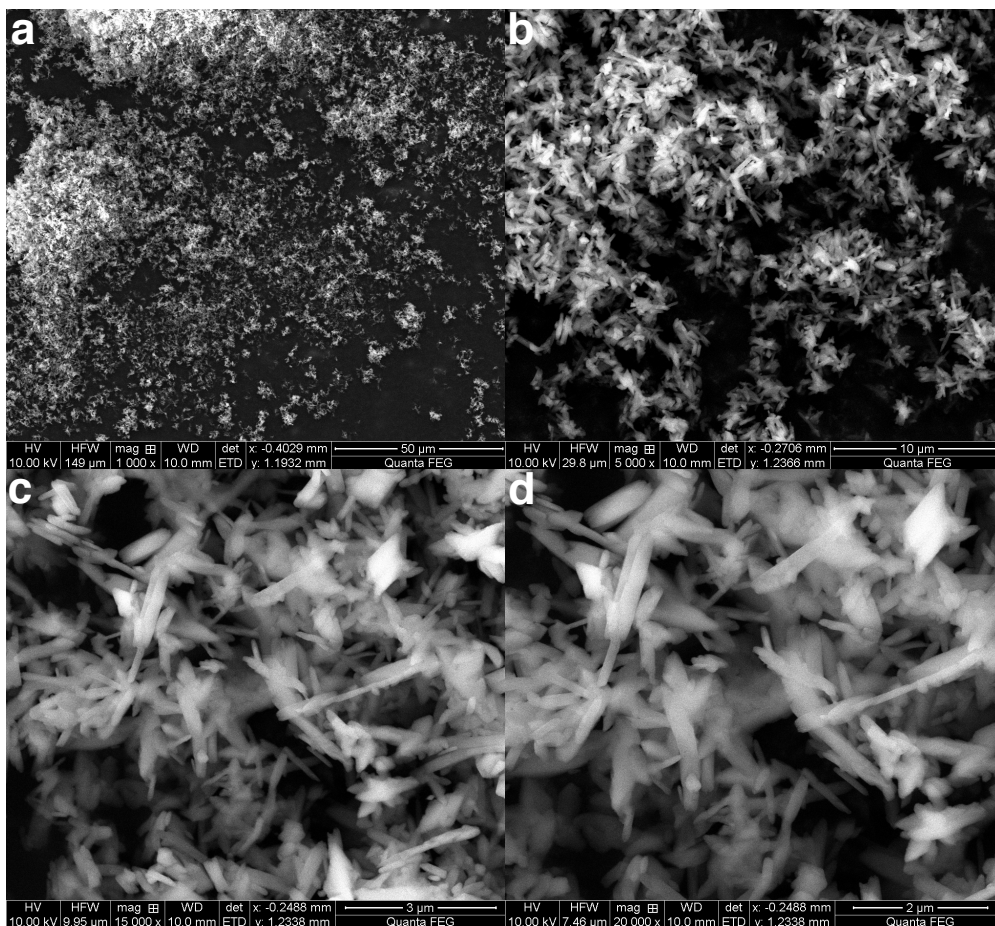


Figure S4-1. White powder of synthesized MIL-53(Al) was placed on top of carbon tape that was attached to a disposable SEM stage. Several SEM images of the synthesized MIL-53(Al) were taken at different magnifications. (a.) 1000x (b.) 5000x (c.) 15000x (d.) 20000x. These SEM images showed that the synthesized MIL-53(Al) is a crystalline white powder with around 1 μm long needle-like crystals.

4.6.2.2. Preparation of Carbon Paper

Carbon paper (Sigracet 29BC) was cut into $\sim 1.3 \text{ cm} \times \sim 1.3 \text{ cm}$ squares. The cut carbon paper was immersed in 70% nitric acid for 15 minutes to remove metallic impurities that may be present in the fibers.³⁴ The carbon paper was then washed with MilliQ water and air-dried for 18 hours.

4.6.2.3. Preparation of MIL-53(Al) Suspension

In a fume hood, a 20 mL scintillation vial was charged with MIL-53(Al) (30 mg, 0.036 mmol). MilliQ water (3.8 mL) and IPA (1.0 mL) were added. Nafion 117 solution (40 μ L) was added. The vial was sealed and sonicated for 30 minutes at room temperature to make a homogeneous suspension. The suspension (40 μ L) and trifluoroethanol (40 μ L) were added to a 2.0 mL microcentrifuge tube. Trifluoroethanol was added to allow the MIL-53(Al) suspension to permeate inside the fiber of carbon paper, which is coated with Teflon and highly hydrophobic.³¹ The microcentrifuge tube was vortexed for 30 seconds to make the final MIL-53(Al) suspension homogeneous.

4.6.2.4. Preparation of Al(OH)₃ Suspension

In a fume hood, a 20 mL scintillation vial was charged with Al(OH)₃ (30 mg, 0.38 mmol). MilliQ water (3.8 mL) and IPA (1.0 mL) were added. Nafion 117 solution (40 μ L) was added. The vial was sealed and sonicated for 30 minutes at room temperature to make a homogeneous suspension. The suspension (40 μ L) and trifluoroethanol (40 μ L) were added to a 2.0 mL microcentrifuge tube. Trifluoroethanol was added to allow the Al(OH)₃ suspension to permeate inside the fiber of carbon paper, which is coated with Teflon and highly hydrophobic.³¹ The microcentrifuge tube was vortexed for 30 seconds to make the final Al(OH)₃ suspension homogeneous.

4.6.2.5. Preparation of Fabricated Working Electrodes

The final suspension (40 μL , 0.124 mg of powder) was deposited onto the prepared carbon paper electrodes. The electrode was then dried in a preheated BINDER oven (90 $^{\circ}\text{C}$) for 18 hours. The back of the electrode was insulated with electroplating tape. The front was contacted with a piece of copper tape, and then covered with a second piece of electroplating tape with a round hole with diameter ~ 1.26 cm. This configuration would insulate the Cu tape as well as provide a precise exposed area of 1.25 cm^2 .

4.6.3. Electrochemical Testing and Characterizations

4.6.3.1. Electrochemical Testing Preparation and Procedures

4.6.3.1.1. Electrolyte Preparation

Potassium carbonate solution (0.05M) was prepared from high purity potassium carbonate (99.995%, Sigma Aldrich) and water from a Milli-Q Water Purification System (resistivity of $18.2\text{ M}\Omega\text{-cm}$, Millipore).

4.6.3.1.2. Electrochemical Testing Procedures

Electrochemical experiments were conducted in a two-compartment flow cell fabricated from PEEK following a reported design (Figure S2).³² A Selemion AMV anion-exchange membrane separated the two chambers. A Pt foil was used as the counter electrode. A Leak-Free Ag/AgCl electrode (LF-1, 1.0 mm outer diameter, Innovative Instruments, Inc.) was used as the reference electrode. The reference

electrode was calibrated against a second reference electrode, which in turn was calibrated in a two-electrode system with H₂ bubbled over a Pt wire as the counter electrode and a 1M H₂SO₄ solution as the electrolyte. The applied potentials were converted from Ag/AgCl scale to the RHE scale via the equation: $E_{\text{RHE}} = E_{\text{Ag/AgCl}} + 0.197 + 0.059 \cdot \text{pH}$, where the pH used is the bulk pH for the CO₂-saturated electrolyte (6.8). In the electrochemical cell, the prepared 0.05 M potassium carbonate solution was used as electrolyte. The electrolyte was saturated with a continuous flow of 5 sccm CO₂ for a minimum of 30 minutes within the experimental cell setup immediately prior to all electrochemical experiments. One cycle of chronoamperometric (CA) measurement was performed by applying a constant potential for 45 minutes. One cycle of CA at -1.5 V vs Ag/AgCl was performed before data collection was started. Electrochemical experiments were carried out using SP-200 potentiostat from BioLogic. Cyclic voltammetry (CV) was then performed and repeated at the end of each run in order to test the stability of material before and after the chronoamperometric measurement. Chronoamperometric measurement was performed for about 45 minutes. Gas products were quantified using gas chromatography (GC), Agilent Technologies 490 Micro GC (Shimadzu 490GC), through a flow mode. Liquid products were quantified after electrochemical measurement using high performance liquid chromatography (HPLC), UltiMate 3000. During the chronoamperometric measurement, gas from the cell was directed through the sampling loop of a gas chromatograph with molecular sieves columns (MOL 5A-Agilent) and was analyzed in 15 minutes intervals. For each interval, concentration of gas produced was collected. With total current density measured at the end of

experiment and applied potential, faradaic efficiency for each gas for each interval was calculated. These recorded faradaic efficiencies were averaged and reported.

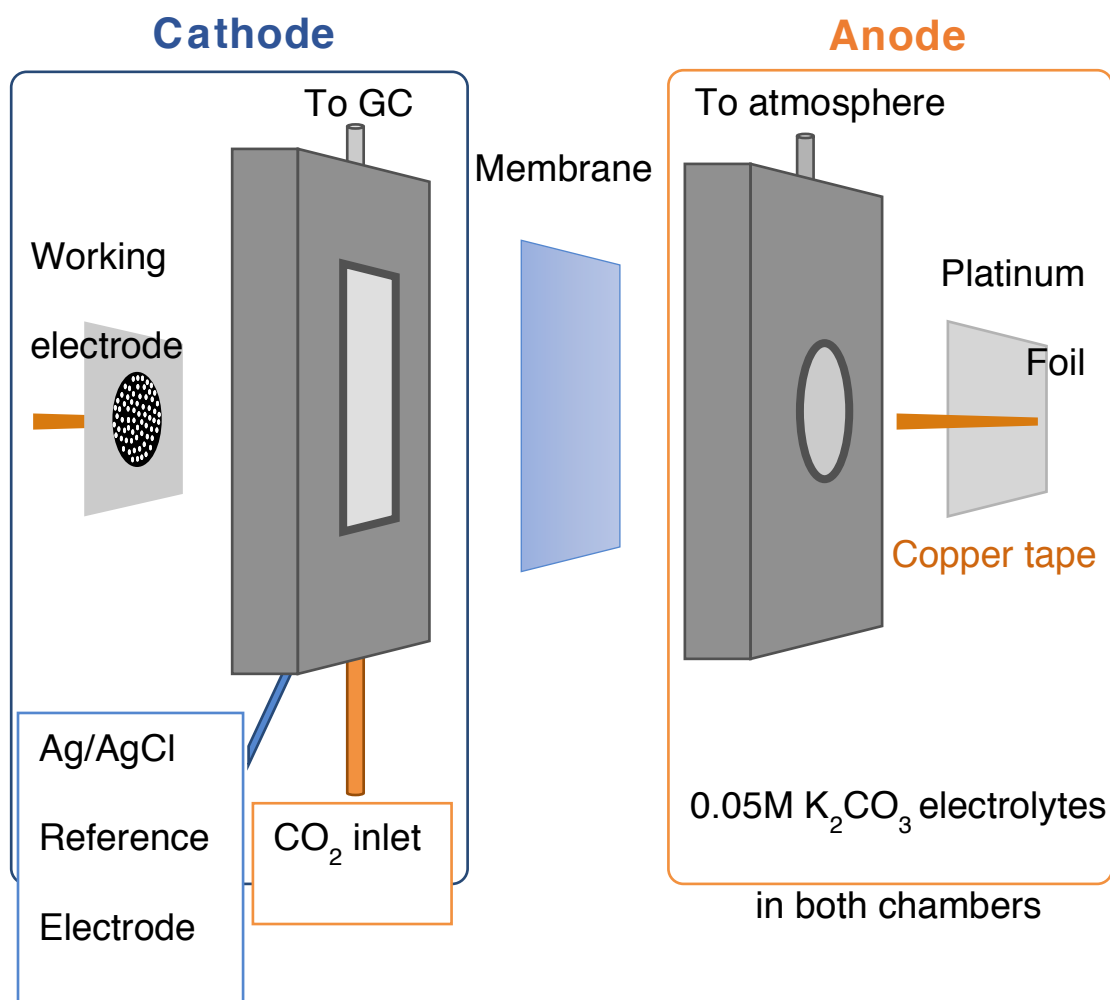


Figure S4-2. Two-compartment flow cell used for electroreduction of carbon dioxide.

4.6.3.2. Electrochemical Characterizations

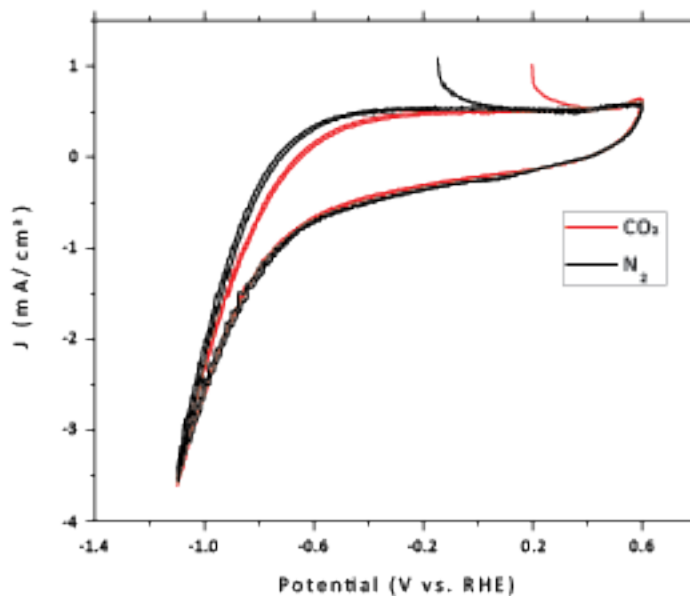


Figure S4-3. Using two-compartment flow cell electrochemical setup, the electrolyte solution in the working compartment was sparged for 10 minutes with N₂ or CO₂.

Cyclic voltammetry (CV) scans were then taken from 0.6 to -1.1 V vs RHE with 10 mV/s scan rate. CV scans were performed for working electrode in two different atmosphere: CO₂ atmosphere (red curve) and N₂ atmosphere (black curve). These CV scans showed that the working electrodes containing MIL-53(Al) were active in CO₂ and N₂ atmosphere. Under N₂ atmosphere, working electrodes undergo hydrogen evolution reaction (HER), similar to metallic Al that is only active for HER.³³

Table S4-1. Fabricated working electrode containing MIL-53(Al) under N₂ atmosphere.
Control experiments were performed for 65 minutes CA at a constant applied potential. There is only hydrogen production detected.

Potential vs. RHE (V)	Faradaic Efficiency					
	Hydrogen	CO	Methane	Ethane	Ethylene	Formic Acid
-1.0	85.7%	0%	0%	0%	0%	0%

Table S4-2. Background: plain carbon paper under CO₂ atmosphere.
Control experiments were performed under the same condition for electrochemical reduction of CO₂ for the reported product detection, 65 minutes CA at a constant applied potential. There is no CO₂R product detected.

Potential vs. RHE (V)	Faradaic Efficiency					
	Hydrogen	CO	Methane	Ethane	Ethylene	Formic Acid
-1.0	42.0%	0%	0%	0%	0%	0%

Table S4-3. Background: plain carbon paper and Nafion (0.17 μL) under CO₂ atmosphere.
Control experiments were performed under the same condition for electrochemical reduction of CO₂ for the reported product detection, 65 minutes CA at a constant applied potential. There is negligible CO₂R product detected.

Potential vs. RHE (V)	Faradaic Efficiency					
	Hydrogen	CO	Methane	Ethane	Ethylene	Formic Acid
-1.0	45.8%	0.93%	0%	0%	0%	0%

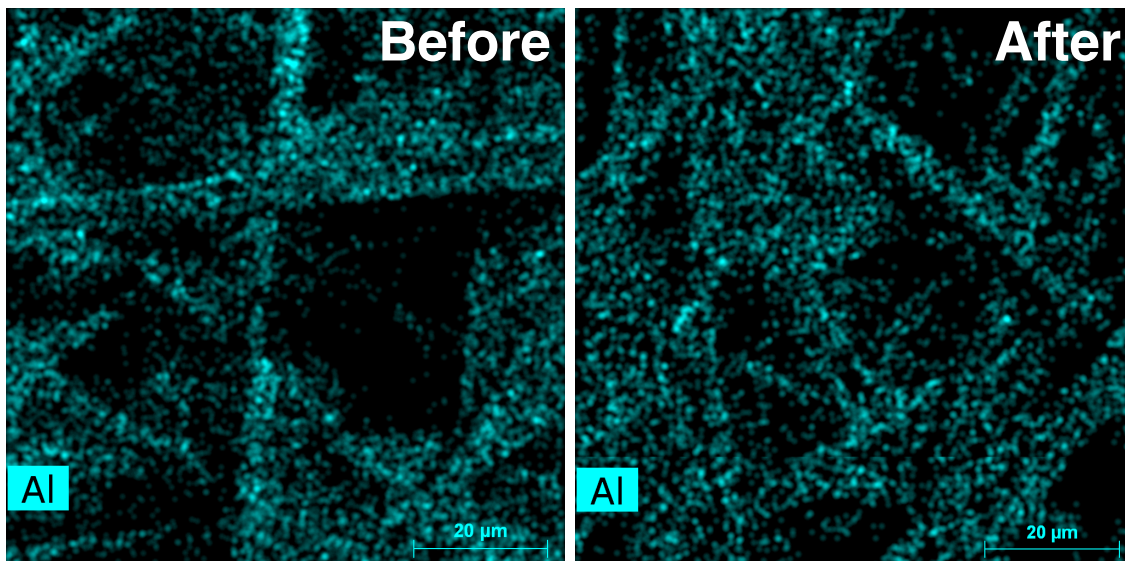


Figure S4-4. Scanning electron microscopes-energy-dispersive X-Ray (SEM-EDX) of Al of the surface of the working electrodes before and after 4 hours 30 minutes electrochemical testing at five different potentials (-1.1 V, -1.0 V, -0.9 V, -0.8 V, and -0.7 V vs RHE) to ensure the presence of the elemental components of MIL-53(Al) on the surface of working electrodes.

The SEM-EDX map of the electrode before electrochemical testing (left) showed that MIL-53(Al) is evenly distributed by the presence of Al(blue) evenly distributed on the electrode. For the sake of clarity, we did not include carbon in the reported SEM-EDX maps, since there is a strong carbon signal coming from the carbon paper support in addition to the MOF's organic linker. The SEM-EDX map of the electrode after electrochemical testing (right) showed that Al (blue) was still evenly distributed on the surface of the electrode, supporting that MIL-53(Al) is relatively stable under the operating condition.

Table S4-4. Initial screening of CO₂R at applied potentials of -0.7 V vs RHE and -0.8 V vs RHE.

Potential vs RHE (V)	Current (mA)	Faradic Efficiency		
		CO	Formic Acid	Hydrogen
-0.7	0.18	3%	0%	53%
-0.8	0.70	3%	7%	64%

Table S4-5. Faradaic efficiency of MIL-53(Al) catalyzed CO₂ reduction at different applied potentials.

Potential vs RHE (V)	Current (mA)	Faradic Efficiency		
		CO	Formic Acid	Hydrogen
-0.9	1.12	7%	12%	84%
-0.9	1.34	9%	16%	80%
-1.0	2.43	12%	16%	75%
-1.0	1.87	13%	22%	71%
-1.1	4.52	15%	20%	68%
-1.1	3.09	26%	17%	63%

Table S4-6. Average and error analysis of faradaic efficiency of MIL-53(Al) catalyzed CO₂ reduction at different applied potentials.

Potential vs. RHE (V)	Average Faradaic Efficiency			Standard Deviation			Standard Error Mean (SEM)		
	CO	Formic Acid	Hydrogen	CO	Formic Acid	Hydrogen	CO	Formic Acid	Hydrogen
-0.9	8%	14%	82%	1%	3%	6%	1%	2%	4%
-1.0	13%	19%	73%	1%	4%	6%	1%	3%	4%
-1.1	21%	19%	66%	8%	2%	7%	6%	2%	5%

Table S4-7. Activity and selectivity of Molecular Organic Frameworks as CO₂R electrocatalysts.

Electrocatalyst	Applied Potential (V vs RHE)	Electrolyte	CO ₂ R products (%FE)	TOF (h ⁻¹)	Reference
MIL-53(Al)	-0.9	0.05 M K ₂ CO ₃	22% ^a	34	This study
MIL-53(Al)	-1.0	0.05 M K ₂ CO ₃	32% ^a	84	This study
MIL-53(Al)	-1.1	0.05 M K ₂ CO ₃	40% ^a	182	This study
COF-367-Co	-0.67	0.5 M KHCO ₃	91% ^b	165	36
[Al ₂ (OH) ₂ TCPP-Co] MOF	-0.7	0.5 M K ₂ CO ₃	76% ^b	~200	37
^a CO ₂ R products composed of CO and formic acid. ^b CO ₂ R products composed of only CO.					

Table S4-8. Activity and selectivity of MIL-53(Al) compared to Al foil as CO₂R electrocatalysts.

Electrocatalyst	Applied Potential (V vs. RHE)	Electrolyte	CO ₂ R products (%FE)	Partial Current Densities toward CO ₂ R (mA/cm ²)	Reference
MIL-53(Al)	-0.9	0.05 M K ₂ CO ₃ (pH=6.8)	22% ^a	0.22	This study
MIL-53(Al)	-1.0	0.05 M K ₂ CO ₃ (pH=6.8)	32% ^a	0.54	This study
MIL-53(Al)	-1.1	0.05 M K ₂ CO ₃ (pH=6.8)	40% ^a	1.2	This study
Al foil	-1.0	0.1 M KHCO ₃ (pH=6.6)	1% ^b	0.008	38

^aCO₂R products composed of CO and formic acid. ^bCO₂R products composed of methane, ethylene, and ethane.

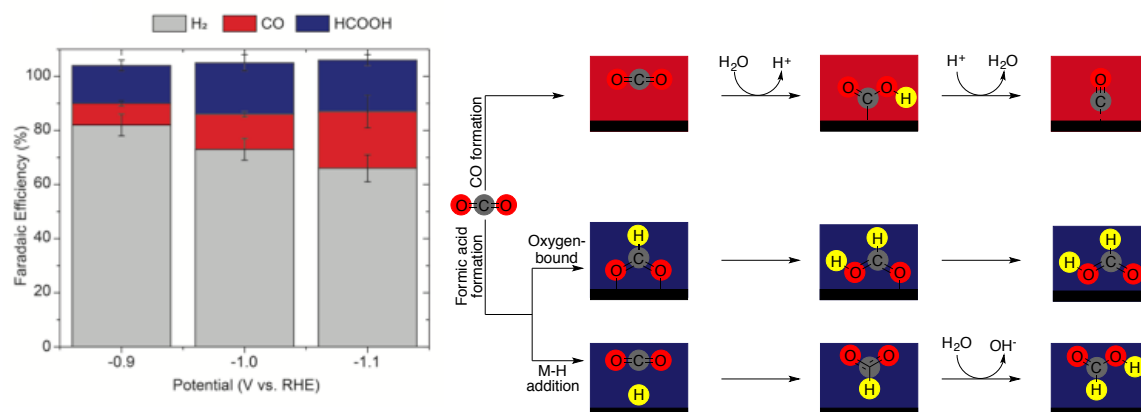


Figure S4-5. Mechanism of CO₂ reduction through two different pathways: carbon-bound pathway leads to CO formation and oxygen-bound pathway or direct addition of CO₂ to a surface metal-hydride lead to formic acid formation.^{35,39}

Table S4-9. Faradaic efficiency of Al(OH)₃ catalyzed CO₂ reduction at different applied potentials.

Potential vs RHE (V)	Current (mA)	Faradic Efficiency		
		Hydrogen	CO	Formic Acid
-0.9	0.52	9.52%	0%	0%
-0.9	0.36	24.70%	0%	0%
-1.0	0.79	40.21%	0%	16.75%
-1.0	0.78	43.86%	0%	18.39%
-1.1	1.33	44.63%	1.97%	23.46%
-1.1	1.32	48.76%	3.97%	27.79%

Table S4-10. Average and error analysis of faradaic efficiency of Al(OH)₃ catalyzed CO₂ reduction at different applied potentials.

Potential vs RHE (V)	Average Faradaic Efficiency			Standard Deviation			Standard Error Mean (SEM)		
	CO	Formic Acid	Hydrogen	CO	Formic Acid	Hydrogen	CO	Formic Acid	Hydrogen
-0.9	0%	0%	17%	0%	0%	11%	0%	0%	8%
-1.0	0%	18%	42%	0%	1%	3%	0%	1%	2%
-1.1	3%	26%	47%	1%	3%	3%	1%	2%	2%

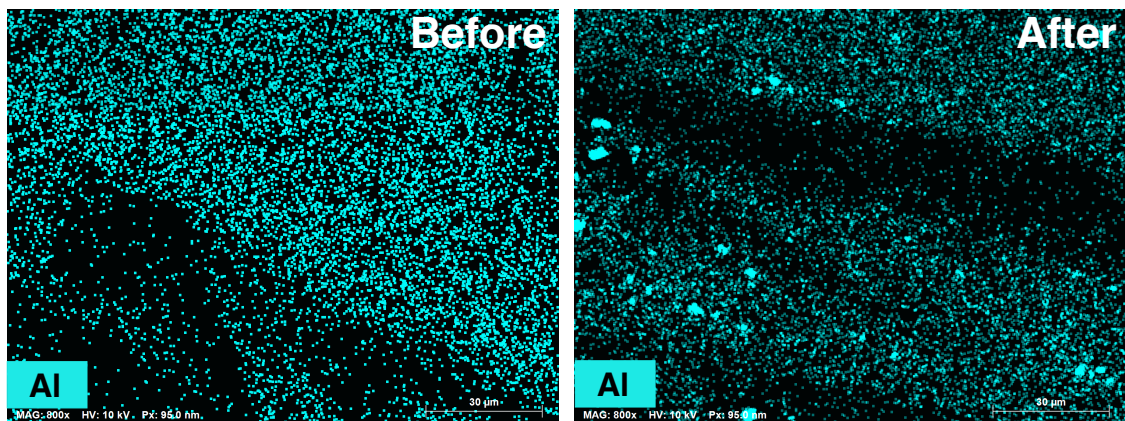


Figure S4-6. Scanning electron microscopes-energy-dispersive X-Ray (SEM-EDX) of Al of the surface of the working electrodes before and after 3 hours and 15 minutes electrochemical testing at three different potentials (-1.1 V, -1.0 V, and -0.9 V vs. RHE) to ensure the presence of the elemental components of $\text{Al}(\text{OH})_3$ on the surface of working electrodes. The SEM-EDX map of the electrode before electrochemical testing (left) showed that $\text{Al}(\text{OH})_3$ is evenly distributed by the presence of Al(blue) evenly distributed on the electrode. The SEM-EDX map of the electrode after electrochemical testing (right) showed that Al (blue) was still evenly distributed on the surface of the electrode, supporting that $\text{Al}(\text{OH})_3$ is relatively stable under the operating condition.

Table S4-11. Turnover frequency (TOF) calculation based on faradaic efficiency and current using:

$$TOF = \frac{Q*FE}{t*N*F*ncatalyst} = \frac{i*FE}{N*F*ncatalyst},$$

where Q is the total charge passed in time t, i is the current, FE is the Faradaic efficiency for the desired product, N is the number of electrons in the half reaction (N = 2 for CO₂ to CO or HCO₂H conversion), F is the Faraday constant (F = 96485 C/mol electrons), and n_{catalyst} is the mole of MIL-53(Al)/unit cell deposited onto active area of CP.

TOF for CO and Formic Acid

Potential vs RHE (V)	Run 1				Run 2				Average TOF (h ⁻¹)
	Current (mA)	FE for CO and formic acid	TOF (s ⁻¹)	TOF (h ⁻¹)	Current (mA)	FE for CO and formic acid	TOF (s ⁻¹)	TOF (h ⁻¹)	
-0.9	1.12	0.19	0.007	27	1.34	0.25	0.012	42	34
-1	2.43	0.28	0.024	85	1.87	0.35	0.023	82	84
-1.1	4.52	0.35	0.055	198	3.09	0.43	0.046	166	182

TOF for CO

Potential vs RHE (V)	Run 1				Run 2				Average TOF (h ⁻¹)
	Current (mA)	FE for CO	TOF (s ⁻¹)	TOF (h ⁻¹)	Current (mA)	FE for CO	TOF (s ⁻¹)	TOF (h ⁻¹)	
-0.9	1.12	0.07	0.003	10	1.34	0.09	0.004	15	12
-1	2.43	0.12	0.01	37	1.87	0.13	0.008	30	33
-1.1	4.52	0.15	0.024	85	3.09	0.26	0.028	101	93

TOF for Formic Acid

Potential vs RHE (V)	Run 1				Run 2				Average TOF (h ⁻¹)
	Current (mA)	FE for formic acid	TOF (s ⁻¹)	TOF (h ⁻¹)	Current (mA)	FE for formic acid	TOF (s ⁻¹)	TOF (h ⁻¹)	
-0.9	1.12	0.12	0.005	17	1.34	0.16	0.007	27	22
-1	2.43	0.16	0.014	49	1.87	0.22	0.014	52	50
-1.1	4.52	0.2	0.031	113	3.09	0.17	0.018	66	89

TOF for Hydrogen

Potential vs RHE (V)	Run 1				Run 2				Average TOF (h ⁻¹)
	Current (mA)	FE for hydrogen	TOF (s ⁻¹)	TOF (h ⁻¹)	Current (mA)	FE for hydrogen	TOF (s ⁻¹)	TOF (h ⁻¹)	
-0.9	1.12	0.84	0.033	118	1.34	0.8	0.037	134	126
-1	2.43	0.75	0.063	228	1.87	0.71	0.046	166	197
-1.1	4.52	0.63	0.099	357	3.09	0.68	0.073	263	310

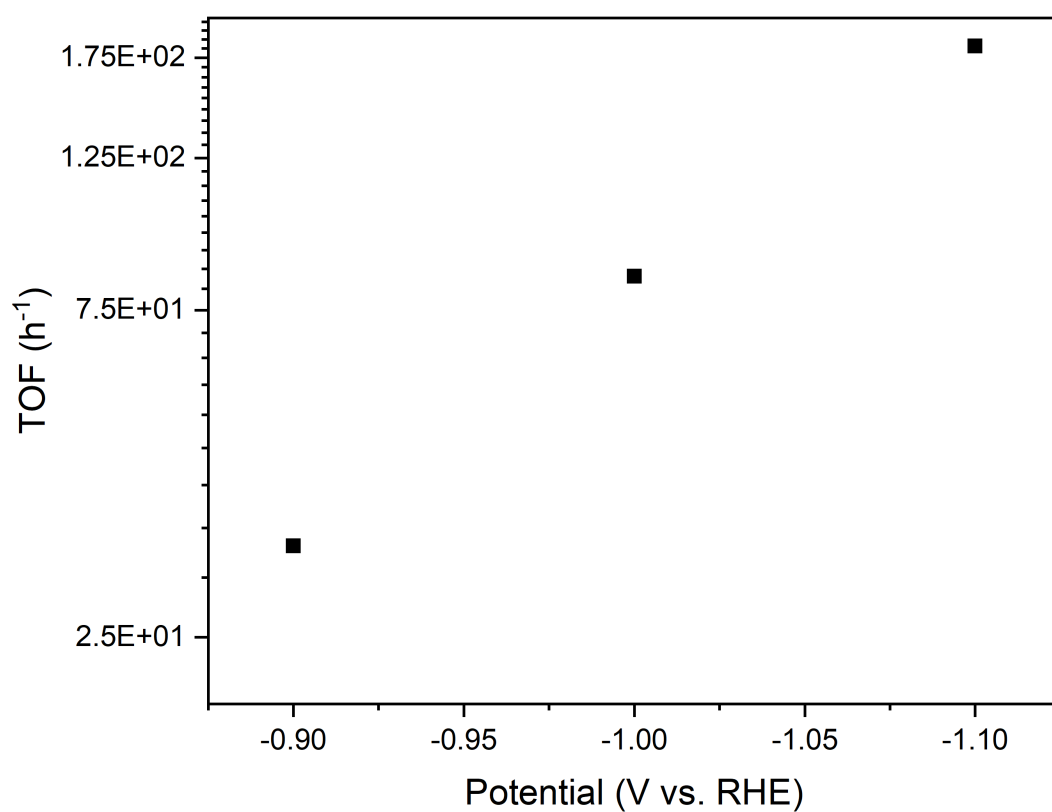


Figure S4-7. Exponential relationship between applied potential (V vs RHE) and turnover frequency (TOF) for carbon-based products.

4.7. Acknowledgements

This material is based upon work performed by the Joint Center for Artificial Photosynthesis, a DOE Energy Innovation Hub, supported through the Office of Science of the U.S. Department of Energy under Award No. DE-SC0004993. We acknowledge Prof. F. Dean Toste and Prof. Christopher K. Ober for fruitful discussions, Dr. Jian Zhang for assistance in making 3D model of MIL-53(Al), and Stefano Dallorto at the Molecular Foundry for assistance in scanning electron microscopy measurements of aluminum hydroxide electrodes. The work at the Molecular Foundry was supported by the Office of Science, Office of Basic Energy Sciences, of the U.S. Department of Energy under Contract No. DE-AC02-05CH11231.

REFERENCES

1. Kaphan, D. M.; Levin, M. D.; Bergman, R. G.; Raymond, K. N.; Toste, F. D., A supramolecular microenvironment strategy for transition metal catalysis. *Science* 2015, *350* (6265), 1235-1238.
2. Gross, E.; Dean Toste, F.; Somorjai, G. A., Polymer-Encapsulated Metallic Nanoparticles as a Bridge Between Homogeneous and Heterogeneous Catalysis. *Catal. Lett.* 2015, *145* (1), 126-138.
3. Seh, Z. W.; Kibsgaard, J.; Dickens, C. F.; Chorkendorff, I.; Nørskov, J. K.; Jaramillo, T. F., Combining theory and experiment in electrocatalysis: Insights into materials design. *Science* 2017, *355* (6321), eaad4998.
4. Hori, Y.; Takahashi, R.; Yoshinami, Y.; Murata, A., Electrochemical Reduction of CO at a Copper Electrode. *J. Phys. Chem. B* 1997, *101* (36), 7075-7081.
5. Kuhl, K. P.; Cave, E. R.; Abram, D. N.; Jaramillo, T. F., New insights into the electrochemical reduction of carbon dioxide on metallic copper surfaces. *Energy Environ. Sci.* 2012, *5* (5), 7050-7059.
6. Hidetomo, N.; Shoichiro, I.; Yoshiyuki, O.; Kazumoto, I.; Masunobu, M.; Kaname, I., Electrochemical Reduction of Carbon Dioxide at Various Metal Electrodes in Aqueous Potassium Hydrogen Carbonate Solution. *Bull. Chem. Soc. Jpn* 1990, *63* (9), 2459-2462.
7. Yang, D.; Gates, B. C., Catalysis by Metal Organic Frameworks: Perspective and Suggestions for Future Research. *ACS Catal.* 2019, *9* (3), 1779-1798.
8. Pascanu, V.; González Miera, G.; Inge, A. K.; Martín-Matute, B., Metal–Organic Frameworks as Catalysts for Organic Synthesis: A Critical Perspective. *J.*

Am. Chem. Soc. 2019, *141* (18), 7223-7234.

9. Maina, J. W.; Pozo-Gonzalo, C.; Kong, L.; Schütz, J.; Hill, M.; Dumée, L. F., Metal organic framework based catalysts for CO₂ conversion. *Mater. Horiz.* 2017, *4* (3), 345-361.

10. Mahmood, A.; Guo, W.; Tabassum, H.; Zou, R., Metal-Organic Framework-Based Nanomaterials for Electrocatalysis. *Adv. Energy Mater.* 2016, *6* (17), 1600423.

11. Diercks, C. S.; Liu, Y.; Cordova, K. E.; Yaghi, O. M., The role of reticular chemistry in the design of CO₂ reduction catalysts. *Nat. Mater.* 2018, *17* (4), 301-307.

12. Roberts, J. M.; Fini, B. M.; Sarjeant, A. A.; Farha, O. K.; Hupp, J. T.; Scheidt, K. A., Urea Metal–Organic Frameworks as Effective and Size-Selective Hydrogen-Bond Catalysts. *J. Am. Chem. Soc.* 2012, *134* (7), 3334-3337.

13. McGuirk, C. M.; Katz, M. J.; Stern, C. L.; Sarjeant, A. A.; Hupp, J. T.; Farha, O. K.; Mirkin, C. A., Turning On Catalysis: Incorporation of a Hydrogen-Bond-Donating Squaramide Moiety into a Zr Metal–Organic Framework. *J. Am. Chem. Soc.* 2015, *137* (2), 919-925.

14. Burgess, S. A.; Kassie, A.; Baranowski, S. A.; Fritzsche, K. J.; Schmidt-Rohr, K.; Brown, C. M.; Wade, C. R., Improved Catalytic Activity and Stability of a Palladium Pincer Complex by Incorporation into a Metal–Organic Framework. *J. Am. Chem. Soc.* 2016, *138* (6), 1780-1783.

15. Wang, L.; Agnew, D. W.; Yu, X.; Figueroa, J. S.; Cohen, S. M., A Metal–Organic Framework with Exceptional Activity for C–H Bond Amination. *Angew. Chem. Int. Ed.* 2018, *57* (2), 511-515.

16. Eppinger, J.; Huang, K.-W., Formic Acid as a Hydrogen Energy Carrier. *ACS*

Energy Lett. 2017, 2 (1), 188-195.

17. Lin, S.; Diercks, C. S.; Zhang, Y.-B.; Kornienko, N.; Nichols, E. M.; Zhao, Y.; Paris, A. R.; Kim, D.; Yang, P.; Yaghi, O. M.; Chang, C. J., Covalent organic frameworks comprising cobalt porphyrins for catalytic CO₂ reduction in water. *Science* 2015, 349 (6253), 1208-1213.

18. Lo, S.-H.; Senthil Raja, D.; Chen, C.-W.; Kang, Y.-H.; Chen, J.-J.; Lin, C.-H., Waste polyethylene terephthalate (PET) materials as sustainable precursors for the synthesis of nanoporous MOFs, MIL-47, MIL-53(Cr, Al, Ga) and MIL-101(Cr). *Dalton T.* 2016, 45 (23), 9565-9573.

19. Loiseau, T.; Serre, C.; Huguenard, C.; Fink, G.; Taulelle, F.; Henry, M.; Bataille, T.; Férey, G., A Rationale for the Large Breathing of the Porous Aluminum Terephthalate (MIL-53) Upon Hydration. *Chem. Eur. J.* 2004, 10 (6), 1373-1382.

20. Lum, Y.; Kwon, Y.; Lobaccaro, P.; Chen, L.; Clark, E. L.; Bell, A. T.; Ager, J. W., Trace Levels of Copper in Carbon Materials Show Significant Electrochemical CO₂ Reduction Activity. *ACS Catal.* 2016, 6 (1), 202-209.

21. NIST X-ray Photoelectron Spectroscopy Database. National Institute of Standards and Technology: Gaithersburg MD, 20899, 2000.

22. Takeno, N., *Atlas of Eh-pH diagrams Intercomparison of thermodynamic databases*. National Institute of Advanced Industrial Science and Technology: 2005.

23. Ashby, M. F.; Jones, D. R. H., Chapter 24 - Oxidation of Materials. In *Engineering Materials 1 (Fourth Edition)*, Ashby, M. F.; Jones, D. R. H., Eds. Butterworth-Heinemann: Boston, 2012; pp 367-375.

24. Kornienko, N.; Zhao, Y.; Kley, C. S.; Zhu, C.; Kim, D.; Lin, S.; Chang, C. J.;

- Yaghi, O. M.; Yang, P., Metal–Organic Frameworks for Electrocatalytic Reduction of Carbon Dioxide. *J. Am. Chem. Soc.* 2015, *137* (44), 14129-14135.
25. Hori, Y., Electrochemical CO₂ Reduction on Metal Electrodes. In *Modern Aspects of Electrochemistry*, Vayenas, C. G.; White, R. E.; Gamboa-Aldeco, M. E., Eds. Springer New York: New York, NY, 2008; pp 89-189.
26. Cheng, T.; Xiao, H.; Goddard, W. A., Reaction Mechanisms for the Electrochemical Reduction of CO₂ to CO and Formate on the Cu(100) Surface at 298 K from Quantum Mechanics Free Energy Calculations with Explicit Water. *J. Am. Chem. Soc.* 2016, *138* (42), 13802-13805.
27. Feaster, J. T.; Shi, C.; Cave, E. R.; Hatsukade, T.; Abram, D. N.; Kuhl, K. P.; Hahn, C.; Nørskov, J. K.; Jaramillo, T. F., Understanding Selectivity for the Electrochemical Reduction of Carbon Dioxide to Formic Acid and Carbon Monoxide on Metal Electrodes. *ACS Catal.* 2017, *7* (7), 4822-4827.
28. Costentin, C.; Drouet, S.; Robert, M.; Savéant, J.-M., Turnover Numbers, Turnover Frequencies, and Overpotential in Molecular Catalysis of Electrochemical Reactions. Cyclic Voltammetry and Preparative-Scale Electrolysis. *J. Am. Chem. Soc.* 2012, *134* (27), 11235-11242.
29. Ahnfeldt, T.; Gunzelmann, D.; Loiseau, T.; Hirsemann, D.; Senker, J.; Férey, G.; Stock, N. Synthesis and Modification of a Functionalized 3D Open-Framework Structure with MIL-53 Topology. *Inorg. Chem.* **2009**, *48*, 3057-3064.
30. Loiseau, T.; Sere, C.; Huguenard, C.; Fink, G.; Taulelle, F.; Henry, M.; Bataille, T.; Férey, G. A. A Rationale for the Large Breathing of the Porous

Aluminum Terephthalate (MIL-53) Upon Hydration. *Chem. Eur. J.* **2004**, *10*, 1373-1382.

31. Jung, S.; McCorry, C. C.; Ferrer, I. M.; Peters, J. C.; Jaramillo, T. F. Benchmarking nanoparticulate metal oxide electrocatalysts for the alkaline water oxidation reaction. *J. Mater. Chem. A*, **2016**, *4*, 3068-3076.

32. Lobaccaro, P.; Singh, M. R.; Clark, E. L.; Kwon, Y.; Bell, A. T.; Ager, J. W. Effects of the temperature and gas-liquid mass transfer on the operation of small electrochemical cell for the quantitative evaluation of CO₂ reduction electrocatalysts. *Phys. Chem. Chem. Phys.* **2016**, *18*, 26777-26785.

33. Hori, Y. in *Modern Aspects of Electrochemistry* Vol. 42, CH. 3 (eds Vayenas, C. G., White, R. E., & Gamboa-Aldeco, M. E.) 89-189 (Springer, New York, 2008).

34. Lum, Y.; Kwon, Y.; Lobaccaro, P.; Chen, L.; Clark, E. L.; Bell, A. T.; Ager, J. W. Trace Levels of Copper in Carbon Materials Show Significant Electrochemical CO₂ Reduction Activity. *ACS Catal.* **2016**, *6*, 202–209.

35. Feaster, J. T.; Shi, C.; Cave, E. R.; Hatuskade, T.; Abram, D. N.; Kuhl, K. P.; Hahn, C. Nørskov, J. K.; Jaramillo, T. F. Understanding Selectivity for the Electrochemical Reduction of Carbon Dioxide to Formic Acid and Carbon Monoxide on Metal Electrodes. *ACS Catal.* **2017**, *7*, 4822-4827.

36. Lin, S.; Diercks, C. S.; Zhang, Y. -B.; Kornienko, N.; Nichols, E. M.; Zhao, Y.; Paris, D. Kim, A. R.; Yang, P.; Yaghi, O. M.; Chang, C. J. Covalent organic

frameworks comprising cobalt porphyrins for catalytic CO₂ reduction in water. *Science*. **2015**, *349*, 1208-1213.

37. Kornienko, N.; Zhao, Y.; Kley, C. S.; Zhu, C.; Kim, D.; Lin, S.; Chang, C. J.; Yaghi, O. M.; Yang, P. Metal-Organic Frameworks for Electrocatalytic Reduction of Carbon Dioxide. *J. Am. Chem. Soc.* **2015**, *137*, 14129-14135.

38. Noda, H.; Ikeda, S.; Oda, Y.; Imai, K.; Maeda, M.; Ito, K. Electrochemical Reduction of Carbon Dioxide at Various Metal Electrodes in Aqueous Potassium Hydrogen Carbonate Solution. *Bull. Chem. Soc. Jpn.* **1990**, *63*, 2459-2462.

39. Cheng, T.; Xiao, H.; Goddard, W. A. Reaction Mechanism for the Electrochemical Reduction of CO₂ to CO and Formate on the Cu (100) Surface at 298 K from Quantum Mechanics Free Energy Calculations with Explicit Water. *J. Am. Chem. Soc.* **2016**, *138*, 13802–13805

CHAPTER 5

INVESTIGATION OF METAL ORGANIC FRAMEWORK BY *IN SITU* X- RAY ABSORPTION SPECTROSCOPY SUGGESTS THE FORMATION OF SINGLE ATOM ACTIVE SITES UNDER ELECTROCHEMICAL CO₂ REDUCTION CONDITIONS

Part of the experiments was carried out in collaboration with Dr. Walter Drisdell from
Lawrence Berkeley National Laboratory at the Stanford Synchrotron Radiation
Lightsource in Stanford, CA, and at the Advanced Light Source in Berkeley, CA.

5.1. Abstract

We utilize *in situ* and *ex situ* x-ray absorption spectroscopy (XAS) to investigate the electrocatalyst transformation of MIL-53(Al) and MIL-53(Ga) under electrochemical CO₂ reduction. We also develop a novel *in situ* XAS methodology to determine the active form of the electrocatalyst and to investigate the chemical state and the surrounding of the catalytic site during the electrochemical CO₂ reduction. Analysis of the X-ray absorption near edge structure (XANES) and Extended X-ray absorption fine structure (EXAFS) spectra acquired under operating conditions supports the presence of Ga⁰ species within an intact MIL-53 structure. The active form of the catalyst is stable for up to 6 hours of chronoamperometry, thus suggesting that the MIL-53 framework helps stabilize the unstable Ga⁰ species. The absence of metal-metal bond, indicative of the formation of gallium nanoparticles, suggests that Ga⁰ species form under operating conditions and are still dispersed in the MOF support as stable single-atom catalysts (SACs). *Ex situ* XANES on MIL-53(Al) after electrocatalytic CO₂R also confirms the presence of Al⁰ species in a largely intact MIL-53 support. The combination of XAS measurements and product detection of these electrocatalysts demonstrates how a confined reaction space can provide unique catalytic performance and stabilize the active form of the catalyst as a single atom center.

5.2. Introduction

The utilization of carbon dioxide (CO₂) as a chemical feedstock to produce valuable carbon-based products is an effective strategy towards providing clean energy. Specifically, highly efficient and selective electrochemical reduction of CO₂ (CO₂R) to yield energy-dense fuels can decrease the atmospheric levels of CO₂, thus mitigating global warming. Extensive efforts have been devoted to developing highly active and selective electrocatalysts for this process.¹⁻³ Among reported catalysts, metal organic frameworks (MOFs) show great potential as electrocatalyst for CO₂R.⁴⁻⁷ These porous materials are composed of organic linkers and metal ions that combine the structural modularity of homogeneous catalysts and the efficiency of heterogeneous catalysts. MOFs' structural modularity enables tunable porosity and tunable interaction with specific molecules, such as CO₂. By providing a unique, confined reaction environment, MOFs have revealed their ability to change reaction selectivity and impart atypical catalytic properties to metal centers, which are different from the catalytic properties of the respective metal electrode.^{6, 7} The confined reaction space has also been shown to enhance catalytic selectivity, lifetime, and turnover number by offering stabilization of active catalysts.⁸⁻¹⁰ Similar to enzymes, MOFs can provide a microenvironment that determines a catalyst's selectivity. For example, Ranocchiari and co-workers demonstrated MOFs' ability to invert molecular reactivity on Lewis acidic phosphonium zwitterions, triphenylphosphine (PPh₃), to favor the unexpected aldol-Tischenko product.¹¹ More recently our group has demonstrated that, while aluminum metal electrodes are solely active for hydrogen

evolution reaction (HER), confining aluminum in a metal organic framework, MIL-53(Al), unexpectedly enables CO₂R.¹²

The rational design of catalytic centers with their surrounding environment with atypical activity and enhanced performance hinges on a better understanding of the chemical state and structure of active surfaces of electrocatalyst under operating conditions. These catalysts may undergo restructuring under the operating condition leading to the formation of the true active sites promoting electrochemical reactions that are different from the initial materials. For example, Wang and co-workers demonstrated that regulating nitrogen coordination environment surrounding cobalt metal centers could enhance cobalt's capability to reduce CO₂ toward CO with up to 95% FE at -0.68 V vs. RHE with Co-N₂ catalyst, unlike the Co nanoparticles that can only reduce CO₂ to CO with FE below 7%.¹³ While it is common that catalyst metal centers play a major role for catalyzing reactions, there are some cases where the catalytic metal center is inactive. A Zn-porphyrin catalyst has been reported as a highly active CO₂R electrocatalyst with the porphyrin ligand works as redox center for the CO₂R. These active forms of the catalysts are hard to probe by conventional ex-situ characterization. Advance characterizations are needed to capture the structures that only exist in intermediate reaction states and how they evolve during electrochemical reactions to understand the structure-property relationship.¹⁴ The combination of X-ray absorption spectroscopy (XAS) with electrochemistry can facilitate an improved understanding of the properties of electrocatalysts in situ.

Here, we investigate the chemical state and the surrounding of the catalytic site by *in situ* and *ex situ* XAS. In an effort to accurately reproduce the CO₂R reaction

conditions while performing XAS measurements, MIL-53(Ga), a group 13 metal center that has similar structural and functional properties to the previously studied MIL-53(Al), has been chosen an excellent model system.¹⁵ The X-ray absorption energy of the Ga K-edge is particularly suited to allow the measurement to be performed at room temperature, under atmospheric pressure, and using the electrochemical cell set up used for the electrochemical testing, consistent with the reaction condition performed in a regular electrochemical CO₂R laboratory.¹⁶ Analysis of the X-ray absorption near edge structure (XANES) and Extended X-ray absorption fine structure (EXAFS) spectra acquired under operating conditions supports the presence of Ga⁰ species within an intact MIL-53 structure. The active form of the catalyst is stable for up to 6 hours of chronoamperometry, thus suggesting that the MIL-53 framework helps stabilizes the unstable Ga⁰ species. The absence of metal-metal bond, indicative of the formation of gallium nanoparticles, suggests that Ga⁰ species form under operating conditions and are still dispersed in the MOF support as stable single atom catalysts (SACs). While the acquisition of the Al-K edge is challenging under operating conditions, ex situ XANES on MIL-53(Al) after electrocatalytic CO₂R also confirms the presence of Al⁰ species in a largely intact MIL-53 support. These results are in agreement with our previous findings, and correlate well with the Ga-MOF counterpart. These findings illustrate how a confined reaction space can provide a unique catalytic performance and stabilize the active form of the catalyst as a single atom center. We provide mechanistic understanding that can stimulate the rational design for new classes of materials as CO₂R electrocatalysts.

5.3. Catalytic activity of MIL-53(Ga) for electrocatalytic CO₂R

Briefly, MIL-53(Ga) was synthesized in a hydrothermal reactor from Ga(NO₃)₃ hydrate respectively and terephthalic acid with a slightly modified procedure from literature (see methods for full details). The final synthesized material was characterized using powder x-ray diffraction (XRD) showing highly crystalline material, with peaks at 9.4°; 12.4°; pseudo triplet with peaks at 17.5°, 17.7°, and 18.4°; and 24.9°, which are in agreement with the simulated and reported powder XRD of MIL-53(Ga) (Supplementary Figure 1).¹⁷ These peaks are also in agreement with powder XRD of MIL-53(Al) showing that these materials are structurally similar (Supplementary Figure 2). Scanning electron microscopy also showed that synthesized MIL-53(Ga) is a white powder with high crystallinity, further confirming its similarity to MIL-53(Al) (Supplementary Figure 3). Working electrodes were prepared by drop casting a MIL-53 suspension onto acid-treated carbon paper (Supplementary Figure 4, see methods for full details). Depositing MOFs onto a highly conductive and porous carbon paper provides a highly conductive pathway and improved mass transport for an increased number of active sites for catalysis.⁴ The resulting electrode has an exposed area of ~1.25 cm². To allow for X-ray to access the active area of the electrodes, the working electrodes were fabricated with kapton tape on the backside.

To assess the catalytic performance of MIL-53(Ga), cyclic voltammetry (CV) of the working electrode was performed under CO₂ atmosphere in a two-compartment flow cell (Supplementary Figure 5). While the acid treated carbon paper has no catalytic current in the potential window under study, the MIL-53(Ga) working electrode shows an electrocatalytic current. To ensure that the production of CO and

formic acid are derived from reduction of CO₂ molecules under operating condition rather than from catalyst decomposition, experiments under argon atmosphere confirmed the absence of carbon products (Supplementary Table 1). In addition, blank experiments in CO₂ atmosphere using a working electrode of acid treated carbon paper or carbon paper coated with Nafion, which is used as a binder, also resulted in no detection of carbon-based products (Supplementary Table S2, S3). Therefore, we can confirm that the MIL-53(Ga) is catalyzing the electrochemical reaction under the operating condition.

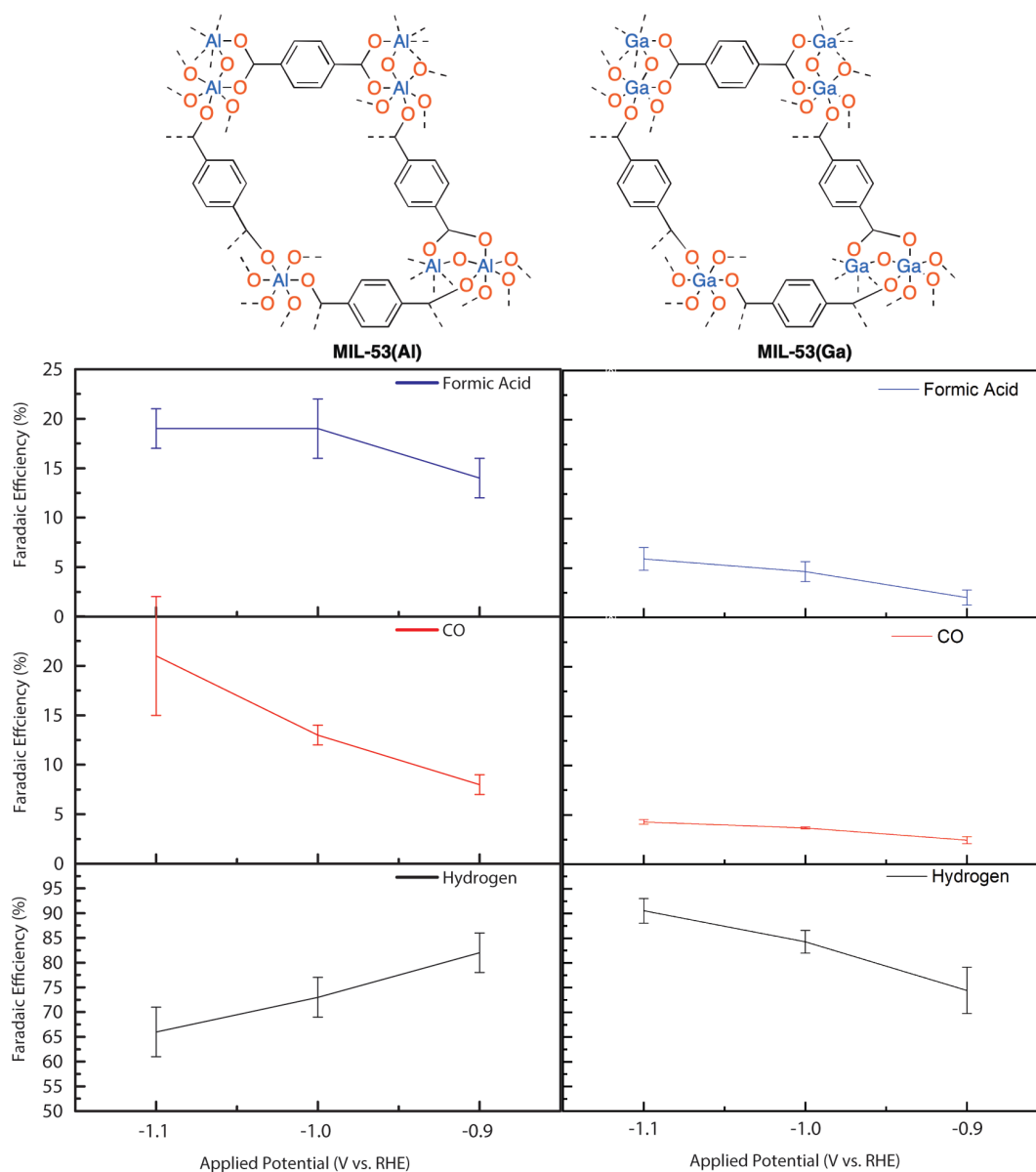


Figure 5-1. Electrocatalytic performance evaluation of MIL-53(Al) and MIL-53(Ga) as electrocatalyst for carbon dioxide reduction.

To assess the catalytic performance of MIL-53(Ga), the working electrode was tested at -1.1 V, -1.0 V, and -0.9 V vs. RHE by conducting chronoamperometry (CA) for 65 minutes at each potential (Figure 1) under CO₂R conditions. MIL-53(Ga) shows some activity toward CO₂R by producing CO and formic acid. At potential of -

0.9 V vs. RHE, MIL-53(Ga) produced 2% faradaic efficiency (FE) toward CO (Fig. 1, Table S4, S5). At a more negative potential, the CO production increases up to 4% FE. For formic acid production, MIL-53(Ga) catalyzed CO₂R toward formic acid at 2% FE at -0.9 V vs. RHE. It increased to 6% FE toward formic acid at -1.1 V vs. RHE. Comparing to Ga foil at -1.0 V vs. RHE under similar reaction condition that can only produce 6% FE toward CO, Ga as metal center in MIL-53 framework shows some CO₂R activity improvement. Comparing to MIL-53(Al), Ga metal center in MIL-53 framework is not as active as Al metal center. At -1.1 V vs. RHE, MIL-53(Al) can produce up to 21% FE toward CO and 19% FE toward formic acid (Figure 1).¹² To provide further insights into the catalytic performance of MIL-53(Ga), we evaluated electrocatalytic activity by calculating the turnover frequency (TOF) for carbon-based products, CO and formic acid (Table S6). At -0.9 V vs. RHE, we observed a combined TOF of 11.2 h⁻¹. At -1.0 V vs. RHE, the combined TOF increases to 31 h⁻¹, a 2.5 fold increased. Finally, at -1.1 V vs. RHE, the combined TOF reaches up to 52.3 h⁻¹. This result further confirm that MIL-53(Ga) is less active compared to MIL-53(Al) that has combined TOF of 182 h⁻¹ at -1.1 V vs. RHE.¹²

The activity for CO₂R of MIL-53(Ga) is lower than MIL-53(Al) and it may be explained by the more oxophilic character of Al with respect to Ga.¹⁸ Specifically, this oxophilicity may result in less interaction between CO₂ molecules with a Ga metal center that yields low production of carbon-based products from CO₂R. Despite the different activity, these two compounds give the same type of products, and have a very similar structure. In addition, the energy of the Ga-K edge is suitable for performing in situ measurements that are compatible with the CO₂R conditions, which

involve room temperature, atmospheric pressure, and ability to continuously purge the solution with CO₂.¹⁶ In situ XAS on MIL-53(Al) will require soft X-rays operating in an ultra-high vacuum chamber with a special electrochemical cell with a different configuration to the that used in a regular electrochemical CO₂R laboratory.¹⁹⁻²⁰ To accurately observe the catalytic behavior of the metal center in MIL-53 organic framework, it is critical to maintain catalytic environments during in situ measurements that are consistent with the catalytic environments used for standard product distribution measurements and performance testing.²¹ Studying MIL-53(Ga) with in situ XAS will enable us to observe MIL-53(Ga)'s catalytic behavior while maintaining these consistent chemical conditions. Furthermore, since the in situ XAS cell is similar in design to the standard electrochemical cells used for testing, product distributions and Faradaic efficiencies can be easily and directly compared between the two. Therefore, in order to understand the changes of and around the catalytic sites under operando conditions, MIL-53(Ga) can be used as a model system to predict changes in the Al system.

5.4. XANES of MIL-53(Ga) under Electrochemical CO₂R conditions

MIL-53(Ga) was used to perform the in situ XAS measurement using two-compartment flow cell with electrolytes in atmospheric pressure and at room temperature. XAS data were collected using a setup in figure 2a. We modified our two-compartment flow cell (Supplementary Figure 5) by adding a window on the back plate on the cathode sides to allow for x-ray to flow in and out (Fig. 2a, Supplementary Figure 6). We also modified the working electrode fabrication (Figure S4) to allow X-rays to be back reflected (Supplementary Figure 7).

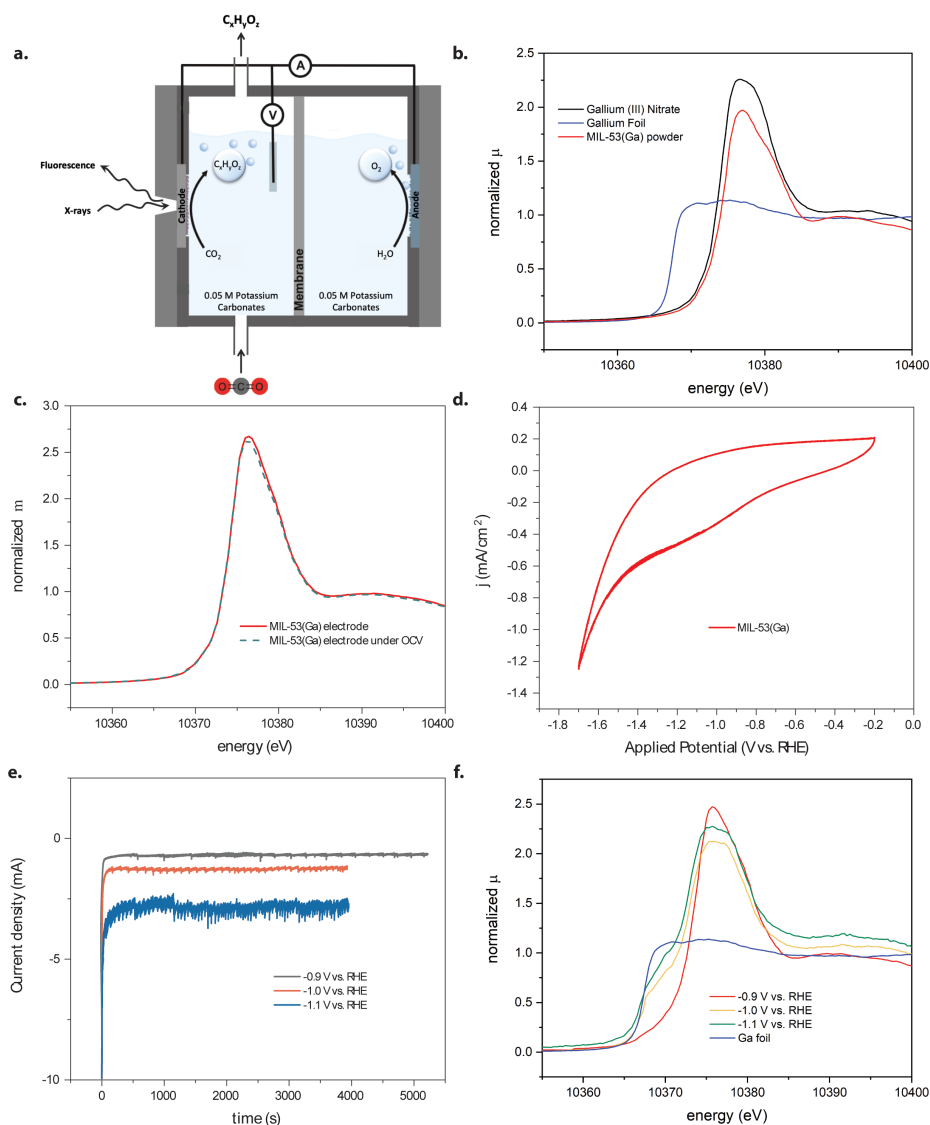


Figure 5-2. a.) In situ XAS setup with the back plate of the kapton window for the cathode facing the x-rays and the cathode is fabricated working electrode with MIL-53(Ga) in CO₂-saturated 0.05 M potassium carbonates (pH=6.8). b.) Ex situ x-ray absorption near edge structures (XANES) were performed on synthesized MIL-53(Ga) powder (orange), gallium (III) nitrate powder (blue), and gallium foil (pink) confirming that only Ga³⁺ species is present in the synthesized MIL-53(Ga). c.) XANES for working electrode in air is compared to XANES for working electrode under OCP for 8 minutes, MIL-53(Ga) working electrode in air (blue) and MIL-53(Ga) working electrode under OCP (orange). d.) Cyclic voltammetry of the MIL-53(Ga) performed in in situ XAS setup. e.) chronoamperometry at three different potentials starting from -1.1 V to -0.9 V vs. RHE for 65 minutes each in the in situ XAS setup. f.) In situ XANES measurements of MIL-53(Ga) working electrode in CO₂-saturated 0.05 M of potassium carbonates at three different applied potentials starting from -0.9 V vs RHE to -1.1 V vs. RHE for 65 minutes each. Gallium foil is used for reference.

First, ex-situ XANES for the synthesized MIL-53(Ga) was compared to gallium (III) nitrate and gallium foil as reference for Ga^{3+} and Ga^0 species, respectively (Fig. 2b). The position of the Ga-K edge in MIL-53(Ga) is consistent with gallium (III) nitrate at 10377 eV, thus confirming that the gallium species in MIL-53(Ga) corresponds to Ga^{3+} . On the other hand, the absence of a peak centered at 13750 eV, supportive of the presence of Ga^0 , further confirms that there is no Ga^0 species in MIL-53(Ga) before electrochemical testing. To investigate changes induced by the interaction with MIL-53(Ga) with the electrolyte (CO_2 -saturated 0.05 M potassium carbonate), in situ XANES was performed on the MIL-53(Ga) electrode under open circuit potential (OCP). Compared to the ex situ spectrum, in situ XANES of MIL-53(Ga) overlaps with that one of the dry MIL-53(Ga) electrode (Fig. 2c). This control experiment was also performed to ensure that the change in oxidation state of metal center in MOFs is a result of electrochemical reaction.

Prior to collecting in situ XAS measurements, cyclic voltammetry (CV) characterization of the catalyst was performed (Fig. 2a, Supplementary Figure 6). The resulting CV behavior (Fig. 2d) is similar to the CV behavior obtained under standard laboratory conditions used in evaluating electrocatalytic performance of MIL-53(Ga) (Fig. 1). To acquire operando XAS data, chronoamperometry (CA) was performed at -1.1 V, -1.0 V, and -0.9 V vs. RHE where MIL-53(Ga) showed catalytic activity for 65 minutes each. The CA shows that the current is stable over time and similar to the CA obtained in standard laboratory conditions used in evaluating electrocatalytic performance of MIL-53(Ga) (Fig. 2e). Additionally, product detection was performed using the modified cell used for in situ XAS measurement (Fig. 2a, Supplementary

Figure 6, and Supplementary Table S7, S8), showing product distributions consistent with the unmodified cell (Supplementary Figure 5).

Under operando conditions, at reducing potentials it is possible to appreciate a peak splitting and broadening at 10377 eV indicating a reduction of the Ga oxidation state (Fig. 2f). This result suggests that the active form of MIL-53(Ga) involves a reduction of the Ga center, as supported by the appearance of an additional peak centered at 10375 eV and a broad shoulder between 10367 and 10371 eV. These peaks are consistent with the both presence of Ga^{3+} and a more reduced Ga species in the MIL-53 framework. We suspect that the more reduced Ga species is Ga^0 , as Ga does not typically adopt oxidation states between Ga^0 and Ga^{3+} , and the shoulder between 10367 and 10371 eV is aligned with the Ga foil reference spectrum. This result suggests that the active form the catalyst involves Ga^0 species. The involvement of Ga^0 species is further confirmed by the strengthen shoulder feature that is consistent with the Ga^0 from Ga foil reference. In addition, another set of CA at the same three potentials was performed on the same MIL-53(Ga) electrode (Supplementary Figure 8). In this case, observable changes in the oxidation state are negligible. This finding indicates that under operating conditions the initial MIL-53(Ga) undergoes an irreversible change and the active form of the catalyst stabilizes Ga^{3+} and Ga^0 species. While Ga^0 is unstable in air,²² XANES measurement in air on the MIL-53(Ga) electrode after 6 hours of electrochemical testing still show the presence of Ga^0 species, thus further confirming that the confined reaction space provided by MIL-53 frameworks help stabilize the unstable Ga(0) species.

Control experiments were performed to ensure that the oxidation state changes are

from electrochemical activity, rather than beam damage. First, a beam damage test with Ga-MOF electrode in CO₂-saturated 0.05 M potassium carbonates was performed where the electrode was exposed to the beam for 8 scans with 8 minutes exposure per scan (Supplementary Figure 9). We observed that the peak stays at 10377 eV without any peak splitting and broadening confirming that the observed oxidation change in Ga is coming from the applied potential under the reaction condition. Then, at each applied potential, the previous and following scan for XANES measurements are similar showing that the changes in Ga oxidation state is a result of electrochemical activity instead of from beam damage (Supplementary Figure 9). After 6 hours of CA at three different potentials and in situ XANES measurements, we took measurement at an area that had not received beam exposure (Supplementary Figure 10). Comparing to the area exposed to x-ray for 6 hours, the area that had not received any x-ray exposure shows the same peak splitting/feature corroborating our findings that the oxidation state changes caused by electrochemical activity.

5.5. Ex Situ XAS MIL-53(Al)

These findings on MIL-53(Ga) are in agreement with previous results on MIL-53(Al).¹² Specifically, we have reported that X-ray photoelectron spectroscopy (XPS) shows the presence of a 1:1 Al⁰/Al³⁺ on MIL-53(Al) electrodes after electrochemical CO₂R, without no obvious degradation of the MIL-53 framework. Operando measurements on the Al-K edge are challenging and require completely different testing conditions with respect to the conventional CO₂R measurements. It requires the measurements to be done in an ultra-high vacuum chamber with a special cell that

has different configuration to the cell used in a regular electrochemical CO₂R lab.^{20, 23} Therefore, to further confirm previous results and gain more insights on the local structure of the catalyst, in this work, we have performed ex situ XANES on the synthesized MIL-53(Al) powder and on the working electrode before and after electrochemical testing (Fig. 3). Ex-situ XANES measurements on the synthesized MIL-53(Al) powder and on the working electrode before electrochemical testing confirm the presence of Al³⁺ species in MIL-53(Al). The comparison of the working electrode before and after electrochemical testing highlights a peak shift and broadening consistent with the presence of more reduced species of Al within the MIL-53 framework.¹⁶ This result is in agreement with previous XPS findings.¹² Additionally, the XANES spectra for the electrode after electrochemical testing are similar in shape to the XANES spectra for the electrode before electrochemical testing. This observation further confirms our previous finding that the metal organic framework is largely intact. Through this ex situ XANES, we also gain more information about the possibility of change in the organic framework to accommodate the electroreduction of CO₂. The shifted XANES peak on Al usually indicated changes the geometry from octahedral to square pyramidal.²⁴

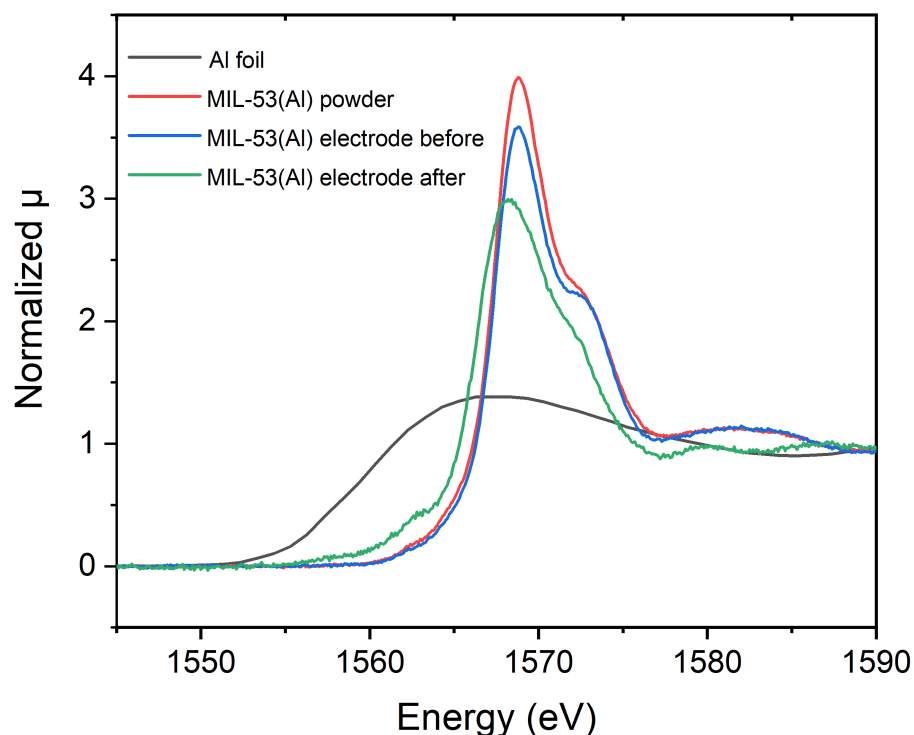


Figure 5-3. Ex situ XANES for MIL-53(Al).

5.6. In Situ EXAFS

To gain more information about the local environment surrounding Ga metal centers in MIL-53 frameworks, we have analyzed the EXAFS spectra of MIL-53(Ga) before and after electrochemical testing (Fig. 4, Supplementary Figure 11, and Supplementary Table S9). The EXAFS spectra of MIL-53(Ga) before electrochemical testing remains similar to the EXAFS spectra of MIL-53(Ga) after 6 hours electrochemical. This result suggests that the local environment surrounding Ga metal center remains similar. It further demonstrates that changes in the organic framework surrounding Ga metal center are negligible despite the presence of Ga^0 species.

As expected, the EXAFS for MIL-53(Ga) after electrochemical testing shows the strongest peak at 1.4 Å consistent with Ga-O bond further confirming that the organic framework surrounding Ga metal center remains similar.¹⁸ Additionally, comparing to EXAFS for MIL-53(Ga) before electrochemical testing, the EXAFS spectra for MIL-53(Ga) after electrochemical testing does not show a stronger peak around 2.48 Å that would suggest the formation of Ga nanoparticle.²⁵ These results demonstrate that there is no Ga nanoparticle formation. These observations further demonstrate that the MIL-53 framework help stabilize the active form of the catalyst that involve Ga⁰ species by preventing aggregation of Ga nanoparticles. These observations are further supported by comparing the SEM-EDX mapping of Ga on the surface of working electrodes before and after 6 hours of electrochemical testing (Supplementary Figure 12). The SEM-EDX mapping of the surface of working electrode after electrochemical testing shows that Ga is still present and evenly distributed on the surface of working electrode.

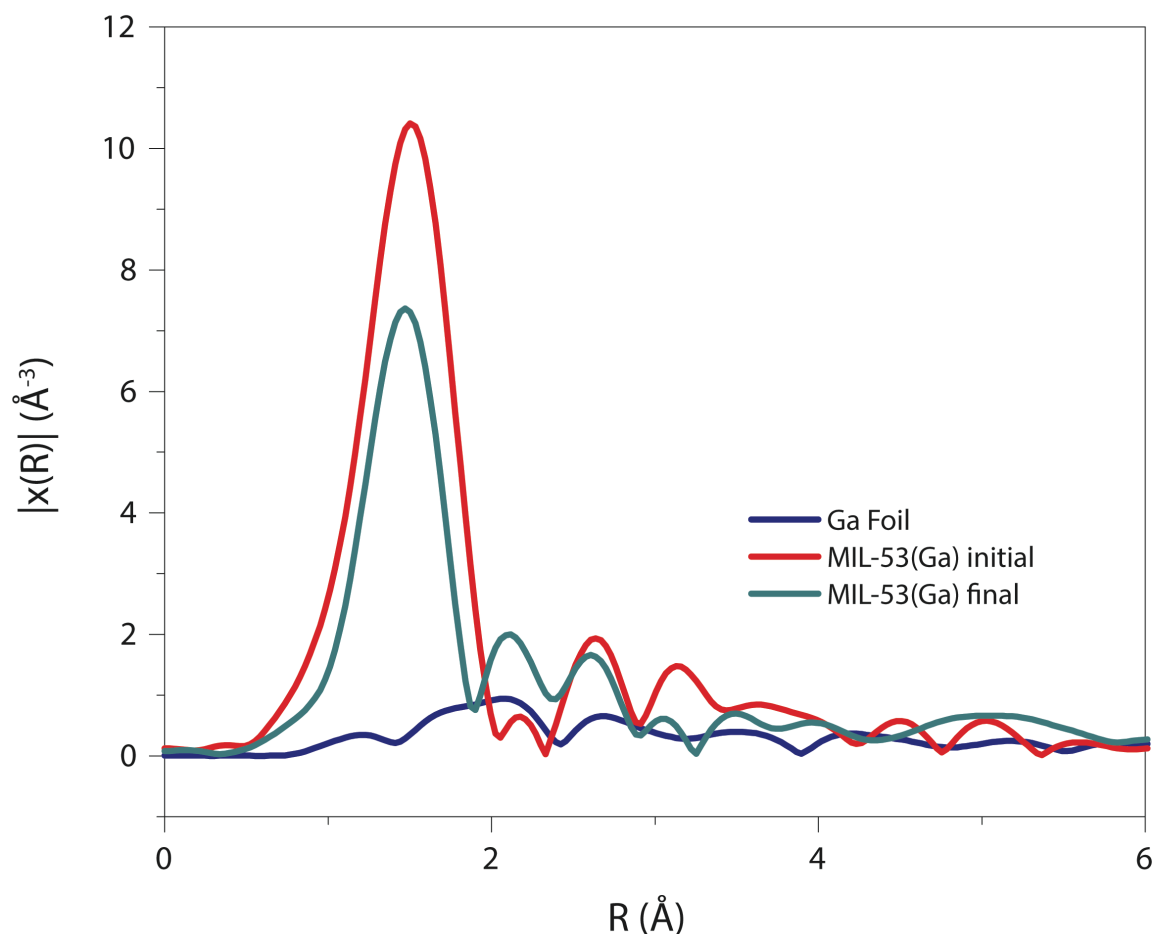


Figure 5-4. R-space of EXAFS measurement and fitting of Ga foil, MIL-53(Ga) working electrode before and after electrochemical testing.

5.7. Possible In Situ Formation of Single Atom Catalyst

Supported metal nanoclusters are widely used heterogeneous catalysts in industry because of its catalytic performance. The size of metal particle is important in determining the performance of catalyst. The activity of the catalyst usually increases with decreasing size of the metal particles. Single atom catalyst (SAC) is a promising catalyst that contains only isolated single atoms dispersed on support to maximize the efficiency of metal atom use and further have potential in achieving highly selectivity

and activity.²⁶ This catalyst is an important direction in the field of electrochemical CO₂R because it will enable us tackle the grand challenge in the field, which is an affordable, highly active, and selective catalyst.²⁷ However, the surface free energy of metals increases with decreasing particle size promoting self-aggregation within the metals making the formation of stable SAC hard.²⁶ The absence of self-aggregation within Al and Ga metal on MIL-53(Al) and MIL-53(Ga) respectively through SEM-EDX mapping led us to suspect the possibility of in situ formation of SACs in these MOFs under the reaction condition. MIL-53 framework seems to be the appropriate support that strongly interacts with the metal species to prevent aggregation. The presence of Al⁰ and Ga⁰ species that are unstable in air and under the reaction condition in both MOFs also further suggests that MIL-53 framework helps creating a stable and finely disperse metal clusters that can be defined as SACs.

In situ XANES on MIL-53(Ga) shows the transformation of MIL-53(Ga) precatalyst only containing Ga³⁺ species to the active form of the catalyst containing more reduced species of Ga. This result shows that MIL-53 MOFs requires activation of the support to promote its activity toward CO₂R. The EXAFS also shows that the coordination number (CN) for oxygen to the metal center reduced from CN=6 to CN=5 after electrochemical testing. This result suggests that the activation of MIL-53 framework of support promote the creation of vacancies adjacent to the metal atoms. These vacancies may lead to superior performance of Al as metal center in MIL-53 framework in reducing CO₂ to valuable carbon-based products compared to Al foil that is lacking these vacancies for strong interaction with CO₂ molecules.

5.8. Conclusion

In conclusion, we demonstrate that MIL-53(Al) as electrocatalyst for CO₂ reduction undergo catalytic transformation to their catalytic active form that involves Al⁰ species under the operating condition. Through ex-situ XAS of the MIL-53(Al), we also observe that the MIL-53 framework remains intact with the possibility of change in the organic framework geometry to accommodate the electroreduction of CO₂ molecules. Using MIL-53(Ga) that has similar structural and functional properties to MIL-53(Al) and allows for the XAS measurement to be performed in the ambient environment, we are able to accurately observe the catalytic transformation observed in MIL-53(Al) under the operating condition. Analysis of in situ XANES and EXAFS acquired under the CO₂R operating condition confirm the presence of Ga⁰ species within an intact MIL-53 structure and show that the MIL-53 framework helps stabilize the unstable Ga⁰ species. Furthermore, we present possible mechanism of the catalytic transformation of the metal centers in the MOFs that impart CO₂R capability to Al and Ga metals that are only active toward HER. Our findings provide new design strategies for the synthesis of novel electrocatalysts for CO₂R using metals that traditionally favor HER.

5.9. Experimental Procedures

5.9.1. Materials

Anhydrous N,N-Dimethylformamide (DMF) (99.8%), nitric acid (70%), gallium (III) nitrate hydrate ($\text{Ga}(\text{NO}_3)_3 \cdot x\text{H}_2\text{O}$) (99%), terephthalic acid (98%), Nafion 117 solution, 2,2,2-trifluoroethanol, and high purity potassium carbonate (99.995%) were purchased from Sigma Aldrich. Hydrochloric acid (36.5 – 38%) was purchased from VWR. Isopropyl alcohol (100%) was purchased from KMG electronic chemicals. Water used for all of the synthesis and electrochemical experiments (MilliQ water) was from a Milli-Q Water Purification System (resistivity of 18.2 M Ω -cm, Millipore). Selemion AMV anion-exchange membrane was purchased from AGC Engineering Co., LTD. Carbon paper (Sigracet 29BC) was purchased from Fuel Cell Store. Carbon dioxide (99.995%) and nitrogen (99.999%) were obtained from Praxair.

5.9.2. MIL-53(Ga) Synthesis

MIL-53(Ga) was synthesized with a slightly modified procedure already present in the literature.^{17, 28} In a fume hood, a 22 mL Teflon reactor was charged with $\text{Ga}(\text{NO}_3)_3 \cdot x\text{H}_2\text{O}$ (2.05 g, 8 mmol). 20 mL of MilliQ water were carefully added. After all the HCl evolved from the hydrolysis was removed, terephthalic acid (TA, 1.38 g, 8 mmol) was added. The Teflon reactor was sealed and placed in a stainless steel autoclave reactor. The reactor was heated in a preheated oven (150 °C) for 24 hours. The reactor was then allowed to cool down to room temperature before filtering the reaction mixture to obtain a white gel via Buchner filtration. The white gel was added into a 50 mL centrifuge tube. MilliQ water (~30 mL) was added into the centrifuge

tube. It was centrifuged for 20 minutes (Eppendorf centrifuge 5804). The supernatant was disposed to remove the unreacted $\text{Ga}(\text{NO}_3)_3$. The white gel was washed again several times using this centrifuge method. The washed white gel was briefly dried in a preheated BINDER oven ($90\text{ }^\circ\text{C}$) for 1 hour before it was suspended in DMF ($\sim 15\text{ mL}$) in a 22 mL Teflon reactor. The Teflon reactor was sealed and placed in a stainless steel autoclave reactor. The reactor was put in preheated sand bath ($145\text{ }^\circ\text{C}$) for 18 hours to remove any unreacted TA that may be trapped in the porous cavity of the MOF.²⁹ The reactor was then allowed to cool down to room temperature before filtering the reaction mixture to obtain a white solid via Buchner filtration. The white solid was washed several times with isopropyl alcohol (IPA) by centrifugation to replace DMF that may be coordinated to the MOF. The supernatant was removed, leaving a white solid. The white solid was dried in a Lindberg Blue M vacuum oven from Thermo Fisher Scientific at $140\text{ }^\circ\text{C}$ and 10 mmHg for 18 hours to remove the remaining DMF and IPA.

5.9.3. Preparation of Carbon Paper

Carbon paper (Sigracet 29BC) was cut into $\sim 1.3\text{ cm} \times \sim 1.3\text{ cm}$ squares. The cut carbon paper was immersed in 70% nitric acid for 15 minutes to remove metallic impurities that may be present in the fibers.³⁰ The carbon paper was then washed with MilliQ water and air-dried for 18 hours.

5.9.4. Preparation of MIL-53(Ga) Suspension

In a fume hood, a 20 mL scintillation vial was charged with MIL-53(Ga) (30 mg, 0.031 mmol). MilliQ water (3.8 mL) and IPA (1.0 mL) were added. Nafion 117 solution (40 μ L) was added. The vial was sealed and sonicated for 30 minutes at room temperature to make a homogeneous suspension. The suspension (40 μ L) and trifluoroethanol (40 μ L) were added to a 2.0 mL microcentrifuge tube. Trifluoroethanol was added to allow the MIL-53(Ga) suspension to permeate inside the fiber of carbon paper, which is coated with Teflon and highly hydrophobic.³¹ The microcentrifuge tube was vortexed for 30 seconds to make the final MIL-53(Ga) suspension homogeneous.

5.9.5. Preparation of Fabricated Working Electrodes¹²

The final suspension (40 μ L, 0.124 mg of powder) was deposited onto the prepared carbon paper electrodes. The electrode was then dried in a preheated BINDER oven (90 °C) for 18 hours. The back of the electrode was insulated with electroplating tape. The front was contacted with a piece of copper tape, and then covered with a second piece of electroplating tape with a round hole with diameter \sim 1.26 cm. This configuration would insulate the Cu tape as well as provide a precise exposed area of 1.25 cm².

5.9.6. Electrolyte preparation

Potassium carbonate solution (0.05M) was prepared from high purity potassium carbonate (99.995%, Sigma Aldrich) and water from a Milli-Q Water Purification

System (resistivity of 18.2 MΩ-cm, Millipore).

5.9.7. Product detection

Electrochemical experiments were conducted in a two-compartment flow cell fabricated from PEEK following a reported design (Figure S5).³² A Selemion AMV anion-exchange membrane separated the two chambers. A Pt foil was used as the counter electrode. A Leak-Free Ag/AgCl electrode (LF-1, 1.0 mm outer diameter, Innovative Instruments, Inc.) was used as the reference electrode. The reference electrode was calibrated against a second reference electrode, which in turn was calibrated in a two-electrode system with H₂ bubbled over a Pt wire as the counter electrode and a 1M H₂SO₄ solution as the electrolyte. The applied potentials were converted from Ag/AgCl scale to the RHE scale via the equation: $E_{\text{RHE}} = E_{\text{Ag/AgCl}} + 0.197 + 0.059 \cdot \text{pH}$, where the pH used is the bulk pH for the CO₂-saturated electrolyte (6.8). In the electrochemical cell, the prepared 0.05 M potassium carbonate solution was used as electrolyte. The electrolyte was saturated with a continuous flow of 5 sccm CO₂ for a minimum of 30 minutes within the experimental cell setup immediately prior to all electrochemical experiments. One cycle of chronoamperometric (CA) measurement was performed by applying a constant potential for 65 minutes. One cycle of CA at -1.5 V vs Ag/AgCl was performed before data collection was started. Electrochemical experiments were carried out using SP-200 potentiostat from BioLogic. Cyclic voltammetry (CV) was then performed and repeated at the end of each run, in order to test the stability of material before and after the chronoamperometric measurement. Chronoamperometric measurement was

performed for about 65 minutes. Gas products were quantified using gas chromatography (GC), multiple gas analyzer #5 from SRI Instruments, through a flow mode. Liquid products were quantified after electrochemical measurement using high performance liquid chromatography (HPLC), UltiMate 3000. During the chronoamperometric measurement, gas from the cell was directed through the sampling loop of a gas chromatograph with molecular sieves columns (MOL 5A-Agilent) and was analyzed in 15 minutes intervals. For each interval, concentration of gas produced was collected. With total current density measured at the end of experiment and applied potential, faradaic efficiency for each gas for each interval was calculated. These recorded faradaic efficiencies were averaged and reported.

5.9.8. Materials characterization techniques.

Powder X-ray diffraction (PXRD) patterns were acquired with a Rigaku-SmartLab diffractometer using Cu K α ($\lambda=0.15406$ nm).

Scanning electron microscopy images of synthesized powder of MIL-53(Ga) and electrode before electrochemical testing were acquired with a Zeiss Gemini Supra 55 VP-SEM. Additionally, scanning electron microscopy images of MIL-53(Ga) electrode after electrochemical testing were acquired with a FEI Quanta FEG250.

X-ray Photoelectron Spectroscopy (XPS) was performed using a monochromatized Al K α source ($h\nu=1486.6$ eV), operated at 225 W, on a Kratos Axis Ultra DLD system at a takeoff angle of 0° relative to the surface normal and a pass energy for the narrow scan core level and valence band spectra of 20 eV to observe the electronic state of the elements within the material. Spectral fitting was conducted

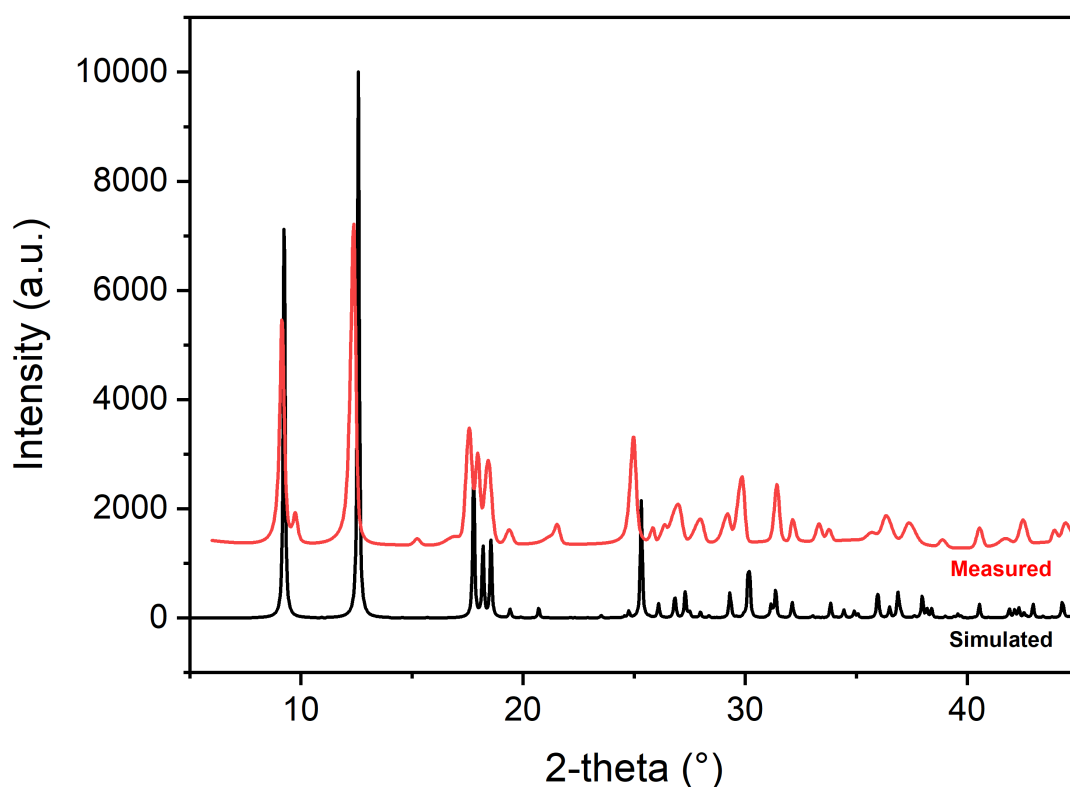
using Casa XPS analysis software. Spectral positions were corrected using adventitious carbon by shifting the C 1s core level position to 284.8 eV and curves were fit with quasi-Voigt lines following Shirley background subtraction.

In Situ and Ex Situ Ga K-edge XAS. X-ray adsorption spectroscopy was conducted on beamline 9-3 at Stanford Synchrotron Radiation Lightsource. The radiation was monochromatized by Si (111) double-crystal monochromator. The spectra were collected in fluorescence mode with a 100-element Ge monolith solid-state detector. All the 100 element spectra were initially averaged in Sixpack software. Data processing and analysis were performed using Athena and Artemis programs of the IFEFFIT data analysis package.³³⁻³⁴ The spectra were calibrated with Ga foil reference. The normalized spectra were from pre-edge and post-edge line subtraction followed by the step-edge normalization. Background removal was conducted using Athena to obtain $\chi(k)$ (where k is the photoelectron wavenumber). FEFF6 code was used to construct the theoretical EXAFS for the considered scattering paths. The EXAFS fitting was conducted using Artemis in r -space. The r -range for the fitting and the k -range for Fourier Transform of the $\chi(k)$ were 0 – 6 Å and 2.5 – 9.1 Å⁻¹, respectively.

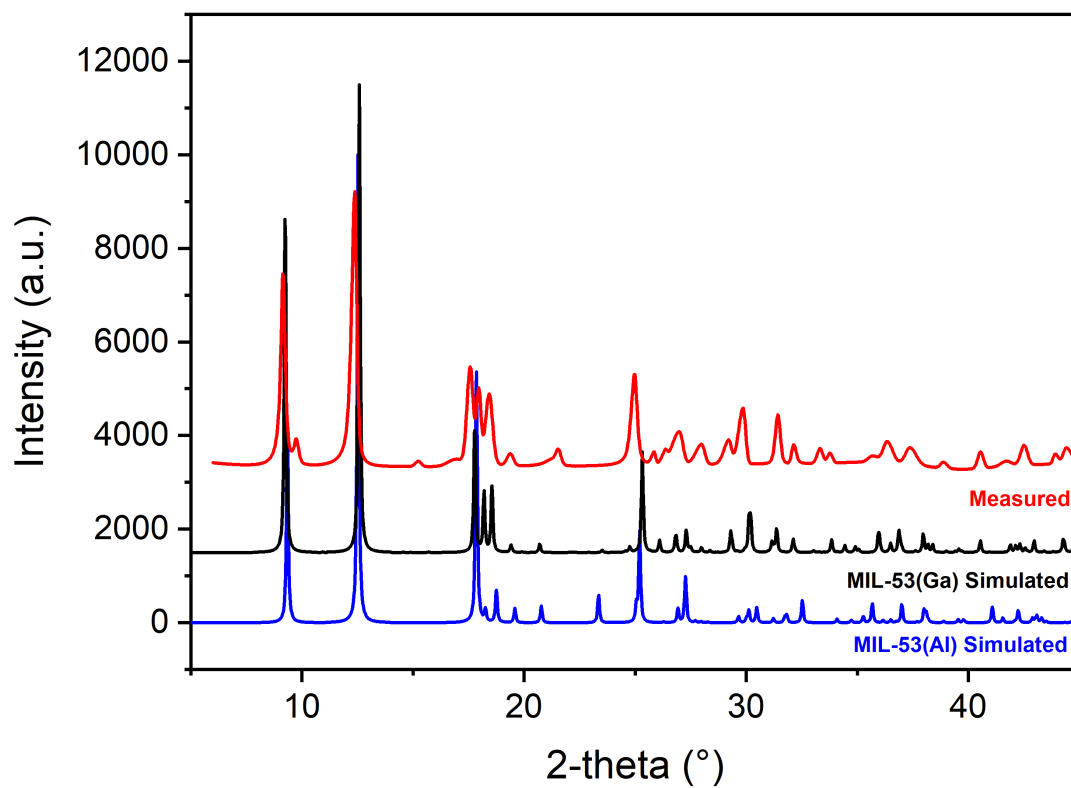
Ex situ Al K-edge XAS. Al K-edge XAS data was collected at beamline 6.3.1 at the Advanced Light Source (ALS) at Lawrence Berkeley National Laboratory. This bending magnet beamline delivers X-rays between 200 and 2000 eV, using a variable line spacing plane grating monochromator (VLS-PGM, 1200 l/s) to select the energy with a resolution of $E/\Delta E \approx 2000$. Data were collected in “fast scanning” mode by continuously scanning the monochromator. The photon flux was on the order of 10^{10}

photons/sec/0.1%BW. The ALS ring operated at 1.9 GeV with an average ring current of 500 mA (in top-off mode). Measured samples were at room temperature and under high vacuum of 10^{-9} Torr. Signal was collected as total electron yield (TEY) measured as replacement current. Data was analyzed using the Athena program from the IFEFFIT data analysis package. Spectra were calibrated using the transmission-absorption spectrum of an upstream Al foil filter, and subjected to pre-edge baseline subtraction followed by edge-step normalization.

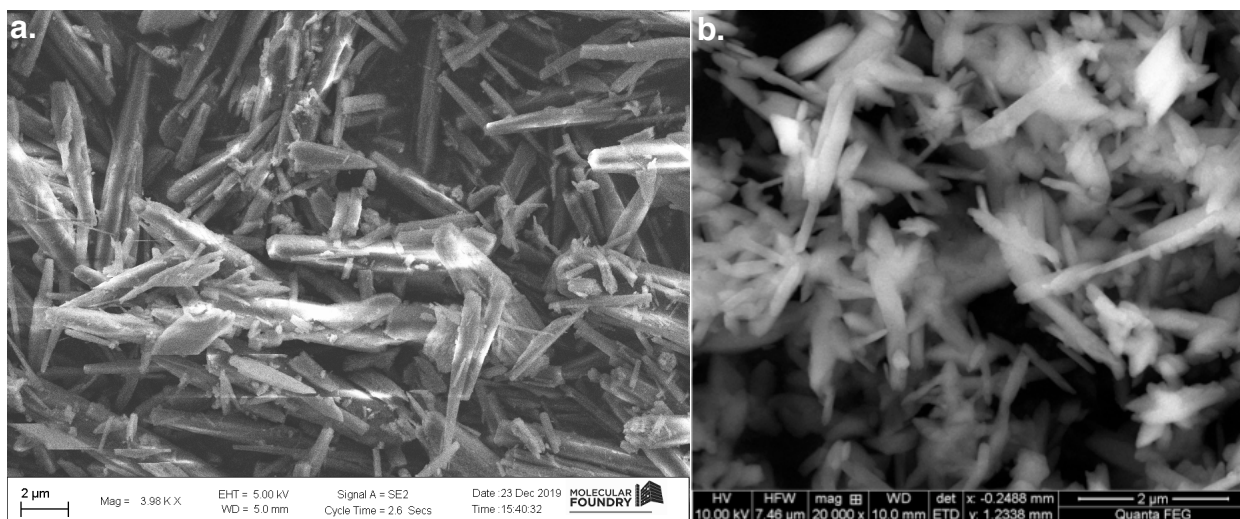
5.10. Supplementary Figures



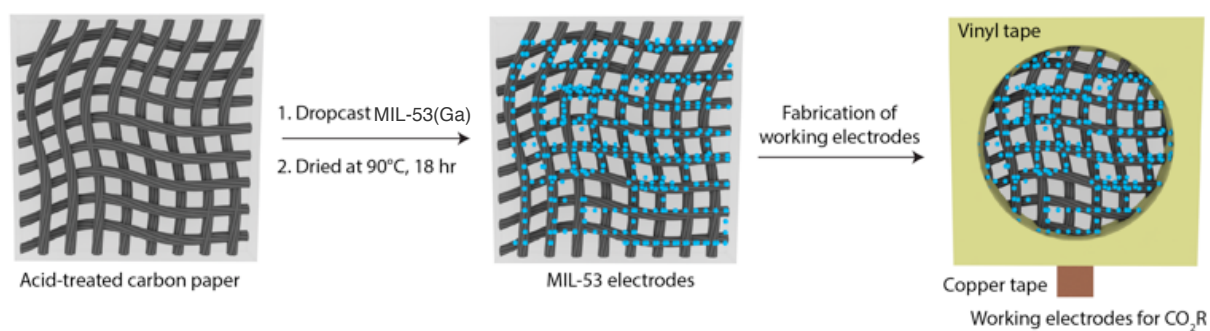
Supplementary Figure 5-1. Powder x-ray diffraction (XRD) of the synthesized MIL-53(Ga) showing experimental (red pattern) and simulated (black pattern).³⁶



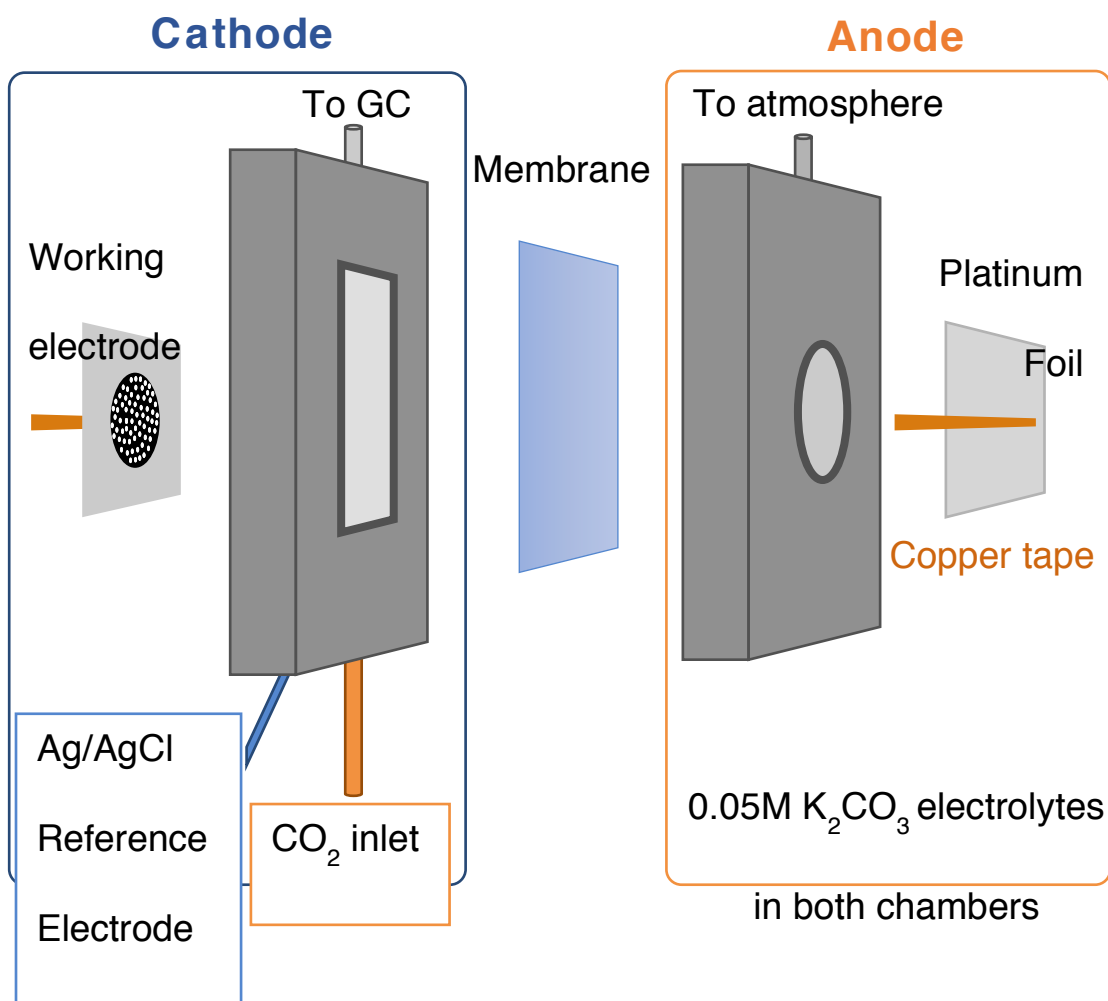
Supplementary Figure 5-2. Similarities in powder x-ray diffraction (XRD) of synthesized MIL-53(Ga) (experimental (red pattern) and simulated (black pattern)) with powder XRD of simulated MIL-53(Al).^{35,36}



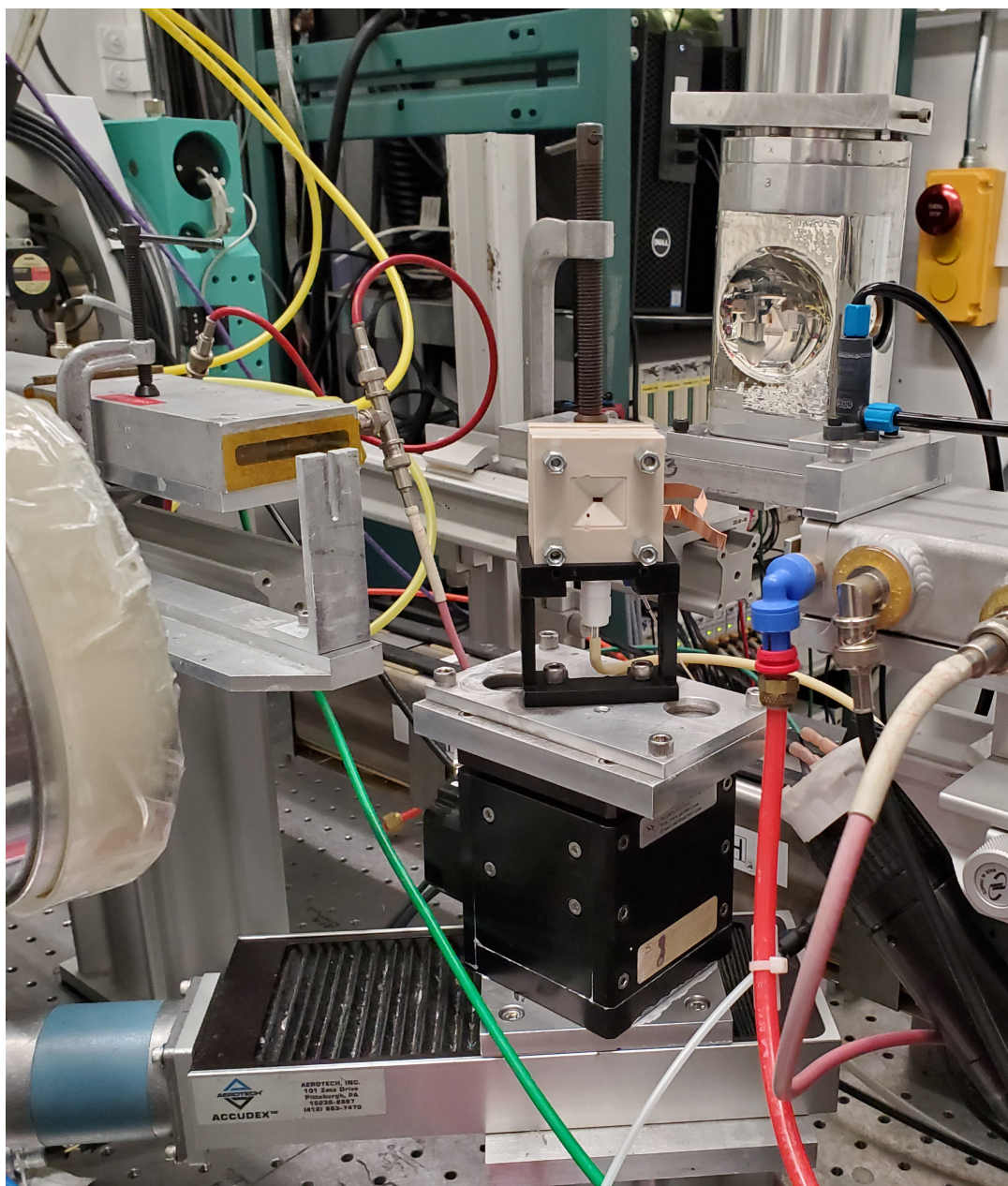
Supplementary Figure 5-3. Scanning electron microscope (SEM) imaging of: a.) MIL-53(Ga) b.) MIL-53(Al)



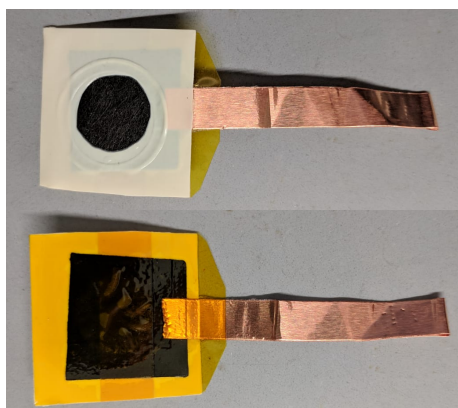
Supplementary Figure 5-4. Scheme to fabricate working electrodes.¹²



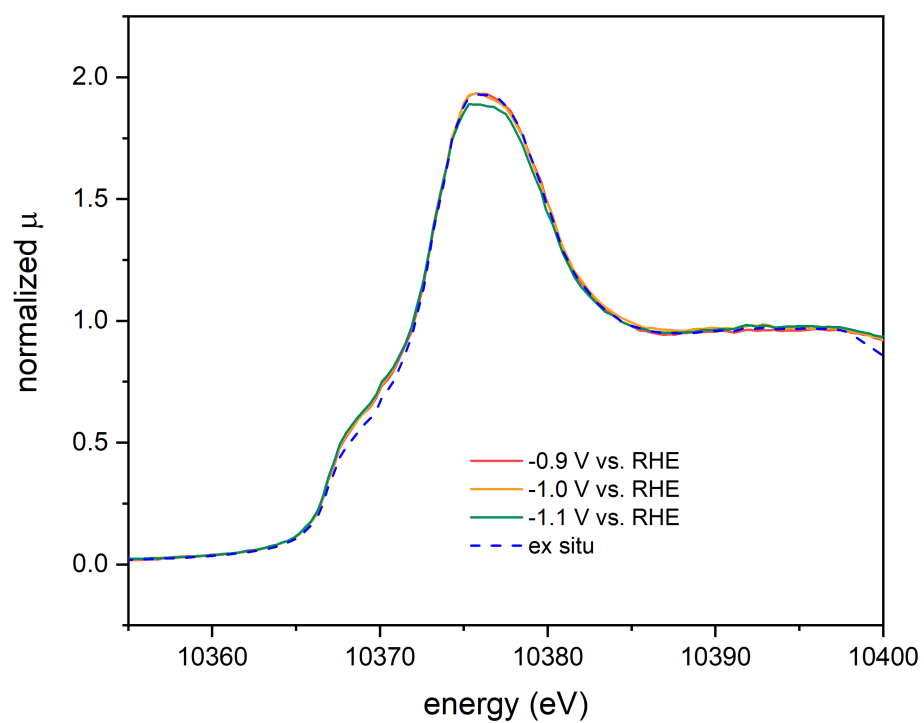
Supplementary Figure 5-5. Two-compartment flow cell used for electroreduction of carbon dioxide.



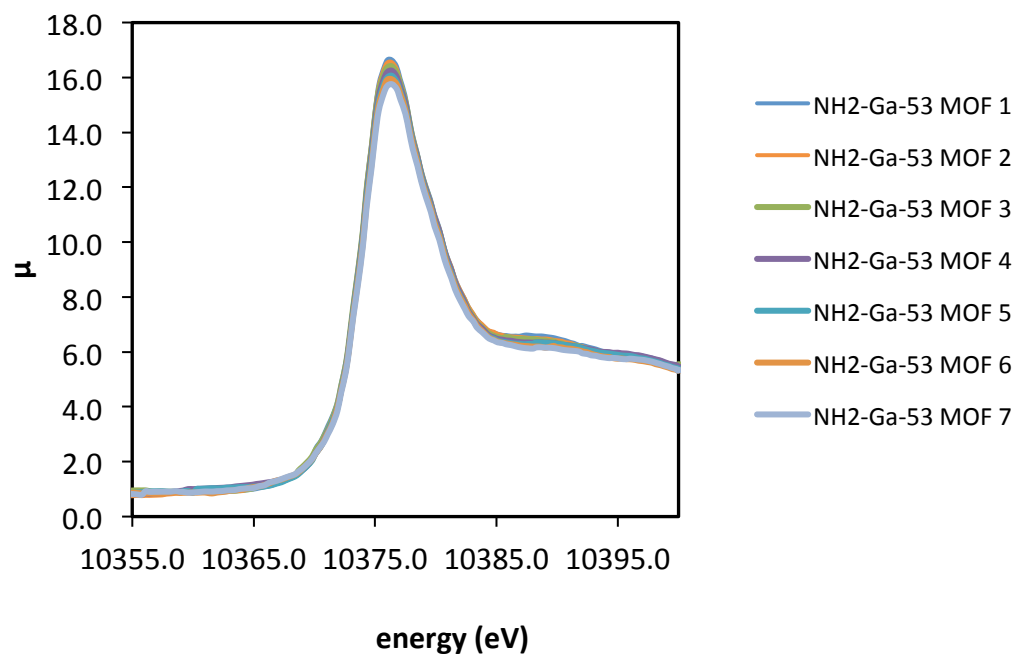
Supplementary Figure 5-6. In situ XAS setup in beamline 9-3 at Stanford Synchrotron Radiation Lightsource.



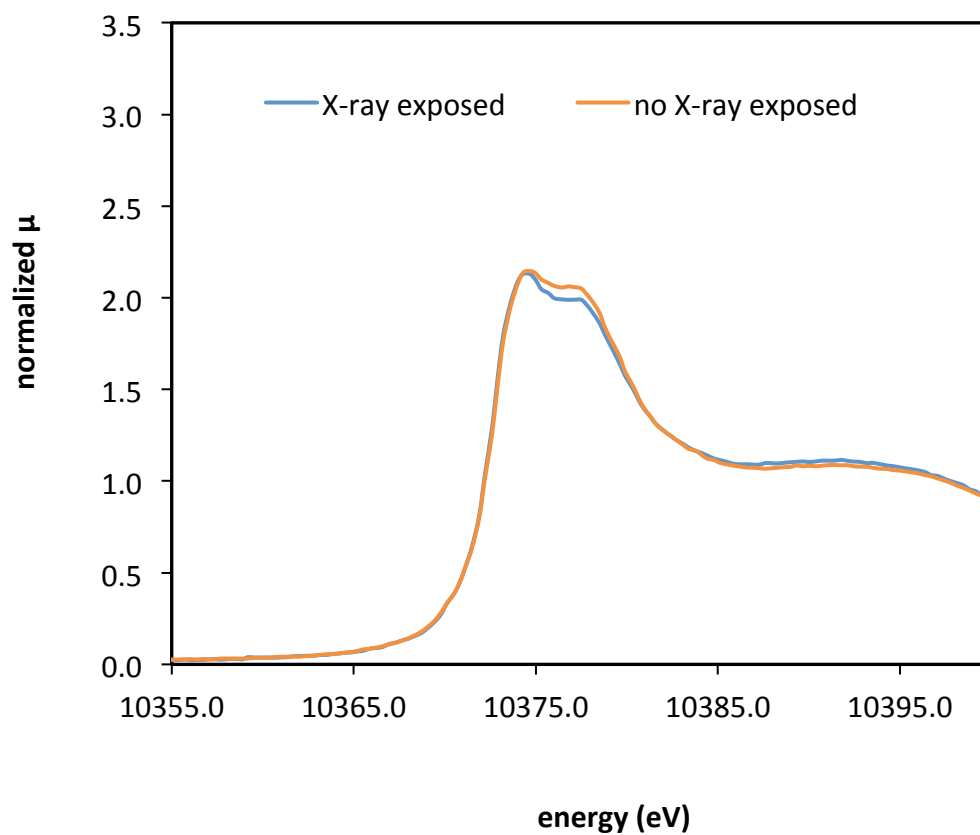
Supplementary Figure 5-7. Modified working electrode for in situ XAS to allow x-rays to be reflected back to the detector.



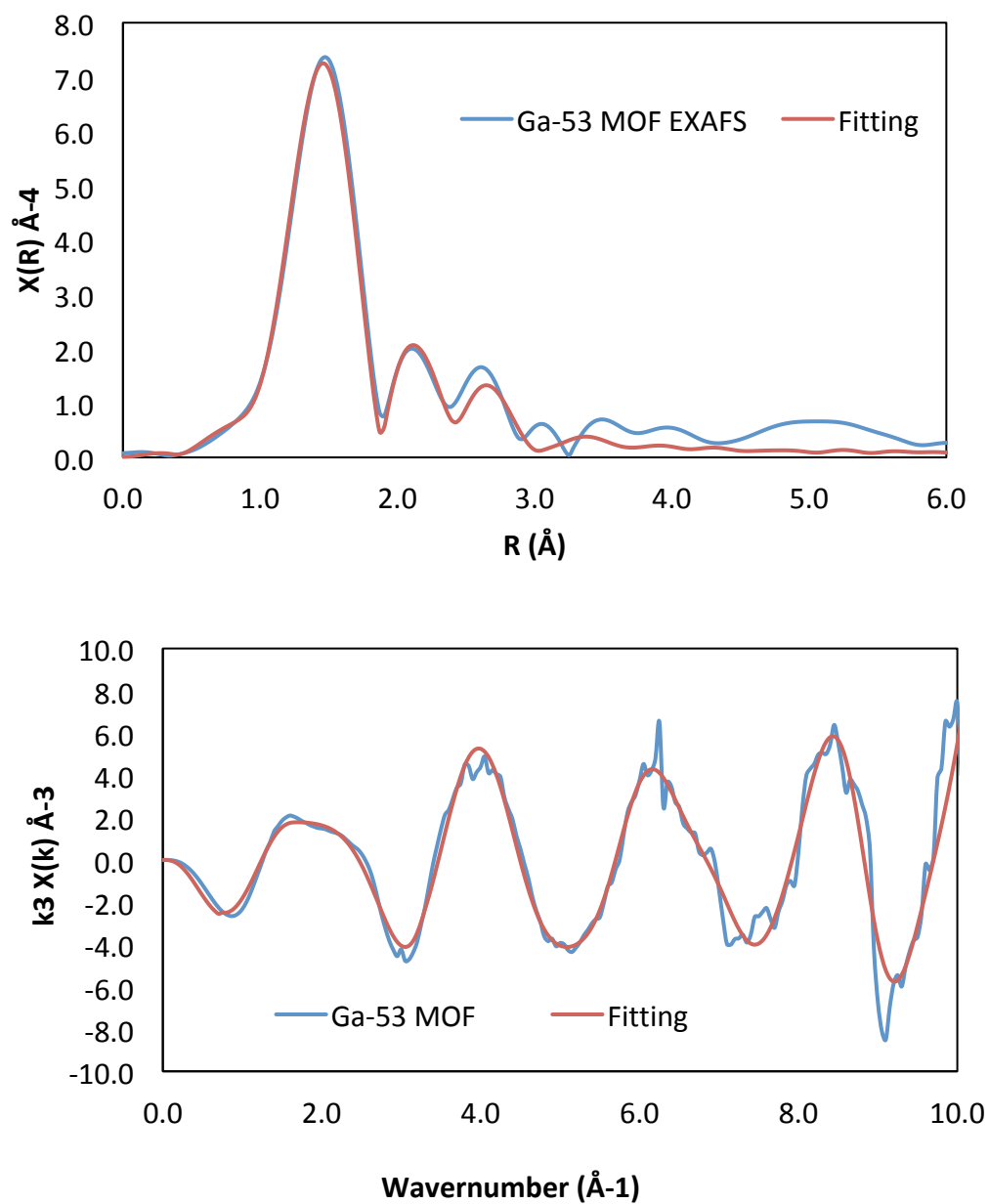
Supplementary Figure 5-8. The second cycle of 3 hours cycle of in situ XANES measurement of the same MIL-53(Ga) working electrode after being used in 3 hours electrochemical testing in CO₂-saturated 0.05 M of potassium carbonates at three different applied potentials for 1 hour each.



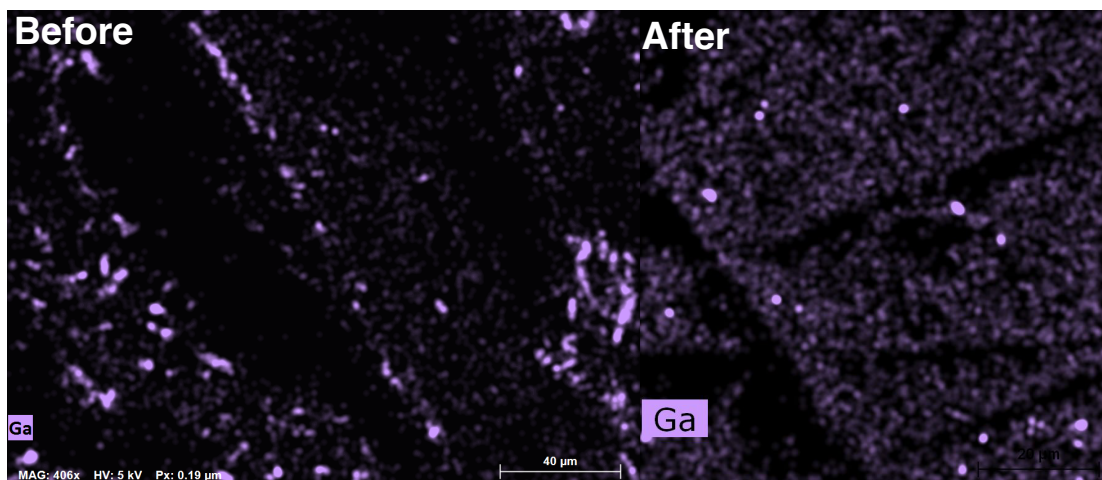
Supplementary Figure 5-9. NH₂-MIL-53(Ga) electrode in CO₂-saturated 0.05 M potassium carbonates are exposed to the beam for 8 scans with 8 minutes exposure per scan.



Supplementary Figure 5-10. After 6 hours of electrochemical testing, two spots on MIL-53(Ga) electrode in CO₂-saturated 0.05 M potassium carbonates were compared. X-ray exposed is area where the electrode received continuous beam exposure while the no x-ray exposed is area where the electrode had not received beam exposure.



Supplementary Figure 5-11. EXAFS measurement and fitting of MIL-53(Ga) working electrode after three different applied potentials starting from -0.9 V vs. RHE to -1.1 V vs. RHE for 65 minutes each. a.) in R-space b.) in K-space. The fitted R range is 0 - 6 Å and k range is 2.5 – 9.1 Å⁻¹.



Supplementary Figure 5-12. Scanning electron microscopes-energy-dispersive X-Ray (SEM-EDX) of Ga of the surface of the working electrodes before and after 6 hours 30 minutes electrochemical testing at three different potentials (-1.1 V, -1.0 V, and -0.9 V vs. RHE) to ensure the presence of the elemental components of MIL-53(Ga) on the surface of working electrodes. The SEM-EDX map of the electrode before electrochemical testing (left) showed that MIL-53(Ga) is evenly distributed by the presence of Ga (purple) evenly distributed on the electrode. For the sake of clarity, we did not include carbon in the reported SEM-EDX maps, since there is a strong carbon signal coming from the carbon paper support in addition to the MOF's organic linker. The SEM-EDX map of the electrode after electrochemical testing (right) showed that Ga (purple) was still evenly distributed on the surface of the electrode, supporting that MIL-53(Ga) is relatively stable under the operating condition.

5.11. Supplementary Tables

Supplementary Table 5-1. Fabricated working electrode containing MIL-53(Ga) under Ar atmosphere. Control experiments were performed for 65 minutes CA at a constant applied potential. There is only hydrogen production detected.

Potential (V vs. RHE)	Faradaic Efficiency					
	Hydrogen	CO	Methane	Ethane	Ethylene	Formic Acid
-1.1	50.2%	0%	0%	0%	0%	0%

Supplementary Table 5-2. Background: plain carbon paper under CO₂ atmosphere. Control experiments were performed under the same condition for electrochemical reduction of CO₂ for the reported product detection, 65 minutes CA at a constant applied potential. There is no CO₂R product detected.

Potential (V vs. RHE)	Faradaic Efficiency					
	Hydrogen	CO	Methane	Ethane	Ethylene	Formic Acid
-1.0	42.0%	0%	0%	0%	0%	0%

Supplementary Table 5-3. Background: plain carbon paper and Nafion (0.17 μL) under CO_2 atmosphere. Control experiments were performed under the same condition for electrochemical reduction of CO_2 for the reported product detection, 65 minutes CA at a constant applied potential. There is negligible CO_2R product detected.

Potential (V vs. RHE)	Faradaic Efficiency					
	Hydrogen	CO	Methane	Ethane	Ethylene	Formic Acid
-1.0	45.8%	0.93%	0%	0%	0%	0%

Supplementary Table 5-4. Faradaic efficiency of MIL-53(Ga) catalyzed CO_2 reduction at different applied potentials.

Potential (V vs. RHE)	Current Density (mA)	Faradaic Efficiency		
		Hydrogen	CO	Formic Acid
-0.9	2.19	70%	2%	1%
-0.9	1.36	84%	3%	4%
-0.9	1.93	70%	2%	1%
-1.0	2.62	88%	4%	4%
-1.0	2.31	85%	4%	7%
-1.0	2.76	80%	4%	3%
-1.1	3.92	92%	4%	4%
-1.1	2.83	94%	5%	8%
-1.1	3.99	86%	4%	5%

Supplementary Table 5-5. Average and error analysis of faradaic efficiency of MIL-53(Ga) catalyzed CO₂ reduction at different applied potentials.

Potential (V vs. RHE)	Current Density (mA)	Average Faradaic Efficiency			Standard Deviation Faradaic Efficiency			SEM Faradaic Efficiency		
		Hydrogen	CO	Formic Acid	Hydrogen	CO	Formic Acid	Hydrogen	CO	Formic Acid
-0.9	1.83	74%	2%	2%	8%	1%	1%	5%	0%	1%
-1.0	2.56	84%	4%	5%	4%	0%	2%	2%	0%	1%
-1.1	3.58	91%	4%	6%	4%	0%	2%	2%	0%	1%

Supplementary Table 5-6. Turnover frequency (TOF) calculation based on faradaic efficiency and current using:

$$TOF = \frac{Q*FE}{t*N*F*n_{catalyst}} = \frac{i*FE}{N*F*n_{catalyst}},$$

where Q is the total charge passed in time t, i is the current, FE is the Faradaic efficiency for the desired product, N is the number of electrons in the half reaction (N = 2 for CO₂ to CO or HCO₂H conversion), F is the Faraday constant (F = 96485 C/mol electrons), and n_{catalyst} is the mole of MIL-53(Ga)/unit cell deposited onto active area of CP.

TOF for CO and Formic Acid

TOF for CO and Formic Acid

Potential (V vs. RHE)	Run 1				Run 2				Run 3				Average TOF (h ⁻¹)	SEM TOF (h ⁻¹)
	Current (mA)	FE for CO and Formic Acid	TOF (s ⁻¹)	TOF (h ⁻¹)	Current (mA)	FE for CO and Formic Acid	TOF (s ⁻¹)	TOF (h ⁻¹)	Current (mA)	FE for CO and Formic Acid	TOF (s ⁻¹)	TOF (h ⁻¹)		
-0.9	2.19	3%	0.0031	11.26	1.36	7%	0.0037	13.28	1.93	3%	0.0025	9.07	11.2	1.2
-1.0	2.62	8%	0.0082	29.52	2.31	10%	0.0096	34.46	2.76	7%	0.0080	28.92	31.0	1.8
-1.1	3.92	8%	0.0131	47.18	2.83	13%	0.0148	53.32	3.99	10%	0.0156	56.31	52.3	2.7

TOF for CO

Potential (V vs. RHE)	Run 1				Run 2				Run 3				Average TOF (h ⁻¹)	SE M T OF (h ⁻¹)
	Current (mA)	FE for CO	TO F (s ⁻¹)	TO F (h ⁻¹)	Current (mA)	FE for CO	TO F (s ⁻¹)	TO F (h ⁻¹)	Current (mA)	FE for CO	TO F (s ⁻¹)	TO F (h ⁻¹)		
-0.9	2.19	2%	0.0 021	7.5 2	1.36	3%	0.0 017	6.1 9	1.93	2%	0.0 015	5.3 7	6.4	0.6
-1.0	2.62	4%	0.0 041	14. 90	2.31	4%	0.0 033	11. 91	2.76	4%	0.0 041	14. 89	13.9	1.0
-1.1	3.92	4%	0.0 062	22. 25	2.83	5%	0.0 054	19. 34	3.99	4%	0.0 071	25. 46	22.3	1.8

TOF for Formic Acid

Potential (V vs. RHE)	Run 1				Run 2				Run 3				Average TOF (h ⁻¹)	SE M T OF (h ⁻¹)
	Current (mA)	FE for Formic Acid	TO F (s ⁻¹)	TO F (h ⁻¹)	Current (mA)	FE for Formic Acid	TO F (s ⁻¹)	TO F (h ⁻¹)	Current (mA)	FE for Formic Acid	TO F (s ⁻¹)	TO F (h ⁻¹)		
-0.9	2.19	1%	0.0 010	3.7 4	1.36	4%	0.0 020	7.0 9	1.93	1%	0.0 010	3.7 0	4.8	1.1
-1.0	2.62	4%	0.0 041	14. 62	2.31	7%	0.0 063	22. 56	2.76	3%	0.0 039	14. 03	17.1	2.7
-1.1	3.92	4%	0.0 069	24. 93	2.83	8%	0.0 094	33. 98	3.99	5%	0.0 086	30. 85	29.9	2.7

TOF for Hydrogen

Potential (V vs. RHE)	Run 1				Run 2				Run 3				Average TOF (h ⁻¹)	SE M T OF (h ⁻¹)
	Current (mA)	FE for Hydrogen	TO F (s ⁻¹)	TO F (h ⁻¹)	Current (mA)	FE for Hydrogen	TO F (s ⁻¹)	TO F (h ⁻¹)	Current (mA)	FE for Hydrogen	TO F (s ⁻¹)	TO F (h ⁻¹)		
-0.9	2.19	70%	0.0 623	224 .24	1.36	84%	0.0 465	167 .38	1.93	70%	0.0 553	199 .04	196. 9	16. 5
-1.0	2.62	88%	0.0 940	338 .44	2.31	85%	0.0 800	287 .91	2.76	80%	0.0 901	324 .48	316. 9	15. 1
-1.1	3.92	92%	0.1 471	529 .52	2.83	94%	0.1 086	390 .98	3.99	86%	0.1 397	503 .07	474. 5	42. 5

Supplementary Table 5-7. Faradaic efficiency of MIL-53(Ga) catalyzed CO₂ reduction in modified cell designed for in situ XAS at different applied potentials.

Potential (V vs. RHE)	Current Density (mA)	Faradaic Efficiency			
		Hydrogen	CO	Formic Acid	Total
-0.9	0.75	63%	4%	2%	68%
-0.9	1.70	80%	3%	1%	83%
-1.0	1.25	67%	3%	3%	73%
-1.0	2.58	85%	1%	1%	88%
-1.1	2.00	80%	5%	6%	91%
-1.1	2.71	84%	3%	2%	89%

Supplementary Table 5-8. Average and error analysis of faradaic efficiency of MIL-53(Ga) catalyzed CO₂ reduction in modified cell designed for in situ XAS at different applied potentials.

Potential (V vs. RHE)	Current Density (mA)	Average Faradaic Efficiency				Standard Deviation Faradaic Efficiency				SEM Faradaic Efficiency			
		Hydrogen	CO	Formic Acid	Total	Hydrogen	CO	Formic Acid	Total	Hydrogen	CO	Formic Acid	Total
-0.9	1.23	71%	3%	1%	76%	12%	0%	1%	11%	7%	0%	1%	6%
-1.0	1.91	76%	2%	2%	80%	13%	1%	1%	10%	7%	1%	1%	6%
-1.1	2.36	82%	4%	4%	90%	3%	2%	3%	2%	2%	1%	2%	1%

Supplementary Table 5-9. EXAFS fitting results for MIL-53(Ga) working electrode after three different applied potentials (-0.9 V, -1.0 V and -1.1 V) . The numbers in parentheses indicate the statistical error in the most significant digit obtained from the fit in Artemis (e.g. 4.1(2) \equiv 4.1 \pm 0.2). The coordination number of first shell oxygen is 5, and the other shells' coordination numbers stay consistent with the original MIL-53(Ga). This result indicates one Ga-O bond broke distorting the carboxylate binding in MIL-53(Ga).

	N	σ^2	e_0	R
O (1st shell)	5	0.0008 +/- 0.0040	2.10 +/- 2.38	1.91 +/-0.02
C (1st shell)	4	0.0016 +/- 0.0068	2.10 +/- 2.38	2.66 +/-0.04
Ga (1st shell)	2	0.0084 +/- 0.0138	2.10 +/- 2.38	3.97 +/-0.11
O (2nd shell)	4	0.0052 +/- 0.0102	2.10 +/- 2.38	3.36 +/-0.07

5.12. Acknowledgements

This material is based upon work performed by the Joint Center for Artificial Photosynthesis, a DOE Energy Innovation Hub, supported through the Office of Science of the U.S. Department of Energy under Award No. DE-SC0004993. Use of the Stanford Synchrotron Radiation Lightsource, SLAC National Accelerator Laboratory, is supported by the U.S. Department of Energy, Office of Science, Office of Basic Energy Sciences under Contract No. DE-AC02-76SF00515. This research used resources of the Advanced Light Source, a U.S. DOE Office of Science User Facility under contract no. DE-AC02-05CH11231. We acknowledge Dr. Alpha T. N'Diaye for assistance with measurements at the Advanced Light Source. We also

acknowledge Prof. F. Dean Toste, Prof. Christopher K. Ober, and Dr. Soohong Lee for fruitful discussions. Work at the Molecular Foundry was supported by the Office of Science, Office of Basic Energy Sciences, of the U.S. Department of Energy under Contract No. DE-AC02-05CH11231.

REFERENCES

1. Seh, Z. W.; Kibsgaard, J.; Dickens, C. F.; Chorkendorff, I.; Norskov, J. K.; Jaramillo, T. F., Combining theory and experiment in electrocatalysis: Insights into materials design. *Science* **2017**, 355 (6321).
2. Hori, Y.; Takahashi, R.; Yoshinami, Y.; Murata, A., Electrochemical Reduction of CO at a Copper Electrode. *The Journal of Physical Chemistry B* **1997**, 101 (36), 7075-7081.
3. Kuhl, K. P.; Cave, E. R.; Abram, D. N.; Jaramillo, T. F., New insights into the electrochemical reduction of carbon dioxide on metallic copper surfaces. *Energy & Environmental Science* **2012**, 5 (5).
4. Mahmood, A.; Guo, W.; Tabassum, H.; Zou, R., Metal-Organic Framework-Based Nanomaterials for Electrocatalysis. *Advanced Energy Materials* **2016**, 6 (17).
5. Diercks, C. S.; Liu, Y.; Cordova, K. E.; Yaghi, O. M., The role of reticular chemistry in the design of CO₂ reduction catalysts. *Nat Mater* **2018**, 17 (4), 301-307.
6. Lin, S.; Diercks, C. S.; Zhang, Y.-B.; Kornienko, N.; Nichols, E. M.; Zhao, Y.; Paris, A. R.; Kim, D.; Yang, P.; Yaghi, O. M.; Chang, C. J., Covalent organic frameworks comprising cobalt porphyrins for catalytic CO₂ reduction in water. *Science* **2015**, 349 (6253), 1208-1213.
7. Kornienko, N.; Zhao, Y.; Kley, C. S.; Zhu, C.; Kim, D.; Lin, S.; Chang, C. J.; Yaghi, O. M.; Yang, P., Metal-organic frameworks for electrocatalytic reduction of carbon dioxide. *J Am Chem Soc* **2015**, 137 (44), 14129-35.
8. Yang, D.; Gates, B. C., Catalysis by Metal Organic Frameworks: Perspective and Suggestions for Future Research. *ACS Catalysis* **2019**, 9 (3), 1779-1798.

9. Pascanu, V.; Gonzalez Miera, G.; Inge, A. K.; Martin-Matute, B., Metal-Organic Frameworks as Catalysts for Organic Synthesis: A Critical Perspective. *J Am Chem Soc* **2019**, *141* (18), 7223-7234.
10. Wang, L.; Agnew, D. W.; Yu, X.; Figueroa, J. S.; Cohen, S. M., A Metal-Organic Framework with Exceptional Activity for C-H Bond Amination. *Angew Chem Int Ed Engl* **2018**, *57* (2), 511-515.
11. Bauer, G.; Ongari, D.; Xu, X.; Tiana, D.; Smit, B.; Ranocchiari, M., Metal-Organic Frameworks Invert Molecular Reactivity: Lewis Acidic Phosphonium Zwitterions Catalyze the Aldol-Tishchenko Reaction. *J Am Chem Soc* **2017**, *139* (50), 18166-18169.
12. Lee, M.; De Riccardis, A.; Kazantsev, R.; Cooper, J. K.; Buckley, A.; Burroughs, P.; Larson, D.; Mele, G.; Toma, F. M., Aluminum Metal Organic Framework Triggers Carbon Dioxide Reduction Activity. *ACS Applied Energy Materials* **2020**.
13. Wang, X.; Chen, Z.; Zhao, X.; Yao, T.; Chen, W.; You, R.; Zhao, C.; Wu, G.; Wang, J.; Huang, W.; Yang, J.; Hong, X.; Wei, S.; Wu, Y.; Li, Y., Regulation of Coordination Number over Single Co Sites: Triggering the Efficient Electroreduction of CO₂. *Angew Chem Int Ed Engl* **2018**, *57* (7), 1944-1948.
14. Wu, Y.; Jiang, J.; Weng, Z.; Wang, M.; Broere, D. L. J.; Zhong, Y.; Brudvig, G. W.; Feng, Z.; Wang, H., Electroreduction of CO₂ Catalyzed by a Heterogenized Zn-Porphyrin Complex with a Redox-Innocent Metal Center. *ACS Cent Sci* **2017**, *3* (8), 847-852.

15. Coudert, F.-X.; Ortiz, A. U.; Haigis, V.; Bousquet, D.; Fuchs, A. H.; Ballandras, A.; Weber, G.; Bezverkhyy, I.; Geoffroy, N.; Bellat, J.-P.; Ortiz, G.; Chaplais, G.; Patarin, J.; Boutin, A., Water Adsorption in Flexible Gallium-Based MIL-53 Metal–Organic Framework. *The Journal of Physical Chemistry C* **2014**, *118* (10), 5397-5405.
16. Kramida, A., Ralchenko, Yu., Reader, J. and NIST ASD Team (2019). NIST Atomic Spectra Database
17. Volkringer, C.; Loiseau, T.; Guillou, N.; Ferey, G.; Elkaim, E.; Vimont, A., XRD and IR structural investigations of a particular breathing effect in the MOF-type gallium terephthalate MIL-53(Ga). *Dalton Trans* **2009**, (12), 2241-9.
18. Kaskel, S.; Synthesis, Structure, and Selected Properties of Aluminum-, Gallium-, and Indium-Based Metal-Organic Frameworks. In *The Chemistry of Metal-Organic Frameworks: Synthesis, Characterization, and Applications*, Wiley-VCH, Weinheim, Germany 2016, pp 105-135
19. Handoko, A. D.; Wei, F.; Jenndy; Yeo, B. S.; Seh, Z. W., Understanding heterogeneous electrocatalytic carbon dioxide reduction through operando techniques. *Nature Catalysis* **2018**, *1* (12), 922-934.
20. De Luna, P.; Quintero-Bermudez, R.; Dinh, C.-T.; Ross, M. B.; Bushuyev, O. S.; Todorović, P.; Regier, T.; Kelley, S. O.; Yang, P.; Sargent, E. H., Catalyst electro-redeposition controls morphology and oxidation state for selective carbon dioxide reduction. *Nature Catalysis* **2018**, *1* (2), 103-110.

21. Burdyny, T.; Smith, W. A., CO₂ reduction on gas-diffusion electrodes and why catalytic performance must be assessed at commercially-relevant conditions. *Energy & Environmental Science* **2019**, *12* (5), 1442-1453.
22. Takeno, N. Atlas of Eh-pH diagrams: Intercomparison of thermodynamic databases; National Institute of Advanced Industrial Science and Technology: Tokyo, 2005.
23. Gu, J.; Hsu, C.-S.; Bai, L.; Chen, H. M.; Hu, X., Atomically dispersed Fe³⁺ sites catalyze efficient CO₂ electroreduction to CO. *Science* **2019**, *364* (6445), 1091.
24. Dodelet, J. P.; Tourillon, G.; Gastonguay, L.; Cote, R.; Guay, D.; Ladouceur, M.; Flank, A. M.; Lagarde, P., X-ray absorption spectroscopy at the aluminum K edge of aluminum phthalocyanine thin films: correlation between aluminum coordination and photoactivity. *The Journal of Physical Chemistry* **1992**, *96* (18), 7202-7206.
25. Wei, S.; Oyanagi, H.; Liu, W.; Hu, T.; Yin, S.; Bian, G., Local structure of liquid gallium studied by X-ray absorption fine structure. *Journal of Non-Crystalline Solids* **2000**, *275* (3), 160-168.
26. Yang, X.-F.; Wang, A.; Qiao, B.; Li, J.; Liu, J.; Zhang, T., Single-Atom Catalysts: A New Frontier in Heterogeneous Catalysis. *Accounts of Chemical Research* **2013**, *46* (8), 1740-1748.
27. Gawande, M. B.; Fornasiero, P.; Zbořil, R., Carbon-Based Single-Atom Catalysts for Advanced Applications. *ACS Catalysis* **2020**, *10* (3), 2231-2259.

28. Ahnfeldt, T.; Gunzelmann, D.; Loiseau, T.; Hirsemann, D.; Senker, J.; Férey, G.; Stock, N., Synthesis and Modification of a Functionalized 3D Open-Framework Structure with MIL-53 Topology. *Inorganic Chemistry* **2009**, *48* (7), 3057-3064.
29. Loiseau, T.; Sere, C.; Huguenard, C.; Fink, G.; Taulelle, F.; Henry, M.; Bataille, T.; Férey, G. A. A Rationale for the Large Breathing of the Porous Aluminum Terephthalate (MIL-53) Upon Hydration. *Chem. Eur. J.* 2004, *10*, 1373-1382.
30. Lum, Y.; Kwon, Y.; Lobaccaro, P.; Chen, L.; Clark, E. L.; Bell, A. T.; Ager, J. W., Trace Levels of Copper in Carbon Materials Show Significant Electrochemical CO₂ Reduction Activity. *ACS Catalysis* **2016**, *6* (1), 202-209.
31. Jung, S.; McCrory, C. C. L.; Ferrer, I. M.; Peters, J. C.; Jaramillo, T. F., Benchmarking nanoparticulate metal oxide electrocatalysts for the alkaline water oxidation reaction. *Journal of Materials Chemistry A* **2016**, *4* (8), 3068-3076.
32. Lobaccaro, P.; Singh, M. R.; Clark, E. L.; Kwon, Y.; Bell, A. T.; Ager, J. W., Effects of temperature and gas-liquid mass transfer on the operation of small electrochemical cells for the quantitative evaluation of CO₂ reduction electrocatalysts. *Physical Chemistry Chemical Physics* **2016**, *18* (38), 26777-26785.
33. Ravel, B.; Newville, M., ATHENA, ARTEMIS, HEPHAESTUS: data analysis for X-ray absorption spectroscopy using IFEFFIT. *J. Synchrotron Rad.* 2005, *12* (4), 537-541.
34. Newville, M., EXAFS analysis using FEFF and FEFFIT. *J. Synchrotron Rad.* 2001, *8* (2), 96-100.

40. Ahnfeldt, T.; Gunzelmann, D.; Loiseau, T.; Hirsemann, D.; Senker, J.; Férey, G.; Stock, N. Synthesis and Modification of a Functionalized 3D Open-Framework Structure with MIL-53 Topology. *Inorg. Chem.* **2009**, *48*, 3057-3064.
41. Volkringer, C.; Loiseau, T.; Guillou, N.; Férey, G.; Elkaim, E.; Vimont, A., XRD and IR structural investigations of a particular breathing effect in the MOF-type gallium terephthalate MIL-53(Ga). *Dalton Trans* **2009**, (12), 2241-9.

CHAPTER 6

CO₂ REDUCTION ON PURE COPPER PRODUCES ONLY HYDROGEN WHEN SUBSURFACE OXYGEN IS DEPLETED: THEORY AND EXPERIMENT

This study was carried out in collaboration with Dr. Guiji Liu from Dr. Francesca M. Toma Lab at Lawrence Berkeley National Laboratory and Dr. Soonho Kwon from Prof. William A. Goddard III at California Institute of Technology.

6.1. Abstract

We elucidate the role of subsurface oxygen on production of C_2 products from CO_2 reduction over Cu electrocatalysts using the newly developed grand canonical potential-kinetics density functional theory method, predicting that the rate of C_2 production is 479 times slower than H_2 evolution on pure Cu (111). Starting with Cu_2O the rate of C_2 production is > 1000 times faster than pure Cu (111). To validate these predictions experimentally, we combined time-dependent product detection with multiple characterization techniques to show that ethylene production decreases substantially with time and that a sufficiently prolonged reaction time leads only to H_2 evolution with negligible ethylene production (1/1000) in agreement with theory. This result shows that maintaining substantial subsurface oxygen is essential for long term C_2 production with Cu catalysts.

6.2. Introduction

Anthropogenic carbon emissions, particularly CO_2 , are surging due primarily to global fossil-fuel consumption, raising serious environmental concerns about global warming¹. Recycling CO_2 via electrochemical reduction of carbon dioxide (CO_2RR) to fuels and valuable chemicals using renewable energy could play an important role in global efforts to address current energy demand and climate challenges². CO_2 can be electrochemically reduced to C_1 products (CO , methane, and formic acid), C_2 products (ethylene, ethane, and ethanol), and C_3 products (n-propanol)^{3, 4}. The major challenge

in this process is to increase selectivity to generate a single higher hydrocarbon product.

In this context, copper (Cu) remains the only single metal capable of producing significant amounts of higher hydrocarbons, such as C₂ products ethylene or ethanol. Interestingly, many experiments report that oxide-derived Cu catalysts lead to higher activity for C₂ products⁵⁻⁸. However, the role of oxygen in the Cu catalyst and the correlation with the underlying C₂ production mechanism remains a subject of debate in the field⁴. We suggested earlier that the optimum catalyst is the partially reduced Cu₂O surface in which surface and/or subsurface oxygen of Cu₂O are adjacent to a reduced Cu⁰ surface, termed MEOM for Metal Embedded in Oxidized Matrix⁹. Density functional theory (DFT) calculations on model systems showed that MEOM leads to a barrier for CO₂ reduction to CO that is 0.22 eV lower than for pure Cu⁰ and to a barrier for CO dimerization (the first step toward C₂ products) that is 0.39 eV lower than for pure Cu⁰. This result suggests that C₂ production on the MEOM surface should be 5000 to a million times faster than for pure Cu⁰. Indeed, other groups have recently hypothesized that surface Cu⁺ and/or subsurface oxygen on Cu might play an essential role in promoting CO dimerization and ethylene production¹⁰⁻¹³. However, many others have argued that such surface or subsurface oxygen species cannot be important because many experiments show that surface oxygen is rapidly depleted under CO₂RR conditions^{14, 15}, and it is rather suggested that surface roughness plays an active role in bolstering ethylene selectivity^{8, 16, 17}. Hence, fundamental understanding into relationship between the presence of oxygen and the increased C₂ production activity on Cu catalyst can solve the existing debates.

Here, we combine theory and experiments to disentangle the contributions from both Cu that contains oxygen and fully depleted Cu⁰ with no oxygen to uncover the role of subsurface oxygen in promoting C-C coupling and consequently C₂ production on Cu catalysts. We predict that the turn-over-frequency (TOF) for hydrogen evolution reaction (HER) on pure Cu (111) is 0.32/s, whereas we predict that the C₂ production is 479 times slower. Our time-course experiments validate these predictions, finding that the C₂ production rate on fully depleted Cu is 680 times slower than C₂ production starting with Cu₂O, and 1600 times slower than starting with Cu. Furthermore, we consider a Cu⁰/Cu₂O model, in which a thin disordered Cu⁰ surface on top of a Cu₂O substrate results from surface O reacting away during reduction of Cu₂O at U_{RHE} = -1 V, pH 7, and 298K. The TOF for C₂ production on the Cu⁰/Cu₂O model is predicted to be 3.95/s, while that for HER is predicted to be 10.02/s, which is 2.58 times faster. This result is consistent with our experiments in which we find HER production to be 2.1 times higher than C₂ during the first 5 hours. In addition, we predict that a TOF = 3.95/s for C₂ production on the Cu⁰/Cu₂O model, which is a factor of 5000 faster than the predicted TOF = 6.77×10⁻⁴ /s for pure Cu (111). Indeed our experiments measured an initial partial current density of ethylene production on Cu₂O of 0.6~0.8 mA/cm², which becomes negligible over time on fully depleted Cu (~ 1/1000 of the H₂ current).

6.3. Theoretical Prediction on Rates of HER and C₂ Production

Recently, we developed grand canonical potential-kinetics (GCP-K) methodology that predicts the evolution of the reaction intermediates and transition states in solvent

to obtain the turn-over-frequency (TOF) as a function of applied potential ¹⁸. In this approach, the solvated structures and energetics of the intermediates adjust adiabatically as the applied potential (U) is changed, leading to very accurate rates vs. U. Here, we apply GCP-K to directly assess the impact of subsurface oxygen on the C₂ production over Cu catalysts. Many theoretical studies have been reported on the product distribution during CO₂RR, but most were not carried out under constant potential conditions ¹⁹⁻²³. In this study, we consider all thermodynamically stable structures of Cu₂O using grand canonical potential-kinetics (GCP-K) DFT calculations at U=-1.0 V_{RHE} with pH 7, common experimental conditions for examining the activity of Cu based catalysts in CO₂RR^{6, 15, 17}. The GCP-K formulation allows the geometries to relax as U is changed so that the micro-kinetics allows all structures (equilibrium states and saddle points for transition states) to remain optimum for each U. This development enables us to track the free energy continuously with U at a computational cost close to conventional canonical DFT calculations.

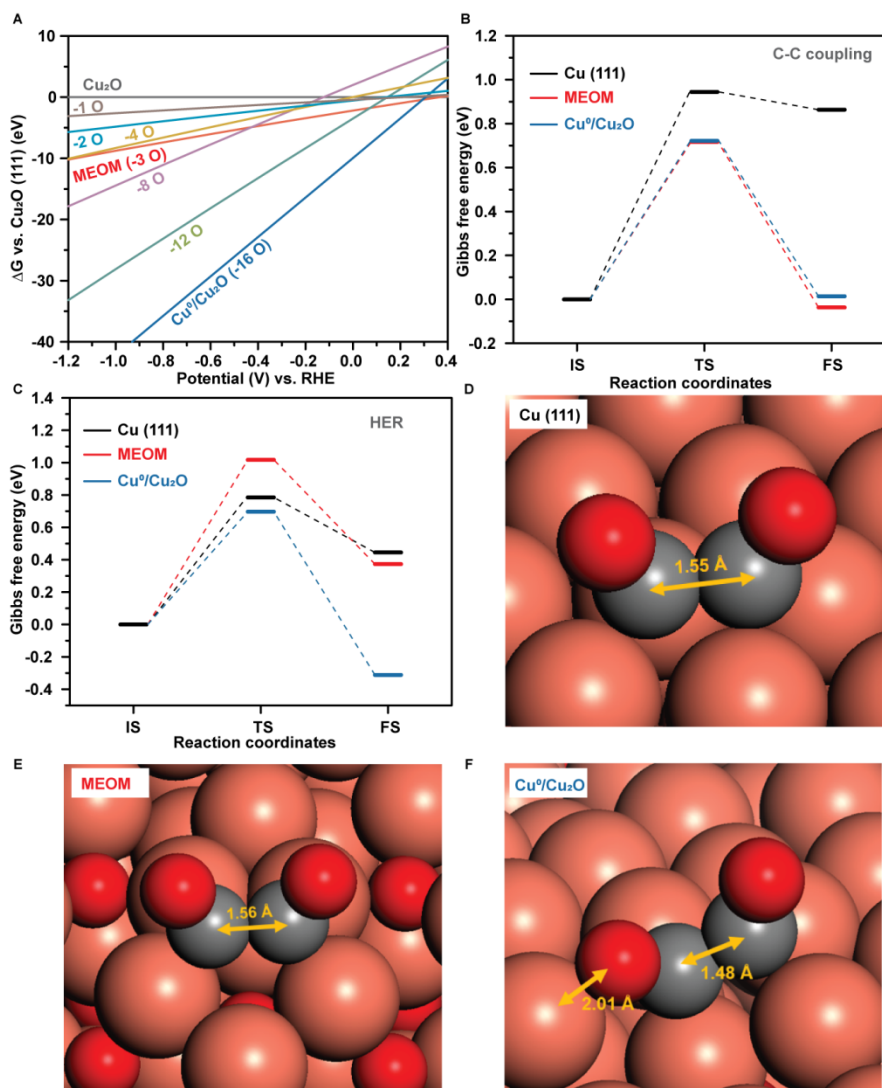


Figure 6-1. GPC-K DFT calculations for different Cu phases and their relation to C_2 production

(A) Surface free energies as a function of applied potential (U) of various surface phases with different numbers of reduced lattice oxygen (B) potential energy surfaces for the CO dimerization RDS for C_2 production and (C) the RDS for HER at $U = -1.0 V_{RHE}$ and pH 7 on Cu(111), MEOM and Cu^0/Cu_2O . These are the Heyrovsky step [$H_{ad} + H_2O(l) + e^- \rightarrow H_2(g) + OH^-(aq)$] for Cu(111) and MEOM and the Volmer step [$H_2O(l) + e^- \rightarrow H_{ad} + OH^-(aq)$] for Cu^0/Cu_2O . (D) OCCO* geometries on Cu(111), (E) OCCO* geometries on MEOM and (F) OCCO* geometries on Cu^0/Cu_2O catalysts. The applied potentials for each state correspond to $-1.25 V_{RHE}$, $-1.15 V_{RHE}$, $-1.02 V_{RHE}$, respectively. The C-C bond distances are indicated for all catalysts and Cu-O bond distance is also indicated for Cu^0/Cu_2O catalysts.

First, we performed GCP-K calculations to construct the surface Pourbaix diagram shown in Fig. 1A. Starting from intact Cu₂O (111), we gradually reduced the surface by removing various numbers of oxygen and plotted the free energies of eight states (fig. S1, Table S1) as a function of U. This shows that the disordered Cu⁰/Cu₂O surface has the highest stability at -1.0 V_{RHE}, compared to MEOM and Cu₂O models. Therefore, we considered the Cu⁰/Cu₂O model as the structure for Cu₂O at -1.0 V_{RHE}. We assume for the pure Cu with no O, that the catalyst relaxes back to Cu (111) (fig. S2), using this as the model for purely depleted Cu₂O or Cu. We also consider the MEOM surface for comparison in the SI. We then predicted the free energy barriers for HER and for CO dimerization (the dominant step in C₂ formation) for these models.

Our previous full solvent QM MD studies showed that C-C coupling of two surface CO is the rate determining step (RDS) for producing C₂ products²⁴. We predict that the $\Delta G^\ddagger = 0.72$ eV for C-C coupling on the disordered Cu⁰/Cu₂O surface (Fig. 1B) leading to TOF= 3.95/s which is 5840 times faster than our predicted to 6.77×10^{-4} /s for oxygen depleted Cu (111) surface, which has a barrier of $\Delta G^\ddagger = 0.94$ eV (close to our previous studies⁹). This enhancement of C-C coupling on Cu⁰/Cu₂O is attributed to its capability of forming (OCC)O-Cu bond which greatly stabilizes OCCO* as shown in Fig. 1F.

For HER, we considered Volmer [H₂O(l) + e⁻ → H_{ad}+OH⁻(aq)] and Heyrovsky [H_{ad}+H₂O(l) + e⁻ → H₂(g) +OH⁻(aq)] steps. Fig. 1C examines both steps on Cu (111) as a function of U. On Cu (111) at U= -1.0 V_{RHE}, the RDS is Heyrovsky, which leads to $\Delta G^\ddagger = 0.79$ eV (0.16 eV lower than for C-C coupling) and to TOF = 0.32 /s. For

$\text{Cu}^0/\text{Cu}_2\text{O}$ at $U = -1 \text{ V}_{\text{RHE}}$, we find the RDS to be the Volmer reaction with $\Delta G^\ddagger = 0.70 \text{ eV}$, only -0.02 eV lower than C-C coupling for the both cases. Thus, the C_2 production rate is predicted to be comparable to HER rate on $\text{Cu}^0/\text{Cu}_2\text{O}$ (0.39 times slower). Whereas on fully depleted Cu (111), the predicted rate for H_2 production is 479 times higher than C_2 production. The predicted ratio of the rate for H_2 production on $\text{Cu}^0/\text{Cu}_2\text{O}$ vs fully depleted Cu (111) is 3.14×10^1 . All atomic configurations for catalytic reactions are shown in fig. S3-S5.

6.4. Experimental CO_2RR Activities of Cu and Cu_2O Catalysts

To validate the above predictions from theory, we synthesized copper-based catalysts through electrochemical deposition of cuprous oxide (Cu_2O) on polycrystalline copper (Cu). Compared to the planar surface of polycrystalline Cu (fig. S6A), our synthesized Cu_2O sample exhibits polycrystalline grains (fig. S6B) with a $1.0 \mu\text{m}$ thickness (fig. S6C). Under bulk electrolysis at $-1.0 \text{ V}_{\text{RHE}}$ with CO_2 -saturated $0.1 \text{ M K}_2\text{CO}_3$ electrolyte for 65 min, the crystalline structures of polycrystalline Cu featuring Cu (111) are retained as shown in *ex situ* grazing incidence X-ray diffraction (GIXRD) analysis (Fig. 2A). On the other hand, Cu_2O is reduced to Cu^0 due to removal of lattice oxygen under CO_2RR , thus leading to disordered Cu^0 surface over time as demonstrated by *ex situ* GIXRD (Fig. 2B). Complementary high-resolution transmission electron microscopy (HRTEM) confirms that the surface of Cu_2O is readily reduced to crystalline Cu^0 after 2 minutes of CO_2RR (Fig. 2C). Then, this crystalline surface evolves into fragmented and disordered Cu based nanoparticles over 60 min CO_2RR (Fig. 2D), in excellent agreement with GIXRD results. Control

experiments further revealed that Cu_2O became crystalline Cu^0 under N_2 saturation at $-1 \text{ V}_{\text{RHE}}$ and at less negative potentials ($-0.6 \text{ V}_{\text{RHE}}$ and $-0.3 \text{ V}_{\text{RHE}}$) under CO_2RR for 1 h (fig. S7). Thus, these experimental observations verify that the theoretically predicted Cu (111) and disordered $\text{Cu}^0/\text{Cu}_2\text{O}$ model are indeed the thermodynamically stable structure for polycrystalline Cu and Cu_2O under CO_2RR at $-1.0 \text{ V}_{\text{RHE}}$.

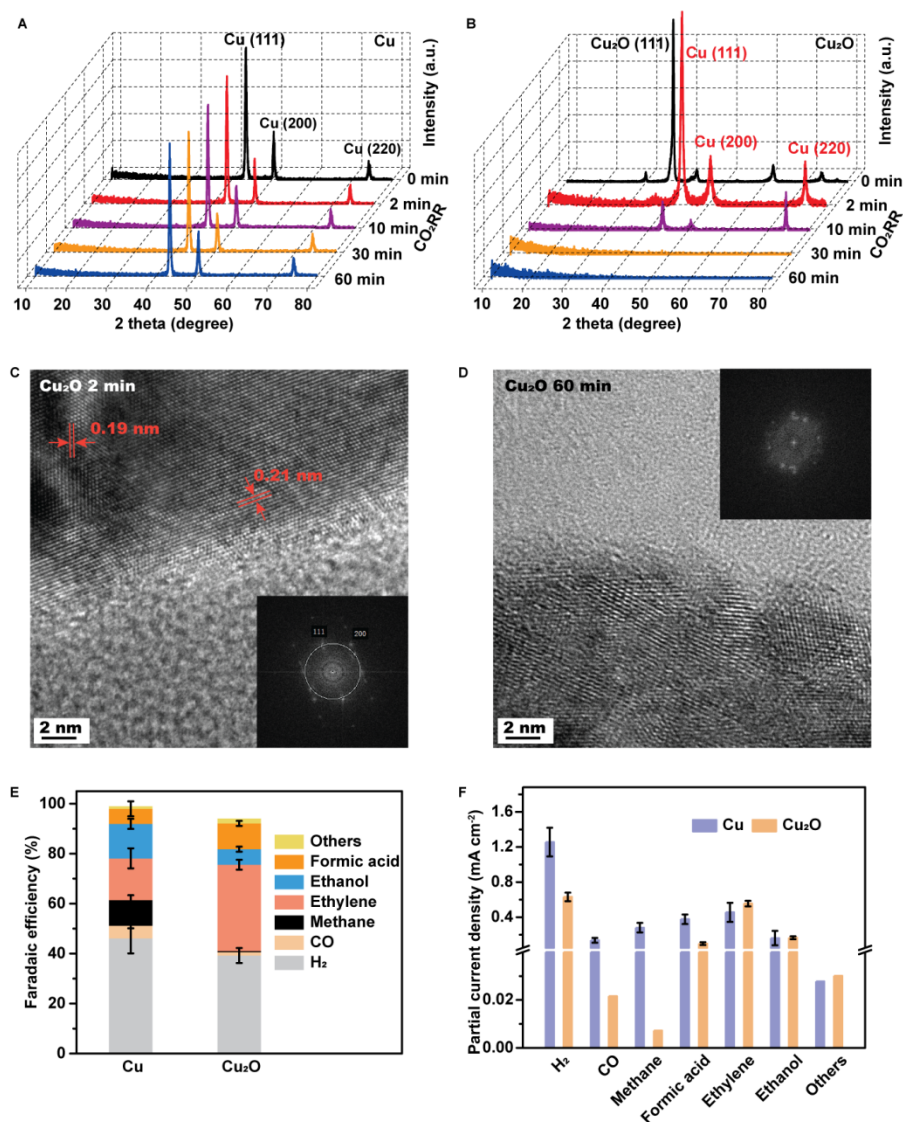


Figure 6-2. Stable phases and catalytic activities of polycrystalline Cu and Cu₂O under CO₂RR. *Ex-situ* GIXRD analysis of (A) polycrystalline Cu, (B) Cu₂O after 0 min (as-prepared), 2 min, 10 min, 30 min and 60 min CO₂RR at -1.0 V vs RHE in 0.1 M CO₂-saturated K₂CO₃ electrolyte (pH 7); HRTEM images of Cu₂O under CO₂RR for (C) 2 min with corresponding fast Fourier transform (insert); and (D) 1 h with corresponding fast Fourier transform (insert); fragmented Cu based nanoparticles with lower crystallinity were observed over 1 h CO₂RR; (E) Faradaic efficiencies of CO₂RR toward H₂ (grey), CO (gold), methane (black), ethylene (pink), ethanol (blue), formic acid (orange) and others: acetate, ethylene glycol and 1-propanol (yellow) for Cu, Cu₂O (thin) and Cu₂O (thick) at -1.0 V vs. RHE; (F) Partial current densities toward H₂, CO, methane, formic acid, ethylene, ethanol and others: allyl alcohol and n-propanol, normalized by ECSA over Cu, and Cu₂O for 1h CO₂RR at -1.0 V vs. RHE in CO₂-saturated 0.1 M K₂CO₃ electrolyte (pH 7); Average values in (E) and (F) are based on triplicates, and the errors correspond to the SEM of data points from individual samples in Table S3.

The initial catalytic activity and selectivity of polycrystalline Cu and Cu₂O catalysts toward CO₂RR was examined over one hour by gas chromatography (GC) and high-performance liquid chromatography (HPLC) in a two-compartment flow cell (fig.S8). We find that selectivity of H₂ evolution is lower and selectivity toward C₂ (ethylene and ethanol) products over C₁ (CO, methane and formic acid) products is higher using Cu₂O catalysts, compared to polycrystalline Cu (Fig. 2E), in agreement with previous reports^{6, 7, 25, 26}. In particular, the C₂/C₁ ratio reaches a value of 5.9 on Cu₂O, while that for polycrystalline Cu is only 0.8, based on the faradaic efficiencies (FE) in Fig. 2E. To understand the intrinsic activity toward each product on polycrystalline Cu and Cu₂O catalysts, we further plotted the partial current densities, normalized by electrochemically active surface area (ECSA), as shown in Fig. 2F. These data highlight that the enhanced C₂/C₁ ratio on Cu₂O mainly stems from great suppression of C₁ products, while similar rates of C₂ (ethylene and ethanol) products were observed on polycrystalline Cu and Cu₂O catalysts during the first hour of measurements. Previous studies have shown that the activity and selectivity of C₂ production on Cu are strongly dependent on the surface morphology and chemical composition^{12, 16, 17, 27}.

To assess the role of surface morphology on Cu and Cu₂O catalysts under operating conditions, we employed *quasi in-situ* electrochemical atomic force microscopy (EC-AFM) (Fig. 3). Briefly, a bias of -0.8 V_{RHE} was applied to the polycrystalline Cu or Cu₂O working electrode in 0.1 M K₂CO₃ solution (CO₂-saturated). This potential allows for similar operating potential in the CO₂RR

measurements ($-1.0\text{ V}_{\text{RHE}}$), while minimizing the adverse impact of bubble formation during AFM measurements. Surface morphology was then collected by AFM under open circuit conditions. This procedure was repeated over a period of 5 min in the same sample region to examine the topography and surface roughness (R_a) on both polycrystalline Cu and Cu_2O catalysts. Compared to as-prepared polycrystalline Cu (0 min), no dramatic topography change was observed on Cu under CO_2RR , with a constant R_a ($\sim 2\text{ nm}$) (Fig.3A-C). On the other hand, electrochemical fragmentation occurred on the Cu_2O catalysts along with nanoparticles formation on Cu_2O grains during the first 1 minute of EC measurements (Fig. 3D and E). Afterwards, the changes in topography remain small on Cu_2O (Fig. 3E and F), leading to constant R_a ($\sim 21\text{ nm}$), which is ten times of that of polycrystalline Cu. The sharp discrepancy in surface topography and roughness of polycrystalline Cu and Cu_2O rules consequently out the possibility that surface topography or roughness plays a predominant role in the similar C_2 production rate on polycrystalline Cu and Cu_2O .

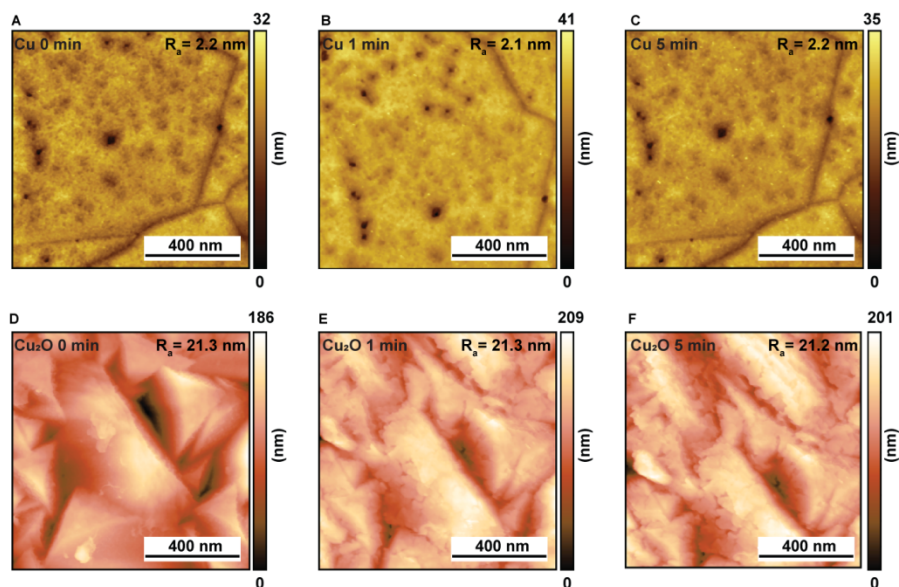


Figure 6-3. Monitoring surface topography or roughness over Cu and Cu₂O under CO₂RR. *Quasi in-situ* EC-AFM images of polycrystalline Cu at (A) 0 min (as-prepared), (B) 1 min, (C) 5 min and Cu₂O at (D) 0 min (as-prepared), (E) 1 min, (F) 5 min in 0.1 M CO₂-saturated K₂CO₃ electrolyte (pH 7) at -0.8 V_{RHE}.

As a result, we argue that a similar chemical composition in polycrystalline Cu and Cu₂O is key to achieve similar activity of ethylene production, as supported by the results during the first hour of activity of Cu and Cu₂O samples (fig. 2). Specifically, X-ray photoelectron spectroscopy (XPS) reveals that polycrystalline Cu initially possesses native oxide surface layers (fig. S9) as it is well known that Cu is readily oxidized in air¹⁵. The co-existence of native surface oxygen and Cu⁰ substrate makes polycrystalline Cu surface similar to a very thin MEOM structure. Meanwhile, the disordered Cu⁰/Cu₂O character was naturally formed on Cu₂O under CO₂RR, as shown in Fig. 2 B, C and D. Thus, similar rates for C₂ products obtained on polycrystalline Cu and Cu₂O during 1 h CO₂RR can be interpreted by taking into account that MEOM structure of polycrystalline Cu and disordered Cu⁰/Cu₂O

character of Cu₂O share a similar kinetic barrier for C-C coupling, as mentioned earlier. However, as native oxygen on polycrystalline Cu is depleted under CO₂RR at -1.0 V_{RHE}, the population of the thin MEOM structure will decrease rapidly over time. In addition, theoretical calculations suggest that disordered Cu⁰ surface in Cu₂O would stabilize to crystalline Cu⁰ after oxygen is fully depleted. In this context, we consider that the long-term CO₂RR selectivity and activity toward ethylene on polycrystalline Cu and Cu₂O catalysts should be time dependent, which is associated with contents of buried oxygen. As buried oxygen is removed completely, it transforms to pure crystalline Cu⁰, resulting in H₂ as the overwhelmingly dominant product, as predicted by the DFT calculations.

6.5. Long-term CO₂RR Activities of Cu and Cu₂O Catalysts

To validate this hypothesis, we further synthesized a thin-Cu₂O with 0.2 μm thickness (fig. S10) and now refer to the 1.0 μm Cu₂O discussed above as thick-Cu₂O. We proceeded to carry out long-term measurements of product distributions on polycrystalline Cu, thin-Cu₂O, and thick-Cu₂O (Fig. 4) at -1.0 V_{RHE} with CO₂-saturated 0.1 M K₂CO₃ electrolyte. As expected, selectivity and production rate of ethylene rapidly decayed on polycrystalline Cu catalyst within 1 h due to the depletion of native oxygen, while the HER rates increase with time. XPS analysis on polycrystalline Cu after 16 h measurements further excludes the role of Pt contamination in determining the HER (fig. S11). By contrast, selectivity and production rate of ethylene on thin-Cu₂O and thick-Cu₂O slightly increased over the first 4 h, which is consistent with the increasing populations of disordered Cu⁰/Cu₂O

character as shown in Fig.2B. Then production rate of ethylene on thin-Cu₂O and thick-Cu₂O slowly decayed over time as disordered Cu⁰/Cu₂O character relaxed back to crystalline Cu⁰ through long-term CO₂RR (fig. S12), in line with DFT predictions. The reservoir of buried oxygen diffuses to the surface to replace depleted subsurface oxygen, maintaining the populations of active MEOM or Cu⁰/Cu₂O structure for ethylene production over long-term CO₂RR. Once subsurface oxygen is completely removed to form pure crystalline Cu⁰, C₂ production goes eventually to a level 1600 smaller than HER for polycrystalline Cu and 680 times lower for Cu₂O catalysts, in excellent agreement with theory predictions. In particular for all cases, ethylene production finally became negligible with sufficient time: 9 h for polycrystalline Cu, 16 h for thin-Cu₂O, and 23 h for thick-Cu₂O.

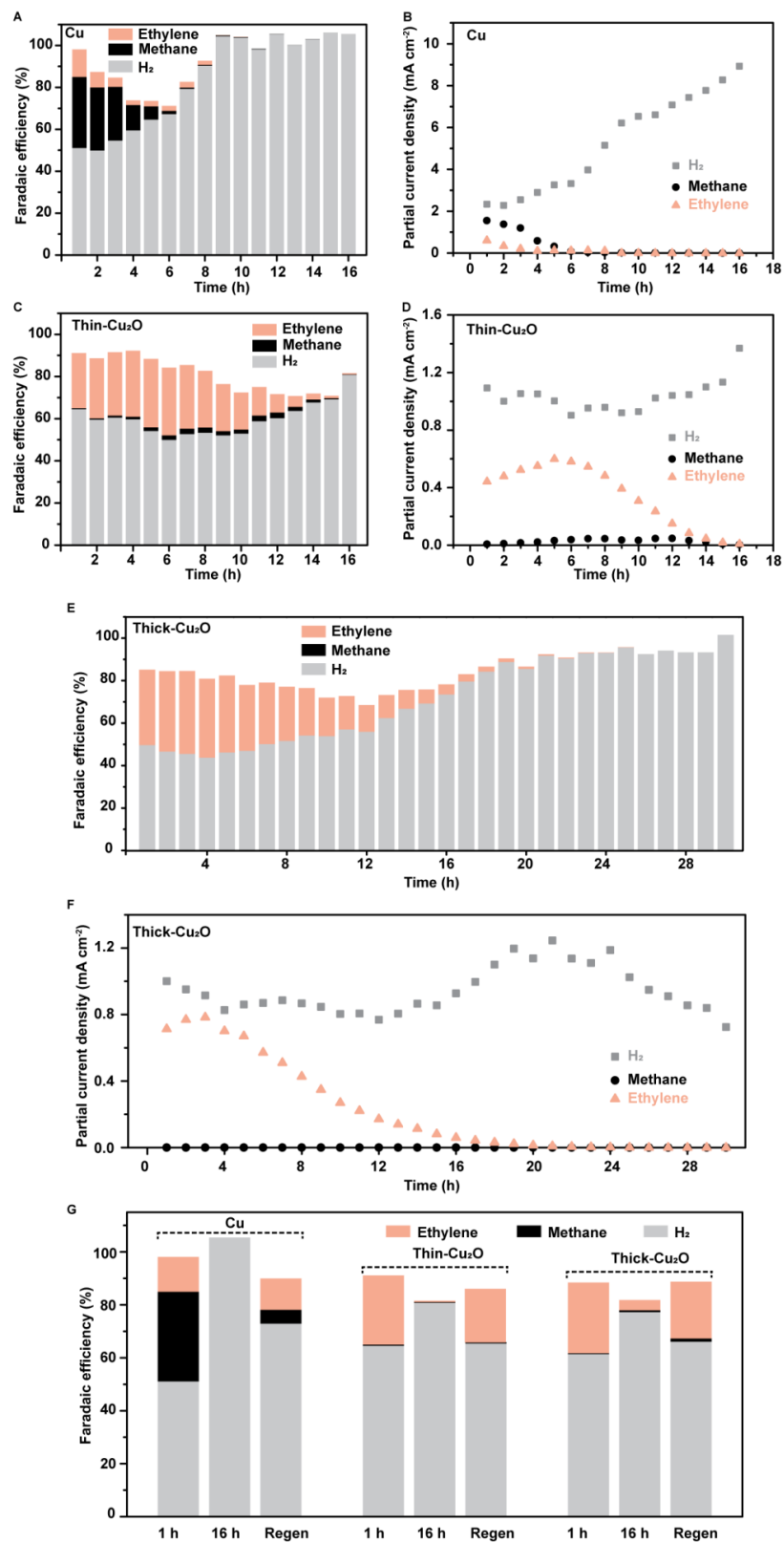


Figure 6-4. Long-term CO₂RR measurements on polycrystalline Cu, thin-Cu₂O and thick-Cu₂O FE of (A) polycrystalline Cu, (B) thin-Cu₂O, (C) thick-Cu₂O at -1.0 V_{RHE} in CO₂-saturated 0.1 M K₂CO₃ electrolyte (pH 7) for CO₂RR over time; Partial current densities toward H₂, methane, and ethylene of (D) polycrystalline Cu, (E) thin-Cu₂O, (F) thick-Cu₂O at -1.0 V_{RHE} in CO₂-saturated 0.1 M K₂CO₃ electrolyte (pH 7) for CO₂RR over time, normalized by electrochemically active surface area (ECSA); (G) FE of Cu, thin-Cu₂O and thick-Cu₂O after 1 h CO₂RR, 16 h CO₂RR and Cu, thin-Cu₂O and thick-Cu₂O experienced 16 h CO₂RR followed by a regeneration process: allowing the above catalysts to sit in air for about two weeks; at -1.0 V_{RHE} in CO₂-saturated 0.1 M K₂CO₃ electrolyte (pH 7).

Notably, we demonstrate that after 16 h CO₂RR polycrystalline Cu, thin-Cu₂O and thick-Cu₂O catalysts were able to largely recover their initial selectivity towards ethylene production, 92%, 77%, and 78% of their initial activity respectively (Fig. 4G). This result was obtained by simply allowing them to regain a native oxide layer via re-oxidization in air. Taken these results together, we conclude that the activity and selectivity of polycrystalline Cu and Cu₂O catalysts toward ethylene are influenced by the oxygen content within the Cu based catalysts.

This explanation is further corroborated by angle resolved X-ray photoelectron spectroscopy (AR-XPS) analysis over as-prepared polycrystalline Cu, Cu after 1 h CO₂RR and Cu after 16 h CO₂RR (Fig. 5). To minimize the oxidation of the sample in air, the sample was rinsed, dried with N₂ flow and transferred to the vacuum chamber of XPS within 2 minutes after the CO₂RR measurements were completed. The O 1s spectra show that lattice oxygen decreases with increasing take-off angle on both as-prepared polycrystalline Cu and Cu after 1 h CO₂RR, indicating that subsurface lattice oxygen is present²⁸. In contrast, only surface absorbed OH/H₂O is observed on polycrystalline Cu after 16 h CO₂RR (Fig. 5), which is consistent with Cu 2p and Cu LMM spectra (fig. S13 and fig. S14). Similarly, lattice oxygen was observed on as-

prepared thin-Cu₂O and thin-Cu₂O after 1h CO₂RR but was absent after 16 h CO₂RR (fig. S15 and S16).

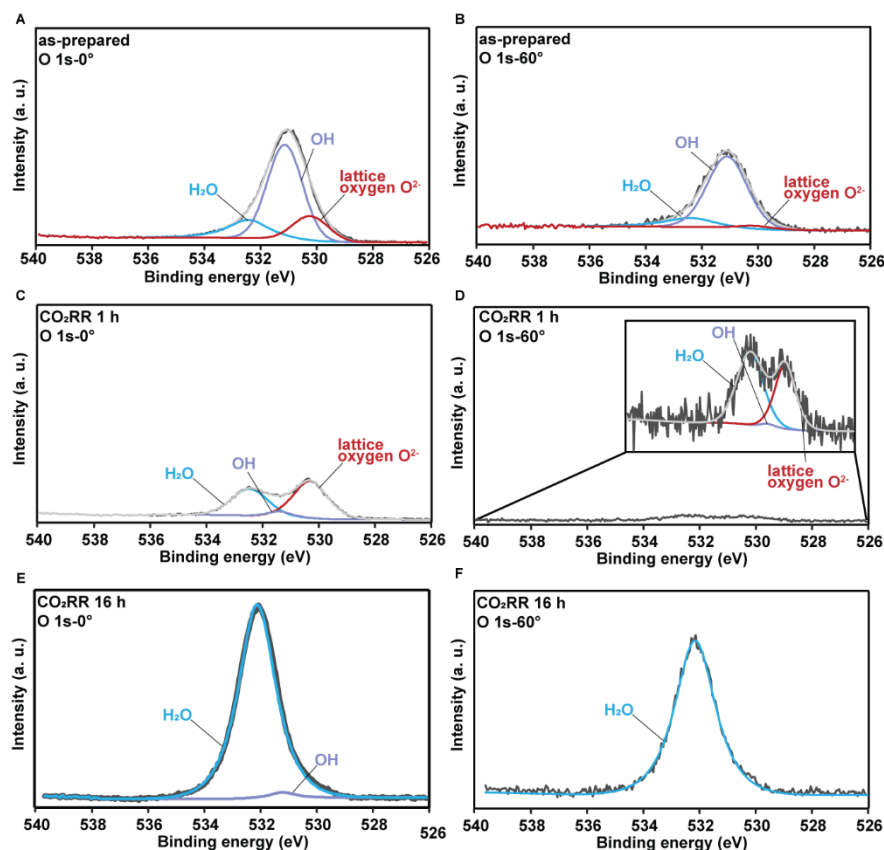


Figure 6-5. Chemical composition analysis of polycrystalline Cu through long-term CO₂RR (A) O_{1s} spectrum of as-prepared polycrystalline Cu at 0°; (B) O_{1s} spectrum of as-prepared polycrystalline Cu at 60°; (C) O_{1s} spectrum of polycrystalline Cu after 1h CO₂RR at 0°; (D) O_{1s} spectrum of polycrystalline Cu after 1h CO₂RR at 60°; (E) O_{1s} spectrum of polycrystalline Cu after 16 h CO₂RR at 0°; (F) O_{1s} spectrum of polycrystalline Cu after 16 h CO₂RR at 60°.

6.6. Conclusion

These findings highlight the essential role of subsurface oxygen in C₂ production on Cu-based catalysts and how this role is related to the inducing the formation of disordered Cu⁰. The disordered Cu⁰/Cu₂O structure represents the thermodynamically

stable structure of Cu₂O based catalysts under CO₂RR, which substantially enhances intrinsic C₂ production, compared to pure crystalline Cu⁰. It can be achieved by dynamic transformation of Cu-based nanocrystals under CO₂RR conditions^{6, 29, 30}. While previous studies on subsurface oxygen on Cu demonstrate that subsurface oxygen may not play an essential role in CO₂ adsorption³¹, Nilsson and coworkers show that subsurface oxygen on Cu is instrumental in enhancing CO adsorption, which can lead to an improved C₂ selectivity^{32, 33}. In contrast, for the first time we propose to calculate C₂ and HER rates on various Cu-based models and further demonstrate that the presence of buried oxygen aids retention and long-term stability of a disordered Cu⁰ surface active towards C₂ production. This finding can explain why disordered Cu-based catalysts and uncoordinated Cu sites at grain boundaries have higher selectivity for C₂ products^{8, 17, 30, 34}. Thus, allowing the bulk oxygen of Cu catalysts to be replenished from other robust oxides under CO₂RR might be a promising direction to design efficient CO₂RR catalysts with sustained C₂ selectivity. Additionally, intrinsic ability of copper to be rapidly oxidized in air and to regain its catalytic ability is beneficial to developing a sustainable/recyclable catalyst.

In summary, we provide mechanistic insights into C₂ production over Cu based catalysts by GCP-K DFT calculations, showing that for pure Cu (111) with no subsurface oxygen the rate of C₂ production is ~500 times smaller than HER, whereas reduced models starting with Cu₂O lead to C₂ production ~ 10,000 times faster. Furthermore, we combined time dependent product detection with a multi-modal characterization technique to confirm that activity and selectivity of polycrystalline Cu and Cu₂O catalysts toward ethylene is determined by the disordered Cu⁰/Cu₂O

character involving oxygen content within Cu based catalysts. Comparing to the MEOM structure, the formation of a disordered Cu⁰ surface induced by removal of lattice oxygen from Cu₂O is thermodynamically favorable under CO₂RR. After long-term CO₂RR, pure crystalline Cu⁰ without subsurface oxygen leads only to HER at -1.0 V_{RHE} in aqueous solutions, in excellent agreement with the DFT calculations. Based on this new theoretical and experimental understanding, we conclude that the key for the rational development of highly active electrocatalysts toward C₂ production is to modify the catalyst conditions in such a way as to preserve surface or subsurface oxygen in the Cu catalyst under CO₂RR conditions.

6.8. Experimental Procedures

6.8.1. Materials and Methods

6.8.1.1. Chemicals

All chemicals were obtained from commercial suppliers and used without further purification, unless otherwise noted. Copper sulfate pentahydrate (98%), lactic acid (85%), sodium hydroxide (98%) were purchased from Sigma Aldrich. Nitric acid (70%) and high purity potassium carbonate (99.995%) were purchased from Sigma Aldrich. Hydrochloric acid (36.5 – 38%) was purchased from VWR. Isopropyl alcohol (100%) was purchased from KMG electronic chemicals. Water used for all of the synthesis and electrochemical experiments (MilliQ water) was from a Milli-Q Water Purification System (resistivity of 18.2 MΩ-cm, Millipore). Selemion AMV anion-exchange membrane was purchased from AGC Engineering Co., LTD. Carbon dioxide (99.995%) and nitrogen (99.999%) were obtained from Praxair.

6.8.1.2. Electrodeposition of Cu₂O

In a typical experiment, a 0.4 M copper sulfate pentahydrate solution was used as the plating solution, prepared by stirring 4.99 g $\text{CuSO}_4 \cdot 5\text{H}_2\text{O}$ in 50 mL of MilliQ water. 3 M (13.51 g) of lactic acid was added to stabilize Cu^{2+} in basic solution, and then 3 M NaOH was added to the solution until the pH of plating solution reaches 12. Cu_2O (thick) and Cu_2O (thin) were deposited on Cu foils (99.999%, Alfa Aesar) for 150 and 15 min, respectively, at a constant current density (-0.1 mA/cm^2) in a three electrodes configuration under room temperature. To obtain a uniform coating, the Cu foil was mechanically polished with sandpapers (1200G Wetordry sandpaper, 3M) and electropolished in 85% phosphoric acid at +2.1 V for 5 min, followed by annealing in air at 300 °C for 30 min prior to use. After the deposition, the sample was gently rinsed with MilliQ water and then dried with a nitrogen gun.

6.8.1.3. Materials characterizations

Scanning electron microscopy (SEM) images were obtained on a scanning electron microscope (Quanta FEG 250, 148 FEI). Quasi in-situ electrochemical atomic force microscopy (EC-AFM) was carried out using a commercial AFM system (Bruker Dimension ICON). PeakForce mode was used to acquire the surface morphology. A planar Cu or Cu₂O samples was compressed within an electrochemical cell as the working electrode and two platinum wires were used as counter electrode and reference electrode. The pristine surface was measured first, then the probe was withdrew and a constant bias with -0.8V vs. RHE was applied to the sample. The surface after this EC treatment was visited again to track the change over time. The surface chemical composition was obtained by XPS using a Kratos Axis Ultra DLD system at a takeoff angle of 0° relative to the surface normal. A monochromatic Al K α source with emission energy of 1486.6 eV was used to excite the core level electrons of the material. C 1s, Cu 2p, and O 1s core levels were collected, with pass energy of 20 eV, step size of 0.05 eV, and 10 sweeps each to obtain a good signal to noise ratio. The sample was loaded to the chamber within 2 minutes after the EC test was done to minimize the oxidation of the material. Spectral fitting was conducted using CasaXPS analysis software. The angle-resolved XPS (AR-XPS) with the sample bar tilted with 60° was also conducted to obtain more surface information.

6.8.1.4. Product detection

Electrochemical experiments were conducted in a two-compartment flow cell fabricated from PEEK (fig. S2C). A Selemion AMV anion-exchange membrane separated the two chambers. A Pt foil was used as the counter electrode. A Leak-Free

Ag/AgCl electrode (LF-1, 1.0 mm outer diameter, Innovative Instruments, Inc.) was used as the reference electrode. The reference electrode was calibrated against a second reference electrode, which in turn was calibrated in a two-electrode system with H₂ bubbled over a Pt wire as the counter electrode and a 1M H₂SO₄ solution as the electrolyte. The applied potentials were converted from Ag/AgCl scale to the RHE scale via the equation: $E_{\text{RHE}} = E_{\text{Ag/AgCl}} + 0.197 + 0.059 \times \text{pH}$, where the pH used is the bulk pH for the CO₂-saturated electrolyte (6.9). In the electrochemical cell, the prepared 0.1 M potassium carbonate solution was used as electrolyte. The electrolyte was saturated with a continuous flow of 5 sccm CO₂ for a minimum of 15 minutes within the experimental cell setup immediately prior to all electrochemical experiments. One cycle of chronoamperometric (CA) measurement was performed by applying a constant potential for 65 minutes. Electrochemical experiments were carried out using SP-200 potentiostat from BioLogic. Cyclic voltammetry (CV) was then performed and repeated at the end of each run in order to test the stability of material before and after the chronoamperometric measurement. Chronoamperometric measurement was performed for about 65 minutes. Gas products were quantified using gas chromatography (GC), SRI Instruments with multiple gas analyzer #5, through flow mode. Liquid products were quantified after electrochemical measurement using high performance liquid chromatography (HPLC), UltiMate 3000. During the chronoamperometric measurement, gas from the cell was directed through the sampling loop of a gas chromatograph and was analyzed in 15 minutes intervals. For each interval, concentration of gas produced was collected. With total current density measured at the end of experiment and applied potential, faradaic efficiency for each

gas for each interval was calculated. These recorded faradaic efficiencies were averaged and reported.

6.8.1.5. Computational Details

Our QM calculations used the Vienna ab initio simulation package (VASP)^{35, 36} with the VASPsol solvation model³⁷ for geometry optimization followed by single point calculations as a function of applied potential using the CANDLE solvation model³⁸ as incorporated in the joint density-functional theory (JDFTx)³⁹.

The electron exchange and correlation were treated within the generalized gradient approximation (GGA)⁴⁰ in the form of the PBE functional, including the D3 correction for London Dispersion (van der Waals attraction).⁴¹ The interaction between the ionic core and the valence electrons was described by the projector-augmented wave (PAW) method.⁴² We used a plane-wave basis up to an energy cutoff of 500 eV. The Brillouin zone was sampled using the 3x3x1 Monkhorst-Pack grid.⁴³ The convergence criteria for the electronic structure and the atomic geometry were 10^{-5} eV and 0.03 eV/Å for IS and FS and 0.01 eV/Å for TS, respectively. We exploited VTST package to search transition state (TS) using both CI-NEB⁴⁴ and the dimer method.⁴⁵

The Gibbs free energies were calculated at 298 K and 1 atm as following:

$$G = H - T\Delta S = E_{DFT} + E_{ZPE} + E_{solv} + \int_0^{298} C_v dT - T\Delta S$$

Where E_{DFT} is the total energy, E_{ZPE} is zero-point vibrational energy, E_{solv} is the solvation energy, $\int_0^{298} C_v dT$ is the heat capacity, and ΔS is the change in entropy.

The Cu (111) system was described by 4 layers of 4×4 supercell with two bottom layers were fixed. Pristine Cu₂O and oxide-derived Cu were described by four tri-

layers of 4 x 4 supercell with two bottom tri-layers were fixed. The model system was described by 3 layers of 4×4 Cu slab with 20 Å of vacuum. The bottom two layers are fixed. All designed models have > 20 Å vacuum.

6.9. Supplementary Figures

6.9.1. H₂ and C₂ production on Cu metal embedded in oxidized matrix (MEOM) model

In a previous study, we suggested the MEOM model in which the surface has adjacent oxidized and metallic regions.⁽⁹⁾ On MEOM, we predict that C-C coupling has a kinetic barrier of 0.71 eV which is 0.4 eV lower compared to that on Cu(111). We showed that the enhancement of C-C coupling on this catalyst is due to the attractive electrostatics involving a carbon on the positively charge Cu⁺ induced by subsurface oxygen next to a C bound to a Cu⁰ site.

In our new calculation on this MEOM catalyst using GCP-K method, we find that C-C coupling has a kinetic barrier of $\Delta G^\ddagger = 0.72$ eV while the RDS for HER (the Heyrovsky reaction) has a barrier of $\Delta G^\ddagger = 1.02$ eV. This leads to a C₂/H₂ ratio of 1.23×10^6 . Compared to Cu(111), C-C coupling is 7.03×10^3 times faster but HER is 1.19×10^{-4} times slower.

All configurations for IS, TS, and FS of C-C coupling, Volmer and Heyrovsky reactions are depicted in Fig. S3-5.

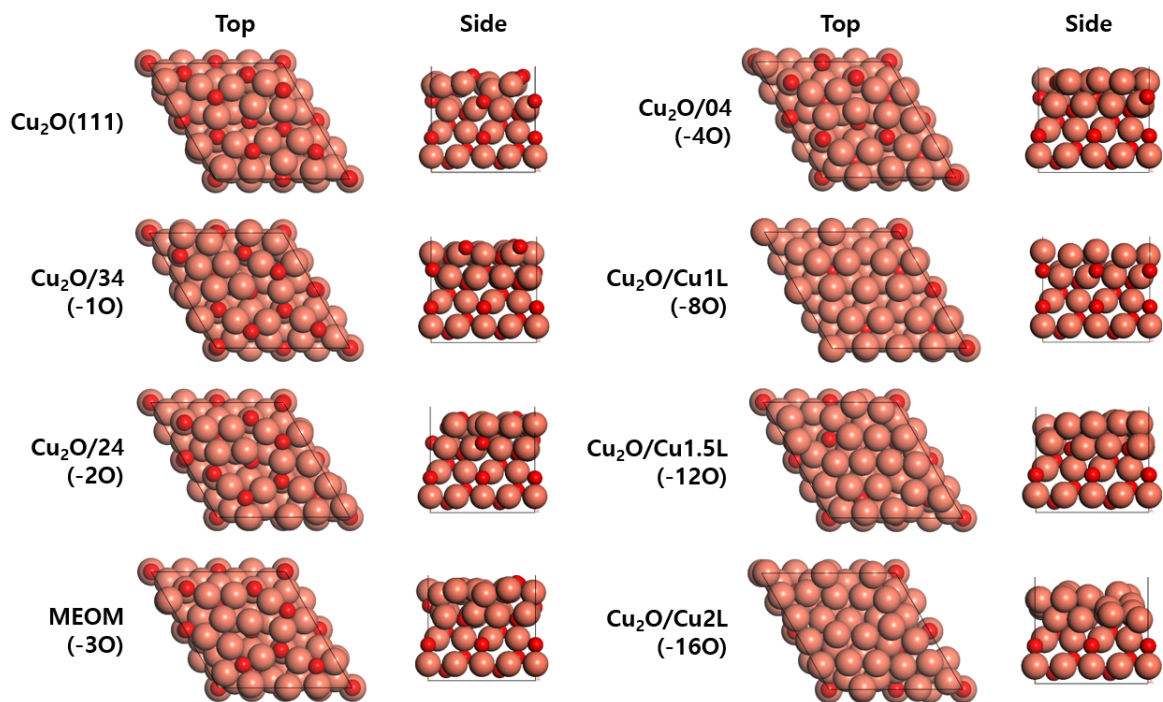


Figure S6-1. Top and side views of various surface phases considered in surface free energy diagrams. Total numbers of oxygen on the top/bottom layers in the top tri-layer (O-Cu-O). The number of reduced oxygen also indicated in the parenthesis.

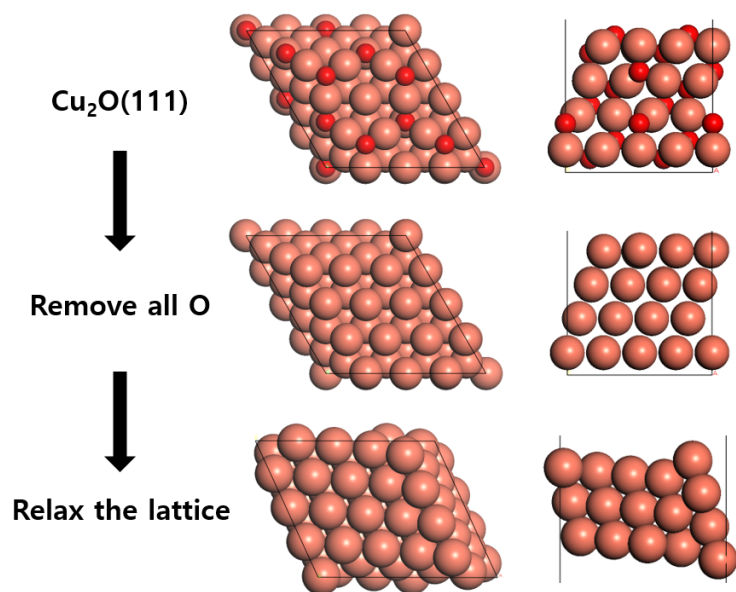


Figure S6-2. Full relaxation after removing all oxygen from $\text{Cu}_2\text{O}(111)$. The final $\text{Cu}(\text{S})[4(111) \times (111)]$ surface has (111) terrace with (111) step. We speculate that the step originates from the small size of supercell we used.

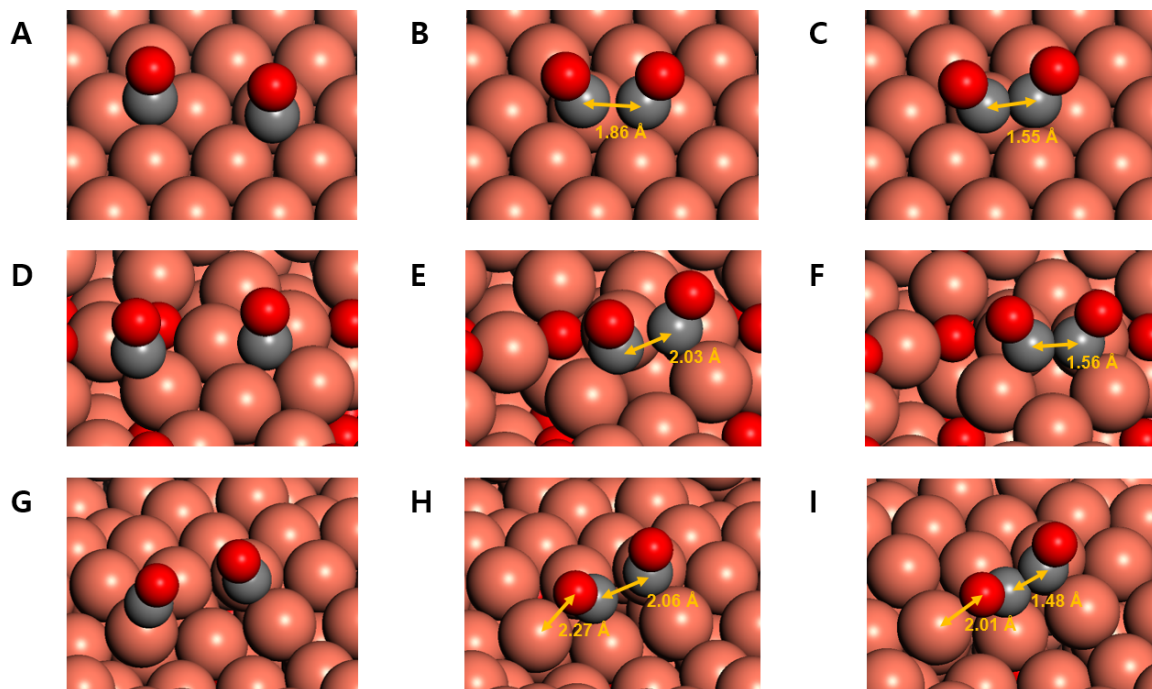


Figure S6-3. The atomic configurations of CO dimerization reaction on (A-C) Cu(111), (D-F) MEOM and (G-I) Cu⁰/Cu₂O catalysts. (A, D, G), (B, E, H), and (C, F, I) corresponds to the initial (IS), transition (TS) and final states (FS), respectively. The C-C bond distances are indicated for all TS and FS and Cu-O bond distance is also indicated for Cu⁰/Cu₂O catalysts.

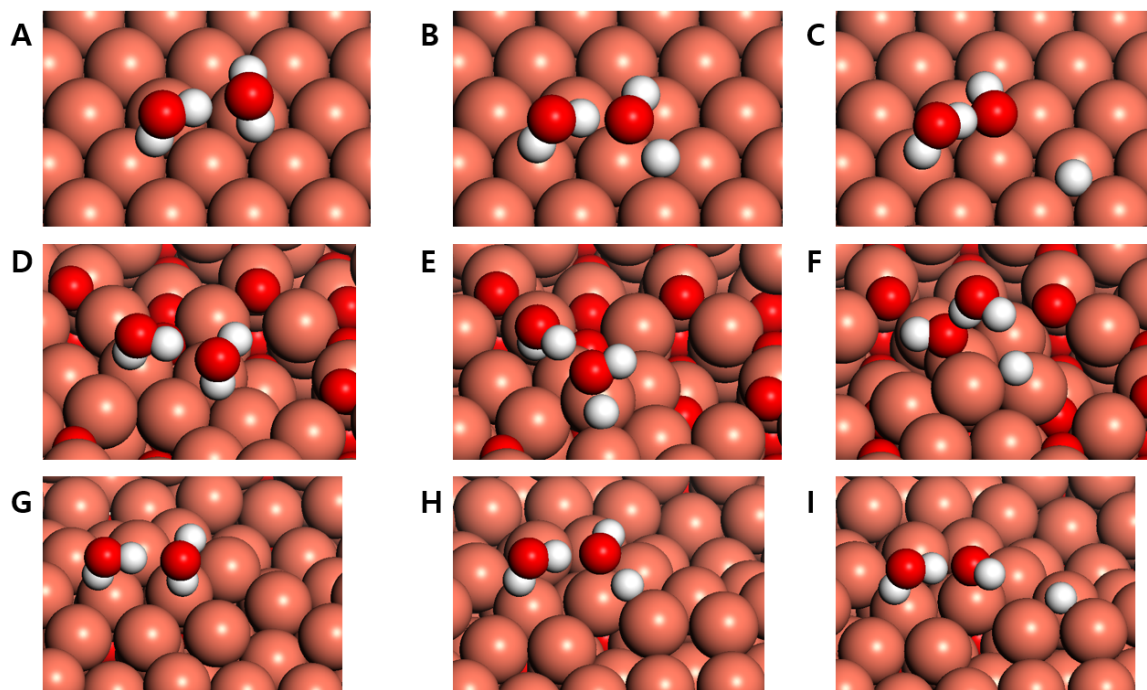


Figure S6-4. The atomic configurations of Volmer reactions on (A-C) Cu(111), (D-F) MEOM and (G-I) $\text{Cu}^0/\text{Cu}_2\text{O}$ catalysts. (A, D, G), (B, E, H), and (C, F, I) corresponds to the initial (IS), transition (TS) and final states (FS), respectively.

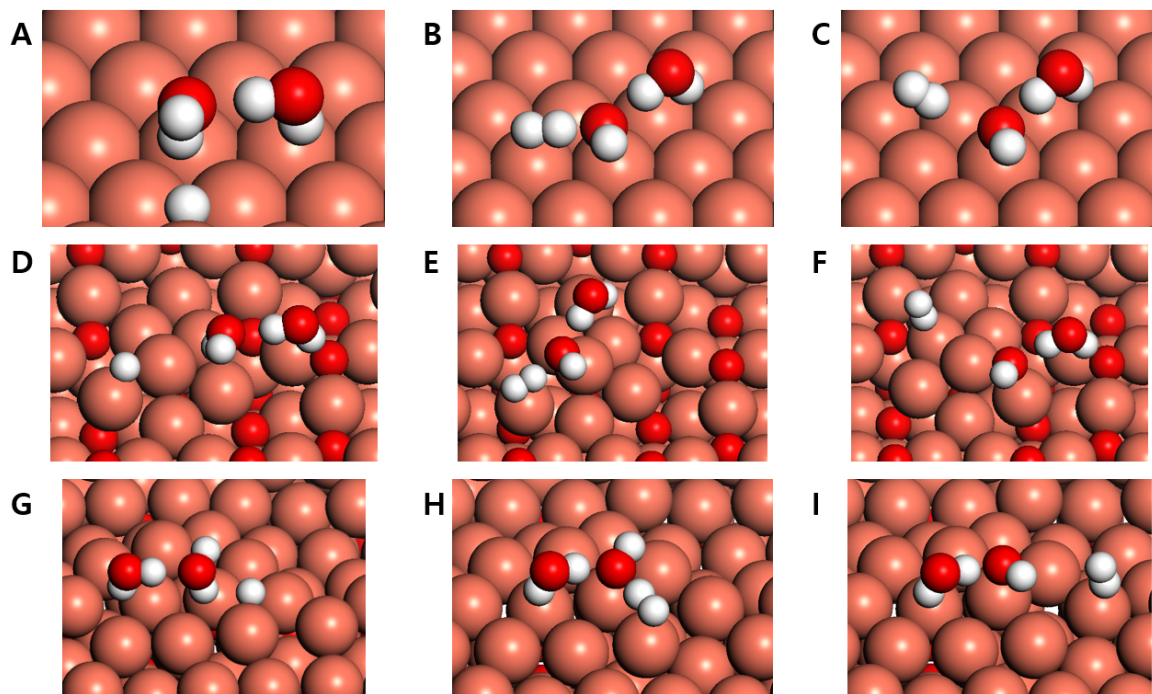


Figure S6-5. The atomic configurations of Heyrovsky reactions on (A-C) Cu(111), (D-F) MEOM and (G-I) Cu⁰/Cu₂O catalysts. (A, D, G), (B, E, H), and (C, F, I) corresponds to the initial (IS), transition (TS) and final states (FS), respectively.

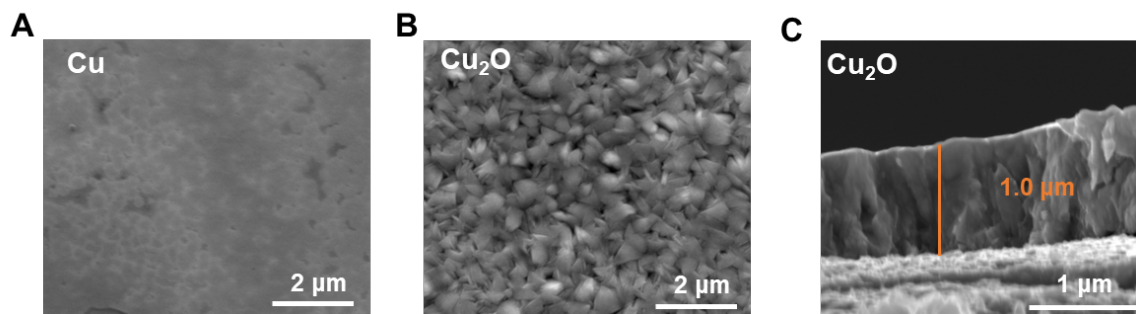


Figure S6-6. SEM images of (A) as-prepared Cu; (B) as-prepared Cu₂O; (C) Cross-section of as-prepared Cu₂O.

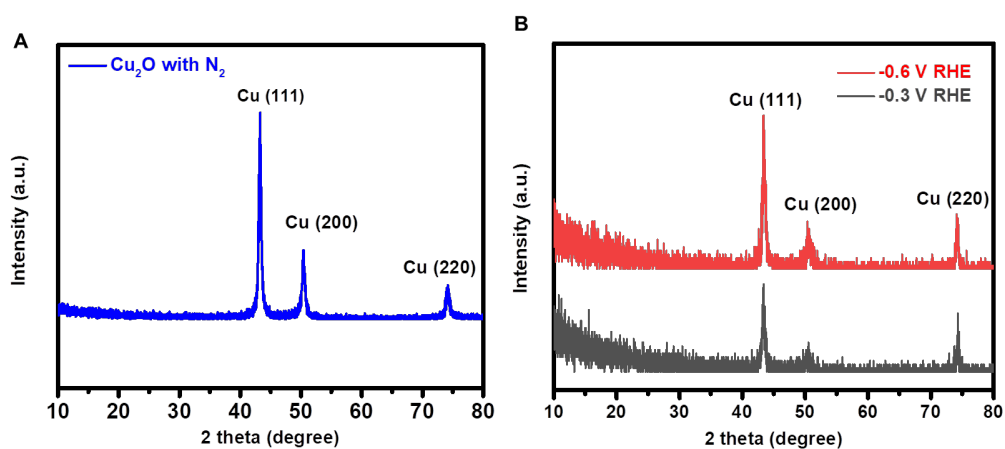


Figure S6-7. *ex-situ* GIXRD analysis of Cu₂O over 1h electrolysis (A) at -1.0 V_{RHE} in N₂-saturated 0.1 M KHCO₃ electrolyte (pH 8); (B) at -0.3 V_{RHE} and -0.6 V_{RHE} in CO₂-saturated 0.1 M K₂CO₃ electrolyte (pH 7).

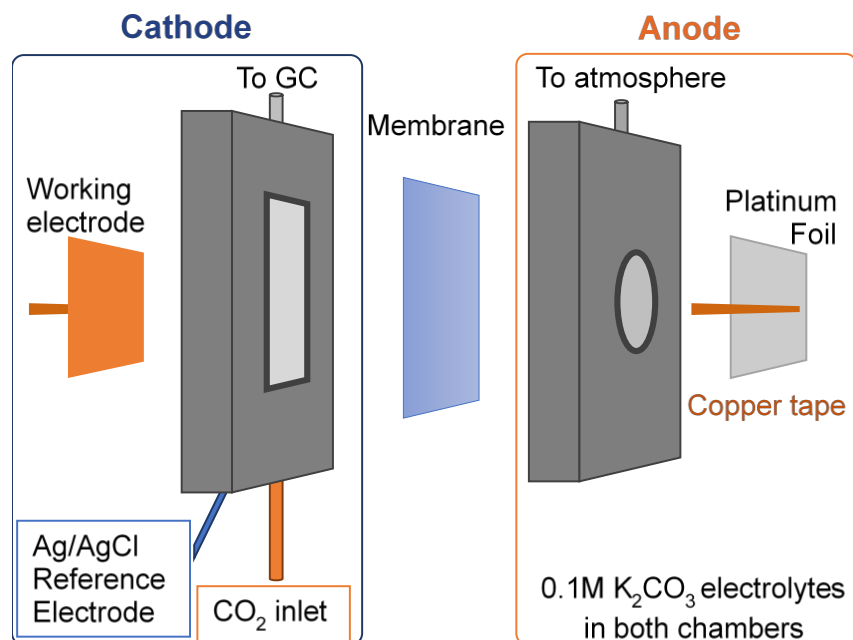


Figure S6-8. Two-compartment flow cell used for bulk electrolysis of carbon dioxide.

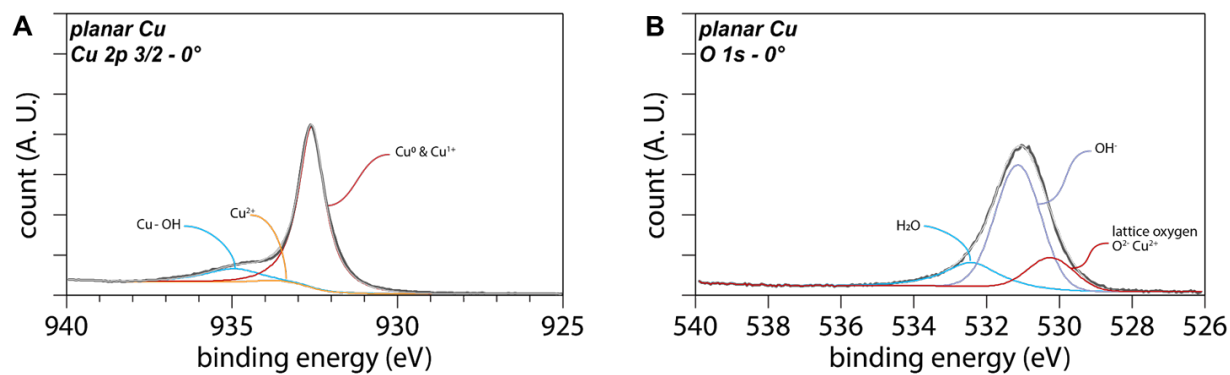


Figure S6-9. XPS analysis on as-prepared Cu: (A) Cu_{2p} spectra of Cu; (B) O_{1s} spectra of Cu.

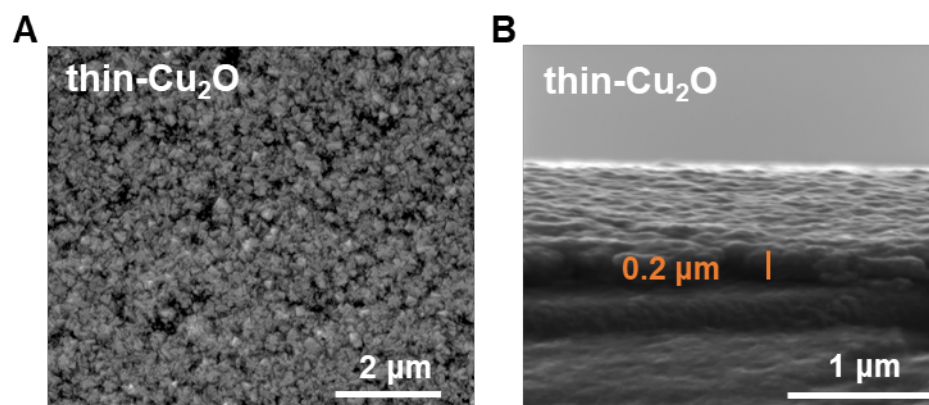


Figure S6-10. SEM images of (A) thin-Cu₂O; (B) Cross-section of thin-Cu₂O.

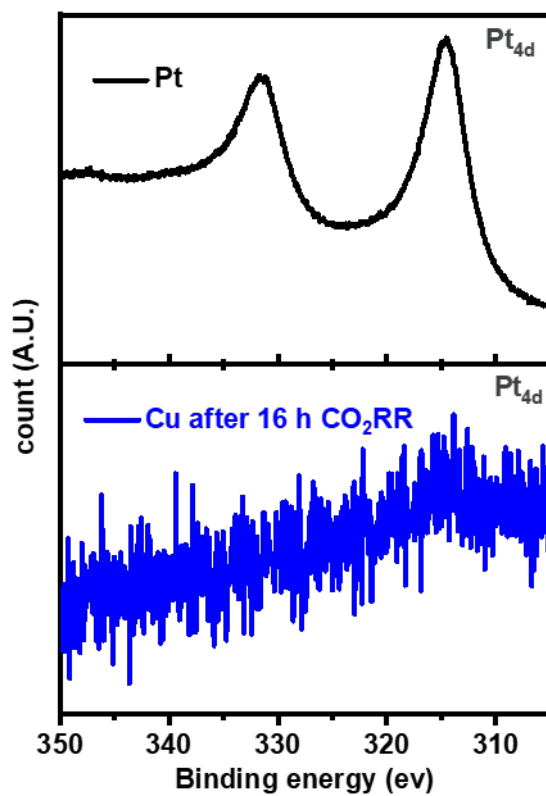


Figure S6-11. Pt_{4d} spectra of Cu through long-term CO₂RR at -1 V_{RHE} in 0.1 M K₂CO₃ electrolyte (pH 7), a Pt foil was used as comparison. No contamination of Pt was found on Cu through long-term CO₂RR.

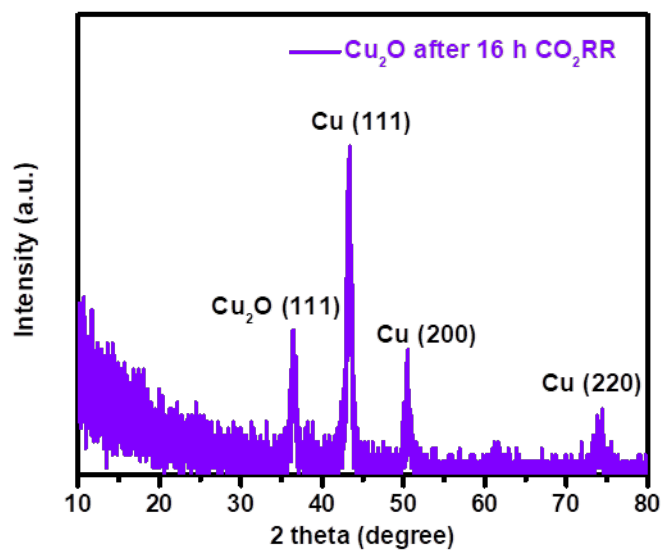


Figure S6-12. *ex-situ* GIXRD analysis of thick-Cu₂O over 16 h CO₂RR at -1.0 V_{RHE} in CO₂-saturated 0.1 M K₂CO₃ electrolyte (pH 7).

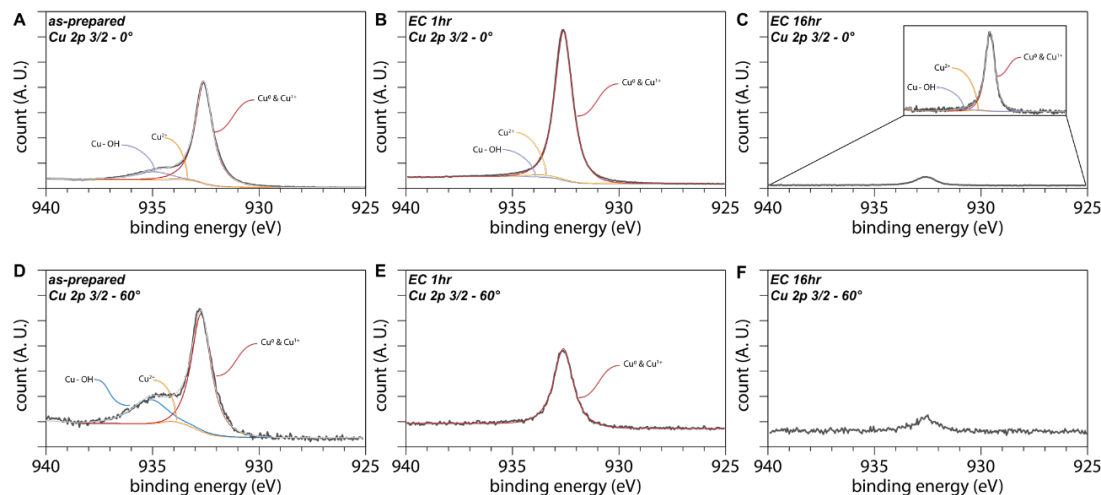


Figure S6-13. AR-XPS analysis of Cu_{2p} spectra on Cu through long-term CO₂RR: (A) Cu_{2p} spectrum of as-prepared Cu at 0°; (B) Cu_{2p} spectrum of Cu after 1h CO₂RR at 0°; (C) Cu_{2p} spectrum of Cu after 16 h CO₂RR at 0°; (D) Cu_{2p} spectrum of as-prepared Cu at 60°; (E) Cu_{2p} spectrum of Cu after 1h CO₂RR at 60°; (F) Cu_{2p} spectrum of Cu after 16 h CO₂RR at 60°.

At 0°: from as prepared sample, small amount of CuO and Cu(OH)₂ exist at the surface of as prepared Cu, while after CO₂RR, both OH and CuO are gradually removed, especially in CO₂RR 16 h case, both CuO and Cu(OH)₂ are negligible.

At 60°: for as-prepared Cu, OH exists at the topmost surface since the intensity increased with the increasing of angle; interestingly, no CuO peak can be observed on CO₂RR 1h and CO₂RR 16h samples, indicating that there were still some subsurface oxygen left after 1h CO₂RR but totally got depleted after 16h.

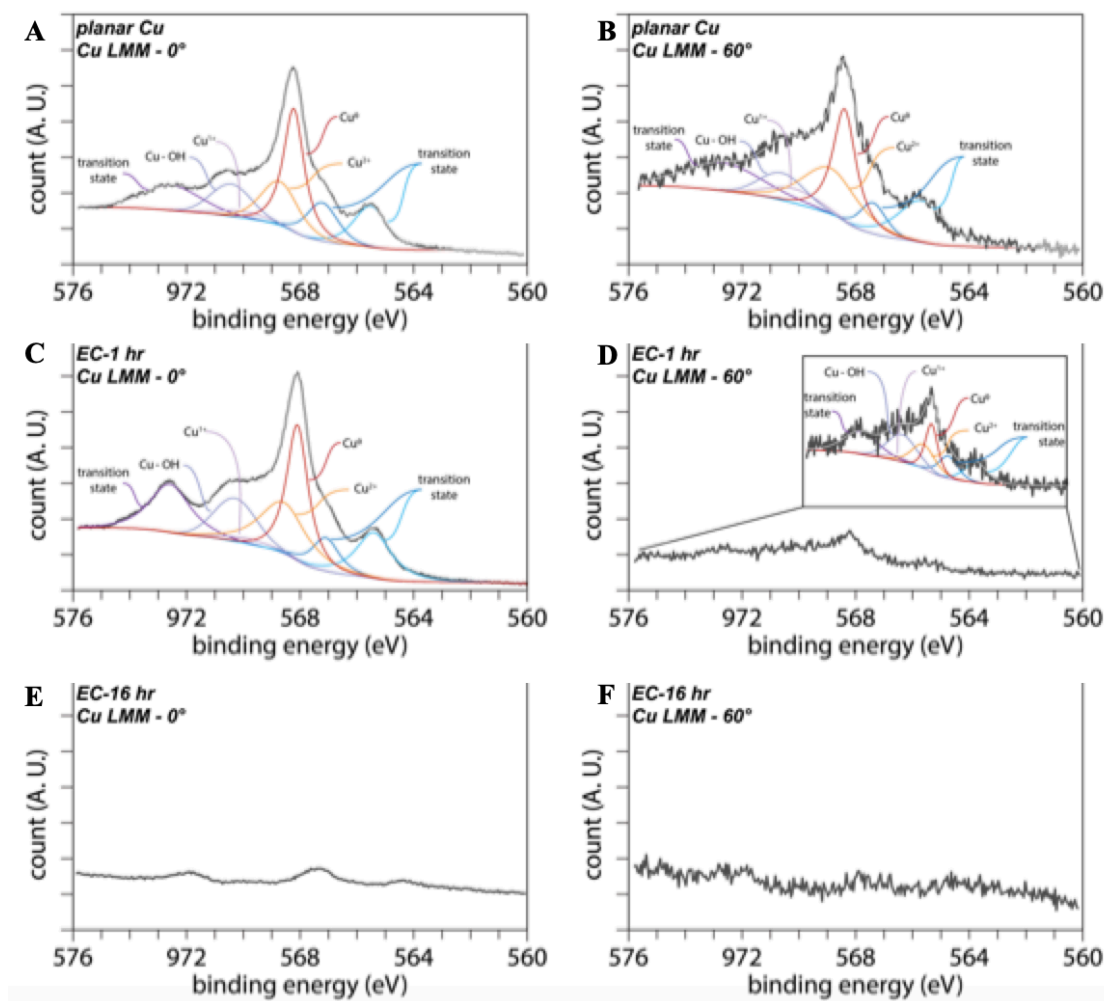


Figure S6-14. AR-XPS analysis of Cu LMM spectra on Cu through long-term CO₂RR: (A) Cu LMM spectrum of as-prepared Cu at 0°; (B) Cu LMM spectrum of Cu after 1h CO₂RR at 0°; (C) Cu LMM spectrum of Cu after 16 h CO₂RR at 0°; (D) Cu LMM spectrum of as-prepared Cu at 60°; (E) Cu LMM spectrum of Cu after 1h CO₂RR at 60°; (F) Cu LMM spectrum of Cu after 16 h CO₂RR at 60°.

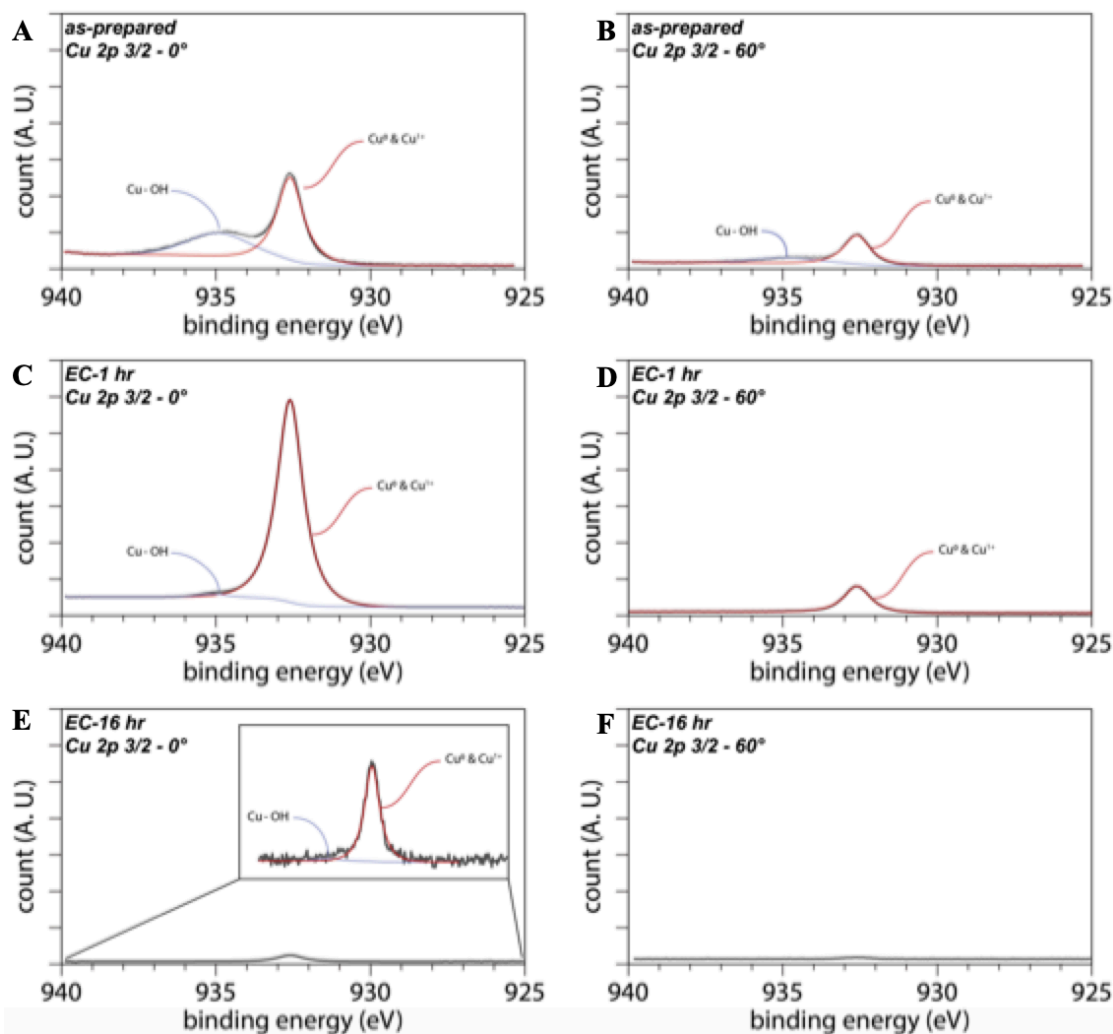


Figure S6-15. AR-XPS analysis of Cu_{2p} spectra on thin- Cu_2O through long-term CO_2RR : (A) Cu_{2p} spectrum of as-prepared thin- Cu_2O at 0° ; (B) Cu_{2p} spectrum of thin- Cu_2O after 1 h CO_2RR at 0° ; (C) Cu_{2p} spectrum of thin- Cu_2O after 16 h CO_2RR at 0° ; (D) Cu_{2p} spectrum of as-prepared thin- Cu_2O at 60° ; (E) Cu_{2p} spectrum of thin- Cu_2O after 1 h CO_2RR at 60° ; (F) Cu_{2p} spectrum of thin- Cu_2O after 16 h CO_2RR at 60° .

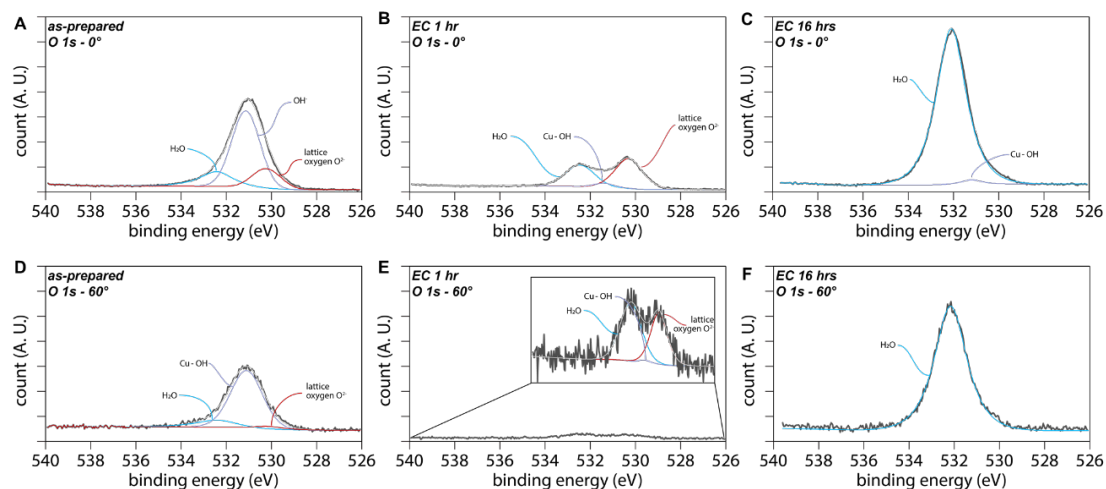


Figure S6-16. AR-XPS analysis of O_{1s} spectra on thin- Cu_2O through long-term CO_2RR : (A) O_{1s} spectrum of as-prepared thin- Cu_2O at 0° ; (B) O_{1s} spectrum of thin- Cu_2O after 1h CO_2RR at 0° ; (C) O_{1s} spectrum of thin- Cu_2O after 16 h CO_2RR at 0° ; (D) O_{1s} spectrum of as-prepared thin- Cu_2O at 60° ; (E) O_{1s} spectrum of thin- Cu_2O after 1h CO_2RR at 60° ; (F) O_{1s} spectrum of thin- Cu_2O after 16 h CO_2RR at 60° .

6.10. Supplementary Tables

Cu ₂ O			-1O			-2O			MEOM (-3O)		
F(n)	n	mu	F(n)	n	mu	F(n)	n	mu	F(n)	n	mu
-	140	-	-	140	-	-	139	-	-	139	-0.1587
13432.21506	8	0.14296	13416.11743	2	0.15453	13400.00752	6	0.15436	13383.95043	0	
-	140	-	-	140	-	-	139	-	-	139	-
13432.36341	9	0.14296	13416.26613	3	0.14448	13400.15734	7	0.14499	13384.10495	1	0.14908
-	141	-0.1326	-	140	-	-	139	-	-	139	-
13432.50228	0		13416.40748	4	0.13538	13400.29849	8	0.13669	13384.25007	2	0.13965
-	141	-	-	140	-	-	139	-0.1237	-	139	-
13432.62778	1	0.11769	13416.53726	5	0.12169	13400.42933	9		13384.38229	3	0.12477
-13432.7387	141	-	-	140	-0.1082	-	140	-	-	139	-
	2	0.10402	13416.65274	6		13400.54616	0	0.10993	13384.49954	4	0.10979
-	141	-	-	140	-	-	140	-	-	139	-
13432.83655	3	0.10402	13416.75597	7	0.09602	13400.65035	1	0.09762	13384.62088	5	0.10017

-4O			-8O			-12O			Cu ⁰ /Cu ₂ O (-16O)		
F(n)	n	mu	F(n)	n	mu	F(n)	n	mu	F(n)	n	mu
-	138	-	-13303.2219	136	-	-	133	-	-13174.7388	131	-
13367.75442	4	0.15408		0	0.15309	13239.00094	6	0.15459		2	0.15367
-	138	-	-	136	-	-	133	-	-	131	-0.1457
13367.90319	5	0.14451	13303.37003	1	0.14474	13239.15116	7	0.14657	13174.88743	3	
-	138	-	-	136	-	-	133	-	-	131	-
13368.04473	6	0.13847	13303.51278	2	0.13919	13239.29537	8	0.14079	13175.03112	4	0.14052
-	138	-	-	136	-	-	133	-	-	131	-
13368.17764	7	0.12651	13303.64706	3	0.12845	13239.43248	9	0.13018	13175.16648	5	0.12949
-	138	-	-	136	-	-	134	-	-	131	-
13368.29769	8	0.11364	13303.76959	4	0.11632	13239.55642	0	0.11772	13175.28965	6	0.11691
-	138	-	-	136	-	-	134	-	-	131	-
13368.40499	9	0.10126	13303.88063	5	0.10466	13239.66859	1	0.10581	13175.40041	7	0.10489

Table S6-1. Total energy (F), number of electrons (n), electrochemical potential (mu) for all eight states considered in surface Pourbaix diagram.

MEOM

CO dimerization

IS			TS			FS		
F(n)	n	mu	F(n)	n	mu	F(n)	n	mu
-13427.83973	1412	-0.13909	-13427.81051	1412	-0.14228	-13427.83317	1412	-0.14637
-13427.97097	1413	-0.12326	-13427.94472	1413	-0.12576	-13427.97158	1413	-0.12979
-13428.08664	1414	-0.10819	-13428.06252	1414	-0.11003	-13428.0931	1414	-0.11393

Volmer

IS			TS			FS		
F(n)	n	mu	F(n)	n	mu	F(n)	n	mu
-13418.83418	1408	-0.14015	-13418.81216	1408	-0.14476	-13418.84477	1408	-0.14193
-13418.96592	1409	-0.12345	-13418.95335	1409	-0.13082	-13418.97923	1409	-0.12686
-13419.08156	1410	-0.10887	-13419.08042	1410	-0.11764	-13419.0988	1410	-0.11237

Heyrovsky

IS			TS			FS		
F(n)	n	mu	F(n)	n	mu	F(n)	n	mu
-13419.45757	1409	-0.14178	-13419.42239	1409	-0.14127	-13419.44713	1409	-0.13915
-13419.59296	1410	-0.12728	-13419.55606	1410	-0.12615	-13419.57985	1410	-0.12554
-13419.71299	1411	-0.11308	-13419.6754	1411	-0.11295	-13419.69918	1411	-0.1133

Cu⁰/Cu₂O

CO dimerization

IS			TS			FS		
F(n)	n	mu	F(n)	n	mu	F(n)	n	mu
-13218.74903	1335	-0.12687	-13218.72147	1335	-0.12879	-13218.74827	1335	-0.1303
-13218.86999	1336	-0.11472	-13218.84385	1336	-0.11665	-13218.87234	1336	-0.11849
-13218.97714	1337	-0.10341	-13218.95389	1337	-0.10477	-13218.98454	1337	-0.10662

Volmer

IS			TS			FS		
F(n)	n	mu	F(n)	n	mu	F(n)	n	mu
-13209.61	1330	-0.13851	-13209.57892	1330	-0.13915	-13209.61369	1330	-0.14139
-13209.7438	1331	-0.12876	-13209.71332	1331	-0.12959	-13209.7499	1331	-0.13037

-13209.86704	1332	-0.11768	-13209.83361	1332	-0.11863	-13209.87409	1332	-0.11877
Heyrovsky								
IS			TS			FS		
F(n)	n	mu	F(n)	n	mu	F(n)	n	mu
-13210.20573	1331	-0.13851	-13210.18543	1331	-0.13861	-13210.18451	1331	-0.13984
-13210.33923	1332	-0.12835	-13210.31921	1332	-0.12867	-13210.3195	1332	-0.12948
-13210.46185	1333	-0.11698	-13210.44218	1333	-0.11757	-13210.44372	1333	-0.11892
Cu(111)								
CO dimerization								
IS			TS			FS		
F(n)	n	mu	F(n)	n	mu	F(n)	n	mu
-12962.10315	1238	-0.1391	-12962.06353	1238	-0.14341	-12962.0623	1238	-0.14069
-12962.23435	1239	-0.12245	-12962.19937	1239	-0.126	-12962.19991	1239	-0.12645
-12962.34825	1240	-0.10546	-12962.31237	1240	-0.10743	-12962.31941	1240	-0.11012
Volmer								
IS			TS			FS		
F(n)	n	mu	F(n)	n	mu	F(n)	n	mu
-12953.10715	1234	-0.13957	-12953.06883	1234	-0.14176	-12953.09661	1234	-0.14249
-12953.23919	1235	-0.1236	-12953.20295	1235	-0.12565	-12953.23128	1235	-0.12586
-12953.35446	1236	-0.10693	-12953.32358	1236	-0.1106	-12953.34859	1236	-0.10872
Heyrovsky								
IS			TS			FS		
F(n)	n	mu	F(n)	n	mu	F(n)	n	mu
-12953.69694	1235	-0.13914	-12953.6652	1235	-0.13916	-12953.6677	1235	-0.14117
-12953.82861	1236	-0.1234	-12953.79622	1236	-0.12325	-12953.80217	1236	-0.12735
-12953.94385	1237	-0.10725	-12953.91057	1237	-0.10644	-12953.92295	1237	-0.1143

Table S6-2. Total energy (F), number of electrons (n), electrochemical potential (mu) for all elementary reactions considered in this study.

A	Cu	H ₂	CO	Methane	Formic Acid	Ethylene	Ethanol	Others	Total FE	Total Current (mA/cm ²)
	Average	46%	5%	10%	14%	17%	6%	1%	99%	2.73
	SEM	6%	1%	2%	2%	4%	3%	0%	3%	0.09
	STD	10%	1%	3%	4%	6%	5%	0%	5%	0.15
	<i>Trial 1</i>	41%	4%	9%	9%	22%	8%	1%	94%	2.90
	<i>Trial 2</i>	57%	5%	8%	16%	10%	0%	1%	98%	2.64
	<i>Trial 3</i>	40%	6%	14%	16%	18%	10%	1%	105%	2.64

B	Cu ₂ O	H ₂	CO	Methane	Formic Acid	Ethylene	Ethanol	Others	Total FE	Total Current (mA/cm ²)
	Average	39%	1%	0%	6%	35%	10%	2%	95%	1.61
	SEM	3%	0%	0%	1%	2%	1%	0%	1%	0.07
	STD	5%	0%	0%	1%	3%	2%	0%	3%	0.11
	<i>Trial 1</i>	36%	1%	1%	7%	37%	11%	2%	94%	1.58
	<i>Trial 2</i>	45%	1%	0%	5%	31%	12%	2%	97%	1.73
	<i>Trial 3</i>	37%	1%	1%	7%	36%	9%	2%	92%	1.51

Table S6-3. Faradaic efficiencies of CO₂RR and total current for (A) Cu and (B) Cu₂O, reported in Fig. 2E.

6.11. Acknowledgements

This study is based on work performed at the Joint Center for Artificial Photosynthesis, a DOE Energy Innovation Hub, supported through the Office of Science of the U.S. Department of Energy under Award Number DE-SC0004993. Work at the Molecular Foundry was supported by the Office of Science, Office of Basic Energy Sciences, of the U.S. Department of Energy under Contract No. DE-AC02-05CH11231. These studies used the Extreme Science and Engineering Discovery Environment (XSEDE), which is supported by National Science Foundation Grant ACI-1548562.

REFERENCES

1. Shih, C. F.; Zhang, T.; Li, J.; Bai, C., Powering the Future with Liquid Sunshine. *Joule* **2018**, *2* (10), 1925-1949.
2. De Luna, P.; Hahn, C.; Higgins, D.; Jaffer, S. A.; Jaramillo, T. F.; Sargent, E. H., What would it take for renewably powered electrosynthesis to displace petrochemical processes? *Science* **2019**, *364* (6438), eaav3506.
3. Gao, D.; Arán-Ais, R. M.; Jeon, H. S.; Roldan Cuenya, B., Rational catalyst and electrolyte design for CO₂ electroreduction towards multicarbon products. *Nature Catalysis* **2019**, *2* (3), 198-210.
4. Nitopi, S.; Bertheussen, E.; Scott, S. B.; Liu, X.; Engstfeld, A. K.; Horch, S.; Seger, B.; Stephens, I. E. L.; Chan, K.; Hahn, C.; Nørskov, J. K.; Jaramillo, T. F.; Chorkendorff, I., Progress and Perspectives of Electrochemical CO₂ Reduction on Copper in Aqueous Electrolyte. *Chemical Reviews* **2019**, *119* (12), 7610-7672.
5. De Luna, P.; Quintero-Bermudez, R.; Dinh, C.-T.; Ross, M. B.; Bushuyev, O. S.; Todorović, P.; Regier, T.; Kelley, S. O.; Yang, P.; Sargent, E. H., Catalyst electro-redeposition controls morphology and oxidation state for selective carbon dioxide reduction. *Nature Catalysis* **2018**, *1* (2), 103-110.
6. Jung, H.; Lee, S. Y.; Lee, C. W.; Cho, M. K.; Won, D. H.; Kim, C.; Oh, H.-S.; Min, B. K.; Hwang, Y. J., Electrochemical Fragmentation of Cu₂O Nanoparticles Enhancing Selective C–C Coupling from CO₂ Reduction Reaction. *Journal of the American Chemical Society* **2019**, *141* (11), 4624-4633.
7. Mistry, H.; Varela, A. S.; Bonifacio, C. S.; Zegkinoglou, I.; Sinev, I.; Choi, Y.-W.; Kisslinger, K.; Stach, E. A.; Yang, J. C.; Strasser, P.; Cuenya, B. R., Highly

selective plasma-activated copper catalysts for carbon dioxide reduction to ethylene.

Nature Communications **2016**, 7 (1), 12123.

8. Li, C. W.; Kanan, M. W. CO₂ Reduction at Low Overpotential on Cu Electrodes Resulting from the Reduction of Thick Cu₂O Films. *Journal of the American Chemical Society* **134**, 7231-7234 (2012).

9. Xiao, H.; Goddard, W. A.; Cheng, T.; Liu, Y., Cu metal embedded in oxidized matrix catalyst to promote CO₂ activation and CO dimerization for electrochemical reduction of CO₂. *Proceedings of the National Academy of Sciences* **2017**, 114 (26), 6685-6688.

10. Gao, D.; Zegkinoglou, I.; Divins, N. J.; Scholten, F.; Sinev, I.; Grosse, P.; Roldan Cuenya, B., Plasma-Activated Copper Nanocube Catalysts for Efficient Carbon Dioxide Electroreduction to Hydrocarbons and Alcohols. *ACS Nano* **2017**, 11 (5), 4825-4831.

11. Lee, S. Y.; Jung, H.; Kim, N.-K.; Oh, H.-S.; Min, B. K.; Hwang, Y. J., Mixed Copper States in Anodized Cu Electrocatalyst for Stable and Selective Ethylene Production from CO₂ Reduction. *Journal of the American Chemical Society* **2018**, 140 (28), 8681-8689.

12. Yang, P.-P.; Zhang, X.-L.; Gao, F.-Y.; Zheng, Y.-R.; Niu, Z.-Z.; Yu, X.; Liu, R.; Wu, Z.-Z.; Qin, S.; Chi, L.-P.; Duan, Y.; Ma, T.; Zheng, X.-S.; Zhu, J.-F.; Wang, H.-J.; Gao, M.-R.; Yu, S.-H., Protecting Copper Oxidation State via Intermediate Confinement for Selective CO₂ Electroreduction to C₂+ Fuels. *Journal of the American Chemical Society* **2020**.

13. Favaro, M.; Xiao, H.; Cheng, T.; Goddard, W. A.; Yano, J.; Crumlin, E. J., Subsurface oxide plays a critical role in CO₂ activation by Cu(111) surfaces to form chemisorbed CO₂, the first step in reduction of CO₂. *Proceedings of the National Academy of Sciences* **2017**, *114* (26), 6706-6711.
14. Mandal, L.; Yang, K. R.; Motapothula, M. R.; Ren, D.; Lobaccaro, P.; Patra, A.; Sherburne, M.; Batista, V. S.; Yeo, B. S.; Ager, J. W.; Martin, J.; Venkatesan, T., Investigating the Role of Copper Oxide in Electrochemical CO₂ Reduction in Real Time. *ACS Applied Materials & Interfaces* **2018**, *10* (10), 8574-8584.
15. Lum, Y.; Ager, J. W., Stability of Residual Oxides in Oxide-Derived Copper Catalysts for Electrochemical CO₂ Reduction Investigated with ¹⁸O Labeling. *Angewandte Chemie International Edition* **2018**, *57* (2), 551-554.
16. Kwon, Y.; Lum, Y.; Clark, E. L.; Ager, J. W.; Bell, A. T., CO₂ Electroreduction with Enhanced Ethylene and Ethanol Selectivity by Nanostructuring Polycrystalline Copper. *ChemElectroChem* **2016**, *3* (6), 1012-1019.
17. Jiang, K.; Huang, Y.; Zeng, G.; Toma, F. M.; Goddard, W. A.; Bell, A. T., Effects of Surface Roughness on the Electrochemical Reduction of CO₂ over Cu. *ACS Energy Letters* **2020**, 1206-1214.
18. Huang, Y.; Nielsen, R. J.; Goddard, W. A. Reaction Mechanism for the Hydrogen Evolution Reaction on the Basal Plane Sulfur Vacancy Site of MoS₂ Using Grand Canonical Potential Kinetics. *Journal of the American Chemical Society* **140**, 16773-16782 (2018).

19. Peterson, A. A.; Abild-Pedersen, F.; Studt, F.; Rossmeisl, J.; Nørskov, J. K. How copper catalyzes the electroreduction of carbon dioxide into hydrocarbon fuels. *Energy & Environmental Science* **3**, 1311-1315 (2010).
20. Nie, X.; Esopi, M. R.; Janik, M. J.; Asthagiri, A. Selectivity of CO₂ Reduction on Copper Electrodes: The Role of the Kinetics of Elementary Steps. **52**, 2459-2462 (2013).
21. Calle-Vallejo, F.; Koper, M. T. M. Theoretical Considerations on the Electroreduction of CO to C₂ Species on Cu(100) Electrodes. **52**, 7282-7285 (2013).
22. Nie, X.; Luo, W.; Janik, M. J.; Asthagiri, A. Reaction mechanisms of CO₂ electrochemical reduction on Cu(111) determined with density functional theory. *Journal of Catalysis* **312**, 108-122 (2014).
23. Luo, W.; Nie, X.; Janik, M. J.; Asthagiri, A. Facet Dependence of CO₂ Reduction Paths on Cu Electrodes. *ACS Catalysis* **6**, 219-229 (2016).
24. Cheng, T.; Xiao, H.; Goddard, W. A. Full atomistic reaction mechanism with kinetics for CO reduction on Cu(100) from ab initio molecular dynamics free-energy calculations at 298 K. *Proceedings of the National Academy of Sciences* **114**, 1795-1800 (2017).
25. Kas, R. *et al.*, Electrochemical CO₂ reduction on Cu₂O-derived copper nanoparticles: controlling the catalytic selectivity of hydrocarbons. *Physical Chemistry Chemical Physics* **16**, 12194-12201 (2014).
26. Lum, Y.; Yue, B.; Lobaccaro, P.; Bell, A. T.; Ager, J. W. Optimizing C–C Coupling on Oxide-Derived Copper Catalysts for Electrochemical CO₂ Reduction. *The Journal of Physical Chemistry C* **121**, 14191-14203 (2017).

27. Dinh, C.-T. *et al.*, CO₂ electroreduction to ethylene via hydroxide-mediated copper catalysis at an abrupt interface. **360**, 783-787 (2018).
28. Eilert, A. *et al.*, Subsurface Oxygen in Oxide-Derived Copper Electrocatalysts for Carbon Dioxide Reduction. *The Journal of Physical Chemistry Letters* **8**, 285-290 (2017).
29. Li, Y. *et al.*, Electrochemically scrambled nanocrystals are catalytically active for CO₂-to-multicarbon. *Proceedings of the National Academy of Sciences* **117**, 9194-9201 (2020).
30. Ebaid, M. *et al.*, Production of C₂/C₃ Oxygenates from Planar Copper Nitride-Derived Mesoporous Copper via Electrochemical Reduction of CO₂. *Chemistry of Materials* **32**, 3304-3311 (2020).
31. Garza, A. J.; Bell, A. T.; Head-Gordon, M. Is Subsurface Oxygen Necessary for the Electrochemical Reduction of CO₂ on Copper? *The Journal of Physical Chemistry Letters* **9**, 601-606 (2018).
32. Eilert, A.; Roberts, F. S.; Friebel, D.; Nilsson, A. Formation of Copper Catalysts for CO₂ Reduction with High Ethylene/Methane Product Ratio Investigated with In Situ X-ray Absorption Spectroscopy. *The Journal of Physical Chemistry Letters* **7**, 1466-1470 (2016).
33. Cavalca, F. *et al.*, Nature and Distribution of Stable Subsurface Oxygen in Copper Electrodes During Electrochemical CO₂ Reduction. *The Journal of Physical Chemistry C* **121**, 25003-25009 (2017).
34. Huang, Y.; Chen, Y.; Cheng, T.; Wang, L.-W.; Goddard, W. A. Identification of the Selective Sites for Electrochemical Reduction of CO to C₂₊ Products on Copper

Nanoparticles by Combining Reactive Force Fields, Density Functional Theory, and Machine Learning. *ACS Energy Letters* **3**, 2983-2988 (2018).

35. Kresse, G.; Hafner, J., Ab initio molecular-dynamics simulation of the liquid-metal--amorphous-semiconductor transition in germanium. *Physical Review B* **1994**, *49* (20), 14251-14269.

36. Kresse, G.; Furthmüller, J., Efficient iterative schemes for ab initio total-energy calculations using a plane-wave basis set. *Physical Review B* **1996**, *54* (16), 11169-11186.

37. Mathew, K.; Sundararaman, R.; Letchworth-Weaver, K.; Arias, T. A.; Hennig, R. G., Implicit solvation model for density-functional study of nanocrystal surfaces and reaction pathways. **2014**, *140* (8), 084106.

38. Sundararaman, R.; III, W. A. G., The charge-asymmetric nonlocally determined local-electric (CANDLE) solvation model. **2015**, *142* (6), 064107.

39. Sundararaman, R.; Letchworth-Weaver, K.; Schwarz, K. A.; Gunceler, D.; Ozhabes, Y.; Arias, T. A., JDFTx: Software for joint density-functional theory. *SoftwareX* **2017**, *6*, 278-284.

40. Perdew, J. P.; Burke, K.; Ernzerhof, M., Generalized Gradient Approximation Made Simple. *Physical Review Letters* **1996**, *77* (18), 3865-3868.

41. Johnson, E. R.; Becke, A. D., A post-Hartree-Fock model of intermolecular interactions: Inclusion of higher-order corrections. **2006**, *124* (17), 174104.

42. Blöchl, P. E., Projector augmented-wave method. *Physical Review B* **1994**, *50* (24), 17953-17979.

43. Monkhorst, H. J.; Pack, J. D., Special points for Brillouin-zone integrations. *Physical Review B* **1976**, *13* (12), 5188-5192.
44. Henkelman, G.; Uberuaga, B. P.; Jónsson, H., A climbing image nudged elastic band method for finding saddle points and minimum energy paths. **2000**, *113* (22), 9901-9904.
45. Henkelman, G.; Jónsson, H., A dimer method for finding saddle points on high dimensional potential surfaces using only first derivatives. **1999**, *111* (15), 7010-7022.

CHAPTER 7

OUTLOOK

7.1. Abstract

Selective transformation for sustainability does not only require a highly selective catalyst but also a sustainable catalyst that can be achieved by developing a selective catalyst from earth-abundant elements. Nature shows its superior ability by providing highly efficient enzymatic reaction space with an earth-abundant catalyst to perform selective transformations. Through this thesis, we gain an understanding of the importance of the catalytic microenvironment in developing these highly selective and sustainable catalysts in homogeneous and heterogeneous systems. The developed catalysts show potential to be further tuned and improved for more cost-, energy-, and atom-efficient processes.

7.2. Conclusions

This thesis is inspired by nature's ability to provide highly efficient enzymatic systems where earth-abundant elements catalyze chemical transformations with high selectivity. This selectivity is achieved within a uniquely tailored, confined reaction space called enzymatic pocket. Our observation motivates us to develop highly selective catalysts with similar design principles as an enzymatic pocket by emphasizing in tuning the microenvironments surrounding the metal centers. Throughout this thesis, we demonstrate that tuning catalytic microenvironments allow us to gain selectivity control in various chemical processes. By utilizing earth-abundant elements, we also provide catalysts design strategy that will enable us to achieve selective transformation for sustainability.

In the homogeneous catalyst system, we provide a unique approach to improve the

selectivity of the reaction through tuning the first and second coordination sphere of the catalyst. In the first study on selective transformation for epoxide transformation to β -amino alcohol, we report that changing the conformation of the catalyst from trans to cis- β conformation improves the selectivity of the catalyst because the cis- β conformation provides a highly selective and active catalytic pocket needed for the epoxide transformation. We further improve the catalyst's selectivity by designing the catalyst to resemble a confined reaction space through tuning its interaction with the counter-anion and solvent. Ultimately, this catalyst design allows for the development of a highly regioselective general methodology for nucleophilic ring-opening of trans-2,3-disubstituted epoxides.

In heterogeneous catalytic systems, we present design strategies for the synthesis of novel electrocatalysts for the electrochemical carbon dioxide reduction, where we utilize metal-organic frameworks (MOFs) due to their unique properties that have the tunability of molecular catalysts and the stability of the heterogeneous catalyst and their ability to provide tailored confined reaction space for CO₂ reduction. We demonstrate that the confined reaction space provided by MIL-53 organic framework imparts atypical catalytic capabilities to Al metals that traditionally are inactive for CO₂R. We further elucidate the mechanism of catalytic transformation of the metal centers in MIL-53 framework using *in situ* and *ex situ* XAS allowing for a better understanding of how the microenvironments improve the metal centers' selectivity toward CO₂R. Additionally, after investigating the role of surface and subsurface oxygen on the production of hydrocarbon from CO₂ reduction over copper electrocatalysts, we gain an understanding of the factors necessary to obtain a more

energy-dense hydrocarbon like ethylene. Overall, in addition to presenting unique design strategies for electrocatalysts for CO₂R, we have also gathered important mechanistic understanding to gain control over selectivity toward a more cost- and energy-efficient electrochemical CO₂R.



Figure 7-1. The developed selective transformations in this thesis can offer solutions for the highlighted UN SDGs.¹

Finally, achieving selective transformation with the reported catalyst design strategies in this thesis for the chemical processes contributes to our effort to achieve sustainability. The selective epoxide transformations and selective electrochemical CO₂R processes can offer solutions in increasing energy efficiencies, reducing GHG emissions, developing sustainable materials, and promoting new uses of current waste that are aligned with the UN SDGs, including the goal for affordable and clean energy; industry, innovation, and infrastructure; responsible consumption and production; and climate action.¹

7.3. Future direction

To achieve energy-, cost-, and atom-efficient processes, it is crucial to transition to heterogeneous catalysis. While homogeneous catalysts can be systematically tuned to achieve high activity and selectivity through organic synthesis, they are often expensive because of the complexity of the synthesis and it cannot be recycled.²⁻⁴ On the other hand, heterogeneous catalysts are often inexpensive and can be recycled but difficult to precisely control the activity and selectivity.^{5,6} Therefore, the development of new catalytic materials that can combine the tunability of homogeneous catalyst and the stability of heterogeneous catalyst becomes important to achieve sustainable selective transformations (**Figure 7-2**).⁷ The development of new materials such as metal-organic frameworks (MOFs) and covalent organic frameworks (COFs) that allows for the combination of properties of homogeneous and heterogeneous catalysis have demonstrated the influence of tailoring the catalytic microenvironment catalysts' performance.⁸ Our work present new opportunity to tune catalytic microenvironments to control catalysts' selectivity and activity in various systems.

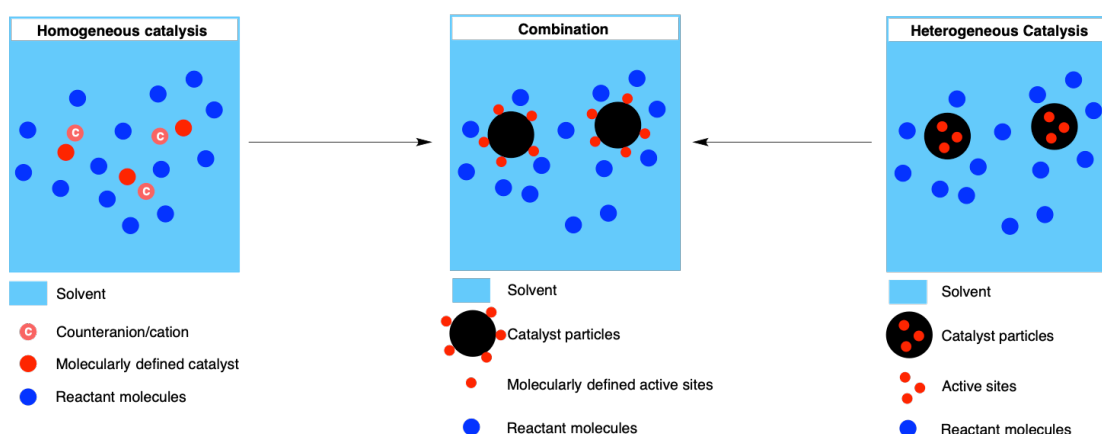


Figure 7-2. The combination of homogeneous and heterogeneous catalysis allows for more stable catalysts particle with molecularly defined active sites.

Transitioning to MOFs or COFs provides new control over selectivity by tuning the catalytic microenvironment. It also can impart atypical capabilities to metals as we demonstrate in this thesis. **Figure 7-3** illustrates the new opportunity to further explore the effect of confined reaction space on metal centers for metal that traditionally is not active for CO₂R. Utilizing the MIL-53(Al), the only reported MOF that can produce both CO and formic acid at ~1:1 ratio, as the basic framework, future work can involve tuning the highly modular MIL-53 framework to further improve the selectivity and activity for electrochemical CO₂R. This framework has three tunable properties that include its porosity that can be tuned by changing the length of the terephthalate linker, its electronic properties, and its surface hydrophobicity or hydrophilicity that can be tuned by varying the substituents in the linker. The MIL-53 framework can also be further improved by attaching substituents that can improve its interaction with CO₂ molecules. Through these systematic tunings, we can gain an understanding of controlling the selectivity and activity for the CO₂R products, not only for the C₁ products but also for the further downstream products, such as ethylene and ethanol.

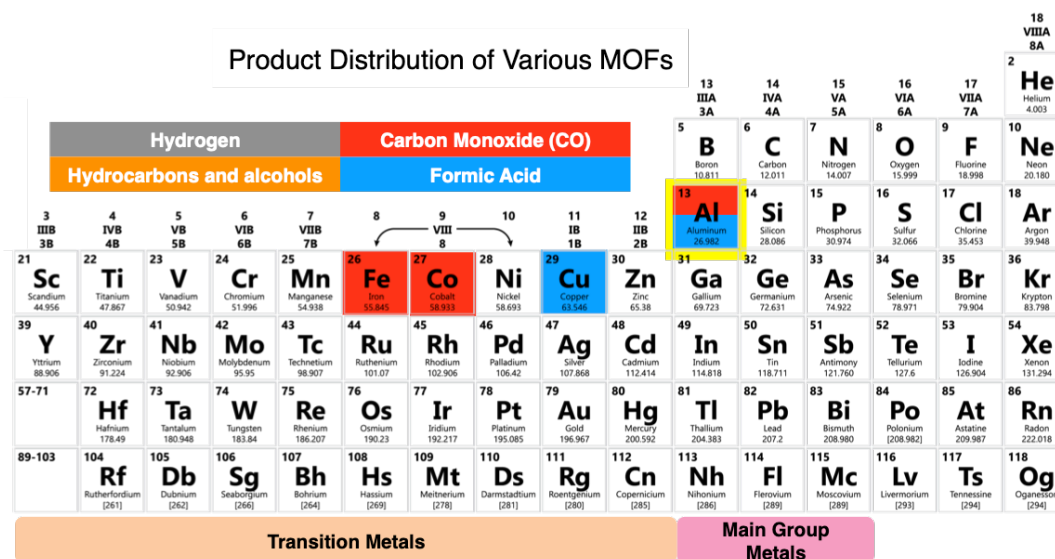


Figure 7-3. Maps of product distribution of various metal-organic frameworks (MOFs) as electrocatalysts for CO₂R.^{4, 9-12}

Additionally, understanding the importance of subsurface oxygen on copper, we can further optimize copper as electrocatalyst for CO₂R by developing novel organic modifiers that can continuously supply oxygen to the copper catalyst to achieve selective transformation toward ethylene. The novel organic modifiers can be in the form of MOFs, COFs, or other 2D materials that can provide a confined reaction space for improved CO₂R activity. These materials should have the ability to improve CO₂ concentration on the surface of copper catalysts to further improve the rate of the reaction. Finally, with the new mechanistic understanding, we accumulate in controlling the selectivity toward CO₂R, we look forward to the development of CO₂R electrocatalysts for more energy-dense products, such as the C₃ products that include propionaldehyde.

REFERENCES

1. Ritchie, Roser, Mispy, Ortiz-Ospina. "Measuring progress towards the Sustainable Development Goals." SDG-Tracker.org, website (2018)
2. Descorme, C.; Gallezot, P.; Geantet, C.; George, C., Heterogeneous Catalysis: A Key Tool toward Sustainability. *ChemCatChem* **2012**, 4 (12), 1897-1906.
3. Kuhl, K. P.; Cave, E. R.; Abram, D. N.; Jaramillo, T. F., New insights into the electrochemical reduction of carbon dioxide on metallic copper surfaces. *Energy & Environmental Science* **2012**, 5 (5).
4. Lin, S.; Diercks, C. S.; Zhang, Y.-B.; Kornienko, N.; Nichols, E. M.; Zhao, Y.; Paris, A. R.; Kim, D.; Yang, P.; Yaghi, O. M.; Chang, C. J., Covalent organic frameworks comprising cobalt porphyrins for catalytic CO₂ reduction in water. *Science* **2015**, 349 (6253), 1208-1213.
5. Zhang, S.; Kang, P.; Meyer, T. J., Nanostructured Tin Catalysts for Selective Electrochemical Reduction of Carbon Dioxide to Formate. *Journal of the American Chemical Society* **2014**, 136 (5), 1734-1737.
6. Zhu, W.; Michalsky, R.; Metin, Ö.; Lv, H.; Guo, S.; Wright, C. J.; Sun, X.; Peterson, A. A.; Sun, S., Monodisperse Au Nanoparticles for Selective Electrocatalytic Reduction of CO₂ to CO. *Journal of the American Chemical Society* **2013**, 135 (45), 16833-16836.
7. Diercks, C. S.; Liu, Y.; Cordova, K. E.; Yaghi, O. M., The role of reticular chemistry in the design of CO₂ reduction catalysts. *Nat Mater* **2018**, 17 (4), 301-307.

8. Zhang, Y.; Pang, S.; Wei, Z.; Jiao, H.; Dai, X.; Wang, H.; Shi, F., Synthesis of a molecularly defined single-active site heterogeneous catalyst for selective oxidation of N-heterocycles. *Nature Communications* **2018**, *9* (1), 1465.
9. Hod, I.; Sampson, M. D.; Deria, P.; Kubiak, C. P.; Farha, O. K.; Hupp, J. T., Fe-Porphyrin-Based Metal–Organic Framework Films as High-Surface Concentration, Heterogeneous Catalysts for Electrochemical Reduction of CO₂. *ACS Catalysis* **2015**, *5* (11), 6302-6309.
10. Lee, M.; De Riccardis, A.; Kazantsev, R.; Cooper, J. K.; Buckley, A.; Burroughs, P.; Larson, D.; Mele, G.; Toma, F. M., Aluminum Metal Organic Framework Triggers Carbon Dioxide Reduction Activity. *ACS Applied Energy Materials* **2020**.
11. Kornienko, N.; Zhao, Y.; Kley, C. S.; Zhu, C.; Kim, D.; Lin, S.; Chang, C. J.; Yaghi, O. M.; Yang, P., Metal-organic frameworks for electrocatalytic reduction of carbon dioxide. *J Am Chem Soc* **2015**, *137* (44), 14129-35.
12. Hinogami, R.; Yotsuhashi, S.; Deguchi, M.; Zenitani, Y.; Hashiba, H.; Yamada, Y., Electrochemical Reduction of Carbon Dioxide Using a Copper Rubeanate Metal Organic Framework. *ECS Electrochemistry Letters* **2012**, *1* (4), H17-H19.